Petersburg Nuclear Physics Institute named by B.P. Konstantinov of National Research Centre «Kurchatov Institute»



Anatolii Iurevich Egorov

# Search for BFKL evolution effects in dijet production with large rapidity separation at energies of the Large Hadron Collider

Scientific specialization 1.3.15. Physics of atomic nuclei and elementary particles, high energy physics

Dissertation is submitted for the degree
of Candidate of Physical and Mathematical Sciences

Translation from Russian



Scientific Supervisor
Doctor in Physical and Mathematical Sciences
Victor Timofeevich Kim

Gatchina — 2024

## Contents

## Introduction

In search for new physics phenomena at existing and future hadron colliders, it is important to correctly take into account the effects of quantum chromodynamics (QCD). As the energy in the center of mass of colliding hadrons, $\sqrt{s}$, increases, the source of strong interaction is expected to be processes of scattering of quarks and gluons in the high-energy semi-hard QCD regime. In this regime, $\sqrt{s} \to \infty$, and the interaction scale, $Q$, remains finite $Q = const \ll \sqrt{s}$, but large enough to allow the use of perturbative QCD, that is, $Q \gg \Lambda_{\rm QCD} \sim 200$ MeV. In the semi-hard high-energy regime, corrections enhanced by large logarithms of $s$ have to be summed, which was achieved within the framework of the Balitsky–Fadin–Kuraev–Lipatov (BFKL) formalism [1—3] in the leading logarithmic (LL) approximation.

Currently, to calculate processes within the Standard model and beyond when searching for new physics, another QCD asymptotics is mainly used, namely the hard QCD regime. In the hard QCD regime $Q \sim \sqrt{s} \to \infty$ with a fixed ratio $Q/\sqrt{s} \simeq x = \text{const}$, therefore the summation of contributions enhanced by large logarithms of $Q$ is required. This was achieved within the framework of the Gribov–Lipatov–Altarelli–Parisi–Dokshitzer formalism (GLAPD). [4—8].

The GLAPD evolution has been well tested at the HERA [9], Tevatron [10] and LHC [11] colliders. At the same time, the results of the search for signals of the BFKL evolution remain ambiguous. On the one hand, difficulties in interpreting experimental results are due to the fact that to compare theoretical calculations and experimental data, predictions of the BFKL formalism in the next-to-leading logarithmic (NLL) approximation are required. The LL approximation of the BFKL evolution being designed for infinite energy limit makes only qualitative predictions, mainly overestimating possible effects at energies available currently in experiments. This is due to the fact that the LL BFKL approximation overestimates the pomeron intercept, predicting its value to be approximately 1.54. The NLL BFKL approximation gives a more realistic estimate of $1.13 - 1.18$ [12—14]. The pomeron intercept is responsible for the growth of the inclusive cross sections with $\sqrt{s}$ and rapidity, $y$. At the moment, methods for calculating with the NLL BFKL approximation have been developed for a small fraction of experimentally measured observables.

On the other hand, the GLAPD predictions, often obtained using Monte Carlo (MC) methods implemented in collision generator software packages, contain corrections beyond the basic GLAPD approximation. Since the search for signals of new effects of the BFKL evolution is carried out as an observation of deviations from the predictions of the GLAPD evolution, it turns out that it is critical to take into account corrections for color coherence added to generators based on the GLAPD evolution. Color coherence leads to additional angular ordering of the emission, which partially reproduces the $y$-ordering of the BFKL formalism. These corrections are small in the domain of the GLAPD formalism and lead to an improvement in the phenomenological description for small $y$. However, they become unstable as $\sqrt{s}$ increases (for a fixed $Q$) or $y$ increases. The presence of corrections for color coherence complicates the interpretation of experimental data, since it is not possible to separate the contributions of the GLAPD logarithms and color coherence. Modern MC generators based on the GLAPD evolution, such as PYTHIA8 [15] and HERWIG [16], do not provide the opportunity to disable color coherence.

Thus, the program for searching for BFKL signals can be developed in several directions. On the experimental side, it is necessary to measure existing observables that are sensitive to the BFKL effects at all available energies and rapidities, since the BFKL and GLAPD evolutions have different $\sqrt{s}$ and $y$ dependences. On the theoretical side, it is necessary to develop calculation methods taking into account the NLL BFKL corrections for measured observables, as well as the development of new observables that are sensitive to possible signals of the BFKL evolution that can be measured. The developed calculation methods can be used in calculations within the Standard model and beyond when interpreting the results of searches for new physics phenomena at colliders.

Currently, to search for signals of the BFKL evolution at hadron colliders, the production of hadron jets in the region of large absolute values of rapidity, $y$, and the production of pairs of hadron jets (dijets) with a large rapidity separation $\Delta y = |y_1 - y_2|$ are studied, where $y_1$ and $y_2$ - rapidities of jets in a pair. Among the existing observables using hadronic jets or dijets, three main types can be distinguished.

The first type includes the measurement of cross sections for the production of jets in the region of large rapidity or dijets with large $\Delta y$, as well as the ratio of cross sections measured at different energies, or with introduced jet veto conditions [17—19]. The veto condition means experimental selection of the events without of the presence of additional hadronic jets in some regions of phase space.

The BFKL evolution predicts an increase of cross sections with $\sqrt{s}$ and $\Delta y$, with the maximum contribution to the cross section expected from dijets with the maximum $\Delta y$ in an event (collision) with transverse momentum of jets forming dijets above a predetermined threshold $p_{\perp\min} \ll \sqrt{s}$. Such jet pairs are called the Mueller-Navelet (MN) dijets. The MN jet pairs are a subset of the inclusive jet pairs, that is, all pairwise jet combinations with $p_\perp > p_{\perp\min}$ in the event [18].

The second type includes the measurement of azimuthal decorrelations between two jets with large $\Delta y$ [20—22]. The diffusion of QCD emission in the transverse momentum, $p_\perp$, which is predicted in the BFKL formalism, leads to an increase of the decorrelation in the transverse plane between the jets with increasing $\Delta y$ between them. At the same time, the strict $p_\perp$-ordering of emission in the GLAPD formalism should leave pairs of the hardest jets strongly correlated in the plane transverse to the axis of the colliding particles.

The third type includes the measurement of events of dijet production with rapidity gap between the jets in the dijet [23—25]. Where the rapidity gap is understood as a region of rapidity in which hadronic activity is completely absent. The rapidity gap is a sign of exchange of a color singlet, which can be described by the pomeron solution of the BFKL equation.

The production of forward jets (jets with large rapidity) was measured at the HERA electron-proton ($ep$) collider for $\sqrt{s}$ up to 319 GeV in the H1 [26; 27] experiment for jets with transverse momentum $p_\perp > 6$ GeV and rapidity $y < 2.79$ and in the ZEUS [28; 29] experiment for $p_\perp > 5$ GeV and $y < 4.3$ . All the listed types of observables were measured in proton-antiproton ($p\bar{p}$) collisions in experiments D0 [30—32] and CDF [33] on the Tevatron for $\sqrt{s} = 0.63$ and 1.8 TeV for $\Delta y < 6$ and $p_\perp > 20$ GeV. Similar measurements were carried out in proton-proton ($pp$) collisions at $\sqrt{s} = 7$ TeV at the LHC collider in the ATLAS [34; 35] experiment for $\Delta y < 8$ and $p_\perp > 60$ GeV and the CMS [36—39] experiment for $\Delta y < 9.4$ and $p_\perp > 35$ GeV. The color singlet exchange process was also measured at the LHC at the higher energy $\sqrt{s} = 13$ TeV in the CMS-TOTEM experiment [40].

Summarizing the results of all previous searches for signals of the BFKL evolution, we can say that none of the considered models based on the GLAPD evolution is capable of describing the entire set of observables, despite the fact that these models include color coherence. At the same time, calculations based on the BFKL evolution, taking into account the NLL corrections developed for some observables, are consistent with experimental data. However, there is no method for

calculating in the NLL BFKL approximation for major fraction of the observables. In particular, this situation occurs for the inclusive and MN cross sections for the production of pairs of hadronic jets with the veto on additional jets [34; 37].

In this paper, we consider the following observables related to the first of the listed types, $\Delta y$-differential cross sections:

$$\begin{aligned} &d\sigma^{\text{incl}}/d\Delta y, \\ &d\sigma^{\text{MN}}/d\Delta y, \end{aligned} \tag{1}$$

and the ratios of cross sections with veto:

$$\begin{aligned} R^{\text{incl}} &= (d\sigma^{\text{incl}}/d\Delta y)/(d\sigma^{\text{excl}}/d\Delta y), \\ R^{\text{MN}} &= (d\sigma^{\text{MN}}/d\Delta y)/(d\sigma^{\text{excl}}/\Delta y), \\ R^{\text{incl}}_{\text{veto}} &= (d\sigma^{\text{incl}}/d\Delta y)/(d\sigma^{\text{excl}}_{\text{veto}}/d\Delta y), \\ R^{\text{MN}}_{\text{veto}} &= (d\sigma^{\text{MN}}/d\Delta y)/(d\sigma^{\text{excl}}_{\text{veto}}/d\Delta y), \end{aligned} \tag{2}$$

where $\sigma^{\text{incl}}$ is the inclusive cross section in which each pairwise combination of jets with $p_\perp > p_{\perp\min}$ contributes to the cross section; $\sigma^{\text{MN}}$ is the MN cross section in which the pair of jets with maximum $\Delta y$ among jets with $p_\perp > p_{\perp\min}$ contributes to the cross section; $\sigma^{\text{excl}}$ is the «exclusive» cross section in which events with strictly one pair of jets with $p_\perp > p_{\perp\min}$ contribute; $\sigma^{\text{excl}}_{\text{veto}}$ is the «exclusive» with veto cross section. «Exclusive» events, in which there are no additional jets with $p_\perp > p_{\perp\text{veto}}$, contribute to $\sigma^{\text{excl}}_{\text{veto}}$. It should be noted that $\sigma^{\text{excl}}$ becomes the cross section for events with jet veto condition $p_{\perp\text{veto}} = p_{\perp\min}$.

It is known that theoretical calculations tend to describe the ratios of the cross sections better than their absolute values, because the contributions of some uncertainties can be dropping out in the ratios. However, some important effects in the cross section rations can be also canceled out, therefore, measuring the absolute values of cross sections will allow for more rigorous testing of theoretical models. The ratios of the cross sections $R^{\text{incl}}$ and $R^{\text{MN}}$ were measured previously in $pp$ collisions at $\sqrt{s} = 7$ TeV [37]. Observing the energy dependence of these observables is of interest, since the GLAPD and BFKL evolutions predict different behavior with $\sqrt{s}$ and $\Delta y$. In the work [19] it was shown on the basis of MC modeling that $R^{\text{incl}}_{\text{veto}}$ and $R^{\text{MN}}_{\text{veto}}$ are more sensitive to possible signals of the BFKL evolution.

**The goal** of this thesis is a search for the BFKL effects in dijet production with large rapidity separation in $pp$ collisions at $\sqrt{s} = 2.76$ TeV at the Large Hadron Collider (LHC).

To achieve the goal, the following **tasks** were solved:

1. To develop a measuring technique for the differential cross sections for the production of the MN dijets, $d\sigma^{\rm MN}/d\Delta y$, and the inclusive dijets, $d\sigma^{\rm incl}/d\Delta y$, as well as for the ratios of the differential cross sections for dijet production with veto, $R^{\rm MN}$, $R^{\rm incl}$, $R^{\rm MN}_{\rm veto}$, $R^{\rm incl}_{\rm veto}$, in $pp$ collisions at center-of-mass energy $\sqrt{s} = 2.76$ TeV using the CMS detector.
2. To perform calculations of measured observables using MC collision generators in various approximations. To obtain predictions with partonic subprocess in the leading order (LO) of perturbation theory improved by modeling parton showers in the LL approximation of the GLAPD evolution, which is implemented in the software generator packages PYTHIA8 [41] and HERWIG [16; 42]. To perform calculations with partonic subprocess taking into account the next-to-leading order (NLO) perturbation theory with the LL GLAPD parton showers in the software generator packages POWHEG+PYTHIA8 and POWHEG+HERWIG [43]. To obtain predictions in the LL BFKL approximation in the software package HEJ+ARIADNE [44; 45].
3. To calculate the differential cross section of the MN dijet production, $d\sigma^{\rm MN}/d\Delta y$, based on analytical expressions taking into account the NLL BFKL approximation [12—14; 46—48] for energy $\sqrt{s} = 2.76$ TeV.
4. To develop a method based on the Banfi–Marchesini–Smye equation (BMS) [49] to calculate the impact of the jet veto condition in the entire available rapidity interval. To calculate $R^{\rm incl}$ and compare with the CMS measurements for $pp$ collisions at $\sqrt{s} = 7$ TeV.
5. To develop a method for taking into account the veto condition based on the BMS equation for calculations within the framework of the NLL BFKL. To calculate in the NLL BFKL+BMS approximation the ratios of cross sections with veto $R^{\rm MN}$ and $R^{\rm MN}_{\rm veto}$ for $pp$ collisions at $\sqrt{s} = 2.76$ and 7 TeV and compare with the CMS measurements.
6. To obtain predictions for the differential MN dijet cross section, $d\sigma^{\rm MN}/d\Delta y$, taking into account the NLL BFKL corrections, and for the ratios of the MN cross sections at various energies (2.76, 8, 13 TeV) and for different $p_{\perp\rm min} = 35$ GeV and 20 GeV, as well as for the ratios of cross sections with veto $R^{\rm MN}$ and $R^{\rm MN}_{\rm veto}$ in the NLL BFKL+BMS approximation for $pp$

collisions at $\sqrt{s} = 13$ TeV, which can be measured in the CMS [50] and ATLAS [51] experiments at the LHC [11].

**Novelty of the research:**

1. A technique has been developed for measuring $\Delta y$-differential cross sections for the production of the MN dijets, $d\sigma^{\mathrm{MN}}/d\Delta y$, and the inclusive dijets, $d\sigma^{\mathrm{incl}}/d\Delta y$, as well as the ratios of cross sections with veto $R^{\mathrm{MN}}_{\mathrm{veto}}$ and $R^{\mathrm{incl}}_{\mathrm{veto}}$ as functions $\Delta y$. The technique for measuring the ratios of cross sections $R^{\mathrm{MN}}$ and $R^{\mathrm{incl}}$ as functions of $\Delta y$ has been modified. The developed and modified techniques comply with the new measurement standards of the CMS collaboration in Run II cycle of the LHC operation, and include the study of an extended set of systematic effects, as well as the use of new unfolding methods in the analysis of detector distortions.
2. The cross sections for dijet production $d\sigma^{\mathrm{MN}}/d\Delta y$, $d\sigma^{\mathrm{incl}}/d\Delta y$, as well as ratios of dijet cross sections with veto $R^{\mathrm{MN}}_{\mathrm{veto}}$ and $R^{\mathrm{incl}}_{\mathrm{veto}}$ were measured for the first time in $pp$ collisions at $\sqrt{s} = 2.76$ TeV and compared with predictions of models based on the LO+LL GLAPD: PYTHIA8, HERWIG++; NLO+LL GLAPD: POWHEG+PYTHIA8, POWHEG+HERWIG++, POWHEG+HERWIG7; and LL BFKL: HEJ+ARIADNE.
3. The ratios of dijet cross sections with veto $R^{\mathrm{MN}}$, $R^{\mathrm{incl}}$ were measured for the first time in $pp$ collisions at $\sqrt{s} = 2.76$ TeV, and a comparison was made with measurements performed earlier, at $\sqrt{s} = 7$ TeV, as well as a comparison with predictions of models based on the LO+LL GLAPD: PYTHIA8, HERWIG++; NLO+LL GLAPD: POWHEG+PYTHIA8, POWHEG+HERWIG++, POWHEG+HERWIG7; and LL BFKL: HEJ+ARIADNE.
4. For the first time, a comparison has been made of the NLL BFKL calculation for the differential cross section, $d\sigma^{\mathrm{MN}}/d\Delta y$, of the production of the MN dijets with the experimental data. New indications of the manifestation of the effects of the BFKL evolution in $pp$ collisions at $\sqrt{s} = 2.76$ TeV have been obtained. Predictions for $pp$ collisions at $\sqrt{s} = 8$ and 13 TeV are presented.
5. For the first time, taking into account the NLL full BFKL corrections, the ratios of the differential cross sections for the production of the MN dijets at different energies were calculated, namely: $R^{\mathrm{MN}}_{13/2.76}$ is the ratio of the MN cross section at $\sqrt{s} = 13$ TeV to the MN cross section at $\sqrt{s} = 2.76$ TeV;

$R^{\mathrm{MN}}_{8/2.76}$ is the same, but 8 TeV to 2.76 TeV and $R^{\mathrm{MN}}_{13/8}$ is the same, but 13 TeV to 8 TeV. The sensitivity of these ratios to signals of the BFKL evolution has been demonstrated.

6. For the first time, a method for calculating the inclusive cross sections for the dijet production with veto to additional jets with $p_\perp > p_{\perp\mathrm{veto}}$ in the entire rapidity interval is presented based on the solution of the BMS equation and a comparison is made with the experimental CMS data for $pp$ collisions at $\sqrt{s} = 7$ TeV.
7. For the first time, a method for calculating the MN dijet cross sections with veto on additional jets with $p_\perp > p_{\perp\mathrm{veto}}$ between the MN jets based on the NLL BFKL+BMS approximation is presented, and a comparison is made with the experimental CMS data for $pp$ collisions at $\sqrt{s} = 2.76$ and 7 TeV. Predictions is presented for $pp$ collisions at $\sqrt{s} = 13$ TeV.

**Practical significance:**

1. The obtained experimental data for the ratios of cross sections with veto $R^{\mathrm{MN}}$ and $R^{\mathrm{incl}}$ in $pp$ collisions at $\sqrt{s} = 2.76$ TeV, which were previously measured only for the energy $\sqrt{s} = 7$ TeV [37], allow us to observe the $\sqrt{s}$ dependence for these physical quantities. Which in turn is of interest for testing phenomenological MC models, such as PYTHIA [15], HERWIG [16], POWHEG [43], HEJ [44], ARIADNE [45], CASCADE [52], as well as analytical calculations within the framework of perturbative QCD.
2. The obtained experimental data for differential cross sections for the production of the MN dijets, $d\sigma^{\mathrm{MN}}/d\Delta y$, and the inclusive dijets, $d\sigma^{\mathrm{incl}}/d\Delta y$, as well as the ratios of cross sections with veto $R^{\mathrm{MN}}_{\mathrm{veto}}$ and $R^{\mathrm{incl}}_{\mathrm{veto}}$, which were measured for the first time, expands the existing set of observables for searching for signals of the BFKL evolution. It was previously shown on the basis of MC modelling that $R^{\mathrm{MN}}_{\mathrm{veto}}$ and $R^{\mathrm{incl}}_{\mathrm{veto}}$ are more sensitive to signals of the BFKL evolution than $R^{\mathrm{MN}}$ and $R^{\mathrm{incl}}$ [19]. Therefore, an expanded set of observables allows more rigorous testing of phenomenological MC models, including those listed in the previous item, and analytical calculations within the framework of perturbative QCD.
3. The technique presented in the thesis for measuring the differential production cross sections of the MN dijets, $d\sigma^{\mathrm{MN}}/d\Delta y$, and the inclusive dijets, $d\sigma^{\mathrm{incl}}/d\Delta y$, as well as the ratios of cross sections with veto $R^{\mathrm{MN}}$, $R^{\mathrm{incl}}$, $R^{\mathrm{MN}}_{\mathrm{veto}}$ and $R^{\mathrm{incl}}_{\mathrm{veto}}$ can be used to measure the production of dijets at

other energies in $pp$ collisions in the CMS and ATLAS experiments at the LHC collider, as well as in $p\bar{p}$ collisions in the D0 experiments and CDF at the Tevatron collider.

4. The presented comparison of experimental data and calculation results in the various GLAPD and BFKL approximations deepen our understanding of the important QCD contributions to the cross sections of processes at energies, $\sqrt{s}$, and rapidities, $y$, currently achievable in experiments, as well as allow one to improve the predictions of the Standard Model in the search for new physics.
5. The obtained predictions of $\Delta y$-differential cross sections for the production of the MN dijets in $pp$ collisions at $\sqrt{s} = 8$ and 13 TeV, as well as the ratios of the MN cross sections at different energies $R^{\rm MN}_{13/2.76}$, $R^{\rm MN}_{8/2.76}$, $R^{\rm MN}_{13/8}$, at different values of $p_{\perp\min} = 35$ and 20 GeV, can be used to search for signals of the BFKL evolution in measurements in the CMS and ATLAS experiments at the LHC.
6. The developed methods for applying the BMS equation to take into account the jet veto in the entire rapidity interval and in calculations of cross sections within the framework of the NLL BFKL approximation can be used in the development of methods for taking into account the veto, completely based on the evolution of BFKL.

**The statements and results put forward for defense:**

1. The $\Delta y$-differential cross sections for the production of the inclusive $d\sigma^{\rm incl}/d\Delta y$ and MN $d\sigma^{\rm MN}/d\Delta y$ dijets and the ratios of the cross sections $R^{\rm incl}_{\rm veto}$, $R^{\rm MN}_{\rm veto}$ were measured for the first time at $\sqrt{s} = 2.76$ TeV.
2. The ratios of cross sections $R^{\rm incl}$ and $R^{\rm MN}$ were measured for the first time in $pp$ collisions at $\sqrt{s} = 2.76$ TeV and compared with measurements performed earlier at $\sqrt{s} = 7$ TeV.
3. The new indications to the manifestation of BFKL effects in $pp$ collisions at $\sqrt{s} = 2.76$ TeV were obtained by measuring the absolute values of the cross sections $d\sigma^{\rm incl}/d\Delta y$ and $d\sigma^{\rm MN}/d\Delta y$. The absolute values of the cross sections $d\sigma^{\rm incl}/d\Delta y$ and $d\sigma^{\rm MN}/d\Delta y$ quickly fall at large values of $\Delta y$. The decline is faster than predicted by the GLAPD-based models PYTHIA8, HERWIG++, POWHEG+PYTHIA8/HERWIG++/ HERWIG7. The measured $\Delta y$-differential cross section for the production of the MN dijets,

$d\sigma^{\mathrm{MN}}/d\Delta y$, agrees within the limits of systematic uncertainties with the NLL BFKL calculation performed in this work.

4. The ratios of cross sections $R^{\mathrm{incl}}$, $R^{\mathrm{MN}}$, $R^{\mathrm{incl}}_{\mathrm{veto}}$, $R^{\mathrm{MN}}_{\mathrm{veto}}$ increase with increasing $\Delta y$, which is associated with an increase in the phase space for emission ordered in rapidity according to BFKL expectations. At the largest $\Delta y$, the increase gives way to a decrease, which is associated with kinematic limitations of the phase space on the emission of jets additional to the MN dijet. The ratios $R^{\mathrm{incl}}$ and $R^{\mathrm{MN}}$ increase faster at the energy $\sqrt{s} = 7$ TeV than at 2.76 TeV, and the transition from increase to decrease is observed at larger values of $\Delta y$.
5. The comparison of the measurements of the cross section ratios with veto $R^{\mathrm{incl}}$, $R^{\mathrm{MN}}$, $R^{\mathrm{incl}}_{\mathrm{veto}}$, $R^{\mathrm{MN}}_{\mathrm{veto}}$ with models using the $p_{\perp}$-ordered GLAPD parton shower with corrections for color coherence (PYTHIA8, HERWIG++, POWHEG+PYTHIA8/HERWIG++/HERWIG7, BMS evolution) demonstrate a strong dependence on the implementation of color coherence at large $\Delta y$. This indicates the need to take into account the jet veto based on the evolution of BFKL, as a formalism that consistently takes into account contributions at large $\Delta y$.

**Reliability.** The technique for measuring the $\Delta y$-differential inclusive cross sections for dijet production and their ratios with the veto was developed in accordance with the recommendations and standards of the CMS collaboration for the Run II cycle of the operation of the LHC collider. The methodology was tested and approved at intra-collaboration workshops and peer review. The developed programs for calculations within the framework of the evolution of BMS and NLL BFKL approximation, as well as calculations using MC software packages, were verified by reproducing the results of other authors. The reliability of the results is also ensured by their publication in peer-reviewed journals and approbation at international conferences.

**Approbation of the research.** The main results of the work were reported at 8 international conferences: 19th Annual Russia and Dubna Member States CMS Collaboration Conference 2016 (Varna, Bulgaria); 2nd CMS Workshop «Perspectives on Physics on CMS at HL-LHC» 2017 (Varna, Bulgaria); LII Winter School of Petersburg Nuclear Physics Institute NRC «Kurchatov Institute», 2018 (Roshchino, Russia); The 5th international conference on particle physics and astrophysics 2020 (Moscow, Russia); LXXII International conference «NUCLEUS

– 2022: Fundamental problems and applications» 2022 (Moscow, Russia); The 6th international conference on particle physics and astrophysics 2022 (Moscow, Russia); LV Winter School of Petersburg Nuclear Physics Institute NRC «Kurchatov Institute», 2023 (Luga, Russia); 21st Lomonosov conference on elementary particle physics 2023 (Moscow, Russia).

The results of the work were presented at seminars of the High Energy Physics Division of Petersburg Nuclear Physics Institute NRC «Kurchatov Institute» (Gatchina, Russia); at regular meetings of the working groups of the CMS collaboration (Geneva, Switzerland), namely: the Forward and Small-x Quantum Chromodynamics (FSQ) group, the Standard Model Physics (SMP) group, the Jet Energy Corrections and Resolution (JERC) group and the CMS Statistics Committee. In addition, the results of the work were presented at the V Annual Youth Scientific Forum «Open Science» 2018 (Gatchina, Russia).

**Personal contribution of the author.** The author made a decisive contribution to the analysis of experimental data in measuring the cross sections for dijet production (1) with large $\Delta y$ and the ratios of the dijet cross sections with the veto of additional jets (2) at $\sqrt{s} = 2.76$ TeV, namely: in the preparation of energy corrections for hadronic jets; in determining trigger efficiencies; in obtaining the $\Delta y$-differential dijet cross sections at the detector level; in the study of detector effects and the development of a procedure for eliminating detector distortions; in the classification and assessment of systematic uncertainties of the measurement; in modelling and calculation in various MC generators. The author made a decisive contribution to obtaining the results of calculation of the MN dijet cross sections at large $\Delta y$ taking into account the NLL BFKL corrections, and to assessing theoretical uncertainties. The author made a decisive contribution to obtaining the results of calculation of the impact of the jet veto condition. The author developed a technique for using the evolution of BMS to take into account the veto condition in the entire range of rapidity, $y$, and when calculating in the NLL BFKL approximation and made a decisive contribution to obtaining the results of calculations in the NLL BFKL+BMS approximation. The author made a significant contribution to the preparation of publications.

**Publications.** The main results of the dissertation are presented in 6 printed publications recommended by the Higher Attestation Commission (VAK) and indexed by Web of Science and Scopus.

## Publications of the author on the topic of the dissertation


A1. Study of dijet events with large rapidity separation in proton-proton collisions at $\sqrt{s} = 2.76$ TeV / A. I. Egorov, A. Tumasyan, [et al.] // JHEP. — 2022. — Vol. 03. — P. 189. — DOI: 10.1007/JHEP03(2022)189. — arXiv: 2111.04605 [hep-ex]. — (Scopus Q2, WoS Q1).

A2. *Egorov A. I.*, *Kim V. T.* Next-to-leading BFKL evolution for dijets with large rapidity separation at different LHC energies // Phys. Rev. D. — 2023. — Vol. 108, № 1. — P. 014010. — DOI: 10.1103/PhysRevD.108.014010. — arXiv: 2305.19854 [hep-ph]. — (Scopus Q1).

A3. *Egorov A. I.* Dijet Events with Large Rapidity Separation in Proton–Proton Collisions at $\sqrt{s}$= 2.76 TeV with CMS Detector // Phys. Atom. Nucl. — 2022. — Vol. 85, № 6. — P. 951. — DOI: 10.1134/S1063778823010192. — (VAK, Scopus).

A4. *Egorov A. Y.*, *Kim V. T.* Production of dijets with large rapidity separation at colliders // J. Phys. Conf. Ser. / ed. by P. Teterin. — 2020. — Vol. 1690, № 1. — P. 012158. — DOI: 10.1088/1742-6596/1690/1/012158. — (Scopus, WoS).

A5. *Egorov A. I.*, *Berdnikov Y. A.* Asymptotic effects in dijet production in proton-proton collisions at extremely high energies // St. Petersburg Polytech. Univ. J. Phys. Math. — 2019. — Vol. 12, № 2. — P. 118—125. — DOI: 10.18721/JPM.12210. — (VAK, Scopus, WoS).

A6. An analysis of unfolding methods for measurement of hadron dijet production cross sections / A. Y. Egorov [et al.] // St. Petersburg Polytech. Univ. J. Phys. Math. — 2019. — Vol. 12, № 3. — P. 123—130. — DOI: 10.18721/JPM.12310. — (VAK, Scopus, WoS).

**Thesis structure.** The thesis consists of introduction, 5 chapters and conclusion. The thesis contains 159 pages, including 37 figures and 7 tables. The bibliography includes 132 items.

# Chapter 1. Asymptotic regimes of QCD at high energy

## 1.1 GLAPD regime

The parton model was created to explain the results of experiments on deep inelastic scattering (DIS) of electrons on protons ($ep$ scattering) [53; 54]. In the parton model, a highly virtual or hard photon (or Z boson) is scattered by the proton's component, the parton, knocking it out of the proton. A parton in the naive parton model is a point-like charged particle. The hard scale of the process is determined by the virtuality of the photon $Q = \sqrt{-q^2} \gg m_p$, where $q$ is the four-momentum of the photon, $m_p$ is the mass of the proton. The characteristic time of the scattering $\sim 1/Q$ is significantly less than the characteristic time of processes inside the proton, which makes a coherent response impossible and indicates that the state of the proton is prepared long before the scattering. The significant difference in the scales of the hard subprocess and soft processes inside the proton qualitatively explains the factorization, while the point nature of the partons explains Bjorken scaling [55; 56]. The DIS cross section is factorized into the parton scattering cross section and the proton structure function. Bjorken scaling is expressed in the fact that the structure function depends only on the dimensionless scaling variable $x_{bj} = Q/(2Pq)$, where $P$ is the four-momentum of the proton before scattering. Within the parton model, $x_{bj}$ can be interpreted as the fraction of the proton momentum $x$ carried by the parton before scattering.

The calculation of perturbative QCD corrections to the parton subprocess leads to a violation of Bjorken scaling, namely, to the appearance of a dependence of structure functions on the scale $Q$. Qualitatively, this can be understood as follows. Suppose a probe (photon or Z boson) interacts with a quark on a scale of $Q_0$. The «resolution» of the probe is determined by its scale. As the probe scale increases to $Q > Q_0$, the «resolution» also increases, and it may turn out that the initial quark on the new scale is the quark and a gluon emitted before the interaction with the probe occurs. Thus, the fraction of the proton's momentum should be redistributed between the quark and the gluon, which will lead to a change in the structure function. Moreover, real gluon emission is known to carry collinear and infrared singularities. In the sufficiently inclusive observables, these

singularities cancel with those in the corresponding virtual diagram. However, in this case, the probe "distinguishes" between real and virtual contributions, which leads to the impossibility of cancellation and the need to take these corrections into account. It should be noted that the collinear and infrared singularity of the real gluon emission in the final state, after the interaction with the probe, is cancelled with the contribution of virtual corrections in the sufficiently inclusive observables.

With a further increase in the scale $\sqrt{s} \sim Q \to \infty$ of the probe, the quark undergoes splitting many times. Diagrams in which the splittings are strictly ordered by transverse momentum, $p_\perp$, turn out to be dominant, since each splitting becomes proportional to $\alpha_s \ln Q^2$, where $\alpha_s$ is the strong coupling constant. For a sufficiently large $Q$, the smallness of $\alpha_s$ is compensated by the large logarithm $\ln Q^2$. Moreover, $Q \to \infty$ allows one to have an infinite number of emissions strictly ordered in transverse momentum. Thus, the need arises to sum all terms $\sim [\alpha_s \ln Q^2]^n$ of the perturbative series. In the so-called Bjorken limit $\sqrt{s} \to \infty$ and $Q \to \infty$, so that $Q/\sqrt{s} \sim 1$, the leading logarithmic contributions $[\alpha_s \ln Q^2]^n$ can be summed up by considering a collinear singular domain, within the framework of the Gribov–Lipatov–Altarelli–Parisi–Dokshitzer (GLAPD) formalism [4—8]. A complete system of the GLAPD equations describing the evolution of structure functions with scale $Q$ can be obtained by considering the scattering of gluons (a strongly interacting probes) on a proton. In the leading logarithmic (LL) approximation, the evolution of parton distribution functions (PDFs) is described by the following GLAPD equations:

$$\begin{aligned}
\frac{df_i(x,\mu^2)}{d\ln\mu^2} &= \frac{\alpha_s}{2\pi}\int_x^1 \frac{dz}{z} P_{qq}\left(\frac{x}{z}\right) f_i(z,\mu^2) + P_{qg}\left(\frac{x}{z}\right) f_g(z,\mu^2), \\
\frac{df_g(x,\mu^2)}{d\ln\mu^2} &= \frac{\alpha_s}{2\pi}\int_x^1 \frac{dz}{z} P_{gq}\left(\frac{x}{z}\right) \sum_{i=q\bar{q}} f_i(z,\mu^2) + P_{gg}\left(\frac{x}{z}\right) f_g(z,\mu^2),
\end{aligned} \tag{1.1}$$

where
- $f_i$ — parton distribution function for quarks ($q$)/antiquarks ($\bar{q}$) of the flavor $i$;
- $f_g$ — parton distribution function for gluons;
- $\mu$ — scale;
- $P_{ij}$ — splitting function of a parton $j$ to a parton $i$. (quarks/antiquarks are denoted by $q$, gluons by $g$).

Splitting functions of the LL GLAPD approximation are:

$$
\begin{aligned}
P_{gq}(z) &= C_F \frac{1+(1-z)^2}{z}, \\
P_{qg}(z) &= T_R\big[z^2+(1-z)^2\big], \\
P_{qq}(z) &= C_F\left[\frac{1+z^2}{(1-z)_+}+\frac{3}{2}\delta(1-z)\right], \\
P_{gg}(z) &= 2C_A\left[\frac{z}{(1-z)_+}+\frac{(1-z)}{z}+z(1-z)\right]+\frac{11C_A-4n_fT_R}{6}\delta(1-z),
\end{aligned} \tag{1.2}
$$

where $C_F, C_A$ — eigenvalues of the quadratic Casimir operator in the fundamental and adjoint representation of the color group, respectively;

$T_R = 1/2$ — normalization of the color group generators;

$n_f$ — number of quark flavors.

The formula (1.2) contains + – prescription:

$$
\int_a^1 d\zeta \frac{F(\zeta)}{(1-\zeta)_+} = \int_a^1 d\zeta \frac{F(\zeta)-F(1)}{1-\zeta} - \int_0^a d\zeta \frac{F(1)}{1-\zeta}, \tag{1.3}
$$

where $F(\zeta)$ — arbitrary function $F(1) < \infty$.

It should be noted that the PDFs contain a perturbative and non-perturbative component, and at the moment cannot be calculated from the first principles. However, the GLAPD equations (1.1) make it possible to construct the evolution of PDFs from the scale on which they are measured to another hard scale $Q$. Factorization also suggests that parton distribution functions are universal, i.e., they do not depend on a hard subprocess. Thus, a formalism arises that allows one to make calculations for background and signal hard processes when studying physics at high energies $\sqrt{s}$ and momentum transfers $Q \sim \sqrt{s}$. For example, the differential cross section for the inclusive production of a hard system $H$ in a $pp$ collision within the framework of collinear factorization can be calculated according to the formula:

$$
d\sigma_{pp\to H+X} = \int dx_1 dx_2 \sum_{ij=q\bar{q}g} f_i(x_1,\mu_F^2) f_j(x_2,\mu_F^2) d\hat{\sigma}_{ij\to H}(\hat{s},\mu_F,\mu_R,...), \tag{1.4}
$$

In formula (1.4):

| | | |
|---|---|---|
| $X$ | — | unmeasured part of the final state; |
| $\sum_{ij=q\bar{q}g}$ | — | summation over all parton flavors ($q$ - quarks, $\bar{q}$ - antiquarks and $g$ - gluons); |
| $\hat{\sigma}_{ij\to H}$ | — | cross section of the hard parton subprocess of the $H$ system production in a collision of partons $i$ and $j$; |
| $\mu_F$, $\mu_R$ | — | factorization and ultraviolet renormalization scales respectively; |
| $\hat{s}$ | — | square of the energy of the center of mass system of colliding partons $i$ and $j$. |

The described approach was developed when accelerator energies were relatively low. Physics was studied at a scale comparable to the $\sqrt{s}$ of accelerators existing at that time. However, this approach remains relevant to this day. Despite the fact that the range of applicability of this formalism is the hard regime $\sqrt{s} \sim Q \to \infty$ and $Q/\sqrt{s} = x \approx 1$, experiments at the HERA collider (Hadron-Elektron-Ringanlage) in DESY (Deutsches Elektronen-Synchrotron) showed that the GLAPD evolution satisfactorily describes the data up to $Q/\sqrt{s} = x \sim 10^{-4}$ [57; 58]. The phenomenological success of the GLAPD formalism at such small $x$ does not mean that the PDFs obtained on its basis are reliable in this area. Because the GLAPD evolution does not take into account all the dominant contributions in this kinematic regime.

## 1.2 BFKL regime

With increasing energy of the center of mass system, $\sqrt{s}$, of colliding hadrons at current and future colliders, the semi-hard QCD regime, in which $\sqrt{s} \gg Q$, becomes important. In the semi-hard asymptotic regime ($\sqrt{s} \to \infty$ for a finite fixed $Q \gg \Lambda_{QCD} \approx 0.2$ GeV), the emission of infinite number of partons strictly ordered in transverse momentum is impossible due to the finiteness of $Q$. On the other hand, infinite energy allows the emission to be strictly ordered in the longitudinal component of the momentum. Strict ordering in the longitudinal component of the momentum of emissions, which are of the same order in the

transverse component of the momentum (the so-called diffusion in $p_\perp$) leads to ordering of emissions in rapidity. This kinematics is called multi-Regge kinematics. In multi-Regge kinematics, each emission is proportional to $\alpha_s \ln(1/x)$. For $\sqrt{s} \to \infty$ the LL contributions $[\alpha_s \ln(1/x)]^n$ are summed within the framework of the Balitsky–Fadin–Kuraev–Lipatov (BFKL) formalism [1—3]. Note that $\ln(1/x) \sim \ln(\sqrt{s}/p_\perp) \sim \ln(s)$ for large $s$, so it is often said that the BFKL evolution sums large logarithms of $s$.

The BFKL evolution equation has the following structure:

$$\frac{\partial f}{d \ln(1/x)} = K \otimes f, \tag{1.5}$$

where $K$ — BFKL kernel;
$\otimes$ — convolution.

The solution to this equation is easy to obtain for the eigenfunctions of the BFKL kernel, $K \otimes f_\omega = \omega f_\omega$:

$$f_\omega \propto e^{\omega \ln(1/x)} = x^{-\omega} \propto \left(\frac{s}{s_0}\right)^\omega \propto e^{\omega \Delta y}, \tag{1.6}$$

where $\omega$ — eigenvalue of the BFKL kernel;
$f_\omega$ — eigenfunction of the BFKL kernel;
$s_0$ — Gribov's parameter determining the transition to the asymptotic high-energy semi-hard regime.

From the last equation it is clear that in the asymptotic regime $s \to \infty$ the dominant contribution will be that corresponding to the maximum eigenvalue $\omega^{\max}$ associated with the value of the pomeron intercept $\alpha_{IP} = 1 + \omega^{\max}$. Calculation in the LL BFKL approximation predicts $\omega^{\max}_{LL} = 12 \ln 2 (\alpha_s/\pi) \approx 0.55 > 0$, and therefore predicts an increase with $s$ and $\Delta y$ of the cross sections for scattering into hadrons. An increase in the cross section with $s$ was detected in $ep$ scattering into hadrons at the HERA collider in ZEUS [59] and H1 [60], in $p\bar{p}$ collisions at SPS UA4 [61], UA5 [62], as well as at Tevatron in E710 [63] and CDF [64], in $\gamma^*\gamma^*$ scattering at LEP OPAL [65] and L3 [66], in $pp$ collisions at TeV energies at the LHC TOTEM [67; 68], ATLAS [69]. Confirmation of the growth of scattering cross sections into hadrons with $\sqrt{s}$ was the first success of the BFKL formalism. However, the LL approximation value of the maximum eigenvalue $\omega^{\max}_{LL} \approx 0.55$ turned out

to be too large, indicating the need to calculate corrections in the next-to-leading logarithmic (NLL) approximation. Thus, the results of calculations with the LL BFKL approximation are qualitative, and for comparison with experiments it is necessary to take into account the corrections of the NLL BFKL approximation.

The NLL BFKL corrections were first calculated in [12; 13]. However, it quickly became clear that they have a strong dependence on the choice of scheme and the scale of ultraviolet renormalization. The problem was resolved by generalizing the procedure for the optimal choice of renormalization scale by Brodsky–Lepage–Mackenzie (BLM) [70] to the non-Abelian case in the work of Brodsky–Fadin–Kim–Lipatov–Pivovarov (BFKLP)[14]. Calculations using the BFKLP procedure show that $\omega_{NLL}^{\max} \approx 0.13 \div 0.18$ in a wide range of $Q$, which is consistent with the conventional Gribov–Regge theory and the increase in scattering cross sections into hadrons with $\sqrt{s}$ in the above mentioned experiments. Calculations within the framework of the NLL BFKL are extremely complex. Therefore, not for all observables used to search for the BFKL signals, calculation methods have been developed that take into account the NLL BFKL corrections. The development of such methods is an important component of the search for signals of the BFKL evolution.

In hadron collisions, the energy of the system of the center of mass of the colliding partons is $\sqrt{\hat{s}} = \sqrt{x_1 x_2 s}$ ($x_1$, $x_2$ are fractions of momentum for the first and second partons). From here we note that:

$$\ln \frac{s}{Q^2} = \ln \frac{1}{x_1} + \ln \frac{\hat{s}}{Q^2} + \ln \frac{1}{x_2}, \tag{1.7}$$

In this case, the logarithms $\ln(1/x)$ appear in the BFKL evolution of the PDFs, and the logarithm $\ln(\hat{s}/Q^2)$ is responsible for the BFKL evolution in the parton subprocess $\hat{\sigma}$. In some calculations, it is convenient for the entire BFKL evolution to be localized in the parton subprocess, and the PDFs to be used for large $x \sim 1$. Thus, when calculating the production of the MN jet pairs, the jets forming an MN pair at large $\Delta y$ carry fractions of the momentum $x \sim 1$ of colliding protons, which justifies the use of the formula for collinear factorization (1.4) in the calculations [17]. Also, at large $\Delta y$, all parton-parton cross sections in the equation (1.4) become proportional to each other up to color factors, so it is possible to consider only the gluon-gluon cross section $\hat{\sigma}_{gg}$ and the effective PDF:

$$\frac{C_F}{C_A} \times f^{\text{eff}}(x, \mu_F) = f_g(x,\mu_F) + \frac{C_F}{C_A} \sum_{a=q,\bar{q}} f_a(x,\mu_F), \tag{1.8}$$

In formula (1.8) the factor $C_F/C_A$ on the left side of the formula is introduced so that the definition of the effective parton function coincides with that in [46].

Within the BFKL framework, the partonic cross section $\hat{\sigma}$, in turn, is also factorized into vertex functions, $V$, depending on the process under study, and the universal Green's function, $G_\omega$, of the BFKL kernel. For example, in the case of the MN dijet production, the gluon-gluon cross section $\hat{\sigma}_{gg}$ in the LL BFKL approximation has the form [71]:

$$\begin{aligned}\frac{d\hat{\sigma}_{gg}}{dp_{\perp1}^2 dp_{\perp2}^2 d\varphi} &= \left[\frac{C_A\alpha_s}{p_{\perp1}^2}\right] \\ &\times \left[\frac{1}{4\pi|p_{\perp1}||p_{\perp2}|}\sum_n e^{in(\varphi-\pi)}\int_0^\infty d\nu e^{\omega_{LL}^{\max}(n,\nu)\Delta y}\cos\left(\nu\ln\frac{p_{\perp1}^2}{p_{\perp2}^2}\right)\right] \\ &\times \left[\frac{C_A\alpha_s}{p_{\perp2}^2}\right],\end{aligned} \tag{1.9}$$

where $\varphi$ — azimuthal angle between jets in a pair;
$p_{\perp i}$ — transverse momentum of the $i$th jet in a pair.

In the formula (1.9) the contribution of the vertex functions $[C_A\alpha_s/p_\perp^2]$ and the Green's function (the second line in the equation) within the LL BFKL approximation is clearly highlighted. The factor responsible for the exponential growth of the cross section with increasing rapidity interval $\Delta y$ is clearly visible. The expression for $\omega_{LL}^{\max}(n,\nu)$ is:

$$\omega_{LL}^{\max} = \frac{2C_A\alpha_s}{\pi}\left[\psi(i) - Re\psi\left(\frac{|n|+1}{2}+i\nu\right)\right], \tag{1.10}$$

where $\psi$ — digamma function.

Let us give as an example the Born approximation for the gluon-gluon scattering cross section at large $\Delta y$:

$$\frac{d\hat{\sigma}_{gg}}{dp_{\perp1}^2 dp_{\perp2}^2 d\varphi} = \left[\frac{C_A\alpha_s}{p_{\perp1}^2}\right]\frac{\pi}{2}\delta(p_{\perp1}^2 - p_{\perp2}^2)\delta(\varphi-\pi)\left[\frac{C_A\alpha_s}{p_{\perp2}^2}\right], \tag{1.11}$$

Comparing calculations with the Born subprocess using the large $\Delta y$ approximation (as the convolution of $\hat{\sigma}_{gg}$ (1.11) with effective PDFs (1.8)) and without its use (Using the formula (1.4)), one can judge the range of applicability of the large $\Delta y$ approximation. Therefore, calculations within the BFKL formalism using the large $\Delta y$ approximation should also be considered in this area.

## 1.3 Observables to search for signals of the BFKL evolution

.

The construction of observables for searching for the BFKL evolution signals is based on the difference in the characteristic final states formed as a result of the GLAPD and BFKL evolutions. As follows from paragraph 1.1, in the GLAPD evolution, hadronic jets in the final state are strictly ordered in transverse momentum. The main contribution comes from scattering at a large angle $\sim \pi/2$, that is, $\Delta y \approx 0$. Although angular ordering for the GLAPD radiation is possible due to ordering in transverse momentum, this evolution does not depend on the rapidity $y$. Also, due to the strict ordering of radiation by $p_\perp$, the leading pair of jets in the event (the pair of jets with the maximum $p_\perp$) turns out to be strongly correlated in transverse momentum, that is, the transverse momentum of one jet in the leading pair balances the transverse momentum of the other jet in the leading pair.

On the other hand, as follows from paragraph 1.2, in the BFKL evolution, all hadronic jets in the event, strictly ordered by rapidity $y$, carry $p_\perp$ of the same order ($p_\perp$-diffusion). The maximum contribution to the cross section is made by pairs of jets with maximum $\Delta y$, as follows from the formula (1.9). In this case, jets separated by large $\Delta y$ quickly lose their correlation in $p_\perp$ due to emission in the $\Delta y$ interval. This phenomenon is called an azimuthal decorrelation. Azimuthal decorrelation increases with increasing $\Delta y$, since the phase space for $y$-ordered emission increases. It should be noted that observables in which hadronic jets are considered at smaller $p_\perp \ll \sqrt{s}$ should have the higher sensitivity to the BFKL effects.

One of the historically first was the proposal to use the dijet production with a large rapidity interval $\Delta y$ as a probe for searching for signals of the BFKL evolution. Thus, in the work [17] it was proposed to study the production of pair of jets with the maximum $\Delta y$ among jets above a certain threshold in transverse momentum $p_{\perp\min} \ll \sqrt{s}$. Such pairs are now called the Mueller–Navelet (MN) pairs. Measuring the cross section for the production of the MN dijets, $\sigma^{\rm MN}$, may encounter the following difficulty. With a sufficiently large $\sqrt{s}$ and low $p_{\perp\min}$ the MN pairs with the maximum $\Delta y$ may fall beyond the acceptance of the detector. In this case, the jets in the interval $\Delta y$ between the MN jets may be mistakenly taken for an MN pair. The measurement of the inclusive cross section for dijet production, $\sigma^{\rm incl}$, proposed in [18], does not have this difficulty. Each pairwise combination of jets

with a transverse momentum above $p_{\perp\min}$ is taken into account in the inclusive dijet section. It should be noted that the MN dijets are a subset of the inclusive dijets, and the MN cross section is essentially also inclusive. The introduction formula (1) determines the $\Delta y$-differential cross sections for the production of the inclusive and MN pairs of hadronic jets

In the works [17; 18] the ratio of the MN/inclusive dijet cross section to the Born cross section (the so-called K-factor) was considered. However, from an experimental point of view, the Born cross section is not measurable, since it is not possible to experimentally exclude virtual corrections and real corrections outside the acceptance and sensitivity range of the detector. Monte Carlo simulation shows that instead of the Born cross section in the denominator of the K-factor, cross sections with veto [19] can be considered. In this case, the veto is understood as the experimental imposition of prohibiting conditions on emission additional to a dijet in some region of rapidity above the $p_{\perp\text{veto}}$ threshold. In this work, we define the following two types of veto cross sections. First, the «exclusive» dijet production cross section, $\sigma^{\text{excl}}$, to which events with strictly one pair of jets with a transverse momentum greater than $p_{\perp\min}$ contribute. In other words, in the «exclusive» cross section, emission additional to dijet is prohibited above the veto threshold $p_{\perp\text{veto}} = p_{\perp\min}$, in the entire rapidity range. Secondly, the «exclusive» cross section with veto, $\sigma^{\text{excl}}_{\text{veto}}$, in which the emission of jets with transverse momentum above the veto threshold $p_{\perp\text{veto}} < p_{\perp\min}$, additional to the «exclusive» pair, is prohibited, in the entire range of rapidity. It should be noted that sometimes the rapidity range, in which the veto condition is imposed, is narrowed down to $\Delta y$ between jets in a pair, as in measurements by the ATLAS [34; 35] experiment. We will call this condition an *inter-jet* veto. In the case when the veto is applied over the entire rapidity range, as in $\sigma^{\text{excl}}$ and $\sigma^{\text{excl}}_{\text{veto}}$, we will call it a *jet* veto or simply a veto. The formula (2) in the introduction defines the ratios of the $\Delta y$-differential MN/inclusive cross sections to cross sections with veto.

Of interest when searching for signals of the BFKL evolution are also the cross sections for the production of jets with large absolute values of rapidities (forward jets with large positive $y$ or backward jets with large negative $y$), as in experiments at the HERA $ep$ collider H1 [26; 27] and ZEUS[28; 29] and in the CMS [36] experiment in $pp$ collisions at the LHC. Also, it is interesting to measure the ratios of the diejt cross sections with large $\Delta y$ at different $\sqrt{s}$, as in the measurement in the D0 [30] experiment in $p\bar{p}$ collisions at Tevatron.

The effect of azimuthal decorrelation is also used in searches for signals of the BFKL evolution. As can be seen, in the formula (1.9) the BFKL cross section is presented in the form of a Fourier expansion. The $n$-order coefficients of the Fourier series are the average cosines of the angle $n\varphi$ due to $\varphi \to -\varphi$ symmetry. Here $\varphi$ is the azimuthal angle between jets of a dijet. Therefore, in the works [21; 71] it was proposed to measure the average cosines $\mathcal{C}_n(\Delta y) = \langle \cos n(\varphi - \pi) \rangle (\Delta y)$ for the MN pairs to search for signals of the BFKL evolution. In the GLAPD evolution, decorrelation is suppressed, so the average cosines should remain close to one throughout the entire interval $\Delta y$. In the case of the BFKL evolution, the decorrelation increasing with $\Delta y$ leads to a decrease in the average cosines. The paper [22] states that the ratio of average cosines $\mathcal{C}_n/\mathcal{C}_m$ may be more sensitive to the expected BFKL signals, since the contributions of the GLAPD evolution to the PDFs are partially canceled.

Within the framework of the BFKL evolution, an increase of cross sections for color singlet exchange with $\sqrt{s}$ and $\Delta y$ [23—25] is also predicted. The color singlet in this case is described by the pomeron solution of the BFKL equation. In the case of color singlet exchange, hard hadronic jets accompanied with rapidity gaps are observed in the final state, analogous to diffraction. A rapidity gap is a region of rapidity in which there is no hadronic activity. The rapidity gap can be located within the rapidity interval between the jets, the so-called jet-gap-jet configuration, or outside this interval (for example, $p$-gap-jet-gap-jet configuration). From the experimental point of view, the jet-gap-jet event corresponds to an event with inter-jet veto with $p_{\perp \text{veto}} = 0$ GeV. One of the difficulties in interpreting the results of measuring jet-gap-jet observables is the need to estimate the gap «survival» probability, since hadronic activity can appear in jet-gap-jet events due to the underlying event.

## 1.4 Monte Carlo generators of hadron collisions

When searching for signals of the BFKL evolution, MC generators based on both GLAPD and BFKL evolutions are used. This section highlights the generators used in this and other works on search for the signals of the BFKL evolution.

Modeling hard $pp$ or $p\bar{p}$ scattering typically consists of modeling the parton subprocess, initial and final state radiation (parton showers), multiparton interactions (underlying event), hadronization and unstable particle decays. Electromagnetic and QCD processes occur in parallel. From the point of view of searching for signals of the BFKL evolution, the parton subprocess and parton showers are the most important. MC modeling shows that for the $p_{\perp\text{min}} = 35$ GeV and $p_{\perp\text{veto}} = 20$ GeV selections used in this work, the multiparton interactions do not introduce significant corrections.

As we will see below, generators based on the GLAPD evolution often include corrections beyond the basic approximation. Corrections for color coherence cause the main difficulty in interpreting results when searching for signals of the BFKL evolution, since they lead to angular ordering of the emission, which mimics rapidity evolution. These corrections are small in the region of small $\Delta y$, but, as we will see, they become unstable at large $\Delta y$. Color coherence is implemented differently in various MC generators based on the GLAPD evolution. This mainly explains the difference in their predictions at large $\Delta y$.

### 1.4.1 MC generators based on the GLAPD evolution

PYTHIA is a universal generator capable of reproducing the exclusive final hadronic state for a large number of processes both within and beyond the Standard model [15]. PYTHIA is widely used in high energy physics to model background and signal events, and in procedures of eliminating the detector distortions to model MC truth events that are fed into a detector model. The current version of the generator is eighth, so in this work we use the notation PYTHIA8.

PYTHIA8 models the partonic hard QCD subprocess in the leading order (LO) of the perturbation series. Parton showers use the GLAPD splitting functions in the LL approximation to model $p_\perp$-ordered cascades. Color coherence is implemented by generating emission with color dipoles.

Using the PYTHIA8 generator involves the use of tunes, which are created based on fit of experimental data at different energies. In this work 4C [72] and CP5 [73] tunes are used. For the most part, the parameters of the underlying event and other non-perturbative model parameters are tuned. Tune 4C uses the collision data fit at

$\sqrt{s} = 7$ TeV, while tune CP5 also uses fits at 8 and 13 TeV. In addition, the CP5 tune employ rapidity ordering in the initial state radiation. Which makes the predictions of PYTHIA8 CP5 more distant from the predictions of the «pure» GLAPD evolution.

Another widely used MC generator, HERWIG [16], performs simulations in the same approximation as PYTHIA8. Namely, it uses the parton subprocess in the LO and the parton shower based on the splitting functions in the LL GLAPD approximation. However, color coherence in parton showers is implemented with the parton cascades ordered in angle. In high energy physics, the MC generator HERWIG has the same applications as PYTHIA. In this work, we use two versions of the generator: HERWIG++ [42] with UE-EE3C [74] tune; and HERWIG7 [16] with the default setting.

The key difference of SHERPA [75] generator from PYTHIA and HERWIG generators is that it is capable to model $2 \to n$ parton subprocess. However, in such a subprocess, SHERPA implements only real, but not virtual, corrections. The parton shower in SHERPA uses the LL GLAPD splitting functions and the dipole implementation of color coherence. In this work, we do not use this generator, since it showed poor agreement with the measurements of azimuthal decorrelations [38].

The accuracy of the predictions of PYTHIA and HERWIG can be improved by using the parton subprocess computed in the next-to-leading order (NLO) of perturbation theory. The NLO modeling of the parton subprocess is provided with the generator POWHEG [43]. Further modeling of parton showers, multiparton interactions and hadronization can be performed in both PYTHIA and HERWIG. In this work, the second version of POWHEG is used.

As follows from the given description of the generators, color coherence modeling is presented in all considered GLAPD-based generators. Disabling color coherence is not provided in the programs. There is also no possibility of separating the contributions from the GLAPD evolution and color coherence. Therefore, when interpreting the results of comparison of the predictions of these generators with the experimental results, it should be remembered that the effects of partial rapidity ordering can also manifest themselves in these generators. However, the systematic account of all important contributions at large rapidities is ensured only in the BFKL evolution.

### 1.4.2 MC generators based on the evolution of BFKL

Currently, there are only generators based on the LL BFKL approximation, but not on the NLL, which is also a difficulty in searching for signals of this evolution. In previous measurements, the generators HEJ [44] and CASCADE [52] were used.

The MC generator HEJ implements the summation of the contributions of the LL BFKL approximation, which dominate in the case of multiple production of jets well separated in rapidity. HEJ generates a final state at the parton level, where each parton is interpreted as a jet, and provides an interface for simulating subsequent parton showers and hadronization using the ARIADNE [45] generator. The ARIADNE generator simulates the subsequent dypole parton shower, hadronization and decays.

The CASCADE generator uses unintegrated parton distribution functions (UPDFs), or, as it is often said, transverse momentum dependent PDFs. Integrating the UPDF over the transverse momentum restores the PDF of the GLAPD formalism. The evolution of the UPDFs in the CASCADE generator is organized according to the Catani–Ciafaloni–Fiorani–Marchesini equations [76—78], which take into account both the GLAPD and LL BFKL evolution. However, the CASCADE generator overestimates the effect of increasing cross section ratios with veto much more strongly than the HEJ generator, as shown in [37]. Therefore, this generator is not considered in this work.

Comparison of simulation results PYTHIA8, HERWIG++ and HEJ+ARIADNE for the cross section ratios with veto $R^{\text{incl}}$, $R^{\text{MN}}$, $R^{\text{incl}}_{\text{veto}}$, $R^{\text{MN}}_{\text{veto}}$ (formula (2) of the introduction) in $pp$ collisions at energies of LHC $\sqrt{s}$ = 2.76, 8, 13, 14 TeV and future colliders: HE-LHC [79] $\sqrt{s}$ = 27 TeV and FCC [80] $\sqrt{s}$ = 100 TeV is shown in Figure 1.1 [A5; 81]. Simulation results are presented for $p_{\perp\text{min}}$ = 35 GeV and $p_{\perp\text{veto}}$ = 20 GeV. Simulations show that these observables are sensitive to the effects of the BFKL evolution. The MC generator HEJ+ARIADNE shows an increase of the ratios with $\sqrt{s}$ and $\Delta y$, exceeding the increase in predictions based on the LL GLAPD provided by the generators PYTHIA8 and HERWIG++. The introduction of $p_{\perp\text{veto}}$ = 20 GeV into $R^{\text{incl}}_{\text{veto}}$ and $R^{\text{MN}}_{\text{veto}}$ enhances the growth of HEJ+ARIADNE predictions with $\Delta y$. Therefore, these observables are more sensitive to the effects of BFKL compared to $R^{\text{incl}}$ and $R^{\text{MN}}$. There is a significant difference in the predictions of PYTHIA8 and HERWIG++ at large $\Delta y$, which indicates a strong dependence on the implementation of the color coherence corrections. Finally, figure 1.1 clearly

demonstrates that the BFKL effects can become significant at rapidities and energies achievable in the near future.

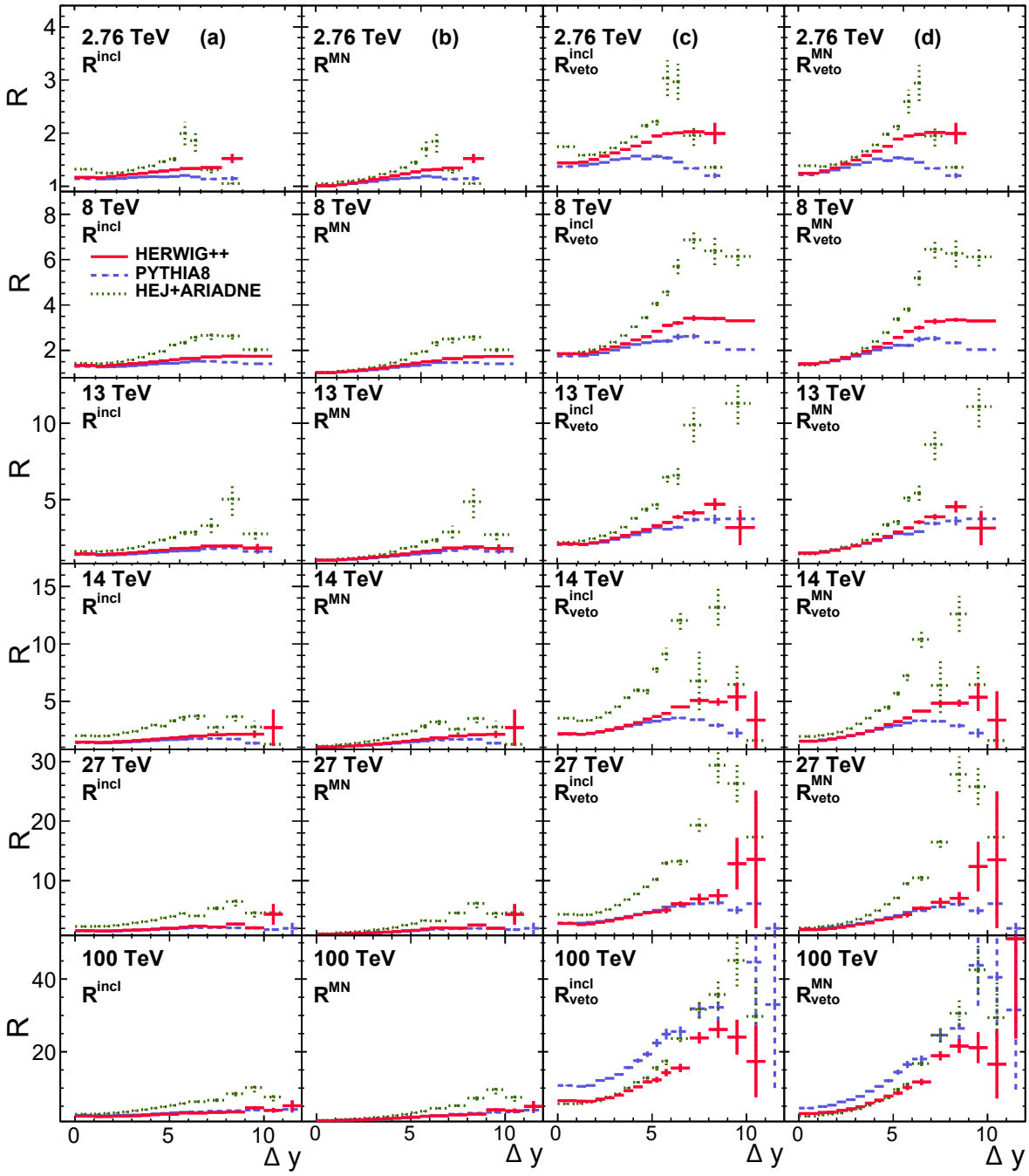


Figure 1.1 — Results of modeling of cross section ratios with veto $R^{\text{incl}}$ (column (a)), $R^{\text{MN}}$ (column (b)), $R^{\text{incl}}_{\text{veto}}$ (column (c)), $R^{\text{MN}}_{\text{veto}}$ (column (d)) in $pp$ collisions at $\sqrt{s} = 2.76$, 8, 13, 14, 27, 100 TeV. Vertical lines denote the statistical uncertainties in the simulation results [A5; 81].

## 1.5 Results of previous measurements searching for BFKL signals in hadron collisions

Observables sensitive to the effects of the BFKL evolution were measured both in $p\bar{p}$ collisions at the Tevatron in the D0 and CDF experiments, and in $pp$ collisions at the LHC in the CMS and ATLAS experiments. Thus, in the D0 experiment, when measuring hadronic jets with transverse energy $E_\perp > 20$ GeV in $p\bar{p}$ collisions at $\sqrt{s} = 0.63$ and 1.8 TeV, a stronger dependence of the MN cross section on energy was observed than predicted in LL BFKL [32]. D0 also observes insufficient azimuthal decorrelations when measuring the average cosine $\mathcal{C}_1$ of the azimuthal angle between jets in the MN pairs of jets with $E_\perp > 20$ at $\sqrt{s} = 1.8$ TeV [30] and $\Delta\eta < 5$, where $\eta$ is pseudorapidity. The azimuthal decorrelations were more likely to match the predictions of the color coherence implemented in HERWIG. Measuring the fraction of jet-gap-jet events in the D0 experiment at $\sqrt{s} = 1.8$ TeV, $E_\perp > 15$ and $4 < \Delta\eta < 6$ [31] and the CDF experiment $\sqrt{s} = 1.8$ TeV, $E_\perp > 20$ and $3.6 < \Delta\eta < 7$ [33] is consistent with the calculation in the LL BFKL approximation improved by the main NLL contributions [24] (partial summation of NLL).

Both experiments using the largest multipurpose detectors at the LHC, ATLAS and CMS, measured the production of dijets with large rapidity separation at $\sqrt{s} = 7$ TeV. In the CMS experiment, hadron jets with $p_\perp > 35$ GeV were measured, with the rapidity interval up to $\Delta y = 9.4$. At the same time, in the ATLAS experiment the region $\overline{p_\perp} = (|p_{\perp 1}| + |p_{\perp 2}|)/2 > 60$ GeV ($|p_{\perp 1}|$ and $|p_{\perp 2}|$ are the absolute values of the transverse momenta of the first and second jets in the pair) and $\Delta y < 8$ is studied. Thus, the CMS measurements turn out to be somewhat more sensitive to the BFKL evolution signals than the ATLAS measurements, since it studied the region with lower $p_\perp$ and larger $\Delta y$ at the same $\sqrt{s} = 7$ TeV.

The ATLAS measurement of the ratio of the cross section for the production of the MN dijets with an interjet veto ($p_{\perp \text{veto}} = 20$ GeV) to the cross section without a veto [34] is consistent with the LL BFKL approximation calculation at the parton level obtained using the HEJ generator and on hadron level HEJ+ARIADNE [35]. The result of measuring azimuthal decorrelations ($\mathcal{C}_2/\mathcal{C}_1$) in the ATLAS experiment for pairs with $60 < \overline{p_\perp} < 200$ GeV (the interval containing the minimal $p_\perp$ in the measurement, the most sensitive to possible BFKL effects) is

consistent with predictions HEJ+ARIADNE, but not consistent with HEJ, POWHEG +PYTHIA8/HERWIG++.

In the CMS experiment, measurements of events in which one of the jets is produced in the forward region (large value of the absolute rapidity $|y| > 3.2$) and one in the central ($|y| < 2.8$), with $p_\perp > 35$ GeV is consistent with the predictions of HEJ [36]. Measurements of ratios with veto $R^{\text{incl}}$ and $R^{\text{MN}}$ at $p_{\perp\text{min}} = p_{\perp\text{veto}} = 35$ GeV and $\Delta y < 9.4$ are overestimated by the predictions of the MC generator HEJ+ARIADNE and significantly overestimated by the predictions of CASCADE, while the GLAPD-based model with color coherence PYTHIA8 well describes the growth of ratios with $\Delta y$. However, color coherence in HERWIG++ overestimates the growth of $R^{\text{incl}}$ and $R^{\text{MN}}$ and shows a noticeable deviation from the predictions of PYTHIA8 at large $\Delta y$, as it is in the case of the simulation presented in the figure 1.1. The measurement of azimuthal decorrelations in the CMS [38] experiment is in good agreement with the analytical calculations with NLL BFKL accuracy [47]. In addition, in the CMS experiment the proportion of jet-gap-jet events was measured at $\sqrt{s} = 7$ TeV [39], and in the CMS-TOTEM experiment the production of jet-gap-jet and p-gap-jet -gap-jet events was measured at $\sqrt{s} = 13$ TeV [40], the results of which are in good agreement with the LL BFKL predictions improved by the main contributions from the NLL approximation (partial summation of the NLL contributions).

Summarizing the results of previous measurements, we can say that not a single GLAPD-based model, even using color coherence, describes the entire set of observables at once. For example, PYTHIA8 describes better the ratios with veto measurements, and HERWIG++ describes better the azimuthal decorrelation measurements. At the same time, analytical NLL BFKL calculations are in good agreement with the experimental results. However, methods for calculating with NLL BFKL accuracy have been developed only for part of the observables, namely: for azimuthal decorrelations between jets of an MN dijet and for the cross sections for the production of the MN dijets [47; 48]. The color singlet exchange can be calculated based on the LL BFKL improved by the main contributions from the NLL corrections, as in the work [24], or with a full account of the NLL BFKL as in the recently presented work [82]. Thus, the most critical situation from the point of view of the development of calculation methods taking into account the NLL BFKL contributions arises for observables using the veto conditions.

## 1.6 Observables studied in this work

In this work, we measured the $\Delta y$-differential sections $d\sigma^{\mathrm{incl}}/d\Delta y$, $d\sigma^{\mathrm{MN}}/d\Delta y$ (formula (1) of the introduction) and the ratios of the differential cross sections with veto $R^{\mathrm{incl}}$, $R^{\mathrm{MN}}$, $R^{\mathrm{incl}}_{\mathrm{veto}}$, $R^{\mathrm{MN}}_{\mathrm{veto}}$ (formula (2) of the introduction) in $pp$ collisions at energy $\sqrt{s} = 2.76$ TeV based on sample 5.4 pb$^{-1}$ of data collected by the CMS collaboration in 2013. The measurements studied hadronic jets with $p_{\perp} > p_{\perp\mathrm{min}} = 35$ GeV and $|y| < 4.7$, as in the $R^{\mathrm{incl}}$ and $R^{\mathrm{MN}}$ measurements at $\sqrt{s} = 7$ TeV [37]. The veto threshold $p_{\perp\mathrm{veto}}$ in $\sigma^{\mathrm{excl}}_{\mathrm{veto}}$ is set at 20 GeV.

The cross sections $d\sigma^{\mathrm{incl}}/d\Delta y$, $d\sigma^{\mathrm{MN}}/d\Delta y$ are measured for the first time. It is known that analytical calculations and MC models tend to better describe the ratios of cross sections, in which part of the contributions are canceled, than the absolute values of the cross sections. Therefore, measuring the absolute values of cross sections will allow better testing of models. The ratios of the cross sections $R^{\mathrm{incl}}_{\mathrm{veto}}$ and $R^{\mathrm{MN}}_{\mathrm{veto}}$ are also measured for the first time. As the MC simulation presented in Figure 1.1 and in work [19] shows, introducing the veto selection for additional jets with the threshold lower than $p_{\perp\mathrm{min}}$ can improve sensitivity to signals of the BFKL evolution. The ratios of the cross sections $R^{\mathrm{incl}}$ and $R^{\mathrm{MN}}$ were measured earlier at an energy of $\sqrt{s} = 7$ TeV. Observing the energy dependence of these observables will allow us to better study the behavior of QCD asymptotics in the region of phase space under the study.

The experimental results are compared with calculations, both based on MC modeling in the software packages PYTHIA8, HERWIG, POWHEG, HEJ+ARIADNE and analytical calculations with LL and NLL BFKL accuracy. In particular, for the first time the comparison of the measured cross section $d\sigma^{\mathrm{MN}}/d\Delta y$ with the calculation taking into account the NLL BFKL corrections is presented, showing the best agreement among all the considered calculations. This may indicate the manifestation of the effects of the BFKL evolution in the obtained experimental results.

# Chapter 2. Description of the experimental setup

## 2.1 Parameters of beams delivered by the LHC

The Large Hadron Collider (LHC) delivers beams of protons that intersect at the nominal interaction point at the center of the CMS detector. The beams are a sequence of bunches. The minimum time interval between intersections of bunches is 25 ns. Large gaps, multiples of 25 ns, between bunches are also possible. In particular, from a technical point of view, gaps for beam dump are required. Thus, the peak bunch intersection frequency reaches 40 MHz. High luminosity is ensured due to the overlap of collisions at the intersections of bunches. The effect of overlap of $pp$ collisions in events is called pileup (PU). Thus, in the Run I cycle of the LHC there were up to 40 inelastic $pp$ collisions with an average of $\sim 21$ per one intersection of bunches, and in the Run II cycle of the LHC there were up to 80 inelastic collisions with an average of $\sim 37$.

In the terminology used in the LHC experiments, event is an intersection of beam bunches. Thus, several $pp$ collisions are possible in one event. Individual $pp$ collisions are observed as vertices to which the tracks of charged particles reconstructed by the detector converge. The vertex to which the maximum sum corresponds of the squares of the transverse momenta of the associated tracks is called the primary vertex. The remaining vertices, as well as the interactions $pp$ corresponding to them, are called secondary.

It should be noted that data with a high probability of secondary $pp$ collisions in an event turn out to be of little use for measuring hadronic jets at high rapidities. This is due to the fact that the tracker system of the CMS detector, which is involved in determining the primary and secondary collisions in events, covers the pseudorapidity region $|\eta| < 2.5$. Thus, it turns out to be technically difficult to separate hadronic jets from different $pp$ collisions at high rapidities $|y| \gtrsim 2.5$, and to estimate the contribution to the energy of the jets from the overlap of jets from secondary $pp$ collisions. Therefore, measurements of the production of hadronic jets with large $y$ are usually carried out on with samples collected in special LHC runs with a low probability of collision overlap (low PU runs).

In this work, we consider data on collisions with energy in the center-of-mass system $\sqrt{s} = 2.76$ TeV collected by the CMS detector in 2013. During this special period of LHC operation, a set of reference $pp$ data was collected for study $pPb$ and $PbPb$ interactions. The average number of $pp$ collisions per event was 0.35, which significantly reduces the effects of overlapped secondary $pp$ collisions. The delivered integral luminosity of the used sample is 5.4 $\text{pb}^{-1}$.

## 2.2 Multipurpose CMS detector

The CMS detector, one of the 4 large detectors installed on the LHC, is a multi-purpose detector. The physics program of the CMS detector coincides with the physics program of the LHC, and mainly consists of studying physics at energy scales up to 14 TeV.

This paragraph provides a brief description of the main detector systems important for the measurements performed. This description is also necessary for understanding the next chapter 3 («Measurement of $\Delta y$-differential dijet production cross sections and their ratios with the veto»). A more detailed description of the CMS detector can be found in [50].

The central element of the CMS detector is a superconducting solenoid that creates a magnetic field of up to 3.8 Tesla. The dimensions of the solenoid are 13 m in length and 6 m in diameter. The internal volume of the solenoid contains a silicon tracker, an electromagnetic calorimeter and a hadronic calorimeter. Each calorimeter consists of a cylindrical part and endcaps. In this work, the forward calorimeter is also actively used, increasing the pseudorapidity coverage beyond the covers of the electromagnetic and hadronic calorimeters. The muon system, consisting of wire gas chambers, is immersed in a steel magnet yoke located outside the solenoid.

CMS collaboration uses a right-handed coordinate system with the origin at the center of the detector. The $x$ axis is directed towards the center of the LHC. The $y$ axis is directed vertically upward (perpendicular to the LHC plane). The $z$ axis is along the beam axis. The polar angle $\theta$ is measured from the positive direction of the $z$ axis, and the azimuthal angle $\varphi$ is measured from the positive direction of the $x$ axis in the ($x$,$y$) plane.

### 2.2.1 Tracker system

The scheme of the CMS tracker is shown in Figure 2.1. The tracker occupies a cylindrical volume 5.8 m long and 2.5 m in diameter. The axis of the cylindrical volume coincides with the axis of the beam. The tracker includes a silicon pixel detector (PIXEL) and silicon strip detectors (TOB, TIB, TID, TEC).

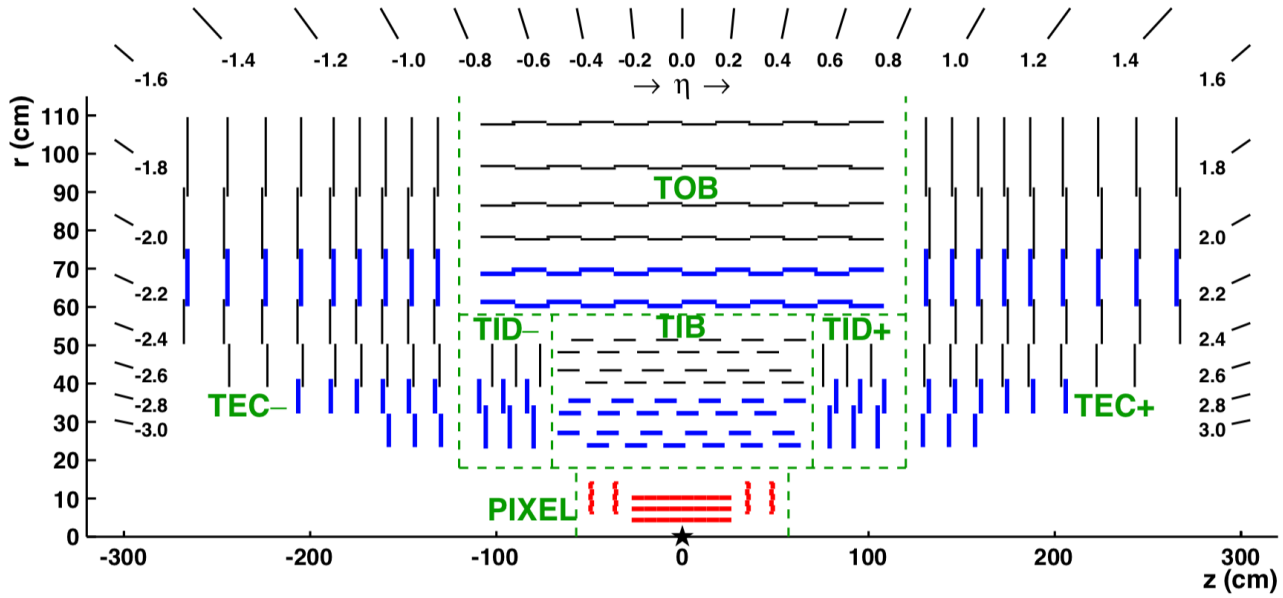


Figure 2.1 — Schematic illustration of the CMS detector tracker [83].

The pixel tracker consists of a cylindrical part and two endcaps and provides 3D measurement of the position of points of interaction of charged particles. In total, the pixel tracker includes 1440 modules with a total area of 1 $m^2$ and has 66 million channels.

The strip tracker has 15148 modules, with a total area of 198 $m^2$. It consists of 4 subsystems: Tracker Inner Barrel (TIB), Tracker Inner Disk (TID), Tracker Outer Barrel (TOB) and Tracker Endcaps (TEC).

The tracker is used to reconstruct tracks and the momenta of particles, as well as to determine the *pp* interaction vertices.

Track reconstruction begins with determining the coordinates of the points of interaction of charged particles with the tracker modules. The interaction points are then combined into tracks using the extended Kalman filter [84]. Tracks are reconstructed in an iterative process, where at the initial iterations, easy-to-reconstruct tracks (particles with large transverse momentum produced in the

interaction region) are determined, and at subsequent iterations, more complex tracks (particles with small transverse momentum and highly displaced tracks) are determined. Before each iteration, interaction points associated with the found tracks that passed the high-purity selection [83] are excluded from further consideration. Each iteration goes through four steps:

- Definition of track seeds consisting of a small number (2 or 3) interaction points.
- Using the Kalman filter. In this step, the seeds trajectories are extrapolated along the expected path of the charged particle to search for points that can be associated with the track.
- Track approximation. At this step, the best estimate of the parameters of each trajectory is determined.
- Checking track quality criteria. Only tracks that meet the criteria are considered reconstructed.

A total of 6 iterations are used. The difference between iterations is in definition of the track seeds and track quality criteria.

The reconstructed track is used to estimate the momentum and spatial parameters of the charged particle. The silicon tracker measures tracks of charged particles at pseudorapidity $|\eta| < 2.5$. For non-isolated charged particles with transverse momentum $1 < p_T < 10$ GeV and pseudorapidity $|\eta| < 1.4$, the resolution of the transverse momentum of the particle is 1.5%. The spatial resolution of the impact parameter of a track is $25-90$ $(45-100)$ µm in the transverse (longitudinal) direction. Where by longitudinal direction we mean the direction along the axis of the beam of colliding protons, and by transverse direction we mean the direction in the plane transverse to the axis of the beam [83].

The purpose of reconstructing $pp$ vertices [85] is to measure the position and position error of the primary and secondary $pp$ interactions in each event. The procedure consists of three steps: selecting tracks; combining tracks that originate from one vertex into clusters; approximating the position of each vertex using the tracks of the corresponding cluster.

### 2.2.2 Calorimetric system

The calorimetric system consists of three parts: a crystal electromagnetic calorimeter ECAL, a brass-scintillator hadronic calorimeter HCAL and a forward hadronic calorimeter HF (HCAL Forward). The barrels and endcaps of the electromagnetic and hadronic calorimeter cover the pseudorapidity region up to $|\eta|$ <3.0. HF extends coverage to $3.0 < |\eta| < 5.2$.

The scheme of the ECAL is shown in Figure 2.2. The ECAL consists of three main parts: a barrel (ECAL Barrel (EB)), two endcaps (ECAL Endcap (EE)) and a preshower detector (Preshower).

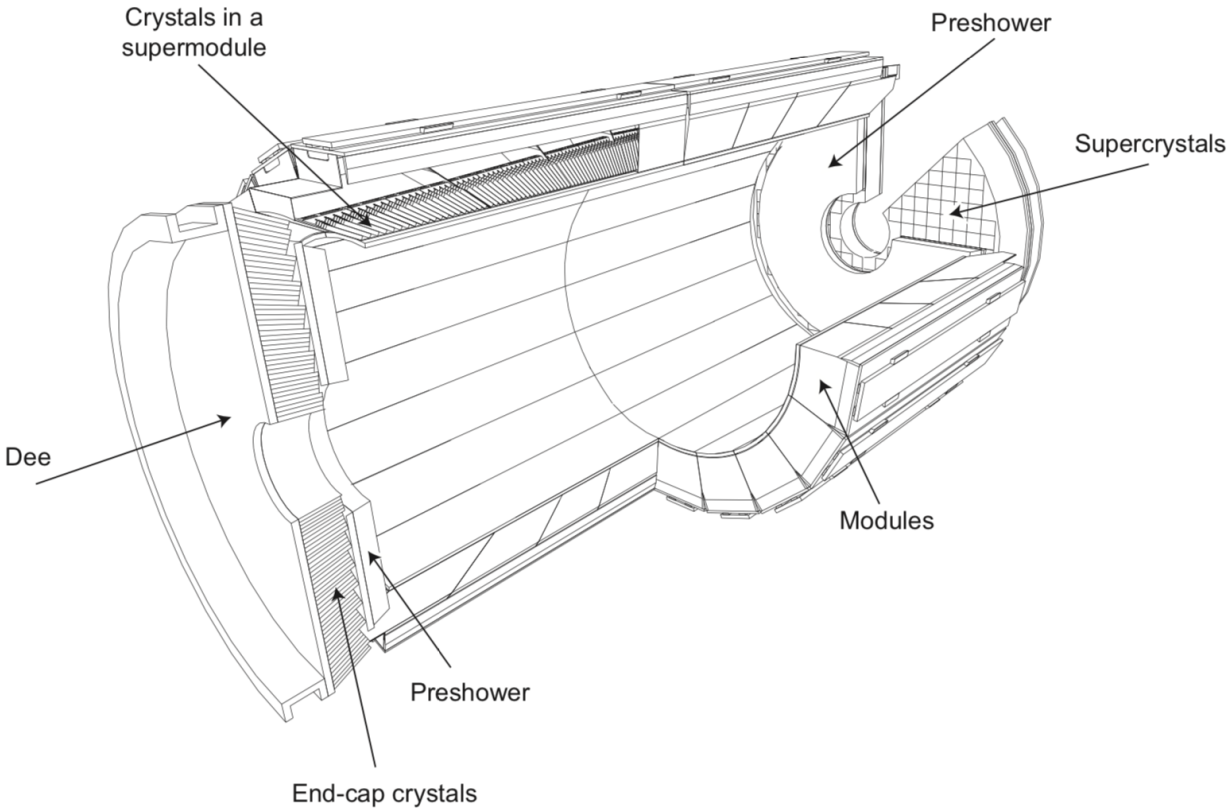


Figure 2.2 — Scheme of the ECAL of the CMS detector [50].

The electromagnetic calorimeter consists of 75848 crystals of lead tungstate ($PbWO_4$). 61200 crystals are located in the barrel part of the EB calorimeter, and 7324 in each endcap of the EE. Lead tungstate has high density of 8.28 g/cm$^3$, short radiation length of 0.89 cm and small Molière radius of 2.2 cm. These properties determine high granularity and compact size of the electromagnetic calorimeter. The time the crystals are illuminated coincides in order with the frequency of

intersection of the beam bunches. 80% of the light is emitted in 25 ns. The light yield at temperature of 18°C is 4.5 photoelectrons per MeV. The crystals emit blue-green light with a broad maximum at wavelength of 420-430 nm. The light is detected by photodetectors located at the ends of the crystals. The crystals in the cylindrical part and in the endcaps have different shapes.

The barrel part of the electromagnetic calorimeter (EB) covers the pseudorapidity region $|\eta| < 1.48$. The EB granularity is 360 in azimuthal angle $\varphi$ and $2 \times 85$ in pseudorapidity $\eta$. The crystals have a wedge shape that changes with pseudorapidity. The section of the end of the crystal directed to the nominal interaction point is $22 \times 22$ mm$^2$, which is $0.0174 \times 0.0174$ in $\eta - \varphi$ space. Crystal length 230 mm or 25.8 radiation lengths. In order to avoid gaps collinear to particle trajectories, the crystal axis has 3° slope in $\varphi$ and $\eta$ with respect to the vector connecting the nominal interaction point and the position of the crystal. The crystals are packaged into thin-walled submodules, which then form a module. In total, the module contains 400-500 crystals, depending on the pseudorapidity. Four modules form a supermodule, which contains 1700 crystals. Nineteen supermodules, each covering 20° in azimuthal angle, form half of the EB. The distance between crystals in submodules is 0.35 mm, and between the crystals of two adjacent submodules is 0.5 mm. The modules are separated by a 4 mm wall.

Two EE endcaps cover area of pseudorapidity $1.48 < |\eta| < 3.0$ and located at a distance of 315 cm from the nominal interaction point. The EE are made of crystals of the same shape, grouped into $5 \times 5$ blocks of crystals called supercrystals. Each endcap is divided into two D-shape halves (Dee). Each half contains 138 standard supercrystals and 18 specially shaped supercrystals located along the inner and outer circumference. The crystals and supercrystals are organized into a rectangular lattice, the axis of the crystals is directed to a focus located 1300 mm behind the nominal interaction point, which gives a deviation from the vector connecting the nominal interaction point and the crystal by 2-8°. The cross section of the end of the crystal directed to the nominal interaction point is $28.62 \times 28.62$ mm$^2$ and the length is 220 mm (24.7 radiation lengths).

The number of emitted photons, as well as the gain of photodetectors, depends on temperature. The cooling system of the ECAL maintains the temperature of the crystals and photodetectors within $18 \pm 0.05$°C.

In addition to EB and EE, the ECAL includes the preshower detector. The preshower detector is designed to identify fast neutral pions decaying into a pair of

photons with a small separating angle. The preshower detector also helps in electron identification and improves the position determination of electrons and photons. The detector is located in front of the EE calorimeter and covers the pseudorapidity region $1.653 < |\eta| < 2.6$. The detector consists of two layers located one behind the other. Each layer includes a lead radiator that initiates electromagnetic showers from incoming photons and electrons, and silicon strip sensors located behind the radiator. Strip sensors measure the position, energy release and transverse profile of showers. The total thickness of the preshower detector is 20 cm. The thickness up to the sensors of the first layer is two radiation lengths, and between the sensors of the first and second layers is one radiation length. So 95% of single photons generate a shower before the second layer of sensors. The orientation of the strips in the two layers of sensors is orthogonal.

The hadronic calorimeter consists of a barrel part (HCAL Barrel (HB)), two endcaps (HCAL Endcap (HE)) and an outer calorimeter (HCAL Outer (HO)). HB is located between the outer surface of the ECAL ($R = 1.77$ m) and the inner radius of the superconducting solenoid ($R = 2.95$ m). This limits the total thickness of the material absorbing the hadron shower. Located outside the superconducting solenoid the HO calorimeter is designed to record hadronic shower tails, that is, hadronic shower particles not absorbed into the HB.

The HB calorimeter covers the pseudorapidity region $|\eta| <1.3$ and consists of 36 identical wedges that form halves HB+ and HB-. That is, the cylinder consists of 18 segments in the azimuthal angle. The wedges consist of flat brass absorber plates aligned parallel to the beam axis. Brass was chosen because of its relatively short interaction length, ease of machining, and non-magnetic properties. The plate closest to the beam and the one farthest are made of stainless steel to give strength to the structure. The overall absorber includes the 40 mm thick stainless steel front plate, eight 50.5 mm thick brass plates, six 56.5 mm thick brass plates and the 75 mm thick stainless steel back plate. The total thickness of the absorber at $\theta = 90^\circ$ is 5.82 interaction lengths. The effective thickness increases with the polar angle as $1/\sin\theta$ and at $\eta = 1.3$ is 10.6 interaction lengths. An ECAL located in front of the HB adds about 1.1 interaction lengths.

The sensitive element of the HCAL is a plastic scintillator. The first active scintillator layer, 9 mm thick, is located immediately behind the ECAL. This layer is designed to register low-energy hadrons, a shower from which can be formed on structural materials between ECAL and HCAL. Subsequent layers located between

the absorber plates have a thickness of 3.7 mm. Individual scintillator tiles of size $\Delta\eta\times\Delta\varphi = 0.87\times0.87$ are equipped with a Wave Length Shifting (WLS) optical fiber designed to read the signal. Scintillator tiles corresponding to a certain azimuthal angle are packaged in half-barrel-long trays. Tiles located at the same azimuthal angle and pseudorapidity form the cells of the hadronic calorimeter (see Fig. 2.3). The cell size is 0.87 in pseudorapidity and 5° in azimuthal angle.

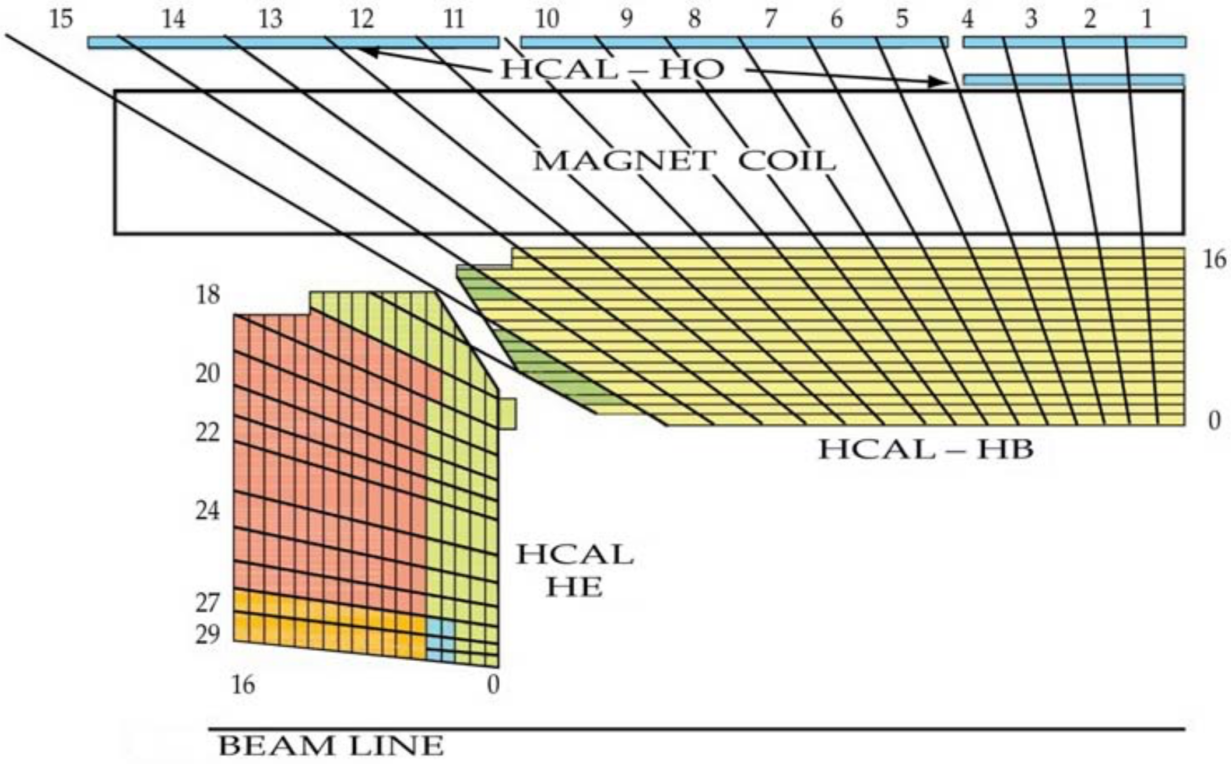


Figure 2.3 — Schematic illustration of the HCAL-HB barrel part of the hadronic calorimeter, the HCAL-HE endcaps of the hadronic calorimeter, and the outer HCAL-HO hadronic calorimeter of the CMS detector. The beam axis (BEAM LINE) and the coil of the superconductive solenoid (MAGNET COIL) are also schematically shown. [50].

The endcaps of the HCAL cover pseudorapidity regions $1.3 < |\eta| < 3.0$, and also consist of 18 segments in the azimuthal angle. The thickness of the brass plates is 78 mm, and the thickness of the plastic scintillator is 3.7 mm. There are 19 active layers in total. The $\Delta\eta \times \Delta\varphi$ cell size is the same as the cell size in HB for $|\eta| < 1.73$ and gradually increases for higher pseudorapidities.

The signal from the WLS fibers is read by fiber optic channels, which transmit the signal to photodetectors.

The outer HO calorimeter consists of two layers of plastic scintillator located outside the superconducting solenoid. Outside the superconducting solenoid there is an iron yoke of the magnet, consisting of five rings, 2.536 m wide along the $z$ axis. The rings are numbered -2, -1, 0 , 1, 2. The nominal positions of the ring centers along the $z$ axis are at distances of -5.342 m, -2.686 m, 0 m, 2.686 m, 5.343 m. The outer HO calorimeter is the first sensitive layer of each ring, and uses the solenoid coil as an absorber with thickness of $1.4/\sin\theta$ of the interaction length. At $\eta = 0$, HB has the smallest thickness, so the central ring (ring 0) has two layers of HO scintillators at radial distances of 3.82 and 4.07 m from the beam axis, separated by a 19.5 cm thick layer of iron absorber. The remaining rings have one scintillator layer at radial distance of 4.07 m from the axis of the beams. Taking into account the outer calorimeter HO, the minimum thickness of the calorimetric system is 11.8 interaction lengths. The size of the HO tiles is approximately the same as the size of the HB cells.

The geometric arrangement of the tracker sensors, electromagnetic calorimeter crystal arrays, hadronic calorimeter cells and outer calorimeter scintillators is such that they form towers, as shown in Figure 2.4. The energy of charged and neutral particles is measured by combining information from the tracker and calorimeters, which provides an energy resolution of hadronic jets of $\Delta E/E \approx 100\%/\sqrt{E(\mathrm{GeV})} \oplus 5\ \%$.

The HF forward calorimeter uses a steel absorber and quartz tubes that detect Cherenkov radiation. The two parts of the forward calorimeter are located at a distance of 11.2 m on either side of the nominal interaction point. Together the two parts of the HF cover the pseudorapidity region $3.0 < |\eta| < 5.2$. In addition to measuring energy release, the forward calorimeter serves as a luminosity monitor. Each part of the forward calorimeter consists of 432 towers containing long and short quartz tubes. Long quartz tubes occupy the entire depth of the calorimeter (165 cm, which is approximately 10 interaction lengths), Short tubes start at a depth of 22 cm. By reading signals from long and short tubes separately, it becomes possible to distinguish between showers generated by electrons/photons and hadrons. Most of the energy release of showers from electrons and photons is detected by long tubes, while the energy release of showers from hadrons is recorded by both long and short tubes. The HF energy resolution for hadronic jets is approximately $\Delta E/E \approx 200\%/\sqrt{E(\mathrm{GeV})}$.

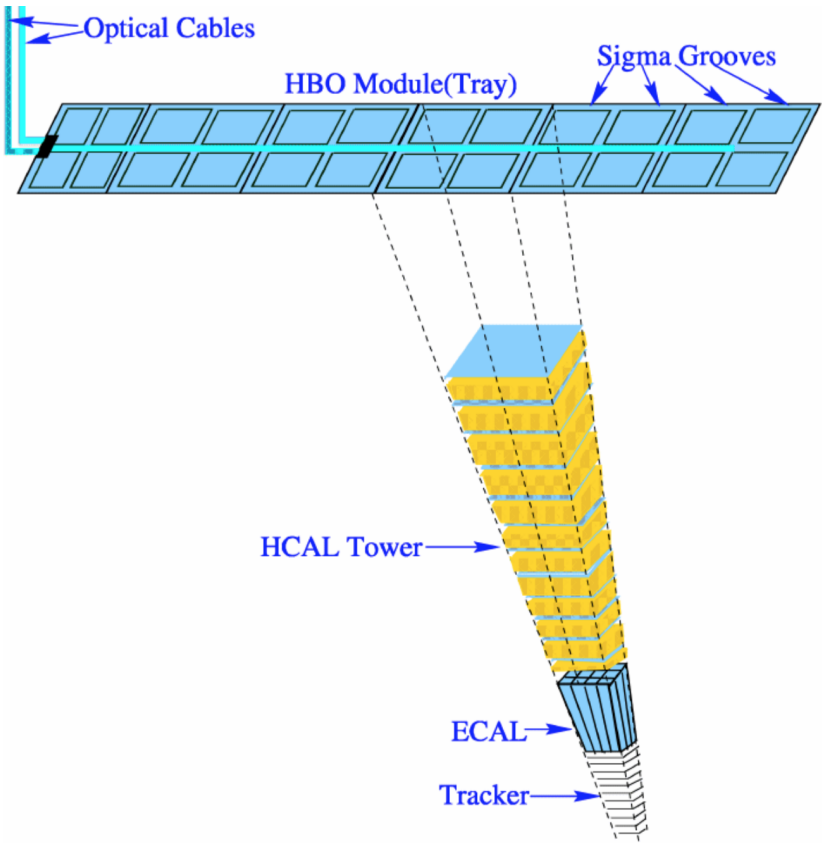


Figure 2.4 — Schematic representation of the CMS detector calorimeter towers [50].

### 2.2.3 Muon system

Due to low ionization losses, muons are able to go through the electromagnetic and hadronic calorimeters. Since electrons, protons, and hadrons are stopped in the calorimeters, charged particles detected outside the calorimeters are most likely muons. The muon system is located outside the superconducting solenoid and is immersed in the steel yoke of the magnet. The muon system consists of three types of gas detectors: Drift Tubes (DT), Cathode Strip Chambers (CSC) and Resistive Plate Chambers (RPC).

Drift tubes DT are located in the central region $|\eta|$ <1.2 and are arranged into 4 layers forming a superlayer. Chambers are formed from superlayers. The superlayers in the chambers are located at right angles, which makes it possible to record the coordinates of the muon passage.

Cathode strip chambers CSC are located in the endcaps and cover the pseudorapidity region $|\eta| < 2.4$. The reason for using different types of detectors for the central and forward regions in different operating conditions of the detector

subsystems is that in the forward region, the muon count rate is higher and the residual magnetic field is larger.

The RPC are located both in the yoke rings of the cylindrical part and in the endcaps. RPCs provide good spatial and temporal resolution. The muon track is reconstructed based on information from the tracker and signals from the RPC and DT in the central region or the RPC and CSC signals from the endcaps in the forward/backward regions.

### 2.2.4 Reconstruction of events and hadronic jets

Global event reconstruction, which aims to reconstruct and identify every particle in the event, is called particle-flow (PF) reconstruction [86]. To achieve the goal, information from all detection systems is used. In this process, identification of the particle type (photon, electron, muon, charged hadron, neutral hadron) plays an important role in reconstructing the direction of the particle's trajectory and its energy. Photons are identified as an energy release in the ECAL cluster not associated with the track of a charged particle. Electrons are identified by a track and an energy deposition in the ECAL cluster corresponding to that track. Muons are defined as tracks in the silicon tracker corresponding to a track or several interaction points in the muon detection system, as well as an energy release in the calorimeters. Charged hadrons are identified as a track of a charged particle not identified as an electron or muon, and the associated energy release in the ECAL and HCAL. Finally, neutral hadrons are identified as an energy release in the HCAL cluster that is not correlated with the track of a charged particle, or as an excess of ECAL and HCAL energy release relative to the expected energy release from a charged hadron.

Photon energy is determined from ECAL measurements. The electron energy is determined from a combination of information about the momentum of the electron track at the proton interaction vertex, the energy of the corresponding ECAL cluster, and the energy of all bremsstrahlung photons from the electron track. The muon energy is determined based on the momentum of the muon track. The energy of charged hadrons is determined from a combination of the track momentum information and the energy deposition in the corresponding ECAL and

HCAL calsters. The energy of neutral hadrons is determined based on the energy release in ECAL and HCAL clusters.

In each event, hadronic jets are reconstructed from reconstructed particles using the infrared and collinear safe anti-$k_T$ algorithm [87; 88]. The value of the jet size parameter depends on $\sqrt{s}$ and at $\sqrt{s} = 2.76$ TeV is $0.5 \div 0.7$. The jet momentum is defined as the vector sum of the particle momenta in the jet. MC modeling shows that the reconstructed jet momemtum is shifted on average within 5-10% of the true jet momentum throughout the entire detector acceptance and momentum range. A description of the multi-level procedure for correcting the energy of hadronic jets is given in [89]. The energy resolution of hadronic jets is 15% at 10 GeV, 8% at 100 GeV and 4% at 1 TeV. Additional jet quality criteria (JetID) are applied to the reconstructed jets to eliminate jets that are potentially dominated by anomalous contributions from noise of detector components and reconstruction errors.

### 2.2.5 Trigger system

The rate of processing and recording events, as well as the available memory capacity, are limited. This leads to the need for quick selection of events. Events are selected using a two-level trigger system [90]. First level (L1) triggers are implemented as hardware processors. L1 triggers use signals from the calorimeters and muon detectors and lower the frequency from 40 MHz (the intersection frequency of beam bunches in the LHC) to a frequency of up to 100 kHz. Second-level triggers, also called high-level triggers (HLT), are a computer cluster that performs full event reconstruction using deployed detector software optimized for fast execution. High level triggers lower the frequency to 1 kHz. Events of this frequency can be recorded.

# Chapter 3. Measurement of $\Delta y$-differential dijet production cross sections and their ratios with the veto

Measuring the cross sections for the dijet production and the ratios of the dijet cross sections with veto comes down to solving the following tasks:

– Selection of dijet events with triggers.
– Combining samples recorded using different triggers.
– Studying the trigger efficiency.
– Studying detector distortions and the correction of the measurement.
– Studying and estimating systematic uncertainties

These tasks are discussed in this chapter in detail, as well as the results of the measurement are presented and discussed.

## 3.1 Event selection, triggers

A sample of experimental data of $pp$ collisions at $\sqrt{s} = 2.76$ TeV with integrated luminosity of 5.34 pb$^{-1}$ used in this work was recorded using the CMS detector in 2013. The data was collected in special LHC runs in which the average number of collisions per event was lowered to 0.35. This allows more accurate measurements of hadronic jets at large rapidities $y$.

The jets are reconstructed with the collinearly and infrared-safe anti-$k_T$ [87] algorithm implemented in the FASTJET [88] package. The jet size parameter in pseudorapidity-azimuthal angle ($\eta - \varphi$) space is chosen equal to 0.5. The same size was used to measure the dijet ratios $R^{\text{incl}}$ and $R^{\text{MN}}$ in proton collisions at energy $\sqrt{s} = 7$ TeV [37]. The anti-$k_T$ cluster algorithm combines particles recnstructed by the particle flow (PF) algorithm [86]. We will denote such hadronic jets as ak5PF jets. It should be noted that hadronic jets with $\eta > 3$ are reconstructed only on the basis of the calorimetric information from HF.

The four-momentum of the jet is determined by the sum of the four-momenta of its constituent particles. MC simulations show that the reconstructed jet momentum is within $5 \div 10$ % of the true value of the hadronic jet momentum. In order to take this difference into account the following corrections are applied: the

correction that takes into account the contribution from secondary $pp$ interactions in the same intersection of the beam bunches or from the neighboring intersections; correction obtained from MC simulation; and a correction taking into account residual differences between the MC simulation and experiment, based on the study of a jet balance [89]. To reduce the calorimetric noise, the reconstructed jets must satisfy soft (loose) jet identification conditions (Jet ID) [91]. The resolution of the jet energy is about 15% at a jet energy of 10 GeV, 8% at 100 GeV and 4% at 1 TeV.

The data was collected using the two-level trigger system of the CMS [90] detector. Combining events selected by different triggers allows us to obtain a sufficient sample size over the entire span of the rapidity interval $\Delta y < 9.4$. The triggers used in this work are listed in table 1. The table 1 also presents the effective luminosities of the samples recorded using the corresponding triggers and the short names of the triggers that will be used in the text of this work.

Table 1 — Triggers used to select events

| Trigger | Effective luminosity | Short name |
|---|---|---|
| HLT_PAZeroBiasPixel_SingleTrack_v1 | 108.0 мкб$^{-1}$ | ZeroBias |
| HLT_PAMinBiasHF_OR_v1 | 91.846 мкб$^{-1}$ | MinBias |
| HLT_PAJet20_NoJetID_v1 | 47.3 нб$^{-1}$ | Jet20 |
| HLT_PAForJet20Eta3_v1 | 382.6 нб$^{-1}$ | ForJet20Eta3 |
| HLT_PADoubleJet20_ForwardBackward_v1 | 4.6 пб$^{-1}$ | DoubleJet20 |

The ZeroBias and MinBias triggers have minimum requirements and are used as reference triggers to evaluate the efficiency of other triggers. The ZeroBias trigger randomly selects events for recording. The condition of the presence of at least one charged particle track in the pixel tracker in an event is introduced into the ZeroBias trigger to increase the probability of the presence of $pp$ interaction in the event. The MinBias trigger selects events in which a signal is present in at least one tower of the forward HF calorimeter.

Jet20 is used to select events with dijets with minimal rapidity separation. This trigger requires the presence in the event of at least one hadronic jet with a transverse momentum $p_\perp$ above the trigger threshold 20 GeV. We will call the sample obtained using this trigger the central sample, and the trigger itself will be called central.

Dijets with intermediate separation in rapidity are selected using the ForJet20Eta3 trigger, which requires the presence in the event of at least one

jet with a transverse momentum above the trigger threshold 20 GeV in the forward or backward pseudorapidity region. By the forward pseudorapidity region we mean the region $\eta > 3$, and by the backward pseudorapidity region we mean the region $\eta < -3$.

Dijet events with maximal rapidity separation are selected using the DoubleJet20 trigger, which requires the presence of at least one jet with a transverse momentum greater than 20 GeV in the forward region and one jet with a transverse momentum greater than 20 GeV in the backward region.

In addition to trigger selection, an offline selection for the number and quality of vertices in an event is applied. The event must have at least one vertex associated with at least 4 tracks of charged particles in the tracker. The vertex should be reconstructed no further than 2 cm from the beam axis in the transverse direction and no further than 24 cm from the nominal intersection point of the beams in the direction along the beam axis. To reduce the possible contribution from events caused by the interaction of beam protons with the residual gas and with the collimation systems of the accelerator, the selection for the number of charged tracks associated with the vertex is increased to 10. At the same time, the percentage of tracks that passed the selection of «high purity» [92] should be at least 25%.

## 3.2 Trigger efficiency

The efficiency of the triggers is studied as a function of the transverse momentum and pseudorapidity ($p_\perp - \eta$) of the jet. As can be seen from the definition of trigger conditions given in the previous paragraph 3.1, the Jet20 and ForJet20Eta3 triggers are single-jet, that is, to trigger them, one jet that has passed the trigger condition is enough. On the other hand, the DoubleJet20 trigger is a two-jet trigger. The determination of the efficiency of single-jet and two-jet triggers is different.

The efficiency of the single-jet triggers is defined as the ratio of the distributions of the leading hadronic jet (the hadronic jet with the maximal transverse momentum in an event) for the studied and reference triggers. A trigger with weaker selection conditions is used as the reference trigger. The reference triggers used in studying the efficiency are given in Table 2.

Table 2 — Reference triggers

| Studied trigger | Reference trigger |
|---|---|
| Jet20 | ZeroBias и MinBias |
| ForJet20Eta3 | PAJet20 |
| DoubleJet20 | ForJet20Eta3 |

The efficiency, $\varepsilon$, of Jet20 trigger is defined as the ratio $(p_\perp, \eta)$ of the leading jet distribution for events selected by this trigger to the same distribution for events selected by the ZeroBias or MinBias trigger. The set of two triggers (ZeroBias and MinBias) is used to increase statistics. Before calculating trigger efficiency, the distributions in the numerator and denominator must be normalized to the cross section using the effective luminosity. The effective luminosity of the sample selected with two ZeroBias or MinBias triggers can be calculated based on the known effective luminosity of each trigger and a correction factor. The correction factor is defined as the result of a constant approximation of the ratio of the $p_\perp$ distributions obtained by the set of triggers (ZeroBias and MinBias) to the $p_\perp$ distribution obtained by only one of the two triggers, for example MinBias.

The efficiency of the Jet20 trigger as a function of $p_\perp$ and $\eta$ is presented in Figure 3.1a. The integrated efficiency of Jet20 is plotted in Figures 3.2a and 3.2b as a function of one variable $p_\perp$ and $\eta$, respectively. Based on the obtained dependencies, we can conclude that the trigger selects events in which there is at least one hadronic jet with a transverse momentum above 35 GeV with an efficiency of at least 90%. At the same time, we are interested in events in which there are at least two hadronic jets with a transverse momentum above 35 GeV. Since the trigger can fire on any of these two jets, the probability of selecting two-jet events determined by formula 3.1 is at least 99% for dijet event selection with $p_\perp$ of jets in dijets above 35 GeV. A more detailed analysis of the influence of trigger inefficiency on measured observables is given in paragraph 3.4 «Account of trigger inefficiency» of this chapter.

$$\varepsilon_{\text{event}} = 1 - \prod_{\text{jet} \in \text{event}} (1 - \varepsilon_{\text{jet}}), \tag{3.1}$$

where $\varepsilon_{\text{event}}$ — trigger efficiency for an event.

$\varepsilon_{\text{jet}}$ — trigger efficiency for a jet.

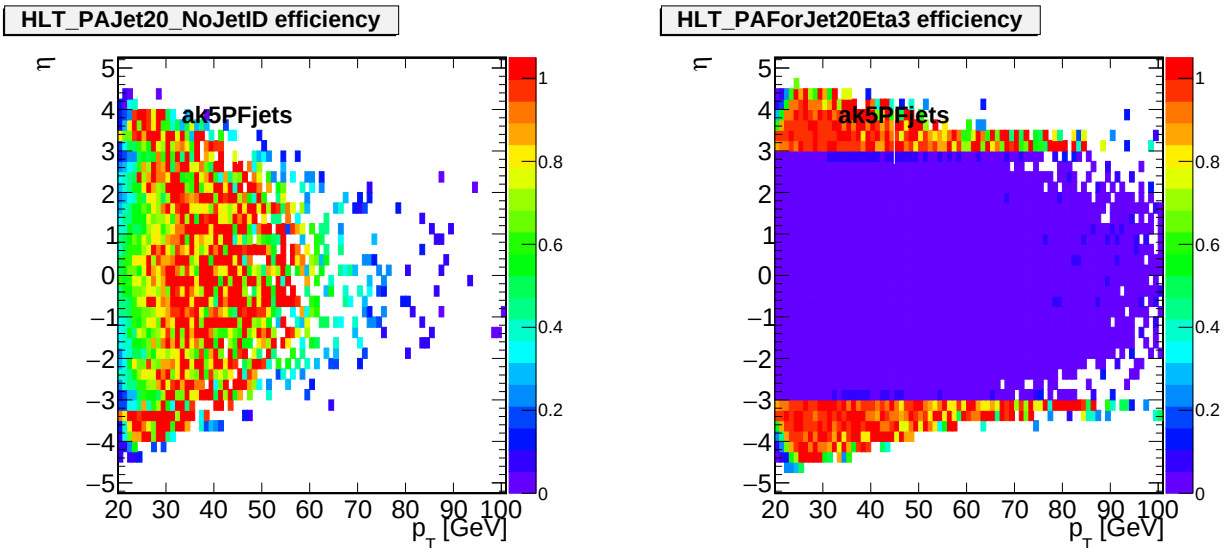


a) b)

Figure 3.1 — Efficiency of single jet triggers Jet20 a) and ForJet20Eta3 b) as a function of the transverse momentum, $p_\perp$, and the pseudorapidity, $\eta$, of the leading hadronic jet.

The efficiency, $\varepsilon$, of the trigger ForJet20Eta3 is defined as the ratio $(p_\perp, \eta)$ of the distribution of the leading jet in the forward, $\eta > 3$, or backward, $\eta < -3$, region for this trigger to the corresponding distribution, obtained using the Jet20 trigger. In events selected by the Jet20 trigger, jets with maximal transverse momentum in the forward or backward region are identified, and their distribution is obtained. Before calculating the trigger efficiency, the distributions in the numerator and denominator are normalized to the cross section using the effective luminosity. The efficiency of the ForJet20Eta3 trigger is shown in Figure 3.1b. The integrated efficiency of the ForJet20Eta3 trigger is plotted in Figures 3.3a and 3.3b as a function of one variable $p_\perp$ and $\eta$, respectively. Based on the obtained dependencies, we can conclude that the trigger ForJet20Eta3 selects events in which there is at least one hadronic jet with a transverse momentum above 35 GeV in the forward or backward region with an efficiency no less than that of the Jet20 trigger, that is, 90%. Two-jet events selected by the ForJet20Eta3 trigger may contain one jet in the forward (backward) region and one jet in the central region $|\eta|$ <3, where this trigger is not effective, so the minimum efficiency of event selection by this trigger is 90%. A more detailed analysis of the influence of trigger inefficiency on the measured observables is given in paragraph 3.4.

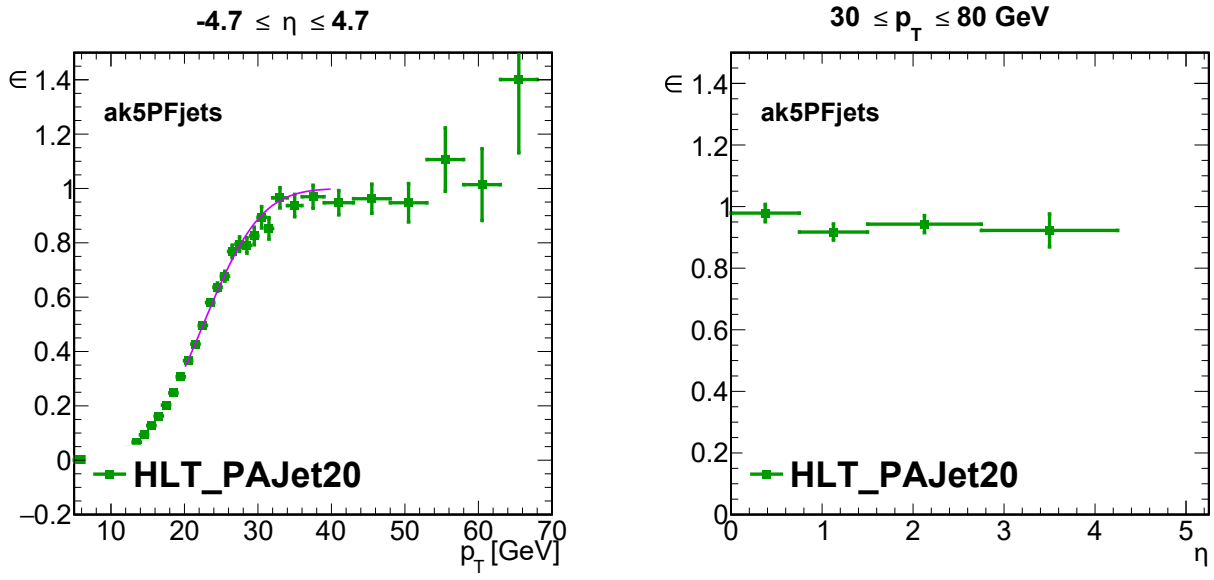


a) b)

Figure 3.2 — Integrated trigger efficiency for Jet20. a) Efficiency 3.1a integrated over pseudorapidity in the interval $\eta \in [-4.7, 4.7]$ as a function of the transverse momentum of the leading jet, $p_\perp$; b) Efficiency 3.1a integrated over the transverse momentum in the interval $30 \leqslant p_\perp \leqslant 80$ GeV as a function of the absolute value of pseudorapidity $|\eta|$. Solid line – result of approximation with the function Eq. (3.3).

The efficiency, $\varepsilon$, of the DoubleJet20 two-jet trigger is determined only as a function of the transverse momentum, $p_\perp$, due to the lack of sufficient statistics for the reference ForJet20Eta3 trigger in the efficiency range of the DoubleJet20 trigger under study. The $p_\perp$ trigger turn-on curve is defined as the ratio of the $p_\perp$ distributions of hadronic jets with maximal transverse momentum in the opposite backward $\eta < -3$ (forward $\eta > 3$) region from the leading jet in the forward (backward) regions. For example, consider an event in which, among the hadronic jets in the forward and backward regions, the jet with the maximal transverse momentum is in the forward region. Then we have to look for the hadronic jet with maximal transverse momentum in the opposite, that is backward, region and use its transverse momentum in the distribution. To calculate the efficiency, the contribution to the numerator is given by events in which DoubleJet20 and ForJet20Eta3 are triggered simultaneously, and the denominator of events in which only ForJet20Eta3 is triggered. This procedure is called a trigger coincidence scheme. With this scheme, the inefficiency of the reference trigger is canceled, which is convenient. However, it is possible to use the coincidence scheme when the prescale

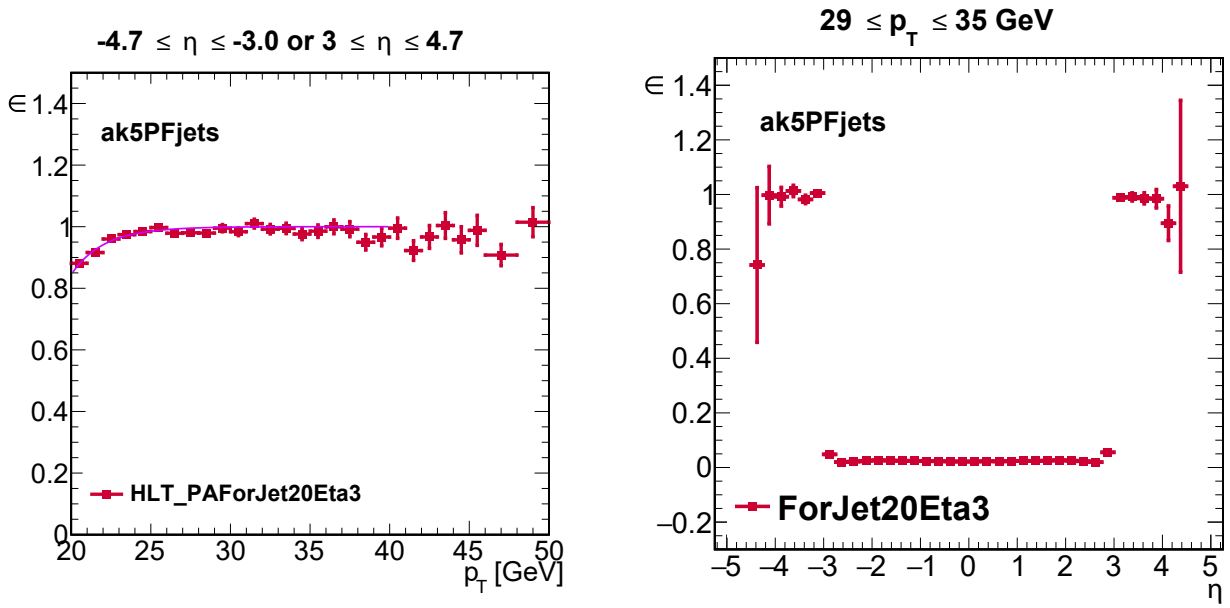


a) b)

Figure 3.3 — Integrated trigger efficiency for ForJet20Eta3. a) Efficiency 3.1b integrated over pseudorapidity in the interval $\eta \in [-4.7, -3] \cup [3, 4.7]$ as a function of the transverse momentum of the leading jet, $p_\perp$; b) Efficiency 3.1b integrated over the transverse momentum in the interval $29 \leqslant p_\perp \leqslant 35$ GeV as a function of the absolute value of pseudorapidity $\eta$. Solid line – result of approximation with the function Eq. (3.3).

of the trigger under study is close to one, otherwise the coincidence scheme becomes ineffective. The prescale is set for triggers, the rate frequency of which does not fit within the limit set for them. Thus, an event is recorded for a fired trigger with a probability of 1/prescale. The efficiency of the DoubleJet20 trigger is shown in figure 3.4. Based on the obtained dependence, we can conclude that the DoubleJet20 trigger is 100% effective in selecting events in which at least one jet with $p_\perp > 35$ GeV in the forward region and at least one jet with $p_\perp > 35$ GeV in the backward region.

## 3.3 Merging trigger samples

The effectiveness region of each trigger covers a part of the phase space under study. To obtain distributions in the entire phase space under study, samples from different triggers must be combined. When combining samples, areas of double

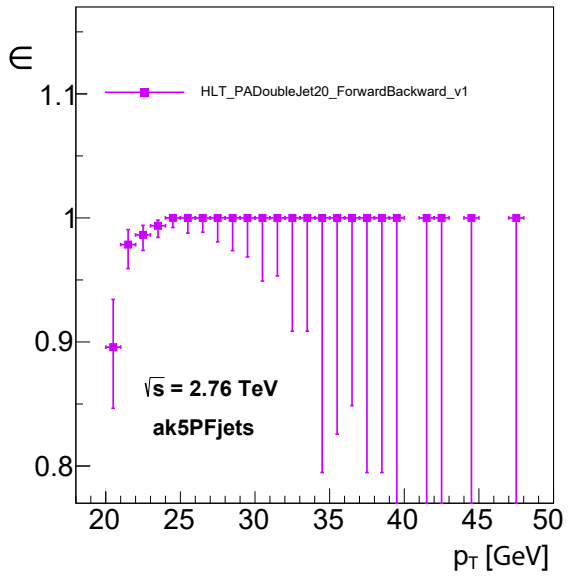


Figure 3.4 — Trigger efficency for DoubleJet20 as function of transverse momentum, $p_\perp$, in opposite backward $\eta < -3$ (forward $\eta > 3$) region from leading jet in forward (backward) region.

counting should be eliminated. To do this, mutually exclusive conditions are imposed on samples obtained by the triggers. Thus, among the events selected by the Jet20 trigger, we leave only events in which there is not a single hadron jet with a transverse momentum $p_\perp > 35$ GeV in the forward ($\eta > 3$) and backward ($\eta < -3$) regions. Among the events selected by the ForJet20Eta3 trigger, we leave events in which there is a jet with transverse momentum $p_\perp > 35$ GeV in the forward or backward region, but not in both regions at the same time. Finally, among the events selected by the DoubleJet20 trigger, we leave events in which there are jets with $p_\perp > 35$ GeV in the forward and backward regions simultaneously.

To obtain cross sections based on the combined sample, the events selected by a trigger must be weighted. The inverse effective luminosity of the trigger multiplied by its efficiency is used as the weight:

$$w = \frac{1}{l\varepsilon_{\text{event}}}, \tag{3.2}$$

where $l$ — effective luminosity of the trigger (Table. 1).

## 3.4 Accounting of trigger inefficiency

To assess the effect of trigger inefficiency on measurements, the trigger turn-on curves for the transverse momentum in Figs. 3.2a and 3.3a are approximated by the function:

$$\varepsilon_{\text{jet}}(p_\perp) = \int_{p_1}^{\infty} \frac{p_3}{\sqrt{2\pi p_0}} \exp\left( -\frac{(p_\perp - t)^2}{2p_0} \right) \times \left( 1 - \exp\left( -\frac{t - p_1}{p_2} \right) \right) dt, \quad (3.3)$$

where $p_0, p_1, p_2, p_3$ — parameters of the approximation.

The result of the approximation is presented in the figures 3.2a and 3.3a with the solid line. The resulting approximation is used to calculate the efficiency of event registration by the trigger using the formula (3.1). Since when calculating the efficiency of the ForJet20Eta3 trigger, the Jet20 trigger is used as a reference, the efficiency of the ForJet20Eta3 trigger is equal to the product of the approximation results for two triggers (Fig. 3.2a and 3.3a).

A comparison of the observables obtained for $\varepsilon_{\text{event}} = 1$ (inefficiency is not taken into account) and for the efficiency based on the approximation of the trigger turn-on curves (inefficiency is taken into account) is presented in figures 3.5 and 3.6. The comparison shows that taking into account inefficiency leads to an adjustment not exceeding 2% for cross sections and 0.2% for cross section ratios. The magnitude of the correction is much less than the statistical uncertainties shown in the figures by the vertical lines. Given the smallness of the correction, a conservative estimate of the uncertainty of the correction is used, that is, the uncertainty is the full value of the correction for the inefficiency. This uncertainty will be taken into account when calculating the total systematic measurement uncertainty.

## 3.5 Study and accounting of detector effects

The finite resolution of the detector in determination of transverse momentum and the rapidity of hadronic jets leads to migration of jets at thresholds of the transverse momentum $p_\perp = 35$ GeV and $p_\perp = 20$ GeV, as well as between histogram

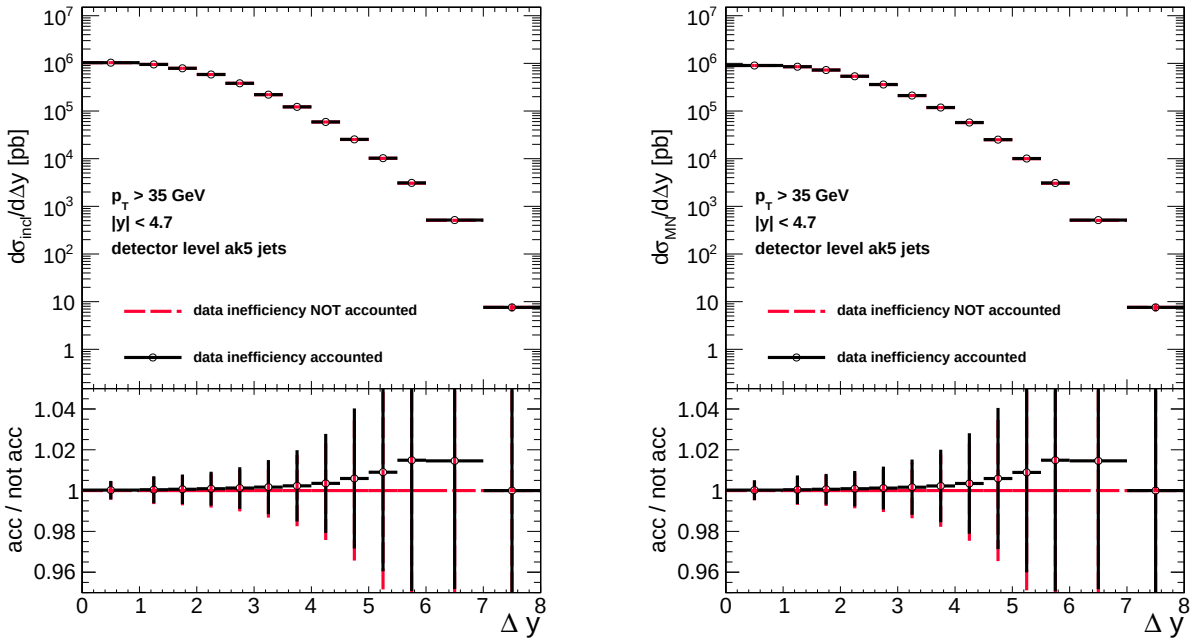


a) b)

Figure 3.5 — Comparison of cross sections before and after taking into account the inefficiency of the triggers a) $d\sigma^{\text{incl}}/d\Delta y$ and b) $d\sigma^{\text{MN}}/d\Delta y$. Red dashed line - before taking into account inefficiency; Solid black line – after accounting for inefficiency.

cells of the rapidity interval $\Delta y$. The study of these effects is carried out on the basis of MC modeling [A6; 93].

To study detector effects, MC samples are obtained using two MC generators PYTHIA8 [41] with tune 4C [72] and HERWIG++ [42] with tune UE-EE3C [74]. To simulate detector distortions, proton collisions obtained using MC generators are passed through a detector model implemented in the GEANT4 software package [94]. In the experimental data used for measurements in this work, the probability of secondary $pp$ collisions in the same intersection of beam bunches is 0.35. To simulate this effect, the signal from the secondary collisions recorded using the MinBias trigger is added to the signal from the primary collisions during the detector simulation stage. The study of the jet energy resolution of the MC simulation of the detector [95] shows that the resolution in the MC model of the detector systematically underestimates the resolution of the detector. Therefore, the resolution of the MC model is further adjusted to match the resolution of the detector. Coefficients that correct the resolution of the MC model of the detector are given in Table 3. Samples and distributions based on MC before modeling the detector will be called samples and distributions at the generator level. The samples

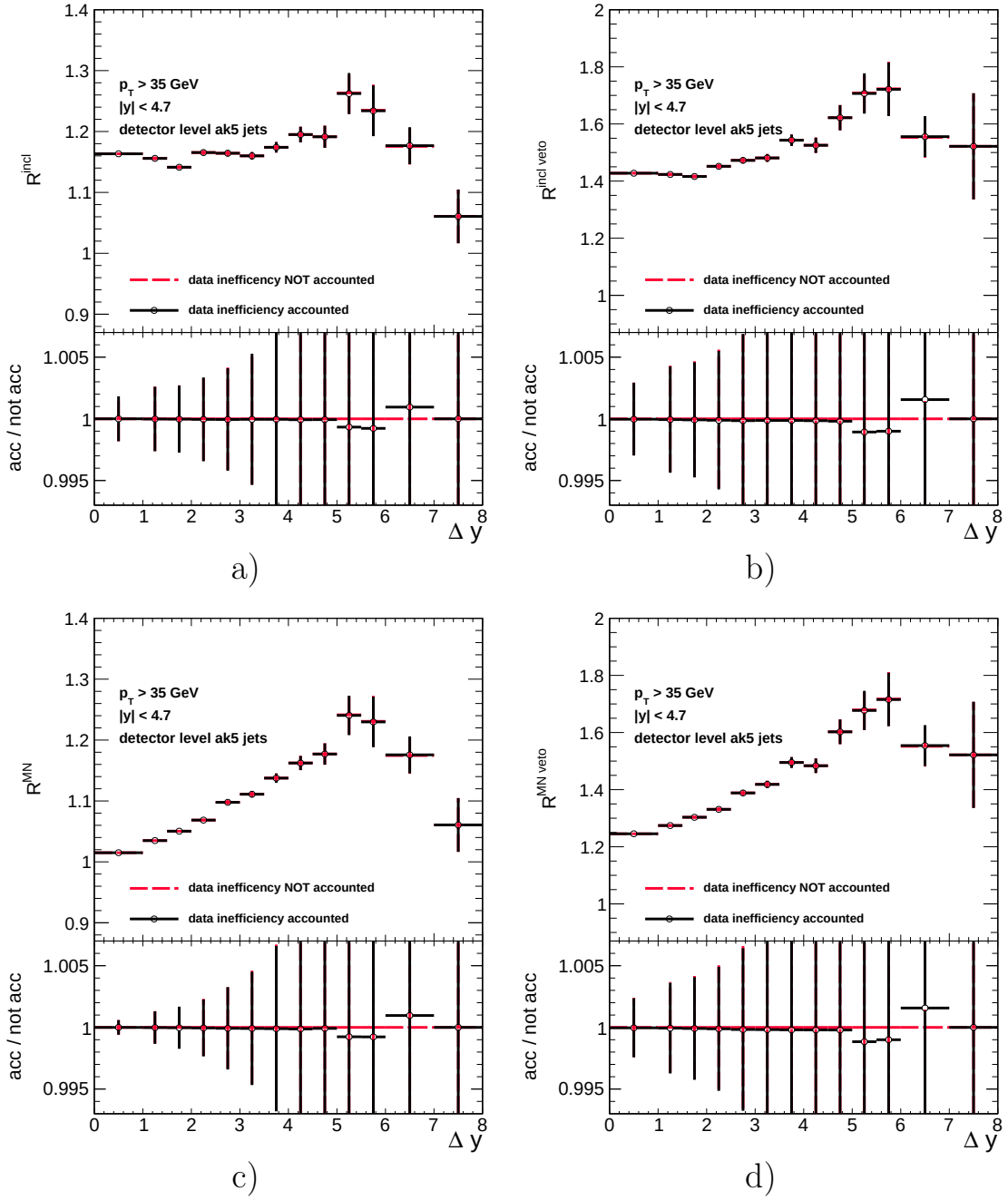


Figure 3.6 — Comparison of cross-section ratios before and after taking into account the inefficiency of the triggers a) $R^{\mathrm{incl}}$, b) $R^{\mathrm{incl}}_{\mathrm{veto}}$, c) $R^{\mathrm{MN}}$ and d) $R^{\mathrm{MN}}_{\mathrm{veto}}$. Red dashed line - before taking into account inefficiency; Solid black line – after accounting for inefficiency.

and distributions for experimental data and MC after detector modeling will be called reconstructed data and reconstructed MC, respectively.

Detector distortions are taken into account using unfolding [A6; 93]. Unfolding is used to reconstruct cross sections. The reconstructed cross section ratios are calculated based on the reconstructed cross sections. However, this procedure does

Table 3 — Correction factors for the energy resolution of hadronic jets of the MC detector model

| $\|\eta\|$ | $c^{data/MC}$ |
|---|---|
| 0.0–0.5 | $1.079 \pm 0.026$ |
| 0.5–1.1 | $1.099 \pm 0.028$ |
| 1.1–1.7 | $1.121 \pm 0.029$ |
| 1.7–2.3 | $1.208 \pm 0.046$ |
| 2.3–2.8 | $1.254 \pm 0.062$ |
| 2.8–3.2 | $1.395 \pm 0.063$ |
| 3.2–5.0 | $1.056 \pm 0.191$ |

not guarantee that the corrected cross section ratios will be greater than unity. At the same time, the measured cross section ratios must be greater than unity by the definition. In order to avoid this difficulty, the cross section ratios are presented in the form:

$$R = \frac{D^{\text{num}}}{D^{\text{den}}} = 1 + \frac{D^{\text{num}} - D^{\text{den}}}{D^{\text{den}}}, \tag{3.4}$$

where $D^{\text{num}}$ — denotes the distribution in the numerator of the ratio ($d\sigma^{\text{incl}}/d\Delta y$ or $d\sigma^{\text{MN}}/d\Delta y$);

$D^{\text{den}}$ — denotes the distribution in the denominator of the ratio ($d\sigma^{\text{excl}}/d\Delta y$ or $d\sigma^{\text{excl}}_{\text{veto}}/d\Delta y$).

Thus, the unfolding is applied to the distributions:

$$
\begin{aligned}
D^{\text{excl}} &= \frac{d\sigma^{\text{excl}}}{d\Delta y}, \\
D^{\text{excl}}_{\text{veto}} &= \frac{d\sigma^{\text{excl}}_{\text{veto}}}{d\Delta y}, \\
D^{\text{incl\_wo\_excl}} &= \frac{d\sigma^{\text{incl}}}{d\Delta y} - \frac{d\sigma^{\text{excl}}}{d\Delta y}, \\
D^{\text{MN\_wo\_excl}} &= \frac{d\sigma^{\text{MN}}}{d\Delta y} - \frac{d\sigma^{\text{excl}}}{d\Delta y}, \\
D^{\text{incl\_wo\_excl}}_{\text{veto}} &= \frac{d\sigma^{\text{incl}}}{d\Delta y} - \frac{d\sigma^{\text{excl}}_{\text{veto}}}{d\Delta y}, \\
D^{\text{MN\_wo\_excl}}_{\text{veto}} &= \frac{d\sigma^{\text{MN}}}{d\Delta y} - \frac{d\sigma^{\text{excl}}_{\text{veto}}}{d\Delta y},
\end{aligned}
\tag{3.5}
$$

After applying the unfolding, all measured quantities can be calculated based on the results.

### 3.5.1 Study of migrations of dijets

The study of hadronic jet migrations associated with limited transverse momentum and rapidity resolution is performed based on jet matching between the generator and reconstructed levels for the MC samples. Two hadronic jets, one at the generator level and one at the reconstructed level, are considered mathced if the distance between them in the space of pseudorapidity and azimuthal angle does not exceed 0.4. If there is more than one jet from the opposite level within the specified distance, then the closest one is selected. The two matched hadronic jets are considered to be representations of one hadronic jet at different levels. For comparison, hadronic jets with transverse momentum greater than 10 GeV are used.

The limited transverse momentum resolution of the detector can lead to the case that the transverse momentum of the jet, which at the generator level had a transverse momentum above (below) the threshold $p_{\perp\min} = 35$ GeV or $p_{\perp\text{veto}} = 20$ GeV, will be reconstructed below (above) the corresponding threshold. Such migration can lead to that the events that did not belong to a given type (inclusive, MN, «exclusive» or «exclusive» with veto) at the generator level will belong to this type at the reconstructed level. We will call such events as background events. The reverse process is also possible. Events that belonged to a certain type at the generator level will no longer belong to this type at the reconstructed level. This leads to limited acceptance.

It should be noted that the background and acceptance can arise due to hadronic jets produced in secondary $pp$ collisions in the same or neighboring intersection of bunches. However, as we will see later, this effect is small compared to the migration of jets at transverse momentum thresholds.

The background $B(\Delta y)$ is determined by the fraction of dijets at the reconstructed level that do not have a matching with a dijet at the generator level. Acceptance $A(\Delta y)$ is defined as the fraction of generator level dijets mathced with reconstruction level dijets. Dijet is considered matched if each of the jets in the dijet has a match and the event is of the same type (inclusive, MN, «exclusive», or «exclusive» with veto) at both levels. The assessment of background and acceptance obtained for two MC models is presented in figures 3.7 and 3.8.

The magnitude of migration of pairs of hadronic jets over the rapidity interval $\Delta y$ is determined only for matched dijets and is characterized by the migration matrix. The migration matrix reflects the probability of a dijet having rapidity separation $\Delta y_{\text{gen}}$ at the generator level to have $\Delta y_{\text{reco}}$ at the reconstructed level. The estimate of migration matrices obtained based on the HERWIG++ generator is presented in Figure 3.9, and based on PYTHIA8 is presented in Figure 3.10. The migration matrices in Figures 3.9, 3.10 are presented in the form of two-dimensional histograms. Cells of the generator level («hadron level $\Delta y$») number the columns of the migration matrix, and cells of the reconstructed level («detector level $\Delta y$») number the rows.

The simulation results show that the background value increases as the rapidity interval increases from 35% to 85% (see Fig. 3.7). The magnitude of acceptance decreases with increasing rapidity interval from 75% to 55% (see Fig. 3.8). The amount of migration between cells of the rapidity interval, $\Delta y$, does not exceed

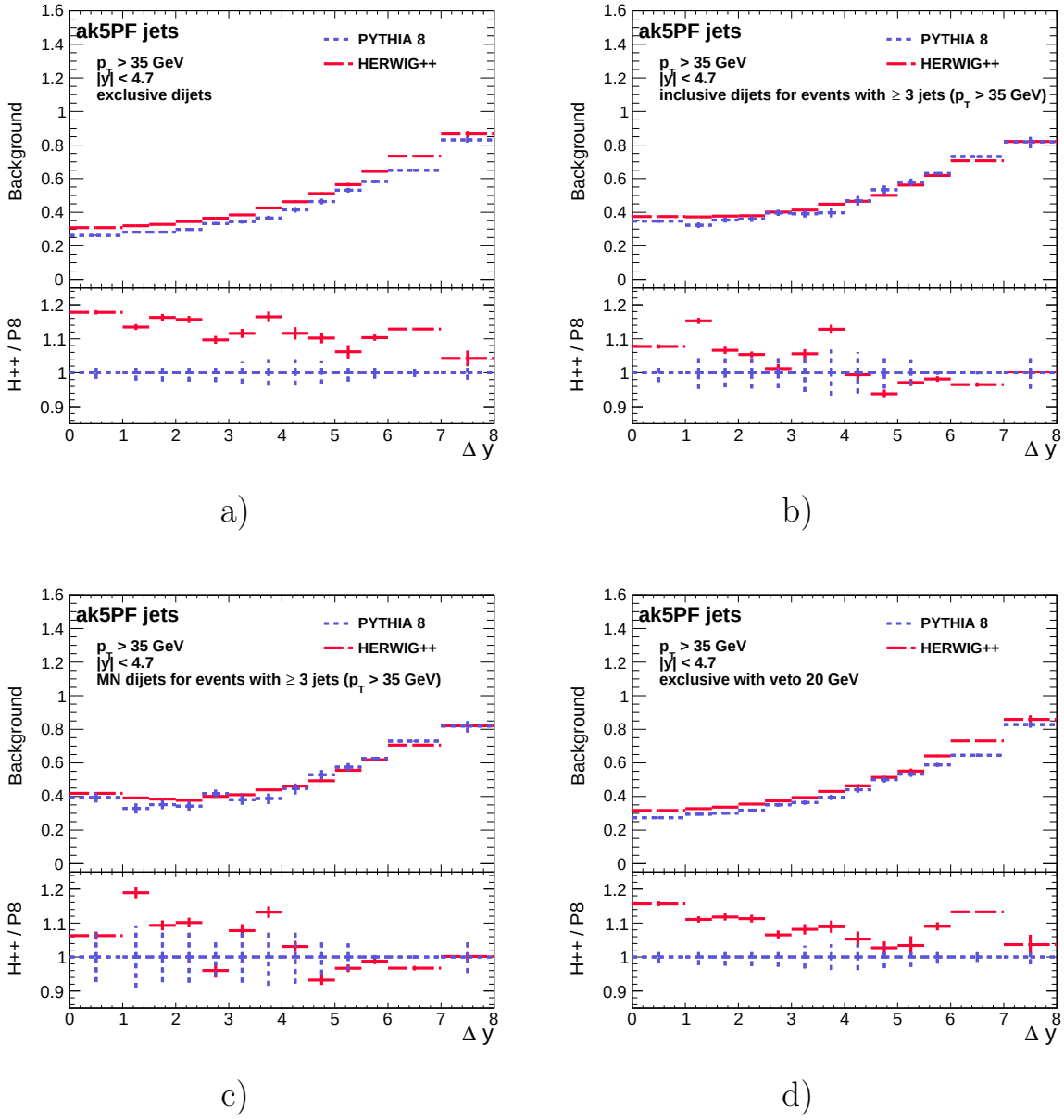


Figure 3.7 — Background estimation obtained for distributions: a) $D^{\text{excl}}$; b) $D^{\text{incl\_wo\_excl}}$; c) $D^{\text{MN\_wo\_excl}}$; and d) $D^{\text{excl}}_{\text{veto}}$. Red wide dashed line – HERWIG++; Blue short dashed line – PYTHIA8.

10% (see Fig. 3.9 and 3.10). Thus, the main contribution to detector distortions comes from background events. In addition, different MC models predict different background values; the difference reaches 18% (Fig. 3.7a). To determine the causes of the difference in the description of the background, the background for the «exclusive» events is examined in more detail. The background of «exclusive» events is divided into 7 types. The types included various variants of migration of hadronic jets relative to the transverse momentum threshold $p_\perp = 35$ GeV, leading to an «exclusive» event at the reconstructed level. Contributions to the background from

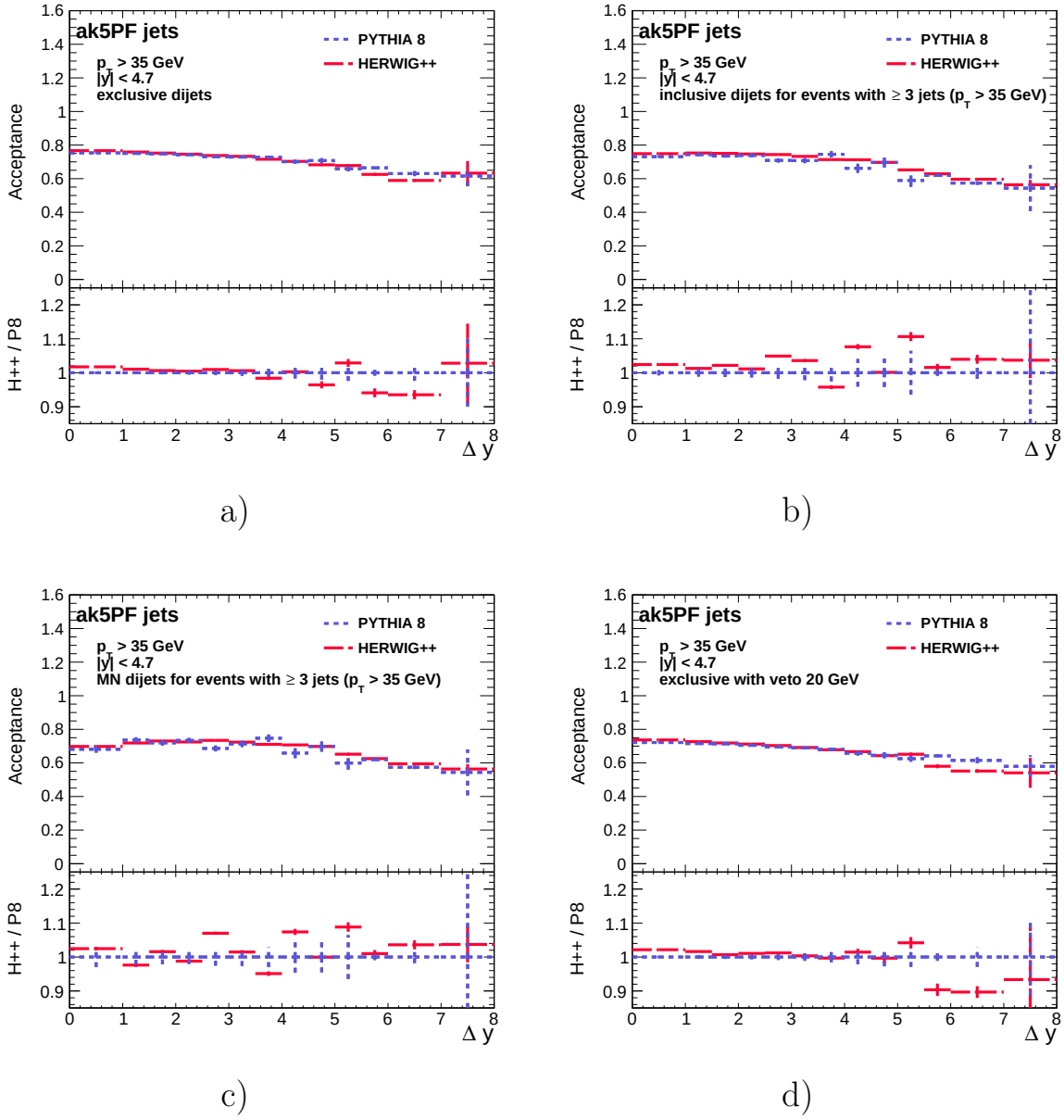


Figure 3.8 — Background estimation obtained for distributions: a) $D^{\text{excl}}$; b) $D^{\text{incl\_wo\_excl}}$; c) $D^{\text{MN\_wo\_excl}}$; and d) $D^{\text{excl}}_{\text{veto}}$. Red wide dashed line – HERWIG++; Blue short dashed line – PYTHIA8.

events that do not correspond to any of the defined types, as well as from secondary collisions in the same or adjacent intersection of beam bunches, are assessed together in an additional eighth type. Modeling showed that the main contribution to the background comes from two types. In the first of them, one hadron jet migrated from under the threshold about the transverse momentum, and in the second, both jets migrated from under the threshold. The contribution of these two types makes up 99% of the total background. The contribution from secondary collisions is less than 0.5%. In this case, the MC model HERWIG++ systematically predicts a

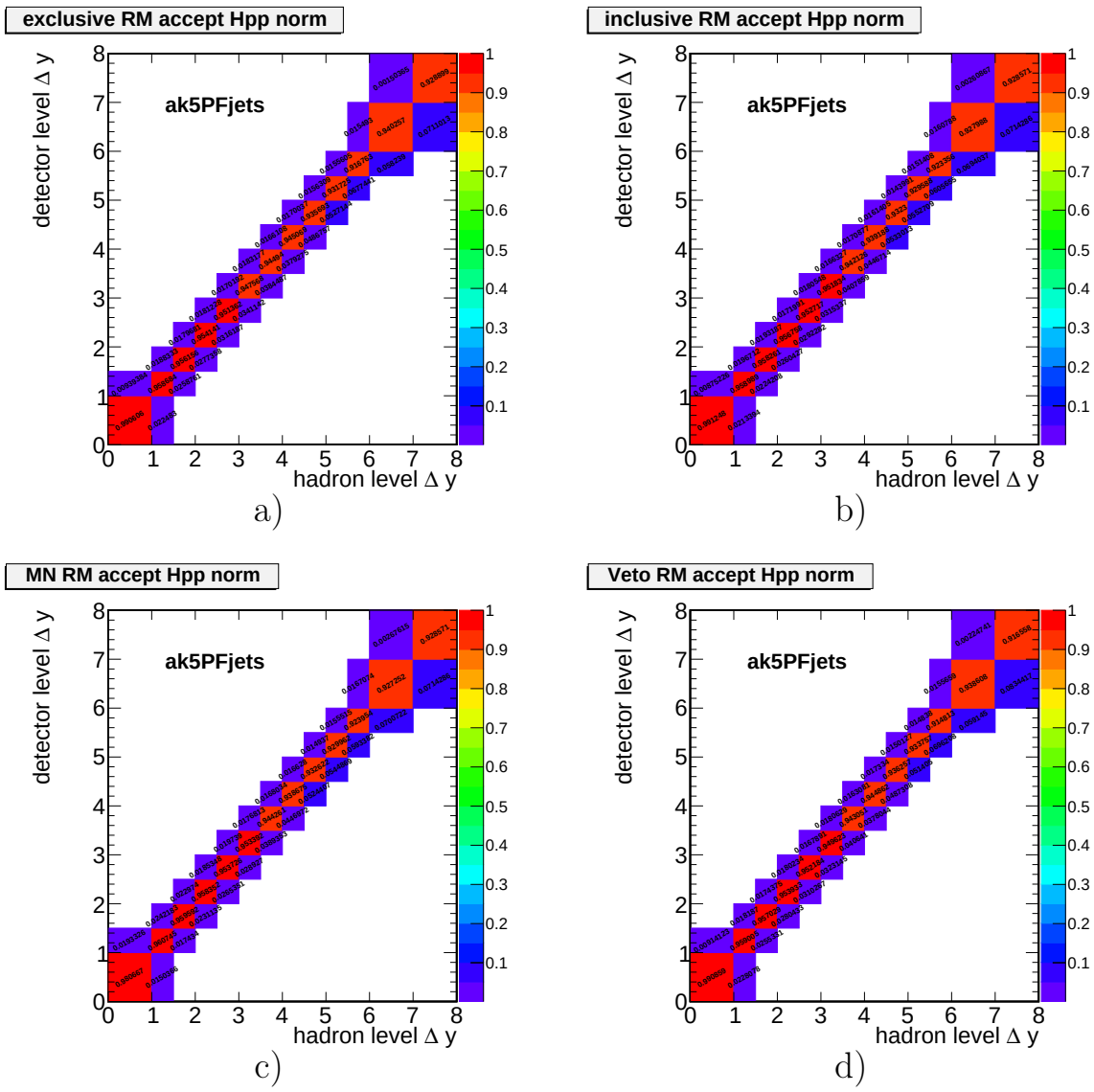


Figure 3.9 — Estimation of migration matrices obtained based on simulation with MC generator HERWIG++ for distributions: a) $D^{\text{excl}}$; b) $D^{\text{incl\_wo\_excl}}$; c) $D^{\text{MN\_wo\_excl}}$; and d) $D^{\text{excl}}_{\text{veto}}$.

larger background than PYTHIA8. The figure 3.11 shows the transverse momentum distributions at the reconstructed level $p_{\perp\text{reco}}$ for jets that have matching with jets of the generator level, for various intervals in the transverse momentum of the jet at the generator level. Figure 3.11 shows the different response of the detector model to hadronic jets obtained in different MC generators. In particular, the transverse momentum of jets modeled in HERWIG++ is systematically reconstructed with a larger value at the reconstructed level than for jets modeled in PYTHIA8. This leads to more intense migration and, accordingly, to greater background. Such systematic is associated with the selected models and will lead to model dependent (MD) uncertainty of the unfolding procedure discussed below (see paragraph 3.5.2).

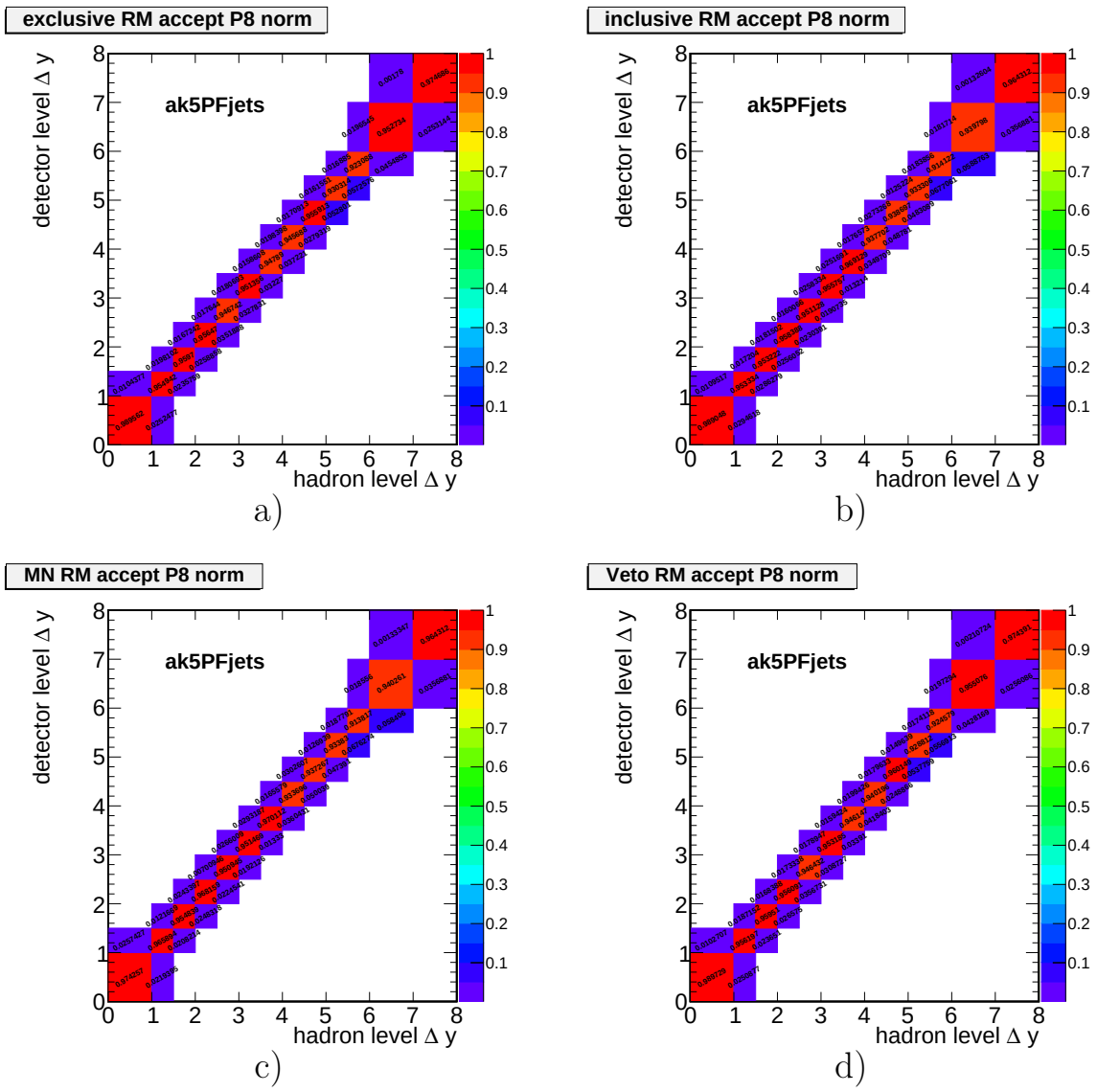


Figure 3.10 — Estimation of migration matrices obtained based on simulation with MC generator PYTHIA8 for distributions: a) $D^{\text{excl}}$; b) $D^{\text{incl\_wo\_excl}}$; c) $D^{\text{MN\_wo\_excl}}$; and d) $D^{\text{excl}}_{\text{veto}}$.

### 3.5.2 Detector distortion correction

Correction of the detector distortions is based on the use of unfolding. MC simulation is used to study the accuracy of generator level reconstruction using various unfolding methods. Methods which are investigated:

- bin-by-bin;
- matrix inversion;
- maximum likelihood method with Tikhonov regularization TUnfold [96];

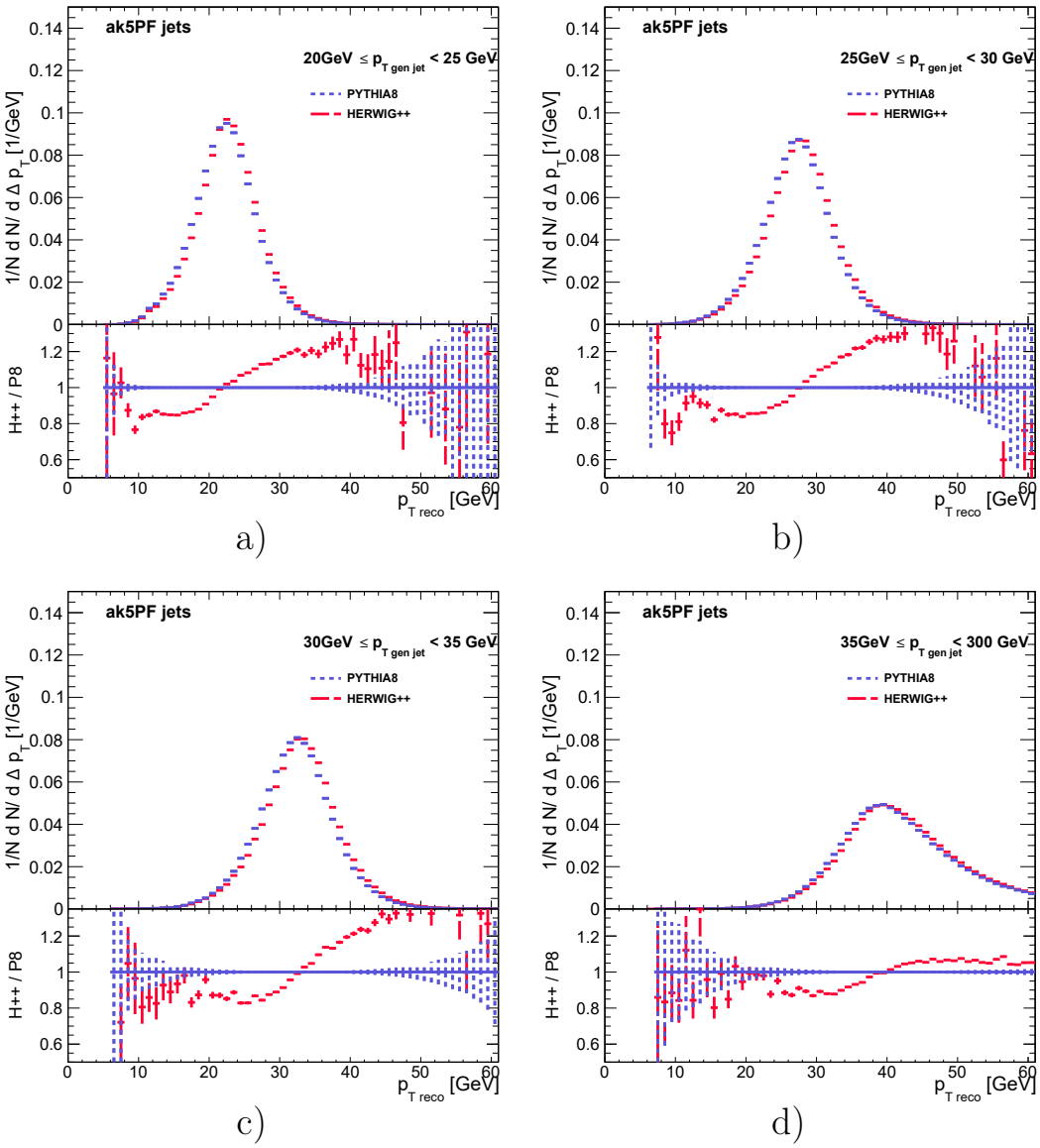


Figure 3.11 — Transverse momentum distribution at the reconstructed level for matched jets, $p_{\perp\text{reco}}$, for different values of the transverse momentum at the generator level: a) $20 \leqslant p_{\perp\text{gen}} \leqslant 25$ GeV, b) $25 \leqslant p_{\perp\text{gen}} \leqslant 30$ GeV, c) $30 \leqslant p_{\perp\text{gen}} \leqslant 35$ GeV and d) $35 \leqslant p_{\perp\text{gen}} \leqslant 300$ GeV. Red wide dashed line – HERWIG++; Blue short dashed line – PYTHIA8.

– maximum likelihood method with Tikhonov regularization based on singular value decomposition (SVD) [97];
– D'Agostini iterations method [98].

The TUnfold and SVD methods are implemented in the ROOT [99] software package. The algerbaic method of matrix inversion and D'Agostini iterations are implemented in the RooUnfold [100] software package. The TUnfold, SVD and D'Agostini methods include regularization, which can be specified using a manual or automatic parameter settings. Various values of the regularization parameters are tested when performing the unfolding procedure.

When taking into account acceptance and background, various options are possible. In the first option, the background can be added to an additional column of the migration matrix, and acceptance is taken into account by the method of correction factors (see formula (3.6)). It should be noted that different unfolding methods have different requirements for the shape of the response matrix. Thus, for TUnfold it is necessary that the number of cells of the generator level (the number of columns of the migration matrix) does not exceed the number of cells of the reconstructed level (the number of rows of the migration matrix). To apply inverse matrix method, the migration matrix must be square, that is, the number of columns of the matrix must be equal to the number of rows. In our case, the migration matrix is square before adding an additional column, so this method of taking into account the background is not suitable for TUnfold and the matrix inversion. In order to make the migration matrix square again, it is possible to add an additional row to the migration matrix containing events that are not reconstructed due to limited acceptance (see formula (3.7)). To summarize the above, in the first method of accounting for background and acceptance, the formula (3.6) is used for the SVD and D'Agostini methods, and the formula (3.7) for the TUnfold and algebraic matrix inversion method. This method of background accounting is the default method in RooUnfold for the D'Agostini method and the algebraic method of matrix inversion.

$$D_i^{\text{corr}} = \frac{\sum_j M_{ij}^{\prime -1} D_j^{\text{uncorr}}}{A_i}, \tag{3.6}$$

In formula (3.6):

$D_i^{\text{corr}}$ — distribution after correction for detector effects;

$M'_{ij}$ — extended migration matrix with background events added to an additional column;

$M_{ij}^{'-1}$ — matrix «inverse» to the extended migration matrix $M'_{ij}$ obtained using the unfolding methods;

$D_j^{\text{uncorr}}$ — distribution at the reconstructed level, that is, before correction for the detector effects;

$A_i$ — acceptance (distribution at Fig. 3.8).

$$D_i^{\text{corr}} = \sum_j M_{ij}^{''-1} D_j^{\text{uncorr}}, \tag{3.7}$$

where $M''_{ij}$ — an extended migration matrix in which background events are added to an additional column, and events that are not reconstructed due to limited acceptance are added to an additional row;

$M_{ij}^{''-1}$ — matrix «inverse» to the extended migration matrix $M''_{ij}$ obtained using the unfolding methods methods.

The second method of accounting for background is to subtract background events from the reconstructed distribution $D^{\text{uncorr}}$, before applying unfolding (see formula (3.8)). Acceptance is taken into account using correction factors. This method is used when the background is a consequence of independent processes that simulate the signal.

$$D_i^{\text{corr}} = \frac{\sum_j M_{ij}^{-1}(D_j^{\text{uncorr}} - F_j)}{A_i}, \tag{3.8}$$

where $M_{ij}$ — migration matrix;

$M_{ij}^{-1}$ — «inverse» matrix to the migration matrix obtained using the unfolding methods;

$F_j$ — background events.

The third method of taking into account the background and acceptance, used in this work, is the method of correction factors for taking into account background and acceptance (see formula (3.9)). This method of taking into account background and acceptance is applicable when the background and acceptance are correlated

with the signal. In our case, the background and acceptance arise as a result of the migration of hadronic jets along the transverse momentum. Migration, in turn, is proportional to the number of events in a given region of phase space, and therefore correlated with the signal.

$$D_i^{\text{corr}} = \frac{\sum_j M_{ij}^{-1} D_j^{\text{uncorr}} (1 - B_j)}{A_i}, \tag{3.9}$$

where $B_j$ — background (distribution at Fig. 3.7).

Closure and cross closure tests are used to determine the accuracy of generator level reconstruction by various unfolding methods. In the closure test, unfolding is applied to the MC distribution based on the migration matrix obtained using the same MC generator. In the cross closure test, unfolding is applied based on the other MC generator. In the cross closure test, the first MC generator plays the role of the reconstructed data, and the second MC generator is used for unfolding.

The closure test results show accurate generator level recovery based on all unfolding methods with minimal or no regularization for all background accounting methods. At the same time, the cross closure test results show that only the third method of taking into account the background (see formula (3.9)) leads to the unfolding result to be close to the generator level [A6; 93]. This result confirms the assumption that the background is correlated with the signal. If the third method of taking into account the background is used, then all unfolding methods give the same result with minimal or no regularization. The residual deviation of the reconstructed distribution from the generator level distribution ranges from 10% to 20%. Moreover, if, during cross closure test, we substitute the background distribution obtained by the same MC generator for which the unfolding is performed, leaving the migration matrix and acceptance, then we obtain restoration with an accuracy of 0.5% to 4%. Consequently, the residual deviation is mainly due to the difference in the description of the background studied in the previous paragraph «Study of migrations of dijets» (see paragraph 3.5.1).

Based on the tests performed, a method is selected and applied to the reconstructed data. Unfolding of the detector distortions is performed using the TUnfold method. The background and acceptance are taken into account according to the formula (3.9). Unfolding is performed based on two MC models: PYTHIA8 and HERWIG++. The unfolded distributions are calculated as half the sum of the results of unfolding with PYTHIA8 and HERWIG++. The assessment of the

systematic uncertainty associated with the choice of the MC model (model-dependent systematic uncertainty of the correction for detector effects) is calculated as the half-difference of the results of unfolding with PYTHIA8 and HERWIG++.

### 3.5.3 Propagation of statistical uncertainty

The propagation of the statistical uncertainty of the reconstructed data through the described unfolding procedure is performed using the statistical bootstrap method. To do this, 1000 pseudo samples are created as follows. In each pseudo sample, events from the original sample are included with a weight calculated based on the Poisson distribution with a mean of 1. Next, the unfolding procedure is applied to these pseudo samples. The results of the unfolding in each cell by $\Delta y$ are approximated by a normal distribution. The standard deviation value for the resulting normal distribution is used as an estimate of the statistical uncertainty of the unfolded distribution in the given $\Delta y$ cell.

## 3.6 Estimation of systematic uncertainties

In this work, the following sources of systematic uncertainties are considered:
– Jet energy scale (JES) uncertainty;
– Jet energy resolution (JER) uncertainty of MC modeling of the detector;
– Model dependence (MD) of unfolding;
– PDF uncertainty;
– Uncertainty of $\mu_R$ and $\mu_F$ scales of QCD;
– Uncertainty associated with limited statistics of MC (MCS) samples;
– Uncertainty in beam luminosity measurements (Lumi.);
– Trigger efficiency corrections (TEC) uncertainty;
– Uncertainty associated with pileup (PU) modeling;

Jet energy corrections are determined based on the multi-level approach described in [95]. The systematic measurement uncertainty associated with JES is estimated by scaling the energy of the hadronic jets within the jet energy correction

uncertainties depending on the transverse momentum and pseudorapidity of the jet. The JES uncertainty value does not exceed 4.6% for jets with transverse momentum $p_\perp = 20$ GeV, and 3.2% for jets with $p_\perp = 35$ GeV. Samples with scaled jets are fully processed until measured observables are obtained. The deviation of the observables thus obtained from those obtained with the nominal jet energy corrections is used as an estimate of the uncertainty of the JES.

The contribution from the uncertainty of the correction factors for the energy resolution (JER) of the MC simulation of the detector is estimated by varying them within the uncertainties presented in the Table 3. The MC samples obtained as a result of varying the resolution are used to correct the detector effects, leading to a deviation in the results of the unfolding. The magnitude of the deviation is used as an estimate of the impact of JER.

Model-dependent uncertainty (MD) of detector effects correction. The half-difference of the correction results based on PYTHIA8 and HERWIG++ is used as an estimate of the uncertainty.

Uncertainty associated with the choice and the uncertainty of PDFs. PYTHIA8 4C and HERWIG++ UE-EE3C use CTEQ6L1 PDF set [101]. The uncertainty associated with the choice of PDFs is assessed in accordance with the recommendations of PDF4LHC15 [102]. The following PDF sets are used for assessment: NNPDF30_lo_as_0130 [103], CT14lo [104] and MMHT2014lo68cl [105]. The reweighting procedure described in [106] is used. Reweighted MC samples are used to perform the unfolding. The envelope of the distributions obtained from the specified set of PDFs is used as an estimate of the uncertainty.

The uncertainty associated with the choice of renormalization, $\mu_R$, and factorization, $\mu_F$, scales is estimated by varying the scales by a factor of 2 and 0.5 independently when simulating events in the PYTHIA8 generator. Cases where one scale is multiplied by 2 and the other by 0.5 are excluded from consideration. The envelope of the distributions obtained by variation is used as an estimate of the uncertainty.

The limited statistics of MC samples leads to the fact that migrations are known with statistical uncertainty (MCS). The impact of this uncertainty is assessed using the statistical bootstrap method described in section 3.5.3. 1000 MC pseudo samples are created, on the basis of which unfolding is performed. The results of the unfolding in each cell by $\Delta y$ are approximated by a normal distribution. The

value of the standard deviation for the resulting normal distribution is used as an estimate of the uncertainty in a given $\Delta y$ cell.

Luminosity (Lumi.) is measured with an uncertainty of 3.7% [107]. This uncertainty is used as the normalization uncertainty when measuring the cross sections.

Corrections to take into account the trigger inefficiency (TEC) are discussed in paragraph 3.4. The uncertainties of the corrections are estimated conservatively and amount to 100% of the corrections.

To study the sensitivity of measurements to the number of secondary $pp$ collisions (PU), the entire sample is divided into events with an increased probability of secondary $pp$ collisions and a reduced probability of secondary $pp$ collisions. The division of the sample into two parts is carried out on the basis of the instantaneous luminosity measured at the time of data collection. Comparison of the results obtained using partial samples shows that there is no dependence on the number of secondary collisions. This is due to the fact that the data set is collected in special LHC runs with a reduced probability of secondary $pp$ collisions.

The study of the influence of differences in the distributions of secondary $pp$ collisions in the MC samples and experimental data is based on reweighting the MC samples. Reweighting is carried out in such a way that the distribution of the number of secondary $pp$ collisions in the MC coincides with that measured in the data. Reweighted MC samples are used to perform unfolding. The deviation of the unfolding results for reweighted MC samples is used as an estimate of the uncertainty associated with the simulation of secondary collisions.

The results of the assessment of various contributions to the relative systematic uncertainty are presented in Table 4 for the measured cross sections and in Table 5 for the ratios of the cross sections with veto, and are also presented in the figure 3.12 for all measured observables. The total systematic uncertainty is determined by the root of the sum of squared contributions from the studied systematic effects.

## 3.7 Results and discussion

The differential cross sections for dijet production are measured: inclusive, $d\sigma^{\mathrm{incl}}/d\Delta y$, and MN, $d\sigma^{\mathrm{MN}}/d\Delta y$, for hadronic jets with transverse momentum

Table 4 — Sources of the systematic effects affecting the measurement of the differential cross sections and the corresponding uncertainties, as well as the statistical uncertainties. The indicated intervals correspond to the maximum and minimum uncertainty values in the studied interval $\Delta y$

| Source | $d\sigma^{\text{incl}}/d\Delta y$ | $d\sigma^{\text{MN}}/\Delta y$ |
|---|---|---|
| JES, % | +(10–60)<br>−(8.9–22) | +(9.9–65)<br>−(8.8–20) |
| JER, % | +(2.5–78)<br>−(2.4–36) | +(2.2–84)<br>−(2.4–34) |
| MD, % | ±(1.2–15) | ±(1.5–22) |
| PDF, % | +(0.37–23)<br>−(0.26–19) | +(0.44–23)<br>−(0.3–19) |
| $\mu_R$, $\mu_F$, % | +(2–14)<br>−(2.2–18) | +(1.9–14)<br>−(2.5–18) |
| MCS, % | ±(0.23–14) | ±(0.24–15) |
| Lumi., % | +3.8<br>−3.6 | +3.8<br>−3.6 |
| TEC., % | +(0–1.5)<br>−(0–1.5) | +(0–1.5)<br>−(0–1.5) |
| PU, % | +(4.2e-02–3.2)<br>−(4.2e-02–3.2) | +(4.1e-02–3.2)<br>−(4.1e-02–3.2) |
| Total systematic unc., % | +(14–104)<br>−(12–55.4) | +(13–113)<br>−(12–53.2) |
| Statistical unc., % | ±(0.46–22) | ±(0.49–22) |

Table 5 — Sources of the systematic effects affecting the measurement of the ratios with veto and the corresponding uncertainties, as well as the statistical uncertainties. The indicated intervals correspond to the maximum and minimum uncertainty values in the studied interval $\Delta y$

| Source | $R^{\text{incl}}$ | $R^{\text{MN}}$ | $R^{\text{incl}}_{\text{veto}}$ | $R^{\text{MN}}_{\text{veto}}$ |
|---|---|---|---|---|
| JES, % | +(0.3–13)<br>−(0.31–1.4) | +(2.3e-02–13)<br>−(2.9e-02–1.5) | +(1.6–7.2)<br>−(1.4–5.1) | +(1.2–6.1)<br>−(1.1–4.9) |
| JER, % | +(0.24–3)<br>−(0.071–1.8) | +(2.6e-02–0.99)<br>−(9.3e-03–1.7) | +(0.72–7.8)<br>−(0.62–6.2) | +(0.48–8.1)<br>−(0.54–7.1) |
| MD, % | ±(0.24–4.5) | ±(0.025–4.4) | ±(0.49–3.8) | ±(0.28–3.8) |
| PDF, % | +(3.3e-02–2.4)<br>−(0.11–3.9) | +(2.3e-03–2.2)<br>−(1.3e-03–4) | +(2.0e-02–6.6)<br>−(5.4e-02–9.4) | +(3.0e-02–6.6)<br>−(2.1e-02–9.4) |
| $\mu_R$, $\mu_F$, % | +(0.68–2.6)<br>−(0.95–5.9) | +(9.4e-02–2.6)<br>−(7.0e-02–5.9) | +(0.92–3.7)<br>−(0.73–14) | +(0.27–3.7)<br>−(8.7e-02–14) |
| MCS, % | ±(0.18–2.8) | ±(5.1e-02–2.8) | ±(0.23–9.6) | ±(0.19–9.5) |
| TEC, % | +(0–0.095)<br>−(0–0.095) | +(0–0.096)<br>−(0–0.096) | +(0–0.16)<br>−(0–0.16) | +(0–0.16)<br>−(0–0.16) |
| PU, % | +(4.4e-03–0.05)<br>−(4.4e-03–0.05) | +(1.6e-04–0.04)<br>−(1.6e-04–0.04) | +(2.6e-03–0.96)<br>−(2.6e-03–0.96) | +(1.2e-03–0.96)<br>−(1.2e-03–0.96) |
| Totoal syst., % | +(0.92–15)<br>−(1.1–7.8) | +(0.12–14)<br>−(0.095–7.4) | +(2–16)<br>−(1.8–21) | +(1.4–16)<br>−(1.3–22) |
| Stat., % | ±(0.17–10) | ±(0.06–10) | ±(0.49–13) | ±(0.21–13) |

$p_\perp > 35$ GeV and rapidity $y < 4.7$. For the same hadronic jets, the ratios of the differential cross sections are measured: the inclusive cross section to the «exclusive» cross section, $R^{\text{incl}} = \frac{d\sigma^{\text{incl}}/d\Delta y}{d\sigma^{\text{excl}}/d\Delta y}$, and the MN cross section to the «exclusive» cross section, $R^{\text{MN}} = \frac{d\sigma^{\text{MN}}/d\Delta y}{d\sigma^{\text{excl}}/d\Delta y}$. In order to increase the sensitivity of the cross section ratios to the possible BFKL effects, a veto on hadronic jets with transverse momentum $p_\perp > p_{\perp\text{veto}} = 20$ GeV additional to the «exclusive» pairs is used. The «exclusive» with veto cross section obtained in this way is used in the denominator of the relations: the inclusive cross section to the «exclusive» with veto cross section, $R^{\text{incl}}_{\text{veto}} = \frac{d\sigma^{\text{incl}}/d\Delta y}{d\sigma^{\text{excl}}_{\text{veto}}/d\ Deltay}$, and the MN cross section to the «exclusive» with veto cross section, $R^{\text{MN}}_{\text{veto}} = \frac{d\sigma^{\text{MN}}/d\Delta y}{d\sigma^{\text{excl}}_{\text{veto}}/d\Delta y}$. Let us recall that the «exclusive» cross section is essentially also the veto cross section with $p_{\perp\text{veto}} = p_{\perp\text{min}} = 35$ GeV, therefore all the indicated ratios are essentially ratios of an inclusive cross section to a veto cross section. The analysis is performed using the sample of $pp$ collisions at a center-of-mass system energy of $\sqrt{s} = 2.76$ TeV with integral luminosity of 5.43 fb$^{-1}$ collected by the CMS detector in 2013 at the LHC.

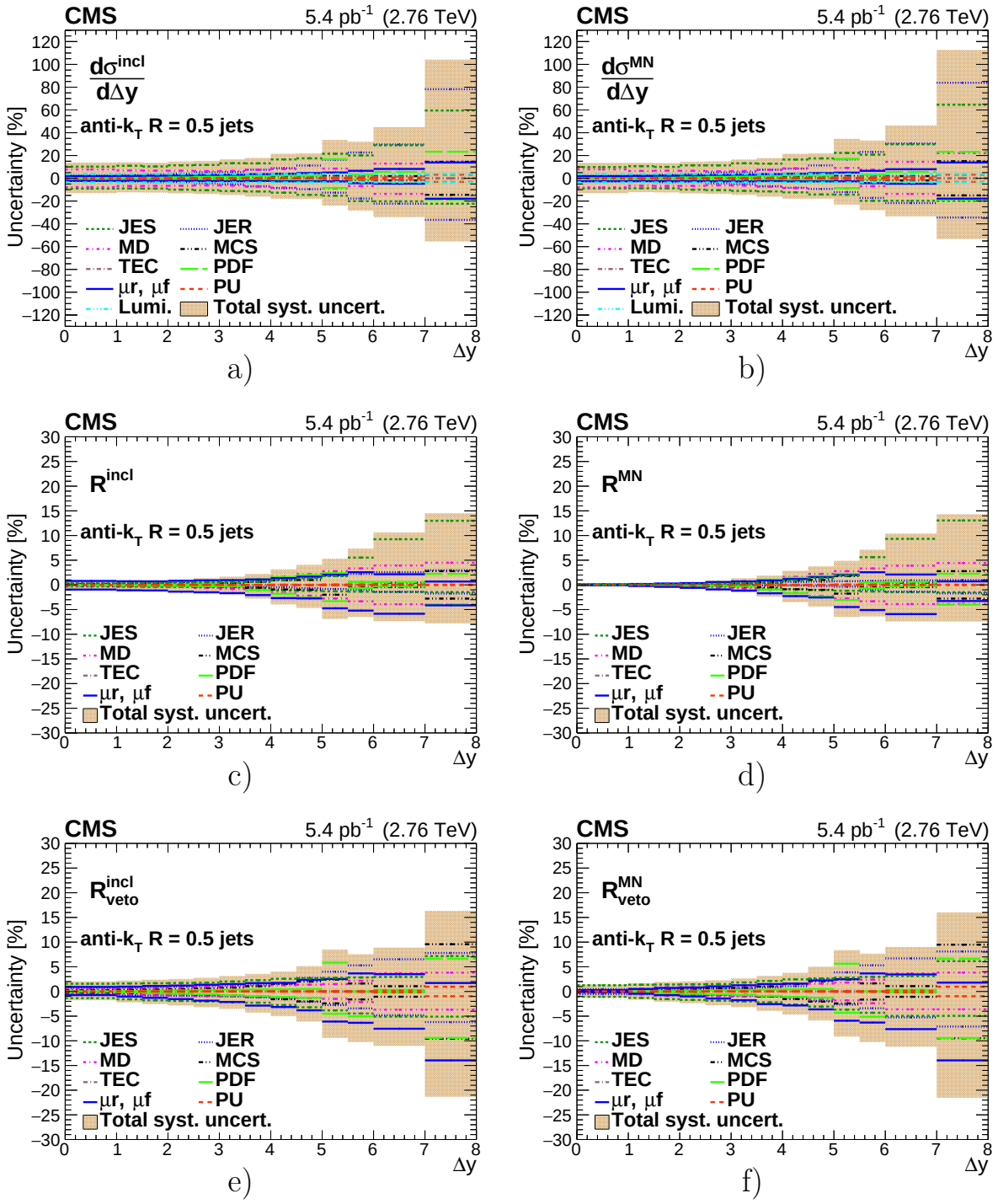


Figure 3.12 — Estimation of contributions to the relative systematic uncertainty of the measurement: a) $d\sigma^{\mathrm{incl}}/d\Delta y$; b) $d\sigma^{\mathrm{MN}}/d\Delta y$; c) $R^{\mathrm{incl}}$; d) $R^{\mathrm{MN}}$; e) $R^{\mathrm{incl}}_{\mathrm{veto}}$; f) $R^{\mathrm{MN}}_{\mathrm{veto}}$ [A1; 108].

The experimental results are compared with calculations performed by various MC models based on both GLAPD and BFKL evolutions. MC generators PYTHIA8 (8153) [41] 4C [72] and HERWIG++ (2.7.1) [42] UE-EE3C [74] are based on calculations in the leading order (LO) of the perturbation theory and the parton cascade in the leading logarithmic (LL) GLAPD approximation. Calculations based

on the next-to-leading order (NLO) of the perturbation theory are performed in the MC generator POWHEG (2.0) at the parton level. Parton cascades in the LL GLAPD approximation and the hadronization of the parton level provided by POWHEG are performed with the MC generators PYTHIA8 (8230), HERWIG7 (7.1.2) [16] and HERWIG++ (2.7.1). Calculations based on the LL BFKL are performed in the MC generator HEJ (1.4.0) [109] at the parton level. Hadronization of the HEJ parton level is performed in the MC generator ARIADNE (4.12J01) [45].

### 3.7.1 Inclusive and MN cross sections for dijet production

The cross sections for the production of the inclusive and MN dijets are presented in Figures 3.13 and 3.14, respectively.

Comparison with the results of MC modeling in the LO+LL GLAPD (see Fig. 3.13a, 3.13b, 3.14a and 3.14b) shows that PYTHIA8 4C overestimates cross sections over the entire available $\Delta y$ interval. HERWIG++ underestimates cross sections in the central region for $\Delta y < 4$ and overestimates the cross sections for large rapidity intervals $\Delta y > 6$. Taking into account the NLO of the perturbation theory and the LL GLAPD parton cascade in POWHEG + PYTHIA8/HERWIG++/HERWIG7 calculations improves the agreement with measurements only in the central region $\Delta y < 4$ (see Fig. 3.13c, 3.13d, 3.14c and 3.14d). Calculations of the cross sections in the LL BFKL approximation, performed in HEJ+ARIADNE (see Fig. 3.13a, 3.13b, 3.14a and 3.14b), underestimate the cross sections in the region of rapidity intervals $1 < \Delta y < 6$ and overestimate it at $\Delta y > 7$. The comparison of MC models with measurements of cross sections for the production of the MN pairs of hadronic jets is the same as for the inclusive cross section. No MC model provides a complete description of the measured dijet cross sections.

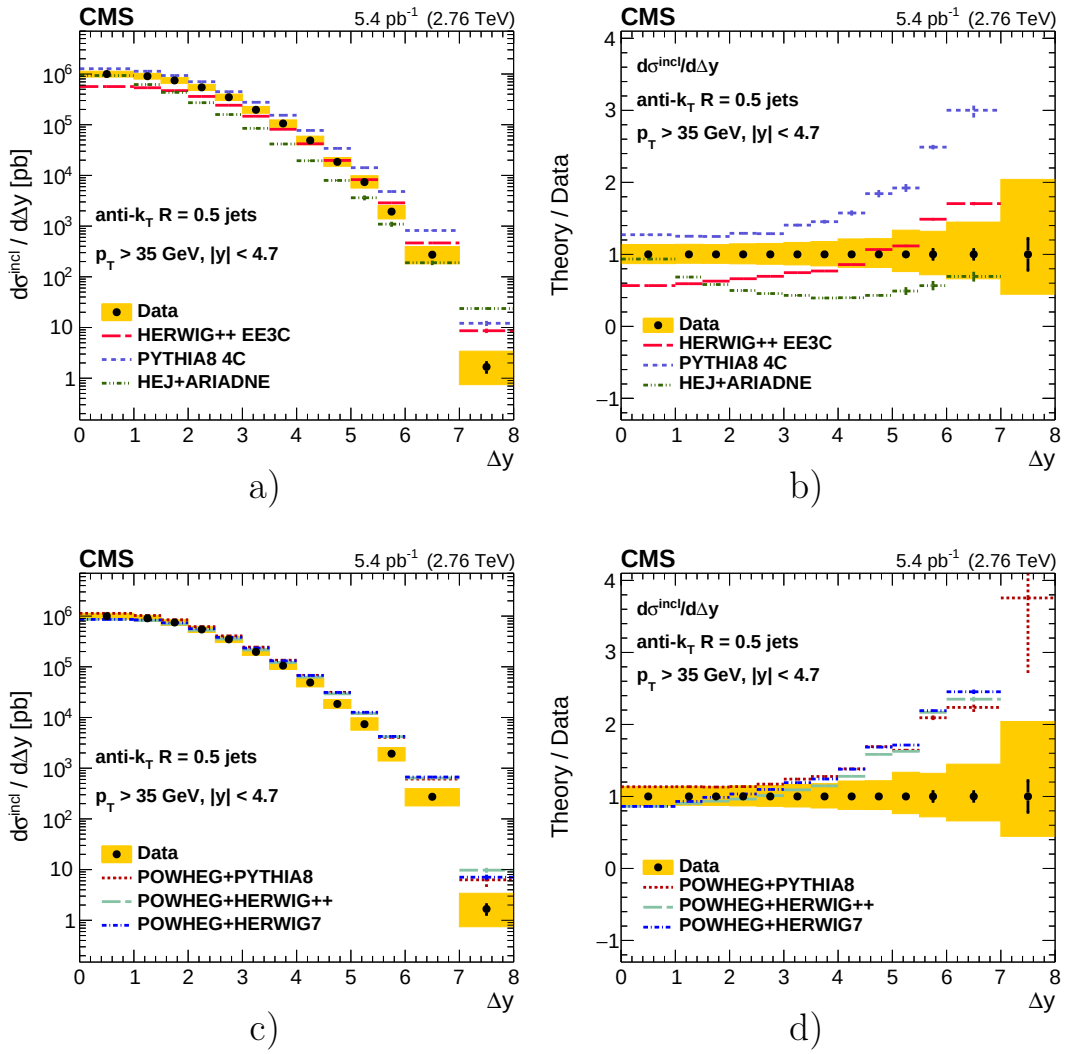


Figure 3.13 — Inclusive differential cross section for dijet production, $d\sigma^{\mathrm{incl}}/d\Delta y$ [A1; A3; 108; 110]. a) comparison with MC calculations PYTHIA8, HERWIG++ and HEJ+ARIADNE, b) ratio of the theoretical calculations to the experimental results, c) comparison with MC calculations POWHEG +PYTHIA8, POWHEG +HERWIG++, POWHEG +HERWIG7 and d) ratio of the theoretical calculations to the experimental results. Colored lines are the results of MC calculations. Black dots are the experimental results. Vertical lines are statistical uncertainties. Yellow band - systematic uncertainties in the experimental results.

### 3.7.2 Ratios of cross sections for dijet production $R^{\mathrm{incl}}$, $R^{\mathrm{MN}}$, $R^{\mathrm{incl}}_{\mathrm{veto}}$, $R^{\mathrm{MN}}_{\mathrm{veto}}$

The ratios of the cross sections for dijet production are shown in Figures 3.15, 3.16, 3.17 and 3.18. The cross section ratios show the expected shape. That

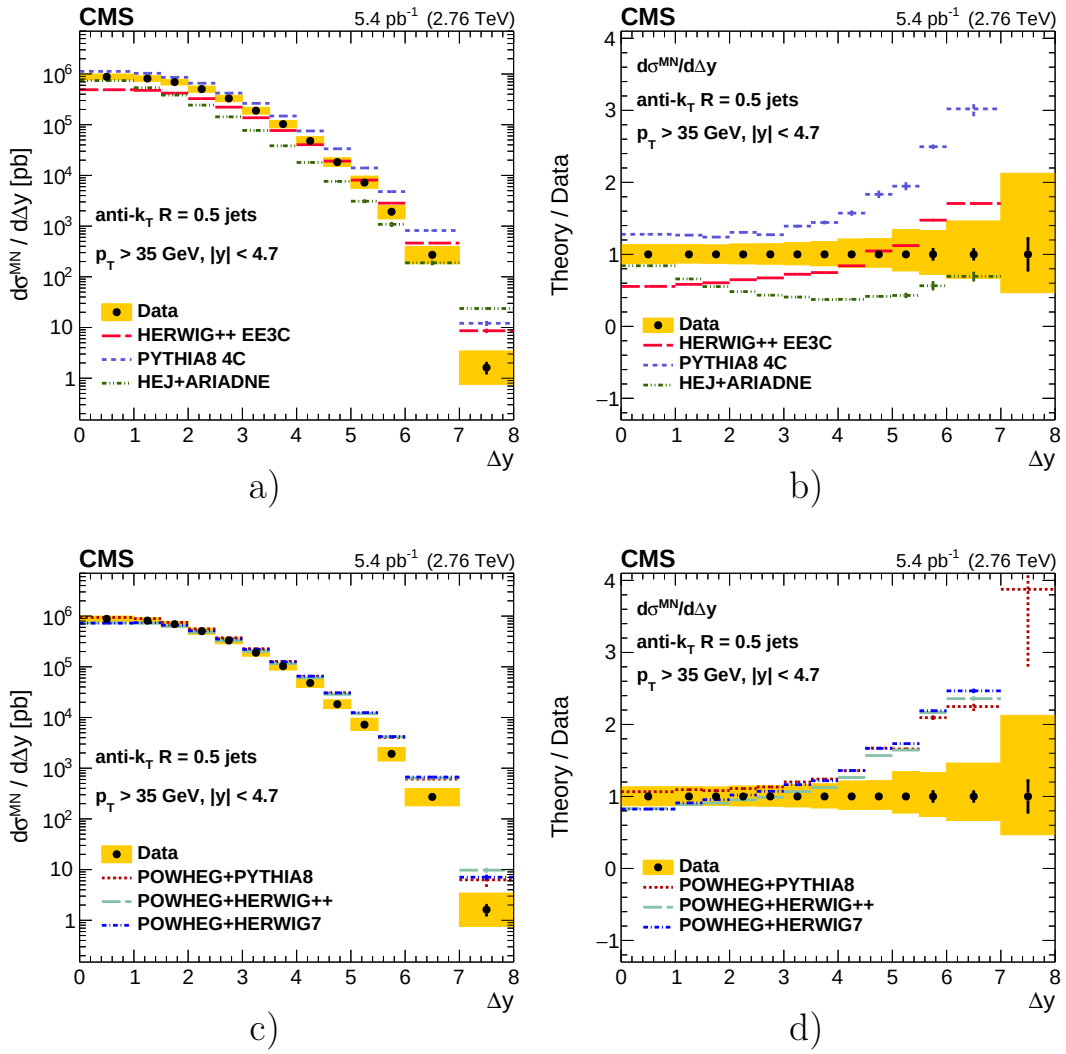


Figure 3.14 — MN differential cross section for dijet production, $d\sigma_{MN}/d\Delta y$ [A1; A3; 108; 110]. a) comparison with MC calculations PYTHIA8, HERWIG++ and HEJ+ARIADNE, b) ratio of the theoretical calculations to the experimental results, c) comparison with MC calculations POWHEG +PYTHIA8, POWHEG +HERWIG++, POWHEG +HERWIG7 and d) ratio of the theoretical calculations to the experimental results. Colored lines are the results of MC calculations. Black dots are the experimental results. Vertical lines are statistical uncertainties. Yellow band - systematic uncertainties in the experimental results.

is, the ratios increase with increasing of rapidity interval $\Delta y$ between jets at first, which is associated with the increase in phase space for hard parton radiation and, possibly, with the BFKL dynamic effects. At large values of the rapidity interval $\Delta y > 5$, the ratios begin to fall, which is associated with the kinematic restrictions on radiation of hadronic jets, additional to «exclusive» dijets. At maximum values of the rapidity interval $\Delta y$, the cross section ratios should become equal to one,

when all the energy will be spent on the production of the «exclusive» dijets with transverse momentum $p_\perp = 35$ GeV.

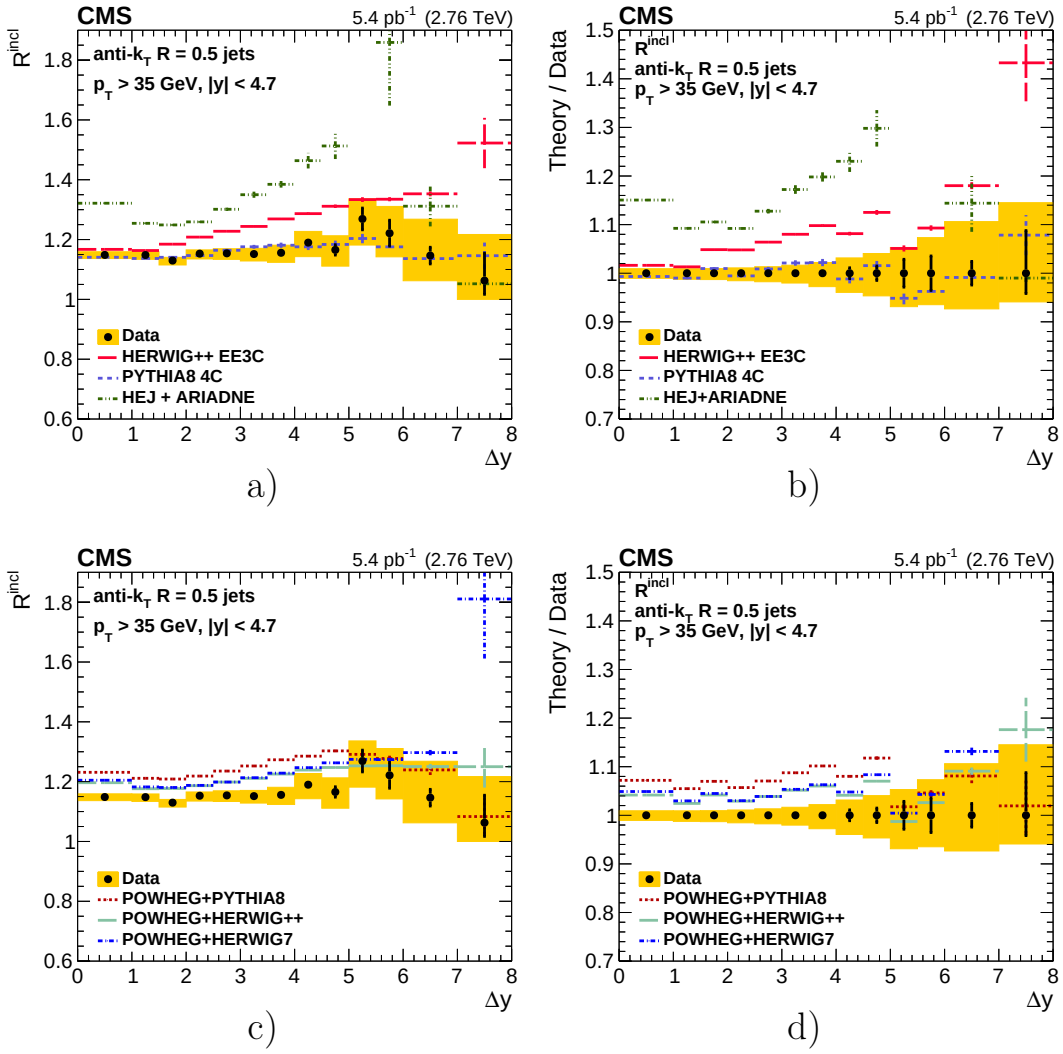


Figure 3.15 — Ratio $R^{\text{incl}}$ of the inclusive to the «exclusive» cross section for dijet production [A1; A3; 108; 110]. a) comparison with MC calculations PYTHIA8, HERWIG++ and HEJ+ARIADNE, b) ratio of the theoretical calculations to the experimental results, c) comparison with MC calculations POWHEG +PYTHIA8, POWHEG +HERWIG++, POWHEG +HERWIG7 and d) ratio of the theoretical calculations to the experimental results. Colored lines are the results of MC calculations. Black dots are the experimental results. Vertical lines are statistical uncertainties. Yellow band - systematic uncertainties in the experimental results.

Comparison of the measured ratios with the calculations of MC models based on the GLAPD evolution shows that only the calculation performed in PYTHIA8 is consistent with the ratios $R^{\text{incl}}$ and $R^{\text{incl}}$. The shape of the ratios $R^{\text{incl}}_{\text{veto}}$ and $R^{\text{MN}}_{\text{veto}}$ calculated in PYTHIA8 differs from the measured one. The PYTHIA8 calculation

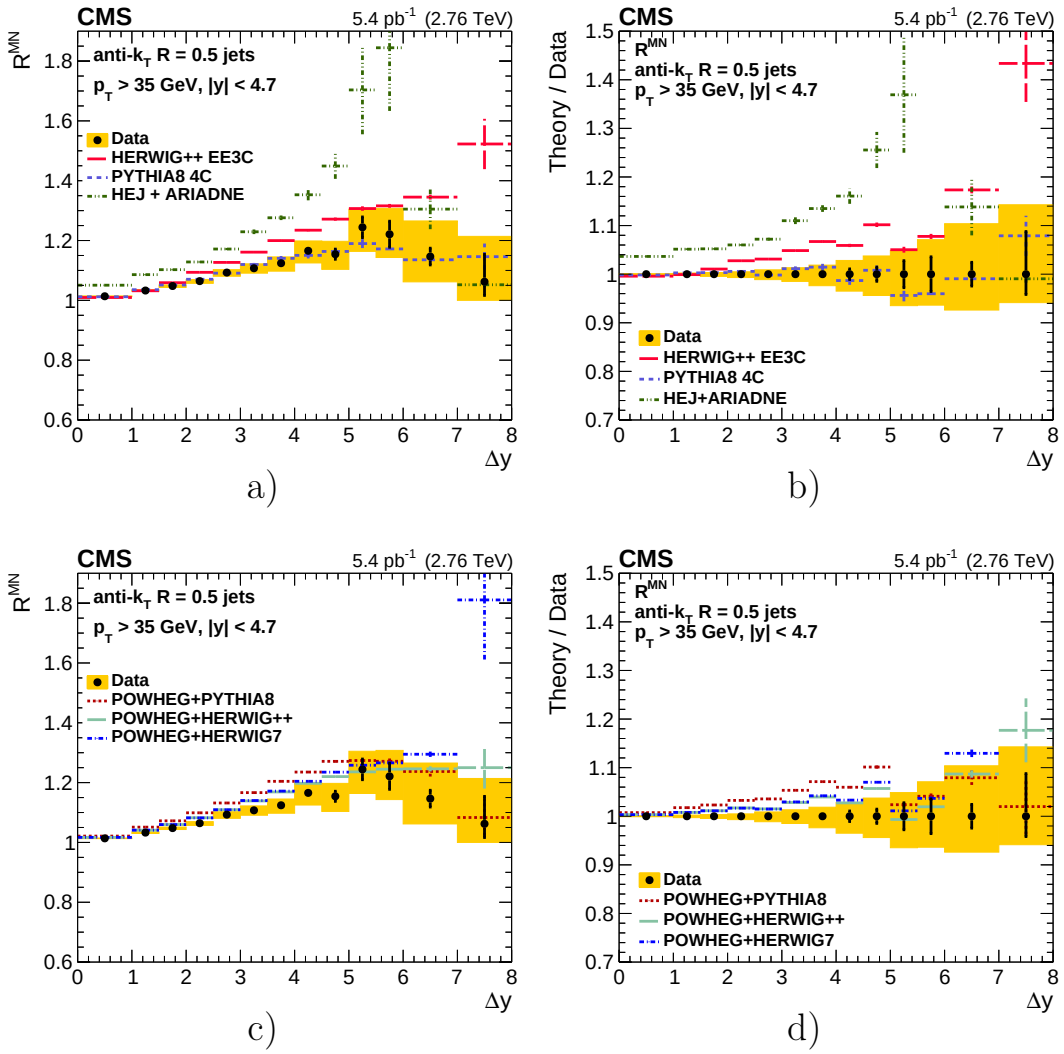


Figure 3.16 — Ratio $R^{\mathrm{MN}}$ of the MN to the «exclusive» cross section for dijet production [A1; A3; 108; 110]. a) comparison with MC calculations PYTHIA8, HERWIG++ and HEJ+ARIADNE, b) ratio of the theoretical calculations to the experimental results, c) comparison with MC calculations POWHEG +PYTHIA8, POWHEG +HERWIG++, POWHEG +HERWIG7 and d) ratio of the theoretical calculations to the experimental results. Colored lines are the results of MC calculations. Black dots are the experimental results. Vertical lines are statistical uncertainties. Yellow band - systematic uncertainties in the experimental results.

agrees with the measurements of $R^{\mathrm{incl}}_{\mathrm{veto}}$ and $R^{\mathrm{MN}}_{\mathrm{veto}}$ for $\Delta y \leqslant 1$, overestimates the measurements for $1 \leqslant \Delta y \leqslant 4$, and underestimates the measurements for $\Delta y > 5$. Calculations performed in the MC model HERWIG++ overestimate all measured cross section ratios. Taking into account the NLO corrections of the perturbation theory, performed using the MC generator POWHEG (2.0), does not improve the

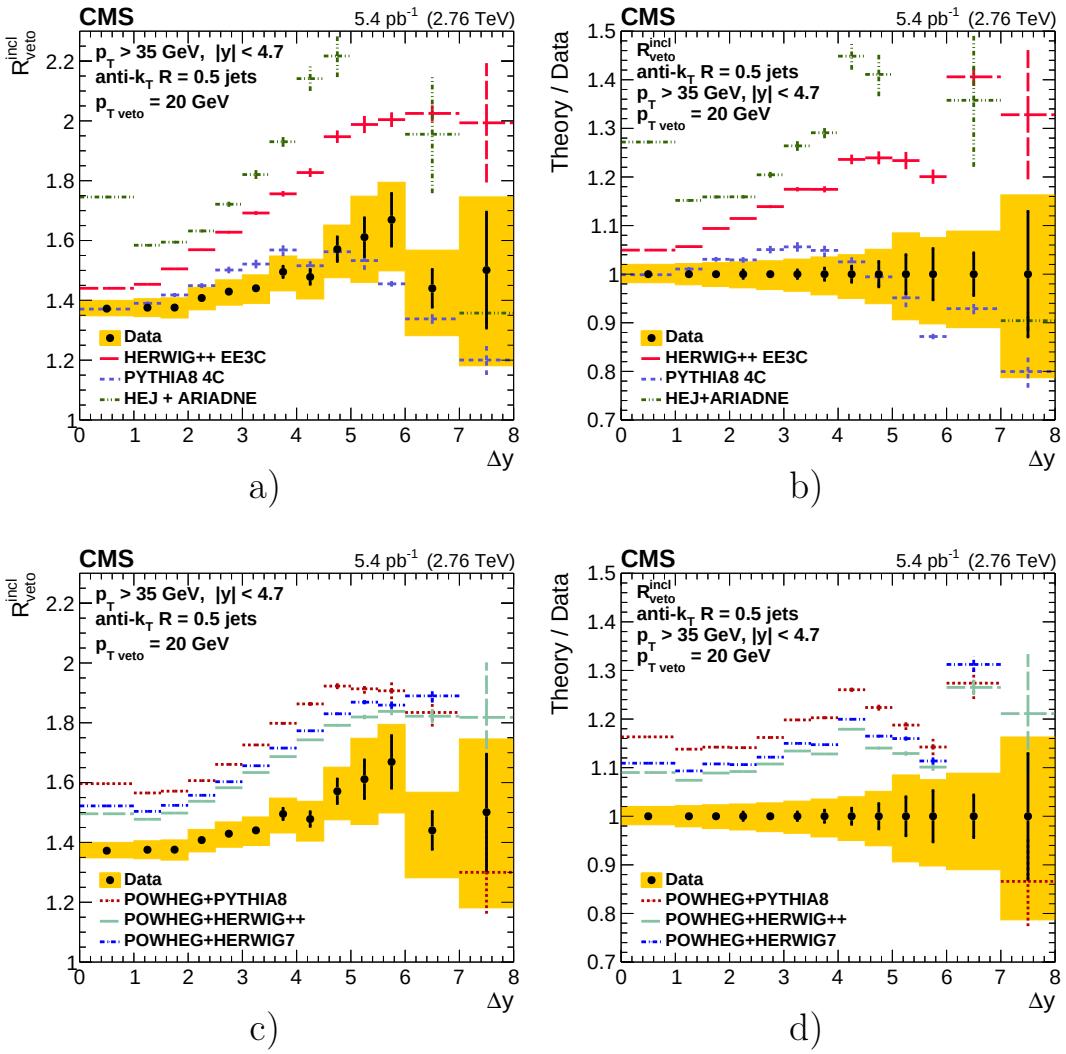


Figure 3.17 — Ratio $R^{\text{incl}}_{\text{veto}}$ of the inclusive to «exclusive» with veto cross section for dijet production [A1; A3; 108; 110]. a) comparison with MC calculations PYTHIA8, HERWIG++ and HEJ+ARIADNE, b) ratio of the theoretical calculations to the experimental results, c) comparison with MC calculations POWHEG +PYTHIA8, POWHEG +HERWIG++, POWHEG +HERWIG7 and d) ratio of the theoretical calculations to the experimental results. Colored lines are the results of MC calculations. Black dots are the experimental results. Vertical lines are statistical uncertainties. Yellow band - systematic uncertainties in the experimental results.

agreement of calculations based on the GLAPD evolution with the measurements of the cross section ratios.

Checking of the $\chi^2$ test for the comparison of the results of calculations PYTHIA8 and measurements of the ratios of the cross sections for dijet production is presented in Table 6. The calculation of $\chi^2$ is performed for the entire range of the rapidity interval $0 < \Delta y < 8$ and for the region $1.5 < \Delta y < 4$, without

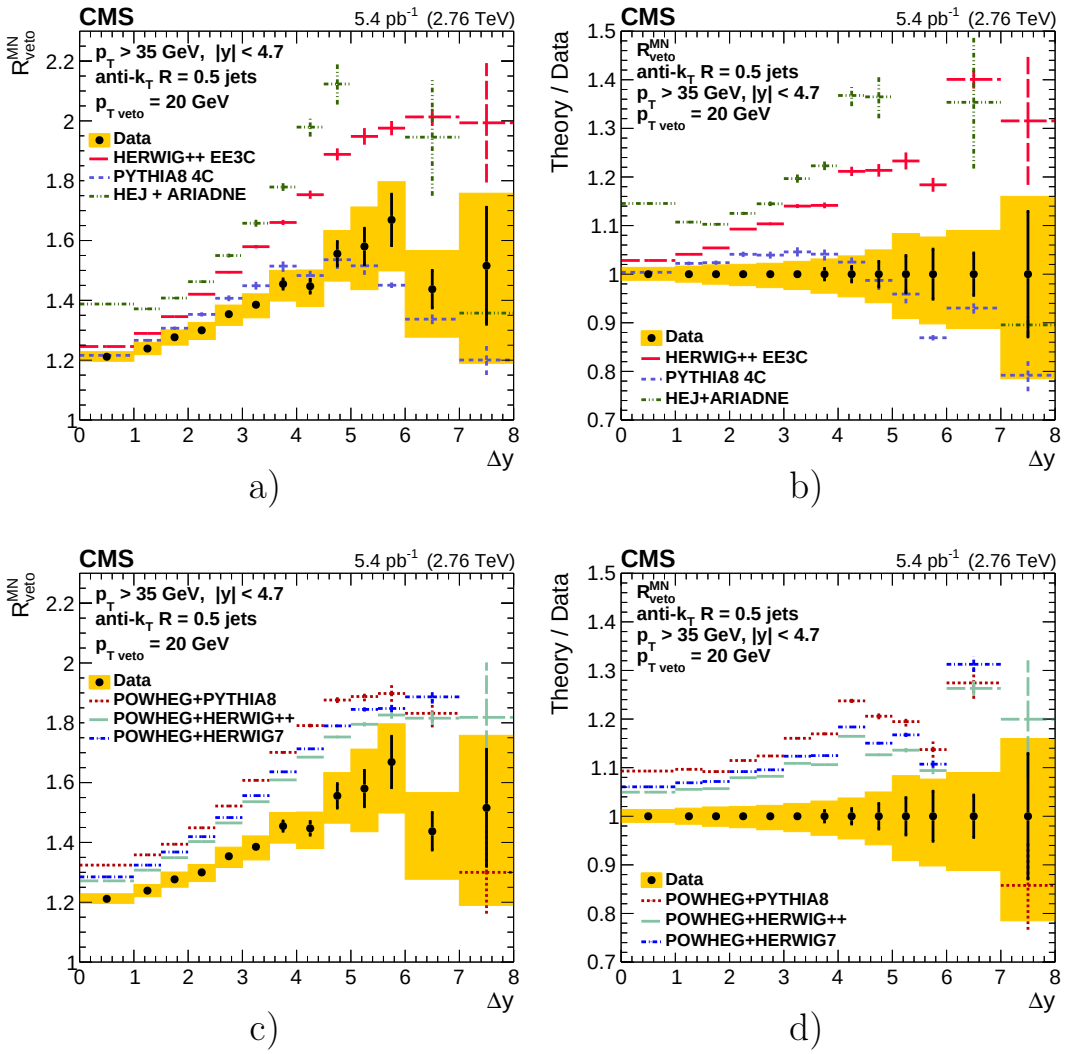


Figure 3.18 — Ratio $R^{\mathrm{MN}}_{\mathrm{veto}}$ of the MN to the «exclusive» with veto cross section for dijet production [A1; A3; 108; 110]. a) comparison with MC calculations PYTHIA8, HERWIG++ and HEJ+ARIADNE, b) ratio of the theoretical calculations to the experimental results, c) comparison with MC calculations POWHEG +PYTHIA8, POWHEG +HERWIG++, POWHEG +HERWIG7 and d) ratio of the theoretical calculations to the experimental results. Colored lines are the results of MC calculations. Black dots are the experimental results. Vertical lines are statistical uncertainties. Yellow band - systematic uncertainties in the experimental results.

taking into account the systematic uncertainties and with taking into account the systematic uncertainties. To take into account the systematic uncertainties, the squares of the latter are added to the squares of the statistical uncertainties. It can be seen that, when considering the interval $1.5 < \Delta y < 4$ and taking into account systematic uncertainties, the achieved significance level (P-value) of the deviation

of the modeling results PYTHIA8 from the measurement is 0.078 for $R^{\text{incl}}_{\text{veto}}$ and 0.045 for $R^{\text{MN}}_{\text{veto}}$, which is less than three standard deviations.

Table 6 — Checking of the $\chi^2$ test for comparing the results of calculations by PYTHIA8 with the measurements of the ratios with veto $R^{\text{incl}}$, $R^{\text{MN}}$, $R^{\text{incl}}_{\text{veto}}$, $R^{\text{MN}}_{\text{veto}}$

| Observable | $\Delta y$ range | account of systematic uncertainty | $\chi^2$ | number of degrees of freedom (n.d.f.) | $\chi^2$/n.d.f. | P-value |
|---|---|---|---|---|---|---|
| $R^{\text{incl}}$ | 0.0–8.0 | No | 44.4 | 13 | 3.41 | 2.7e-05 |
| | | Yes | 5.7 | | 0.44 | 0.96 |
| | 1.5–4.0 | No | 22.0 | 5 | 4.39 | 0.00053 |
| | | Yes | 3.5 | | 0.70 | 0.62 |
| $R^{\text{incl}}_{\text{veto}}$ | 0.0–8.0 | No | 91.5 | 13 | 7.04 | 7.1e-14 |
| | | Yes | 12.9 | | 0.99 | 0.46 |
| | 1.5–4.0 | No | 76.5 | 5 | 15.30 | 4.6e-15 |
| | | Yes | 9.9 | | 1.98 | 0.078 |
| $R^{\text{MN}}$ | 0.0–8.0 | No | 22.4 | 13 | 1.72 | 0.05 |
| | | Yes | 6.2 | | 0.48 | 0.94 |
| | 1.5–4.0 | No | 10.2 | 5 | 2.04 | 0.07 |
| | | Yes | 2.6 | | 0.52 | 0.76 |
| $R^{\text{MN}}_{\text{veto}}$ | 0.0–8.0 | No | 120.8 | 13 | 9.30 | 1.4e-19 |
| | | Yes | 15.9 | | 1.22 | 0.25 |
| | 1.5–4.0 | No | 85.9 | 5 | 17.18 | 4.9e-17 |
| | | Yes | 11.4 | | 2.27 | 0.045 |

The calculation based on the LL BFKL approximation, performed by the MC generator HEJ+ARIADNE, greatly overestimates the cross section ratios.

### 3.7.3 Comparison of measurements of the ratios $R^{\text{incl}}$ and $R^{\text{MN}}$ in $pp$ collisions at $\sqrt{s} = 2.76$ and 7 TeV

The comparison of the results on the ratios $R^{\text{incl}}$ and $R^{\text{MN}}$, found in this work at $\sqrt{s} = 2.76$ TeV and in Ref. [37] for $\sqrt{s} = 7$ TeV, presented in Figure 3.19, shows that the increase in the ratios with increasing rapidity interval $\Delta y$ is stronger at higher energy, which may be due to the increaseing phase space and with the possible BFKL dynamics. At higher energy, larger values of $\Delta y$ are achieved. The transition

from growth to decline is also observed at larger values of $\Delta y$ for higher center-of-mass energy. PYTHIA8 satisfactorily describes the measurements of the ratios of the cross sections $R^{\text{incl}}$ and $R^{\text{MN}}$ both at $\sqrt{s} = 2.76$ TeV and at $\sqrt{s} = 7$ TeV [37]. The remaining MC generators considered provide an unsatisfactory description of these ratios.

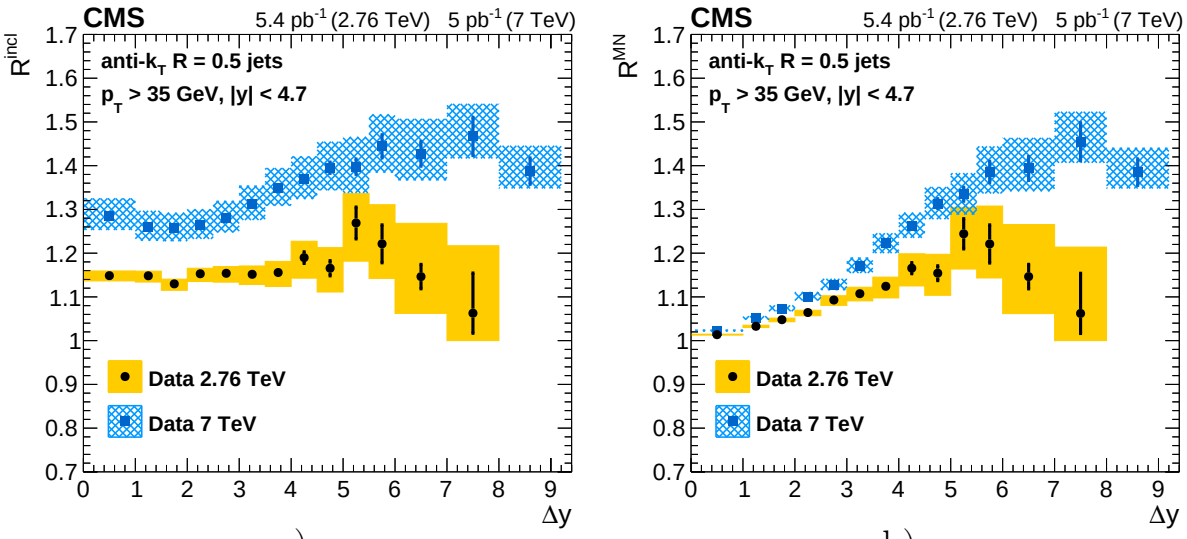


Figure 3.19 — Comparison a) $R^{\text{incl}}$ and b) $R^{\text{MN}}$, measured in the CMS experiment in $pp$ collisions at $\sqrt{s} = 2.76$ [A1; A3; 108; 110] and 7 TeV [37]. Black dots are the experimental results at $\sqrt{s} = 2.76$ TeV. Blue squares are the experimental results at $\sqrt{s} = 7$ TeV. Vertical lines are statistical uncertainties. The bands are systematic uncertainties in the experimental results.

### 3.7.4 Discussion of the experimental results

None of the MC generators used, based on calculations in the GLAPD approximation, describes the complete set of measured quantities. Thus, none of the considered generators describes the differential sections $d\sigma^{\text{incl}}/d\Delta y$ and $d\sigma^{\text{MN}}/d\Delta y$. Predictions of the MC generator PYTHIA8 are consistent within the limits of statistical and systematic uncertainties with the ratios of cross sections with veto $R^{\text{incl}}$, $R^{\text{MN}}$, $R^{\text{incl}}_{\text{veto}}$. There is a local deviation of the PYTHIA8 predictions from the $R^{\text{MN}}_{\text{veto}}$ measurements at the level of two standard deviations. All other MC generators

used, based on the GLAPD evolution, do not describe the ratios of the sections with veto $R^{\rm incl}$, $R^{\rm MN}$, $R^{\rm incl}_{\rm veto}$ and $R^{\rm MN}_{\rm veto}$.

The results of calculations of PYTHIA8 and HERWIG++, based on the LO of perturbation theory and the modeling of the parton cascades in the LL GLAPD approximation, predict an increase in the cross section ratios. It is known that evolution in rapidity is not taken into account in the GLAPD approximation. The observed increase of the ratios calculated based on the GLAPD evolution is associated with corrections that take into account color coherence. These corrections are implemented differently in the PYTHIA8 and HERWIG++ generators. In PYTHIA8 they are taken into account in the dipole cascade, and in HERWIG++ using the angular ordering in the parton cascade. In the central region, $\Delta y < 1$, these corrections are relatively small. However, at large rapidties they exhibit unstable behavior, leading to a significant difference between the predictions of PYTHIA8 and HERWIG++. Color coherence partially accounts for the effects of the BFKL evolution. Based on the results obtained, we can conclude that at large rapidity, such a partial summation is insufficient. For clearer conclusions about the role of color coherence, calculations based on the GLAPD approximation, without corrections taking into account color coherence, are needed.

The MC generator based on the LL BFKL evolution HEJ+ARIADNE does not describe the differential cross sections $d\sigma^{\rm incl}/d\Delta y$ and $d\sigma^{\rm MN}/d\Delta y$, and also predicts too strong increase of the ratios of the cross sections with the veto $R^{\rm incl}$, $R^{\rm MN}$, $R^{\rm incl}_{\rm veto}$ and $R^{\rm MN}_{\rm veto}$ compared to the measurements performed, which indicates the need to obtain predictions in the NLL BFKL approximation. It is known, however, that the LL approximation overestimates the BFKL effects. We also note that the NLL BFKL calculation performed in [104] is in good agreement with the measurements of the azimuthal decorrelation in pairs of the MN hadronic jets in $pp$ collisions at $\sqrt{s} = 7$ TeV and $p_{\perp\min} = 35$ GeV [38]. Consequently, in order to draw a conclusion about the manifestation of the BFKL effects, it is necessary to develop calculations in the NLL BFKL approximation for the cross section ratios measured in this work.

# Chapter 4. Calculation of cross sections for Mueller-Navelet dijet production and their ratios with NLL BFKL accuracy.

As discussed in the introduction, the development of methods for calculating observables that can be measured experimentally with NLL BFKL accuracy is an important component for searching for signals of this evolution. Since the NLL BFKL corrections were first calculated, it has become clear that they have a strong dependence on the choice of the scheme and the scale of ultraviolet renormalization. The problem was resolved by generalizing the procedure for optimal selection of renormalization scale by Brodsky-Lepage-Mackenzie (BLM) to the non-Abelian case in the work of Brodsky-Fadin-Kim-Lipatov-Pivovarov (BFKLP) [14]. The calculation of the MN cross sections taking into account the NLL BFKL corrections, based on the BFKLP procedure, is described in [47; 48]. This chapter presents the first comparison of calculations of cross sections for the production of MN dijets taking into account the NLL BFKL corrections with the results of the CMS measurements in $pp$ collisions at $\sqrt{s} = 2.76$ TeV [A1; A3; 108; 110], which is presented in Chapter 3. This chapter also presents the predictions of the $\Delta y$-differential MN cross sections, $d\sigma^{\rm MN}/d\Delta y$, for different center-of-mass system energies of 8 and 13 TeV, which can be verified experimentally at the LHC.

The ratio of the cross sections for the production of the MN dijets at different energies can also be a good observable in searching for signals of the BFKL evolution, since a partial cancellation of the contributions of the GLAPD evolution is possible. Next, we denote $R^{\rm MN}_{13/2.76}$ the ratio of the MN cross section at $\sqrt{s} = 13$ TeV to the MN cross section at $\sqrt{s} = 2.76$ TeV, $R^{\rm MN}_{8/2.76}$ for 8 TeV to 2.76 TeV, and $R^{\rm MN}_{13/8}$ for 13 TeV to 8 TeV.

The calculations presented in this chapter are performed for the value $p_{\perp\min} = 35$ GeV, which is used in measurements by the CMS experiment [37; 38; A1; A3; 108; 110], as well as for $p_{\perp\min} = 20$ GeV. Lowering the threshold $p_{\perp\min}$ can lead to an increase in the sensitivity of observables to possible signals of the BFKL evolution, since a lower threshold allows one to achieve lower values of $x \approx p_\perp/\sqrt{s}$.

## 4.1 Calculation of the MN dijet production cross sections with NLL BFKL accuracy

In the semi-hard regime, when $\Lambda_{\rm QCD} \ll p_\perp \ll \sqrt{s}$, at large $\Delta y$ the MN jets carry the large fractions of the proton momenta $x \sim 1$, so it is possible to use the factorization formula (1.4), which in the case of the production of dijets has the form:

$$\frac{d\sigma}{dy_1 dy_2 d^2\vec{k}_1 d^2\vec{k}_2} = \sum_{ij} \int_0^1 dx_1 dx_2 f_i(x_1, \mu_F) f_j(x_2, \mu_F) \frac{d\hat{\sigma}_{ij}(x_1 x_2 s, \mu_F, \mu_R)}{dy_1 dy_2 d^2\vec{k}_1 d^2\vec{k}_2}, \quad (4.1)$$

where $y_{1(2)}$ — rapidity of the first (second) jet in a dijet;
$\vec{k}_{1(2)}$ — transverse momentum of the first (second) jet in a dijet;
$x_{1(2)}$ — fractions of proton momenta carried by partons before the scattering;
$f_{i(j)}$ — PDF of the $i$-th and $j$-th partons in the first and second colliding hadron, respectively.

As mentioned in Chapter 1, the LL/NLL BFKL parton-parton cross section, $\hat{\sigma}$, is itself factorized into process-dependent vertices, $V$, and universal Green's function, $G$:

$$\frac{d\hat{\sigma}_{ij}(x_1 x_2 s, \mu_F, \mu_R)}{dy_1 dy_2 d^2\vec{k}_1 d^2\vec{k}_2} = \frac{x_{J1} x_{J2}}{(2\pi)^2} \int \frac{d^2\vec{q}_1}{\vec{q}_1^{\,2}} V_i(\vec{q}_1, x_1, s_0, \vec{k}_1, x_{J1}, \mu_F, \mu_R)$$
$$\int \frac{d^2\vec{q}_2}{\vec{q}_2^{\,2}} V_j(-\vec{q}_2, x_2, s_0, \vec{k}_2, x_{J2}, \mu_F, \mu_R) \int_C \frac{d\omega}{2\pi i} \left(\frac{x_1 x_2 s}{s_0}\right)^\omega G_\omega(\vec{q}_1, \vec{q}_2), \quad (4.2)$$

where $x_{J1(J2)}$ — longitudinal fractions of proton momenta carried by the first and second jets in an MN dijet;
$\vec{q}_{1(2)}$ — transverse momenta of reggeized gluons;
$C$ — integration contour, which is a vertical line in the complex $\omega$ plane to the right of all poles of the Green's function $G_\omega$.

The vertex functions, $V(\vec{q}, x, \vec{k}, x_J)$, describe the transition of a parton carrying a proton momentum fraction $x$ into a hadronic jet with a momentum fraction $x_J$ and transverse momentum $\vec{k}$ when scattered by a reggeized gluon with transverse momentum $\vec{q}$. The Green's function satisfies the BFKL equation:

$$\omega G_\omega(\vec{q}_1, \vec{q}_2) = \delta^2(\vec{q}_1 - \vec{q}_2) + \int d^2\vec{q} K(\vec{q}_1, \vec{q}) G_\omega(\vec{q}, \vec{q}_2), \quad (4.3)$$

In formula (4.3):

$K(q_1, q)$ — the BFKL kernel;

$\omega$ — eigenvalue of the BFKL kernel.

The vertices for the production of the MN dijets, $V(\vec{q}, x, \vec{k}, x_J)$, are calculated taking into account the NLL BFLKL corrections as in Ref. [111] in the small cone approximation. The convolution of the vertex with PDF is called the impact factor, $\Phi$:

$$\Phi(\vec{q}, \vec{k}, x_J, \omega, s_0, \mu_F, \mu_R) \equiv \sum_i \int_0^1 dx f_i(x, \mu_F) \left(\frac{x}{x_J}\right)^{\omega} V_i(\vec{q}, x, s_0, \vec{k}, x_J, \mu_F, \mu_R), \tag{4.4}$$

Then the hadron-hadron cross section (4.1) can be rewritten as:

$$\begin{aligned} \frac{d\sigma}{dy_1 dy_2 d^2\vec{k}_1 d^2\vec{k}_2} &= \frac{x_{J1} x_{J2}}{(2\pi)^2} \int_C \frac{d\omega}{2\pi i} e^{\omega(Y - Y_0)} G_\omega(\vec{q}_1, \vec{q}_2) \\ &\times \int \frac{d^2\vec{q}_1}{\vec{q}_1^{\,2}} \Phi_1(\vec{q}_1, \vec{k}_1, x_{J1}, \omega, s_0, \mu_F, \mu_R) \\ &\times \int \frac{d^2\vec{q}_2}{\vec{q}_2^{\,2}} \Phi_2(-\vec{q}_2, \vec{k}_2, x_{J2}, \omega, s_0, \mu_F, \mu_R), \end{aligned} \tag{4.5}$$

where $Y = \ln \frac{x_{J1} x_{J2} s}{|\vec{k}_1||\vec{k}_2|}$;

$Y_0 = \ln \frac{s_0}{|\vec{k}_1||\vec{k}_2|}$.

In the kinematic regime of large $\Delta y$, $Y \approx \Delta y$.

Consider the transverse momentum basis:

$$\begin{aligned} \hat{\vec{q}} |\vec{q}_i\rangle &= \vec{q} |\vec{q}_i\rangle, \\ \langle \vec{q}_1 | \vec{q}_2 \rangle &= \delta^{(2)}(\vec{q}_1 - \vec{q}_2), \end{aligned} \tag{4.6}$$

The kernel operator and Green's function in this basis are such that:

$$K(\vec{q}_1, \vec{q}_2) = \langle \vec{q}_1 | \hat{K} | \vec{q}_2 \rangle, \tag{4.7}$$

$$G_\omega(\vec{q}_1, \vec{q}_2) = \langle \vec{q}_1 | \hat{G}_\omega | \vec{q}_2 \rangle, \tag{4.8}$$

In the representation (4.6), the cross section (4.5) has the form:

$$\frac{d\sigma}{dy_1 dy_2 d^2\vec{k}_1 d^2\vec{k}_2} = \frac{x_{J1} x_{J2}}{(2\pi)^2} \int_C \frac{d\omega}{2\pi i} e^{\omega(Y - Y_0)} \left\langle \frac{\Phi_1}{\vec{q}_1^{\,2}} \middle| \hat{G}_\omega \middle| \frac{\Phi_2}{\vec{q}_2^{\,2}} \right\rangle, \tag{4.9}$$

The basis of the eigenfunctions of the LL BFKL kernel, which are determined by the conformal spin, $n$, and the conformal weight, $\nu$, is also useful:

$$\begin{aligned}
\langle\vec{q}|n,\nu\rangle &= \frac{1}{\pi\sqrt{2}}\big(|\vec{q}|^2\big)^{i\nu-1/2}e^{in\varphi_q},\\
\hat{K}^0|n,\nu\rangle &= \overline{\alpha}_s(\mu_R)\chi(n,\nu)|n,\nu\rangle,\\
\chi(n,\nu) &= 2\psi(1)-\psi\left(\frac{n+1}{2}+i\nu\right)-\psi\left(\frac{n+1}{2}-i\nu\right),
\end{aligned} \tag{4.10}$$

where $\overline{\alpha}_s=\frac{\alpha_s C_A}{\pi}$;

$\varphi_q$ — azimuthal angle of the vector $\vec{q}$;

$\hat{K}^0$ — the LL BFKL kernel;

$\psi$ — digamma function.

After transforming to $|n,\nu\rangle$ representation (4.10), the cross section (4.9) is expressed by the formula:

$$\begin{aligned}
\frac{d\sigma}{dy_1dy_2d^2\vec{k}_1d^2\vec{k}_2} &= \frac{x_{J1}x_{J2}}{(2\pi)^2}\int_C\frac{d\omega}{2\pi i}e^{\omega(Y-Y_0)}\\
&\times\sum_{n=-\infty}^{\infty}\int_{-\infty}^{\infty}d\nu\sum_{n'=-\infty}^{\infty}\int_{-\infty}^{\infty}d\nu'\left\langle\frac{\Phi_1}{\vec{q}_1^{\,2}}|n,\nu\rangle\langle n,\nu|\hat{G}_\omega|n',\nu'\rangle\langle n',\nu'|\frac{\Phi_2}{\vec{q}_2^{\,2}}\right\rangle.
\end{aligned} \tag{4.11}$$

### 4.1.1 Green's function $G_\omega$ with NLL BFKL accuracy

The BFKL equation (4.3) in the $|q\rangle$ basis has the from:

$$\hat{1}=(\omega-\hat{K})\hat{G}_\omega, \tag{4.12}$$

and has the formal solution:

$$\hat{G}_\omega=(\omega-\hat{K})^{-1}, \tag{4.13}$$

Expanding the operator $\hat{K}$ in powers of $\overline{\alpha}_s$:

$$\hat{K}=\overline{\alpha}_s\hat{K}^0+\overline{\alpha}_s^2\hat{K}^1, \tag{4.14}$$

where $\hat{K}^1$ — the NLL BFKL corrections to the kernel.

we obtain the solution of Eq. (4.13) with the required NLL accuracy:

$$\hat{G}_\omega = (\omega - \overline{\alpha}_s\hat{K}^0)^{-1} + (\omega - \overline{\alpha}_s\hat{K}^0)^{-1}(\overline{\alpha}_s^2\hat{K}^1)(\omega - \overline{\alpha}_s\hat{K}^0)^{-1} + \mathcal{O}[(\overline{\alpha}_s^2\hat{K}^1)^2], \tag{4.15}$$

Further, it is convenient to calculate the inverse matrices $(\omega - \overline{\alpha}_s\hat{K}^0)^{-1}$ in the basis of the eigenvectors $|n,\nu\rangle$ of the LL approximation kernel.

The NLL BFKL corrections of the Green's function were calculated in [12; 13; 112; 113]. The action of the kernel (4.14) on vectors is expressed as:

$$\begin{aligned}\hat{K}|n,\nu\rangle &= \overline{\alpha}_s(\mu_R)\chi(n,\nu)|n,\nu\rangle \\ &+ \overline{\alpha}_s^2(\mu_R)\left(\chi^{(1)}(n,\nu) + \frac{\beta_0}{4N_c}\chi(n,\nu)\ln(\mu_R^2)\right)|n,\nu\rangle \\ &+ \overline{\alpha}_s^2(\mu_R)\frac{\beta_0}{4N_c}\chi(n,\nu)\left(i\frac{\partial}{\partial\nu}\right)|n,\nu\rangle,\end{aligned} \tag{4.16}$$

where $\beta_0 = \frac{11N_c}{3} - \frac{2n_f}{3}$ — the leading coefficient of the QCD $\beta$ function;
$n_f$ — number of active flavors;
$\chi^{(1)}$ — defined below.

The first line in Eq. (4.16) represents the action of the LL part of the BFKL kernel on $|n,\nu\rangle$, the second line is the action of the diagonal part of the NLL corrections, and the third line is the action of the non-diagonal part of the NLL corrections.

$$\chi^{(1)}(n,\nu) = -\frac{\beta_0}{8N_c}\big(\chi^2(n,\nu) - \frac{10}{3}\chi(n,\nu) - i\chi'(n,\nu)\big) + \overline{\chi}(n,\nu), \tag{4.17}$$

where $\chi'(n,\nu) = d\chi(n,\nu)/d\nu$;

$$\begin{aligned}\overline{\chi}(n,\nu) = -\frac{1}{4}\Bigg[&\frac{\pi^2-4}{3}\chi(n,\nu) - 6\zeta(3) - \chi''(n,\nu) + 2\varphi(n,\nu) + 2\varphi(n,-\nu) \\ &+ \frac{\pi^2\,\mathrm{sh}(\pi\nu)}{2\nu\,\mathrm{ch}^2(\pi\nu)}\left(\left(3 + \left(1 + \frac{n_f}{N_c^3}\right)\frac{11+12\nu^2}{16(1+\nu^2)}\right)\delta_{n0}\right. \\ &\left. - \left(1 + \frac{n_f}{N_c^3}\right)\frac{1+4\nu^2}{32(1+\nu^2)}\delta_{n2}\right)\Bigg],\end{aligned} \tag{4.18}$$

where $\chi''(n,\nu) = d^2\chi(n,\nu)/d\nu^2$;
$\zeta$ — Riemann zeta function.

$$\varphi(n,\nu) = \sum_{k=0}^{\infty} \frac{(-1)^{k+1}}{k+(n+1)/2+i\nu}\Big[\psi'(k+n+1) - \psi'(k+1) + \\ + (-1)^{k+1}\big(\beta'(k+n+1) + \beta'(k+1)\big) \\ - \frac{1}{k+(n+1)/2+i\nu}\big(\psi(k+n+1) - \psi(k+1)\big)\Big], \tag{4.19}$$

where

$$\beta'(z) = \frac{1}{4}\left[\psi'\left(\frac{z+1}{2}\right) - \psi'\left(\frac{z}{2}\right)\right], \tag{4.20}$$

$\psi'$ — trigamma function.

Then the matrix element of the operator $\hat{G}_\omega$ with NLL BFKL accuracy:

$$\langle n,\nu|\hat{G}_\omega|n',\nu'\rangle = \delta_{nn'}\Bigg[\delta(\nu-\nu')\Bigg(\frac{1}{\omega - \overline{\alpha}_s(\mu_R)\chi(n,\nu)} \\ + \frac{\overline{\alpha}_s^2(\mu_R)\big(\overline{\chi}(n,\nu) + \frac{\beta_0}{8N_c}\big(-\chi^2(n,\nu) + \frac{10}{3}\chi(n,\nu) + 2\chi(n,\nu)\ln\mu_R^2 + i\frac{d}{d\nu}\chi(n,\nu)\big)\big)}{(\omega - \overline{\alpha}_s(\mu_R)\chi(n,\nu))^2}\Bigg) \\ + \frac{\frac{\beta_0}{4N_c}\overline{\alpha}_s^2(\mu_R)\chi(n,\nu')}{(\omega - \overline{\alpha}_s(\mu_R)\chi(n,\nu))(\omega - \overline{\alpha}_s(\mu_R)\chi(n,\nu'))}\left(i\frac{d}{d\nu'}\delta(\nu-\nu')\right)\Bigg], \tag{4.21}$$

The matrix element Eq. (4.21) can be used in cross section calculations in the formula (4.11).

### 4.1.2 Impact factors with NLL BFKL accuracy

The projection of the impact factors onto the LL BFKL eigenfunctions:

$$\left\langle \frac{\Phi_1}{\vec{q}_1^{\,2}}|n,\nu\right\rangle = \int d^2q_1 \frac{\Phi_1(\vec{q}_1)}{\vec{q}_1^{\,2}} \frac{1}{\pi\sqrt{2}} (\vec{q}_1^{\,2})^{i\nu-1/2} e^{in\varphi_{q1}}, \\ \left\langle n,\nu|\frac{\Phi_2}{\vec{q}_2^{\,2}}\right\rangle = \int d^2q_2 \frac{\Phi_2(-\vec{q}_2)}{\vec{q}_2^{\,2}} \frac{1}{\pi\sqrt{2}} (\vec{q}_2^{\,2})^{-i\nu-1/2} e^{-in\varphi_{q2}}, \tag{4.22}$$

Consider the expansion of the projection Eq. (4.22) in powers of $\alpha_s$:

$$\left\langle \frac{\Phi_1}{\vec{q}_1^{\,2}}|n,\nu\right\rangle = \alpha_s(\mu_R)\big[c_1(n,\nu) + \overline{\alpha}_s(\mu_R)c_1^{(1)}(n,\nu)\big]e^{in\varphi_1}, \\ \left\langle n,\nu|\frac{\Phi_2}{\vec{q}_2^{\,2}}\right\rangle = \alpha_s(\mu_R)\big[c_2(n,\nu) + \overline{\alpha}_s(\mu_R)c_2^{(1)}(n,\nu)\big]e^{-in\varphi_2}, \tag{4.23}$$

In formula (4.23):

$c_{1(2)}$ — impact factors in the LL BFKL approximation;
$c^{(1)}_{1(2)}$ — NLL correction to the BFKL impact factor;
$\varphi_{1(2)}$ — azimuthal angles of vectors $\vec{k}_{1(2)}$.

From the equations (4.23) it is obvious that:

$$c_2(n,\nu,|\vec{k}|,x_J) = \left[c_1(n,\nu,|\vec{k}|,x_J)\right]^*,$$
$$c_2^{(1)}(n,\nu,|\vec{k}|,x_J) = \left[c_1^{(1)}(n,\nu,|\vec{k}|,x_J)\right]^*, \tag{4.24}$$

Therefore, we present expressions only for $c_1(n,\nu,|\vec{k}|,x_J)$ and $c_1^{(1)}(n,\nu,|\vec{k}|,x_J)$. So the LL BFKL approximation of the impact factor:

$$c_1(n,\nu,|\vec{k}|,x_J) = 2\sqrt{\frac{C_F}{C_A}}(\vec{k}^2)^{i\nu-1/2}\left(\frac{C_A}{C_F}f_g(x,\mu_F) + \sum_{a=q,\bar{q}} f_a(x,\mu_F)\right), \tag{4.25}$$

From equation (4.25) it is clear that the LL BFKL accuracy impact factors are proportional to the effective PDF Eq. (1.8)

The NLL BFKL corrections to the impact factor were calculated in [111] using the small cone approximation and the rather old Furman cone algorithm [114] for reconstructing hadronic jets. However, in modern experiments the anti-$k_t$ algorithm [87] is more often used. In the work [115] the dependence of the NLL BFKL impact factors on the jet reconstruction algorithm was studied and corrections for the $k_t$ algorithm [116] were calculated. In this work, we use the expression

$c_1^{(1)}(n,\nu,|\vec{k}|,x_J)$ for the $k_t$ algorithm:

$$
\begin{aligned}
c_1^{(1)}(n,\nu,|\vec{k}|,x_J) = {} & \frac{1}{\pi}\sqrt{\frac{C_F}{C_A}}(\vec{k}^2)^{i\nu-1/2}\int_x^1 \frac{d\zeta}{\zeta}\zeta^{-\overline{\alpha}_s(\mu_R)\chi(n,\nu)}\Big\{\sum_{a=q\bar{q}} f_a\Big(\frac{x}{\zeta}\Big) \\
& \times\Bigg[\Big(P_{qq}(\zeta)+\frac{C_A}{C_F}P_{gq}(\zeta)\Big)\ln\frac{\vec{k}^2}{\mu_F^2} - 2\zeta^{-2\gamma}\ln R\big\{P_{qq}(\zeta)+P_{qg}(\zeta)\big\} \\
& - \frac{\beta_0}{2}\ln\frac{\vec{k}^2}{\mu_R^2}\delta(1-\zeta) + C_A\delta(1-\zeta)\Big(\chi(n,\nu)\ln\frac{s_0}{\vec{k}^2}+\frac{85}{18}+\frac{\pi^2}{2} \\
& + \frac{1}{2}\Big(\psi'\Big(1+\gamma+\frac{n}{2}\Big)-\psi'\Big(\frac{n}{2}-\gamma\Big)-\chi^2(n,\nu)\Big)\Big) \\
& + (1+\zeta^2)\Big\{C_A\Big(\frac{(1+\zeta^{-2\gamma})\chi(n,\nu)}{2(1-\zeta)_+} - \zeta^{-2\gamma}\Big(\frac{\ln(1-\zeta)}{1-\zeta}\Big)_+\Big) \\
& + \Big(C_F-\frac{C_A}{2}\Big)\Big[\frac{\overline{\zeta}}{\zeta^2}I_2 - \frac{2\ln\zeta}{1-\zeta}+2\Big(\frac{\ln(1-\zeta)}{1-\zeta}\Big)_+\Big]\Big\} \\
& + \delta(1-\zeta)\Big(C_F\Big(3\ln 2-\frac{\pi^2}{3}-\frac{9}{2}+\Big\langle 3-\frac{\pi^2}{3}-3\ln 2\Big\rangle_K\Big)-\frac{5n_f}{9}\Big) \\
& + C_A\zeta + C_F\overline{\zeta} + \frac{1+\overline{\zeta}^2}{\zeta}\Big(C_A\frac{\overline{\zeta}}{\zeta}I_1 + 2C_A\ln\frac{\overline{\zeta}}{\zeta} + C_F\zeta^{-2\gamma}\big(\chi(n,\nu)-2\ln\overline{\zeta}\big)\Big)\Bigg] \\
& + f_g\Big(\frac{x}{\zeta}\Big)\frac{C_A}{C_F}\Bigg[\Big(P_{gg}(\zeta)+2n_f\frac{C_F}{C_A}P_{qg}(\zeta)\Big)\ln\frac{\vec{k}^2}{\mu_F^2} \\
& - 2\zeta^{-2\gamma}\ln R\big(P_{gg}(\zeta)+2n_fP_{qg}(\zeta)\big) - \frac{\beta_0}{2}\ln\frac{\vec{k}^2}{4\mu_R^2}\delta(1-\zeta) \\
& + C_A\delta(1-\zeta)\Big(\chi(n,\nu)\ln\frac{s_0}{\vec{k}^2}+\frac{1}{12}+\frac{\pi^2}{6}+\Big\langle\frac{131}{36}-\frac{\pi^2}{3}-\frac{11}{3}\ln 2\Big\rangle_K \\
& + \frac{1}{2}\Big(\psi'\Big(1+\gamma+\frac{n}{2}\Big)-\psi'\Big(\frac{n}{2}-\gamma\Big)-\chi^2(n,\nu)\Big)\Big) \\
& + 2C_A\big(1-\zeta^{-2\gamma}\big)\Big(\Big(\frac{1}{\zeta}-2+\zeta\overline{\zeta}\Big)\ln\overline{\zeta}+\frac{\ln(1-\zeta)}{1-\zeta}\Big) \\
& + C_A\Big[\frac{1}{\zeta}+\frac{1}{(1-\zeta)_+}-2+\zeta\overline{\zeta}\Big]\Big(\big(1+\zeta^{-2\gamma}\big)\chi(n,\nu)-2\ln\zeta+\frac{\overline{\zeta}^2}{\zeta^2}I_2\Big) \\
& + n_f\Big[2\zeta\overline{\zeta}\frac{C_F}{C_A}+\big(\zeta^2+\overline{\zeta}^2\big)\Big(\frac{C_F}{C_A}\chi(n,\nu)+\frac{\overline{\zeta}}{\zeta}I_3\Big) \\
& + \Big(-\frac{1}{12}+\Big\langle\frac{2}{3}\ln 2-\frac{23}{36}\Big\rangle_K\Big)\delta(1-\zeta)\Big]\Bigg]\Big\}, \qquad (4.26)
\end{aligned}
$$

In formula (4.26):

$\gamma = i\nu - 1/2$;
$\overline{\zeta} = 1 - \zeta$;
$I_1$, $I_2$ и $I_3$ — defined below;
$P_{qq}$, $P_{gq}$, $P_{qg}$ and $P_{gg}$ — the LL GLAPD splitting functions;
$(...)_+$, — +–prescription.

In the formula (4.26), the angle brackets $\left\langle ... \right\rangle_K$ denote the contribution of corrections from the use of the $k_t$ algorithm obtained in [115]. The expression without these corrections corresponds to the algorithm used in [111].

$$I_2 = \frac{\zeta^2}{\overline{\zeta}^2}\Bigg[\zeta\Bigg(\frac{{}_2F_1(1,1+\gamma-\frac{n}{2},2+\gamma-\frac{n}{2},\zeta)}{n/2-\gamma-1} - \frac{{}_2F_1(1,1+\gamma+\frac{n}{2},2+\gamma+\frac{n}{2},\zeta)}{n/2+\gamma+1}\Bigg) + \zeta^{-2\gamma}\Bigg(\frac{{}_2F_1(1,-\gamma-\frac{n}{2},1-\gamma-\frac{n}{2},\zeta)}{n/2+\gamma} - \frac{{}_2F_1(1,-\gamma+\frac{n}{2},1-\gamma+\frac{n}{2},\zeta)}{n/2-\gamma}\Bigg) + \big(1+\zeta^{-2\gamma}\big)\big(\chi(n,\nu) - 2\ln\overline{\zeta}\big) + 2\ln\zeta\Bigg], \tag{4.27}$$

$$I_1 = \frac{\overline{\zeta}}{2\zeta}I_2 + \frac{\zeta}{\overline{\zeta}}\Bigg[\ln\zeta + \frac{1-\zeta^{-2\gamma}}{2}\big(\chi(n,\nu) - 2\ln\overline{\zeta}\big)\Bigg], \tag{4.28}$$

$$I_3 = \frac{\overline{\zeta}}{2\zeta}I_2 - \frac{\zeta}{\overline{\zeta}}\Bigg[\ln\zeta + \frac{1-\zeta^{-2\gamma}}{2}\big(\chi(n,\nu) - 2\ln\overline{\zeta}\big)\Bigg], \tag{4.29}$$

where ${}_2F_1$ — hypergeometric function;

Let's redefine +–prescription Eq. (1.3) in a more general form:

$$\int_a^1 d\zeta F(\zeta) \times \big(g(\zeta)\big)_+ = \int_a^1 d\zeta\big(F(\zeta) - F(1)\big) \times g(\zeta) - \int_0^a d\zeta F(1) \times g(\zeta), \tag{4.30}$$

where $F(\zeta)$ — an arbitrary function such that $F(1) < \infty$;
$g(\zeta)$ — an arbitrary function such that $g(\zeta) \underset{\zeta\to 1}{>} \ln(1-\zeta)$ and $g(\zeta) \underset{\zeta\to 1}{\leqslant} \text{const} \times \frac{\ln(1-\zeta)}{(1-\zeta)}$.
Usually $g(\zeta) = 1/(1-\zeta)$ or $g(\zeta) = \ln(1-\zeta)/(1-\zeta)$;

### 4.1.3 Cross section for the MN dijet production in the BFKL formalism

Taking into account the symmetry of the problem, it is convenient to represent the cross section for the production of the MN dijets in hadron-hadron collisions (4.11) in the form of an expansion in average cosines $\mathcal{C}_n$ (Fourier expansion):

$$\frac{d\sigma}{dy_1 dy_2 d|\vec{k}_1| d|\vec{k}_2| d\varphi_1 d\varphi_2} = \frac{1}{(2\pi)^2}\left[\mathcal{C}_0 + \sum_{n=1}^{\infty} 2\cos(n\Delta\varphi)\mathcal{C}_n\right], \tag{4.31}$$

where $\Delta\varphi = \varphi_1 - \varphi_2 - \pi$;

The coefficients $\mathcal{C}_n$ can be obtained as:

$$\mathcal{C}_n = \int_0^{2\pi} d\varphi_1 \int_0^{2\pi} d\varphi_2 \cos(n\Delta\varphi)\frac{d\sigma}{dy_1 dy_2 d|\vec{k}_1| d|\vec{k}_2| d\varphi_1 d\varphi_2}, \tag{4.32}$$

Combining formulas (4.11), (4.12) and (4.23), one obtain an expression for the coefficients $\mathcal{C}_n$ with NLL BFKL accuracy:

$$\begin{aligned}\mathcal{C}_n = {} & \frac{x_{J1}x_{J2}}{|\vec{k}_1||\vec{k}_2|}\int_{-\infty}^{+\infty} d\nu e^{(Y-Y_0)\bar{\alpha}_s(\mu_R)\chi(n,\nu)}\alpha_s^2(\mu_R)c_1(n,\nu)c_2(n,\nu) \\ & \times\left[1 + \bar{\alpha}_s(\mu_R)\left(\frac{c_1^{(1)}(n,\nu)}{c_1(n,\nu)} + \frac{c_2^{(1)}(n,\nu)}{c_2(n,\nu)}\right)\right. \\ & \left. + \bar{\alpha}_s^2(\mu_R)\ln\frac{x_{J1}x_{J2}s}{s_0}\left\{\bar{\chi}(n,\nu) + \frac{\beta_0}{4N_c}\chi(n,\nu)\left(-\frac{\chi(n,\nu)}{2} + \frac{5}{3} + \ln\frac{\mu_R^2}{|\vec{k}_1||\vec{k}_2|}\right)\right\}\right],\end{aligned} \tag{4.33}$$

Let us also write down the expression for $\mathcal{C}_n$ with LL BFKL accuracy:

$$\mathcal{C}_n{}^{LL} = \frac{x_{J1}x_{J2}}{|\vec{k}_1||\vec{k}_2|}\int_{-\infty}^{+\infty} d\nu e^{(Y-Y_0)\bar{\alpha}_s(\mu_R)\chi(n,\nu)}\alpha_s^2(\mu_R)c_1(n,\nu)c_2(n,\nu), \tag{4.34}$$

Note that in fact $\mathcal{C}_n{}^{LL}$ is the convolution of the gluon-gluon parton cross section with the effective parton distribution functions $f^{\text{eff}}$. This is characteristic behavior for the large $\Delta y$ approximation ($|\hat{t}| \ll \hat{s}, |\hat{u}|$, where $\hat{t}$, $\hat{s}$ and $\hat{u}$ are the Mandelstam variables for the parton subprocess $2 \to 2$), when all parton-parton cross sections become equal up to color factors. At what value of $\Delta y$ this approximation is

reliable one can assess by comparing calculations of the inclusive cross sections for dijet production based on the Born subprocess, with and without using this approximation.

To obtain the $\Delta y$-differential section it is necessary to integrate Eq. (4.31). The integration over $\varphi_1$ and $\varphi_2$ is simple:

$$\frac{d\sigma}{dy_1 dy_2 d|\vec{k}_1| d|\vec{k}_2|} = \mathcal{C}_0, \tag{4.35}$$

The integration over other variables is performed as follows:

$$\frac{d\sigma}{d\Delta y} = \int d|\vec{k}_1| d|\vec{k}_2| dy_1 dy_2 \delta(\Delta y - |y_1 - y_2|)\mathcal{C}_0, \tag{4.36}$$

### 4.1.4 Effects of the running coupling constant in the NLL BFKL calculations and the BFKLP procedure

Perturbative QCD calculations rely on the definition of a small parameter, that is the coupling constant $\alpha_s(\mu_R)$ (the exact definition of which depends on the choice of the ultraviolet renormalization scheme). After the renormalization scheme has been chosen, there remains an ambiguity in the choice of the $\mu_R$ renormalization scale. The summation of the complete perturbation theory series does not depend on the choice of the scheme and the scale of renormalization. However, when calculating in finite order or in logarithmic approximations, freedom in their choice can lead to ambiguity. The NLL BFKL corrections, calculated for the first time in [12; 13] in a non-physical modified minimal subtraction scheme ($\overline{\text{MS}}$), turned out to be negative and too large in absolute value (more than the LL BFKL corrections at $\alpha_s > 0.157$). The large value of the corrections indicated a possible strong dependence on the scheme and scale of ultraviolet renormalization [117].

Renormalization schemes can be divided into non-physical and physical types. Non-physical schemes are not associated with any physical process. Examples of non-physical renormalization schemes include MS [118] and $\overline{\text{MS}}$-schemes [119]. Physical schemes are concerned with computing a physical process. Examples of physical ultraviolet renormalization schemes are: the momentum subtraction scheme (MOM) [120], based on the calculation of corrections to the off-shell three-gluon

vertex; $\Upsilon$-scheme based on the decay of the quarkonium $\Upsilon \to ggg$ [121]; $V$-scheme based on the interaction of heavy quarks [70].

The dependence of the NLL BFKL corrections on the choice of renormalization scheme was studied in [14]. The results showed that the large NLL BFKL correction does not significantly depend on the choice of the ultraviolet renormalization scheme. Thus, the dependence on the choice of the renormalization scale remains.

The BLM paper [70] describes a procedure for optimal scale selection, which takes into account $q\bar{q}$ vacuum polarization. In the BLM approach, it is proposed to choose the scale in such a way that corrections for $q\bar{q}$ vacuum polarizations in gluon propagators are effectively summed up in the coupling constant $\alpha_s$. This approach works well for processes that do not contain non-Abelian (three-gluon) vertices in the leading order. An example is the process of annihilation of $e^+e^-$ into hadrons or DIS. This is due to the fact that in the three-gluon vertex, quark loops appear in the one-loop approximation not only in the gluon propagators but also in the vertex. This circumstance makes it impossible in general to unambiguously separate the divergent part of the vertex, which is responsible for the renormalization of the constant $\alpha_s$, from the finite process-dependent part. In the case of the BFKL formalism, the three-gluon vertex plays a significant role in the leading order, so direct application of the BLM procedure turns out to be impossible.

In the work of Brodsky-Fadin-Kim-Lipatov-Pivovarov (BFKLP) [14], another approach to optimal scale setting was proposed, which is a generalization of the BLM approach. The approach is based on the assumption that nonconformal contributions to the BFKL kernel in the NLL approximation are associated with the inclusion of running coupling constant effects that were absent in the LL BFKL approximation. Therefore, it is essential for the BFKLP approach that the summation of non-conformal contributions should be performed in physical schemes that contain the non-Abelian part (three-gluon vertex) in the physical process in the leading approximation. For example, this is the MOM scheme. Briefly, the BFKLP procedure is that in calculations in the MOM scheme in NLL BFKL accuracy it is necessary to separate the conformal ($\beta$-independent) and non-conformal ($\beta$-dependent) parts. After this, the scale $\mu_R = \mu_R^{\rm BFKLP}$ is chosen in such a way as to set the $\beta$-dependent part to zero. The resulting coefficients of the perturbative QCD series correspond to the conformally invariant theory. Thus, the conformal properties of the LL BFKL approximation are restored to some extent in the NLL approximation by applying the BFKLP procedure.

Calculations using the BFKLP procedure performed in the work [14] showed that resummation of non-conformal contributions to the running coupling constant in the MOM scheme gives a result consistent with the conventional Gribov-Regge theory. Namely, the pomeron intercept within the NLL BFKL approximation improved with the BFKLP procedure gets more realistic value $\alpha_{IP}^{\mathrm{BFKLP}} \approx 1.13 \div 1.18$, while remaining insensitive to the hardness of the subprocess in a wide range of $Q = 1 \div 100$ GeV. A more detailed description of the BFKLP procedure can be found in [117].

The $\overline{\mathrm{MS}}$ scheme in which the first NLL BFKL calculations were performed is nonphysical, but more convenient for many calculations. On the other hand, calculations in the MOM scheme can be much more labor-intensive. In the work [117] it is proposed to use the $\overline{\mathrm{MS}}$-scheme as an intermediate one to perform calculations, and then proceed in the results to the MOM scheme using finite transformation [122]. The coupling constants in $\overline{\mathrm{MS}}$ and MOM schemes are related by the following expressions:

$$\alpha_s^{\overline{\mathrm{MS}}} = \alpha_s^{\mathrm{MOM}} \left( 1 + \frac{\alpha_s^{\mathrm{MOM}}}{\pi} \left( T^{\beta} + T^{\mathrm{conf}} \right) \right), \tag{4.37}$$

$$T^{\beta} = -\frac{\beta_0}{2} \left( 1 + \frac{2}{3} I \right), \tag{4.38}$$

$$T^{\mathrm{conf}} = \frac{C_A}{8} \left[ \frac{17}{2} I + \frac{3}{2} (I - 1) \xi + \left( 1 - \frac{1}{3} I \right) \xi^2 - \frac{1}{6} \xi^3 \right], \tag{4.39}$$

where $T^{\beta}$ — non-conformal part of the transformation;
$T^{\mathrm{conf}}$ — conformal part of the transformation;
$I \approx 2.3439$;
$\xi$ — gauge parameter.

The result for the coefficients $\mathcal{C}_n$ (4.33) is also obtained in $\overline{\mathrm{MS}}$ with $\xi = 0$. Before moving to the MOM-scheme, let us separate explicitly non-conformal

($\beta$-dependent) contribution in the expression for $\mathcal{C}_n$:

$$\mathcal{C}_n = \frac{x_{J1}x_{J2}}{|\vec{k}_1||\vec{k}_2|}\int_{-\infty}^{+\infty} d\nu e^{(Y-Y_0)\bar{\alpha}_s(\mu_R)\chi(n,\nu)}\alpha_s^2(\mu_R)c_1(n,\nu)c_2(n,\nu)$$
$$\times\left[1+\bar{\alpha}_s(\mu_R)\left(\frac{\bar{c}_1^{(1)}(n,\nu)}{c_1(n,\nu)}+\frac{\bar{c}_2^{(1)}(n,\nu)}{c_2(n,\nu)}+\frac{\beta_0}{2N_c}\left(\frac{5}{3}+\ln\frac{\mu_R^2}{|\vec{k}_1||\vec{k}_2|}\right)\right)\right.$$
$$\left.+\bar{\alpha}_s^2(\mu_R)\ln\frac{x_{J1}x_{J2}s}{s_0}\left\{\bar{\chi}(n,\nu)+\frac{\beta_0}{4N_c}\chi(n,\nu)\left(-\frac{\chi(n,\nu)}{2}+\frac{5}{3}+\ln\frac{\mu_R^2}{|\vec{k}_1||\vec{k}_2|}\right)\right\}\right], \tag{4.40}$$

In formula (4.40):

$\bar{c}_{1(2)}^{(1)} = c_{1(2)}^{(1)} - \tilde{c}_{1(2)}^{(1)}$;

$\tilde{c}_{1(2)}^{(1)}$ — $\beta$-dependent part of the NLL BFKL impact factors.

$$\tilde{c}_1^{(1)} = \frac{\beta_0}{4N_c}\left[+i\frac{d}{d\nu}c_1(n,\nu)+\left(\ln\mu_R^2+\frac{5}{3}\right)c_1(n,\nu)\right], \tag{4.41}$$

$$\tilde{c}_2^{(1)} = \frac{\beta_0}{4N_c}\left[-i\frac{d}{d\nu}c_2(n,\nu)+\left(\ln\mu_R^2+\frac{5}{3}\right)c_2(n,\nu)\right], \tag{4.42}$$

Transforming in (4.40) to the MOM scheme we obtain:

$$\mathcal{C}_n^{\rm MOM} = \frac{x_{J1}x_{J2}}{|\vec{k}_1||\vec{k}_2|}\int_{-\infty}^{+\infty} d\nu e^{(Y-Y_0)\bar{\alpha}_s^{\rm MOM}(\mu_R)\chi(n,\nu)}\left(\alpha_s^{\rm MOM}(\mu_R)\right)^2 c_1(n,\nu)c_2(n,\nu)$$
$$\times\left[1+\bar{\alpha}_s(\mu_R)\left(\frac{\bar{c}_1^{(1)}(n,\nu)}{c_1(n,\nu)}+\frac{\bar{c}_2^{(1)}(n,\nu)}{c_2(n,\nu)}+\frac{2T^{\rm conf}}{N_c}\right.\right.$$
$$\left.\left.+\frac{\beta_0}{2N_c}\left(\frac{5}{3}+\ln\frac{\mu_R^2}{|\vec{k}_1||\vec{k}_2|}-2\left(1+\frac{2}{3}I\right)\right)\right)\right.$$
$$+\left(\bar{\alpha}_s^{\rm MOM}(\mu_R)\right)^2\ln\frac{x_{J1}x_{J2}s}{s_0}\left\{\bar{\chi}(n,\nu)+\frac{T^{\rm conf}}{N_c}\chi(n,\nu)\right.$$
$$\left.\left.+\frac{\beta_0}{4N_c}\chi(n,\nu)\left(-\frac{\chi(n,\nu)}{2}+\frac{5}{3}+\ln\frac{\mu_R^2}{|\vec{k}_1||\vec{k}_2|}-2\left(1+\frac{2}{3}I\right)\right)\right\}\right], \tag{4.43}$$

Now, according to the BFKLP procedure, the scale $\mu_R = \mu_R^{\rm BFKLP}$ is chosen in such a way that the contributions proportional to $\beta_0$ vanish, which leads to the

need to solve the equation:

$$\mathcal{C}_n^{\beta} = \frac{x_{J1}x_{J2}}{|\vec{k}_1||\vec{k}_2|}\int_{-\infty}^{+\infty} d\nu e^{(Y-Y_0)\bar{\alpha}_s^{\rm MOM}(\mu_R^{\rm BFKLP})\chi(n,\nu)}\Big(\alpha_s^{\rm MOM}(\mu_R^{\rm BFKLP})\Big)^3 c_1(n,\nu)c_2(n,\nu)$$
$$\times\frac{\beta_0}{2N_c}\left[\frac{5}{3}+\ln\frac{(\mu_R^{\rm BFKLP})^2}{|\vec{k}_1||\vec{k}_2|}-2\left(1+\frac{2}{3}I\right)+\bar{\alpha}_s^{\rm MOM}(\mu_R^{\rm BFKLP})\ln\frac{x_{J1}x_{J2}s}{s_0}\frac{\chi(n,\nu)}{2}\right.$$
$$\left.\times\left(-\frac{\chi(n,\nu)}{2}+\frac{5}{3}+\ln\frac{(\mu_R^{\rm BFKLP})^2}{|\vec{k}_1||\vec{k}_2|}-2\left(1+\frac{2}{3}I\right)\right)\right]=0. \qquad (4.44)$$

Having found the solution $\mu_R^{\rm BFKLP}$ of this equation, we substitute it into Eq. (4.43) and get:

$$\mathcal{C}_n^{\rm BFKLP} = \frac{x_{J1}x_{J2}}{|\vec{k}_1||\vec{k}_2|}\int_{-\infty}^{+\infty} d\nu e^{(Y-Y_0)\bar{\alpha}_s^{\rm MOM}(\mu_R^{\rm BFKLP})\chi(n,\nu)}\Big(\alpha_s^{\rm MOM}(\mu_R^{\rm BFKLP})\Big)^2 c_1(n,\nu)c_2(n,\nu)$$
$$\times\left[1+\bar{\alpha}_s(\mu_R^{\rm BFKLP})\left(\frac{\bar{c}_1^{(1)}(n,\nu)}{c_1(n,\nu)}+\frac{\bar{c}_2^{(1)}(n,\nu)}{c_2(n,\nu)}+\frac{2T^{\rm conf}}{N_c}\right)\right.$$
$$\left.+\Big(\bar{\alpha}_s^{\rm MOM}(\mu_R^{\rm BFKLP})\Big)^2\ln\frac{x_{J1}x_{J2}s}{s_0}\left\{\bar{\chi}(n,\nu)+\frac{T^{\rm conf}}{N_c}\chi(n,\nu)\right\}\right], \qquad (4.45)$$

which can also be rewritten in the form where the correction to the eigenvalue of the BFKL kernel is clearly visible:

$$\mathcal{C}_n^{\rm BFKLP} = \frac{x_{J1}x_{J2}}{|\vec{k}_1||\vec{k}_2|}\int_{-\infty}^{+\infty} d\nu e^{(Y-Y_0)\bar{\alpha}_s^{\rm MOM}(\mu_R^{\rm BFKLP})\left[\chi(n,\nu)+\bar{\alpha}_s^{\rm MOM}(\mu_R^{\rm BFKLP})\left(\bar{\chi}(n,\nu)+\frac{T^{\rm conf}}{N_c}\chi(n,\nu)\right)\right]}$$
$$\times\Big(\alpha_s^{\rm MOM}(\mu_R^{\rm BFKLP})\Big)^2 c_1(n,\nu)c_2(n,\nu)$$
$$\times\left[1+\bar{\alpha}_s(\mu_R^{\rm BFKLP})\left(\frac{\bar{c}_1^{(1)}(n,\nu)}{c_1(n,\nu)}+\frac{\bar{c}_2^{(1)}(n,\nu)}{c_2(n,\nu)}+\frac{2T^{\rm conf}}{N_c}\right)\right]. \qquad (4.46)$$

At the moment, it is only possible to obtain a numerical solution of the equation (4.44), which may be impractical, especially considering the fact that the solution is used in the integrand (to obtain the $\Delta y$-differential cross section for the MN dijet production, it is necessary to integrate $\mathcal{C}_0^{\rm BFKLP}$ over rapidities and momenta, as shown in Eq. (4.36)).

The paper [48] proposes two approximate expressions for calculating $\mu_R^{\rm BFKLP}$, which we will call «case (a)» and «case (b)». In «case (a)», the scale $\mu_R = \mu_{R,a}^{\rm BFKLP}$ vanishes the third line in the equation (4.43), which is responsible for non-conformal contributions to the NLL impact factors. In «case (b)», the scale $\mu_R = \mu_{R,b}^{\rm BFKLP}$ vanishes the last line in the equation (4.43), which is responsible for non-conformal

contributions to the Green's function in the NLL BFKL corrections. We present expressions for $\mu_R$ and $\mathcal{C}_n$ for both cases. «case (a)»:

$$(\mu_{R,a}^{\rm BFKLP})^2 = |\vec{k}_1||\vec{k}_2| \exp\left[2\left(1+\frac{2}{3}I\right)-\frac{5}{3}\right], \tag{4.47}$$

$$\begin{aligned}\mathcal{C}_n^{{\rm BFKLP},a} &= \frac{x_{J1}x_{J2}}{|\vec{k}_1||\vec{k}_2|} \\ &\times \int_{-\infty}^{+\infty} d\nu e^{(Y-Y_0)\bar{\alpha}_s^{\rm MOM}\left(\mu_{R,a}^{\rm BFKLP}\right)\left[\chi(n,\nu)+\bar{\alpha}_s^{\rm MOM}(\mu_{R,a}^{\rm BFKLP})(\bar{\chi}(n,\nu)+\frac{T^{\rm conf}}{N_c}\chi(n,\nu)-\frac{\beta 0}{8N_c}\chi^2(n,\nu))\right]} \\ &\times (\alpha_s^{\rm MOM}(\mu_{R,a}^{\rm BFKLP}))^2 c_1(n,\nu)c_2(n,\nu) \\ &\times \left[1+\bar{\alpha}_s^{\rm MOM}(\mu_{R,a}^{\rm BFKLP})\left\{\frac{\bar{c}_1^{(1)}(n,\nu)}{c_1(n,\nu)}+\frac{\bar{c}_2^{(1)}(n,\nu)}{c_2(n,\nu)}+\frac{2T^{\rm conf}}{N_c}\right\}\right],\end{aligned} \tag{4.48}$$

«case (b)»:

$$(\mu_{R,b}^{\rm BFKLP})^2 = |\vec{k}_1||\vec{k}_2| \exp\left[2\left(1+\frac{2}{3}I\right)-\frac{5}{3}+\frac{1}{2}\chi(n,\nu)\right], \tag{4.49}$$

$$\begin{aligned}\mathcal{C}_n^{{\rm BFKLP},b} &= \frac{x_{J1}x_{J2}}{|\vec{k}_1||\vec{k}_2|} \\ &\times \int_{-\infty}^{+\infty} d\nu e^{(Y-Y_0)\bar{\alpha}_s^{\rm MOM}\left(\mu_{R,b}^{\rm BFKLP}\right)\left[\chi(n,\nu)+\bar{\alpha}_s^{\rm MOM}(\mu_{R,b}^{\rm BFKLP})(\bar{\chi}(n,\nu)+\frac{T^{\rm conf}}{N_c}\chi(n,\nu))\right]} \\ &\times (\alpha_s^{\rm MOM}(\mu_{R,b}^{\rm BFKLP}))^2 c_1(n,\nu)c_2(n,\nu) \\ &\times \left[1+\bar{\alpha}_s^{\rm MOM}(\mu_{R,b}^{\rm BFKLP})\left\{\frac{\bar{c}_1^{(1)}(n,\nu)}{c_1(n,\nu)}+\frac{\bar{c}_2^{(1)}(n,\nu)}{c_2(n,\nu)}+\frac{2T^{\rm conf}}{N_c}+\frac{\beta_0}{4N_c}\chi(n,\nu)\right\}\right],\end{aligned} \tag{4.50}$$

The work [123] shows that «case (a)» better reproduces the exact solution of the equation (4.44) in the case of calculating the $\Delta y$-differential MN dijet cross section. Therefore, it is convenient to use «case (a)» as an estimate of the cross section, and the difference between «case (a)» and «case (b)» as an estimate of the systematic theoretical uncertainty associated with the uncertainty in the choice of scale. This estimate of systematic uncertainty provides approximately a two-fold variation in $\mu_R$ at $\nu = 0$.

The comparison of the calculations of the $\Delta y$-differential MN dijet cross section, $d\sigma^{\rm MN}/d\Delta y$, taking into account the NLL BFKL corrections using the procedure for the optimal scale setting by BFKLP with the experimental results performed in the CMS experiment in $pp$ collisions at energy $\sqrt{s} = 2.76$ TeV are presented at the end of this chapter.

## 4.2 Numerical calculations and theoretical uncertainty

The differential MN cross section, $d\sigma^{\rm MN}/d\Delta y$, is calculated with NLL BFKL accuracy using the procedure for the optimal ultraviolet renormalization scale setting by BFKLP [14], in $pp$ collisions with energy $\sqrt{s} = 2.76$, 8 and 13 TeV for jets with $p_\perp > p_{\perp\min} = 35$ GeV, and 20 GeV and $|y| < 4.7$. The selection of $p_{\perp\min} = 35$ GeV and $|y| < 4.7$ corresponds to the selection of events in measurements with the CMS detector [37; 38; A1; A3; 108; 110]. Calculations are performed for the $k_T$ algorithm of hadronic jet reconstruction [116], with the jet size parameter 0.5 for $\sqrt{s} = 2.76$ and 8 TeV and 0.4 for 13 TeV. The number of flavors $n_f$ is chosen to be 5. The strong coupling constant, $\alpha_s$, and the PDFs are provided in the LHAPDF [106] library and the MSTW2008nlo68cl [124] set. The ratios $R^{\rm MN}_{13/2.76}$, $R^{\rm MN}_{8/2.76}$, $R^{\rm MN}_{13/8}$ are also calculated for the MN dijets with $p_\perp > p_{\perp\min} = 35$, and 20 GeV and $|y| < 4.7$.

When calculating the MN dijet cross sections, $d\sigma^{\rm MN}/d\Delta y$, with NLL BFKL accuracy with the optimal scale setting BFKLP procedure, the following sources of theoretical uncertainty are taken into account:

1. Uncertainty of factorization and renormalization scales. This uncertainty is estimated using the difference between the calculation results of «case a» and «case b». This approach provides the scale variation of about 2 times at $\nu = 0$. In the procedure described in paragraph 4.1.4, $\mu_R = \mu_F = \mu_R^{\rm BFKLP}$;
2. Uncertainty in the choice of the Gribov scale $s_0$. For the central value of $s_0$, the natural scale $s_0 = |\vec{k}_1||\vec{k}_2|$ was chosen. This scale is varied by multiplying by 2 and 0.5 to estimate theoretical uncertainty;
3. Uncertainty of PDFs. This uncertainty was assessed using the MC replica of PDF4LHC15_NLO_MC set [125].

The listed sources make approximately the same contribution to the total theoretical uncertainty. However, for the largest available $\Delta y$, the uncertainty from the parton distribution functions can dominate, since this uncertainty grows with $x \to 1$.

The total theoretical uncertainty is calculated as the root of the sum of squared uncertainties from the sources.

## 4.3 Results of calculations of the MN dijet cross section. Comparison with the measurements of the CMS experiment and discussion

Comparison of the differential MN diejt cross section, $d\sigma^{\mathrm{MN}}/d\Delta y$, calculated with the NLL BFKL accuracy for $pp$ collisions at energy $\sqrt{s} = 2.76$ TeV, with the experimental data by CMS [A1; A3; 108; 110] is presented in the Figure 4.1. The minimum transverse momentum, $p_{\perp\min}$, is chosen to be 35 GeV. The absolute value of the rapidity of hadronic jets is $|y| < 4.7$.

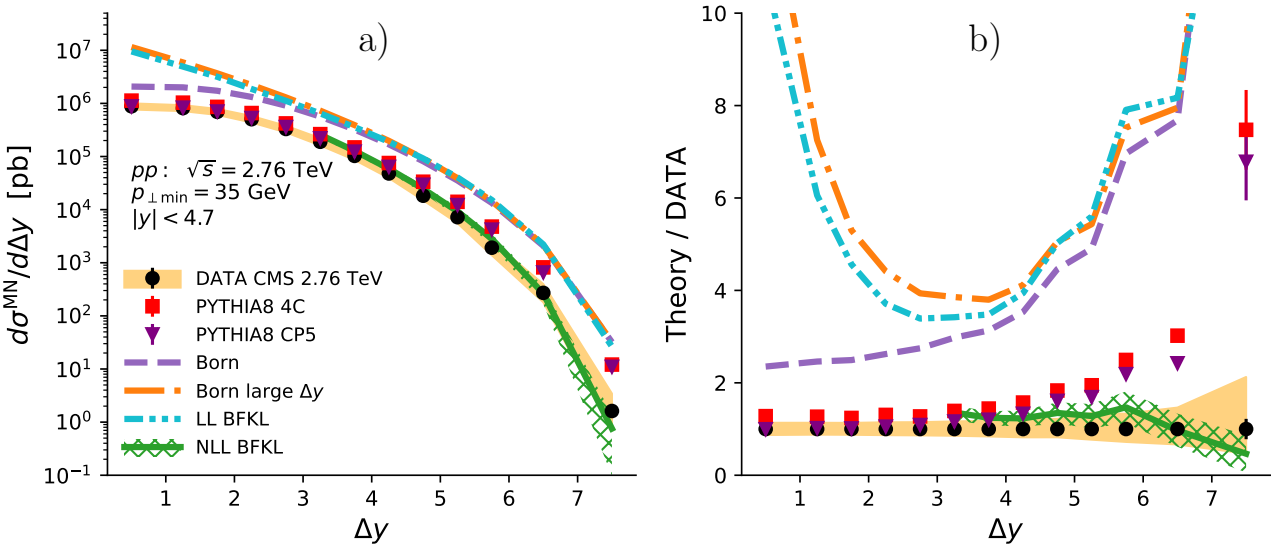


Figure 4.1 — Comparison of the results of calculation of the MN cross section, $d\sigma^{\mathrm{MN}}/d\Delta y$, based on the NLL BFKL approximation [A2; 126] with the results of CMS measurements in $pp$ collisions at $\sqrt{s} = 2.76$ TeV [A1; A3; 108; 110]. a) the MN cross section $d\sigma^{\mathrm{MN}}/d\Delta y$; b) the ratios of theoretical calculations to the measured data. The experimental results are represented by black dots. Vertical lines are statistical uncertainties of the measurement and MC modeling. Yellow band is the systematic uncertainty of the experimental results. Colored lines are the calculation results. Hatched band is the theoretical uncertainty of the NLL BFKL calculation.

For comparison, Figure 4.1 shows calculations with the Born subprocess without using (Born) and with using (Born large $\Delta y$) the large $\Delta y$ approximation, and also presents the results of calculating with LL BFKL accuracy, performed according to [71]. MC calculation based on the LO+LL GLAPD, performed in the PYTHIA8 generator, is presented for two tunes: 4C [72] and CP5 [73]. The 4C tune, based on the approximation of early LHC data at $\sqrt{s} = 7$ TeV, was used

for comparison with the CMS measurements in [37; 38; A1; A3; 108; 110]. The CP5 tune includes an approximation to the LHC data at $\sqrt{s} = 8$ and 13 TeV. In addition, the CP5 tune uses the strong coupling constant, $\alpha_s$, and the PDFs in the next-next-first-order (NNLO) approximation, and the rapidity ordering in the initial state radiation. Thus, PYTHIA8 CP5 provides a prediction even further from the pure LO+LL GLAPD than the 4C tune. At the same time, PYTHIA8 CP5 takes into account even more BFKL contributions due to the inclusion of rapidity ordering in the initial state radiation. It should be noted that the anti-$k_t$ jet reconstruction algorithm was used to reconstruct jets in the CMS measurements and in the PYTHIA8 simulations.

As can be seen from the Figure 4.1, the NLL BFKL calculation coincides with the experimental results up to statistical and systematic uncertainties, while other calculations greatly overestimate the experimental data at large $\Delta y$. This strongly supports the manifestation of the BFKL effects in dijet production with large $\Delta y$ in $pp$ collisions at $\sqrt{s} = 2.76$ TeV. Moreover, it is clear that the NLL corrections are significant for the BFKL calculations. Comparing calculations with the Born subprocess without and with the use of the large $\Delta y$ approximation, it is clear that the range of applicability of the large $\Delta y$ approximation when calculating cross sections begins for $\Delta y > 4$, therefore the NLL BFKL calculation is presented only for this region. It can be seen that the new CP5 tune improves the agreement of the PYTHIA8 predictions with the experimental results only in the central region of small $\Delta y < 4$. The agreement between the PYTHIA8 predictions and the experimental data at large $\Delta y$ is still unsatisfactory.

Predictions for the $\Delta y$-differential cross section for the production of the MN dijets in $pp$ collisions at $\sqrt{s} = 8$ and 13 TeV for $p_\perp > p_{\perp\min} = 35$ GeV and $|y| < 4.7$ are shown in the Figure 4.2. It can be seen that the NLL BFKL predicts lower values of cross sections at large $\Delta y$ than all other calculations. Predictions for the $\Delta y$-differential cross section for the production of the MN jet pairs in $pp$ collisions at $\sqrt{s} = 2.76$, 8 and 13 TeV for $p_\perp > p_{\perp\min} = 20$ GeV and $|y| < 4.7$ are shown in the Figure 4.3. Comparing the results of the LL BFKL calculation and calculation with the Born subprocess and the large $\Delta y$ approximation for $p_{\perp\min} = 35$ GeV (Fig. 4.2) and $p_{\perp\min} = 20$ GeV (Fig. 4.3), it can be seen that lowering the threshold $p_{\perp\min}$ and increasing $\sqrt{s}$ leads to an increase in sensitivity to the BFKL effects.

Predictions of the ratios of the MN cross sections $R^{\mathrm{MN}}_{13/2.76}$, $R^{\mathrm{MN}}_{8/2.76}$ and $R^{\mathrm{MN}}_{13/8}$ for $pp$ collisions and $p_{\perp\min} = 35$ GeV are presented in Figure 4.4, and for $p_{\perp\min} =$

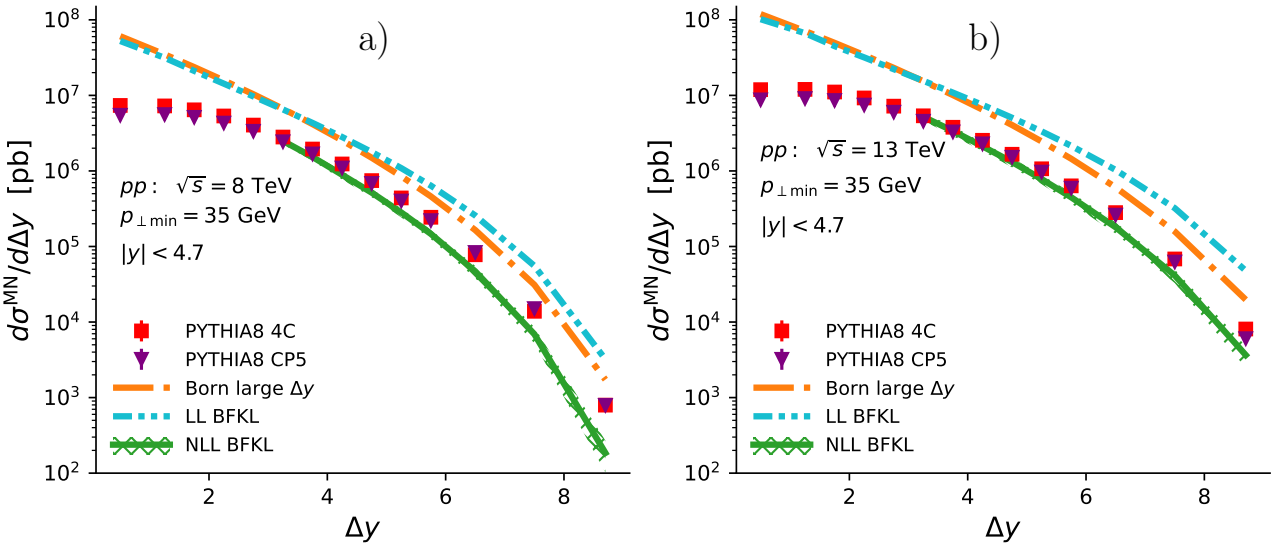


Figure 4.2 — Results of calculation of the MN cross section $d\sigma^{\mathrm{MN}}/d\Delta y$ [A2; 126]. a) at $\sqrt{s} = 8$ TeV; b) at $\sqrt{s} = 13$ TeV for hadronic jets with $p_\perp > p_{\perp\mathrm{min}} = 35$ GeV. Vertical lines are statistical uncertainties of the MC modeling. Colored lines are the calculation results. Hatched band is the theoretical uncertainty of the NLL BFKL calculation.

20 GeV in Figure 4.5. As can be seen from the figures, calculations based on the GLAPD and BFKL approximations are well separable, indicating that these ratios are good observables for searching for signals of the BFKL evolution. The NLL BFKL calculation predicts the strongest growth of the ratios than all other calculations. Comparing calculations with the Born subprocess and PYTHIA8, it is clear that modeling the LL GLAPD parton shower significantly changes the $\sqrt{s}$ dependence of the MN cross sections.

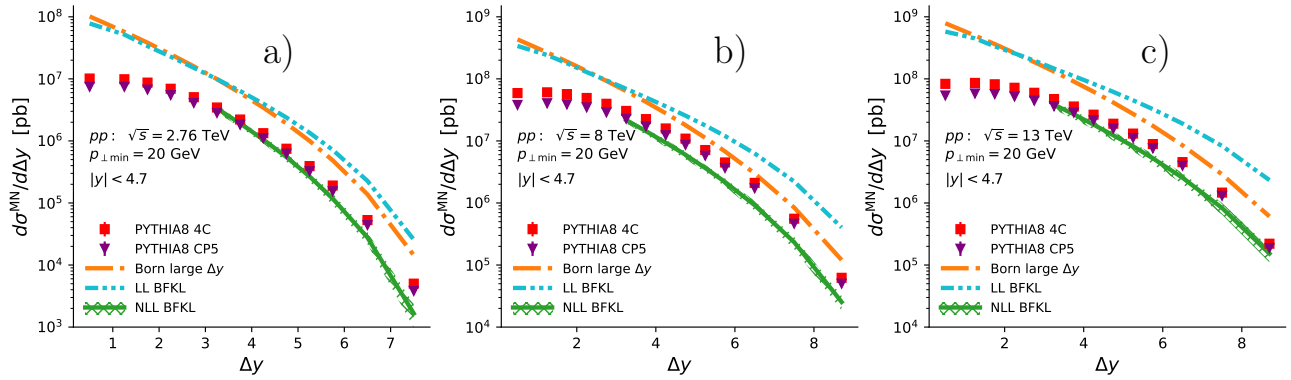


Figure 4.3 — Results of calculation of the MN cross section $d\sigma^{\mathrm{MN}}/d\Delta y$ [A2; 126]. a) at $\sqrt{s} = 2.76$ TeV; b) at $\sqrt{s} = 8$ TeV; c) at $\sqrt{s} = 13$ TeV for hadronic jets with $p_\perp > p_{\perp\mathrm{min}} = 20$ GeV. Vertical lines are statistical uncertainties of the MC modeling. Colored lines are the calculation results. Hatched band is the theoretical uncertainty of the NLL BFKL calculation.

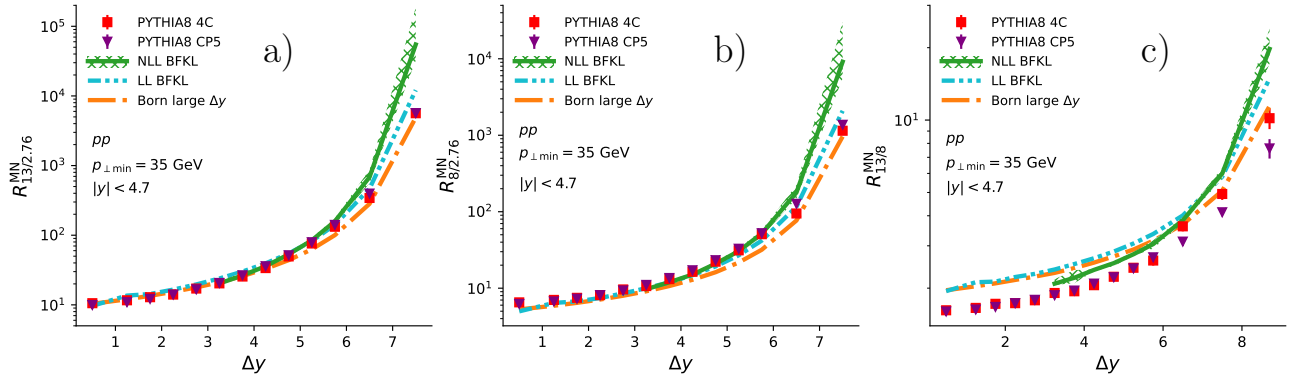


Figure 4.4 — Results of calculation of the ratios of the MN cross sections [A2; 126]. a) $R^{\mathrm{MN}}_{13/2.76}$; b) $R^{\mathrm{MN}}_{8/2.76}$; and c) $R^{\mathrm{MN}}_{13/8}$ for hadronic jets with $p_\perp > p_{\perp\mathrm{min}} = 35$ GeV. Vertical lines are statistical uncertainties of the MC modeling. Colored lines are the calculation results. Hatched band is the theoretical uncertainty of the NLL BFKL calculation.

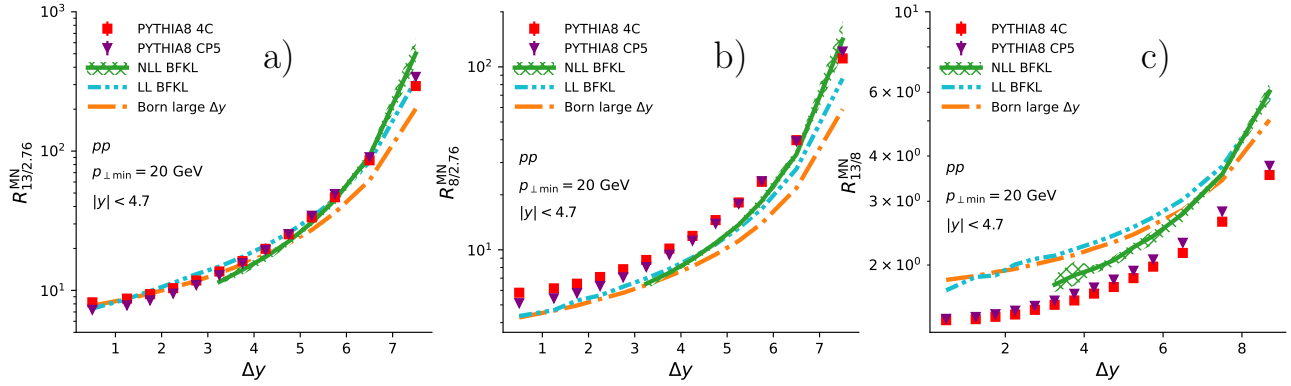


Figure 4.5 — Results of calculation of the ratios of the MN cross sections [A2; 126]. a) $R^{\mathrm{MN}}_{13/2.76}$; b) $R^{\mathrm{MN}}_{8/2.76}$; and c) $R^{\mathrm{MN}}_{13/8}$ for hadronic jets with $p_\perp > p_{\perp\mathrm{min}} = 20$ GeV. Vertical lines are statistical uncertainties of the MC modeling. Colored lines are the calculation results. Hatched band is the theoretical uncertainty of the NLL BFKL calculation.

# Chapter 5. Energy flow for inter-jet and jet veto.

## 5.1 Energy flow from hard jets for jet veto calculation

Currently, the ratios of the cross sections for dijet production with the veto on additional jets, measured in [37; A1; A3; 108; 110], can be calculated within the BFKL approach only with LL accuracy using MC generators. This chapter is devoted to the development of methods for calculating the cross sections for dijet production with jet veto. There is no developed analytical method for calculating the influence of the jet veto condition on the transverse momentum $p_\perp$, based on the BFKL approximation. However, calculations based on the Banfi–Macrchesini–Smye equation (BMS) [49] show good agreement with measurements of the ratios of cross sections for the dijet production with inter-jet veto in the ATLAS experiment [34] at $\sqrt{s} = 7$ TeV [127] at the LHC.

In this chapter, we generalize the approach based on the BMS equation to calculate the jet veto over the entire available rapidity interval with the Born parton-parton subprocess. We also apply the BMS approach for the inter-jet veto with the parton-parton subprocess within the NLL BFKL approximation, calculated as described in the previous chapter. As we saw in the previous chapter, the NLL BFKL calculation for the cross section for the MN dijet production is in better agreement with the experimental measurements, compared with calculations with the Born subprocess, which justifies our approach. The CMS measurements in $pp$ collisions at $\sqrt{s} = 2.76$ TeV [A1; A3; 108; 110] and 7 TeV [37] allow us to test the $\sqrt{s}$ dependence of the predictions of the BMS approach to veto.

The BMS approach describes the physics of energy flow. The energy flow is understood as the leakage of energy and transverse momentum from hard jets due to multiple radiation of soft gluons at large angles. On the one hand, the energy flow leads to a decrease in the energy of hard jets. On the other hand, if the transverse momentum is transmitted to the area where the veto condition is imposed, then this can lead to a violation of the veto.

The region of phase space where the physics of energy flow is applicable is somewhat different from the one in which the effects of the BFKL evolution should dominate. Since the physics of energy flow uses the emission of soft gluons at large

angles, the sequential emission of gluons leads to a $p_\perp$-ordered parton cascade, with all angles of approximately the same order. At the same time, the BFKL evolution is dominated by $p_\perp$ diffusion and rapidity ordering, which can lead to strong angular ordering.

In the work [127], calculations based on the physics of energy flow demonstrated agreement between the calculation results and the experimental observation using the inter-jet veto and intended for searching for BFKL signals. Thus, calculations showed agreement with measurements of the production of pairs of forward-backward hadronic jets with inter-jet veto in $pp$ collisions at $\sqrt{s} = 7$ TeV in the ATLAS [34] experiment. Forward-backward selection included the selection of jets with maximum and minimum rapidity in events, which enhances the contribution of BFKL logarithms. At the same time, to study the physics of energy flow in the work [34], pairs of the leading jets in the event was selected. However, calculations [127] significantly overestimated the impact of the veto when selecting the leading dijets. Thus, the question of the mutual contribution of the BFKL and BMS regimes to the observables employing veto conditions remains open.

In this chapter several approaches is analyzed to the generalization of the method used in [127] for the case where the veto is imposed over the entire available rapidity interval (jet veto), as in the CMS measurement presented in Chapter 3 and in [37; A1; A3; 108; 110]. A comparison of the results of calculations with the measurements in $pp$ at $\sqrt{s} = 7$ TeV carried out in the CMS experiment [37] is presented.

It is also shown that the color factor $C_A$ should be replaced by $C_F$ in the approach described in [127] in order to eliminate the double counting of gluon emission by color dipoles. The method for applying the BMS approach to calculations within the framework of the LL/NLL BFKL is presented, and a comparison of the calculation results with the CMS measurements in $pp$ collisions at $\sqrt{s} = 2.76$ TeV [A1; A3; 108; 110] and 7 TeV [37] is presented.

## 5.2 Banfi–Marchesini–Smye equation

In the work of Banfi–Marchesini–Smye (BMS) [49], infrared and collinearly safe inter-jet observables are considered. This, for example, is the distribution of

the total energy $E_{\text{out}}$ (or transverse momentum) of hadrons emitted into the region $\mathcal{C}_{\text{out}}$ away from all hard hadronic jets. Infrared and collinear safety enable finite perturbative calculations in QCD. The normalized distribution $E_{\text{out}}$ determines the probability that all radiation into the region $\mathcal{C}_{\text{out}}$ will be less than $E_{\text{out}}$, that is, the probability of not violating the veto set for radiation $E > E_{\text{out}}$. The paper [49] considers the case when $E_{\text{out}} \ll Q$, the scale of hard jets, which leads to the need to sum the logarithmic terms $\alpha_s^n \ln^n Q/E_{\text{out}}$. In the work of BMS [49] the large-angle approximation of soft gluon emission was used to sum such logarithms.

For simplicity, $e^+e^-$ annihilation into jets was considered in [49] as the main process. The pair of partons produced in an annihilation (the color dipole designated $\text{G}\overline{\text{G}}$ in Fig. 5.1) was considered as a source of coherent gluon radiation. $\mathcal{C}_{\text{in}}$ the region complementary to $\mathcal{C}_{\text{out}}$ is defined by two cones with an angle of generatrices to the trust axis $\theta_{\text{in}}$, as shown in Fig. 5.1. The probability that the total energy of hadrons in the $\mathcal{C}_{\text{out}}$ region is less than $E_{\text{out}}$ is determined by the formula:

$$P_{e^+e^-}(Q, E_{\text{out}}) = \sum_n \int \frac{d\sigma_n}{\sigma_T} \Theta\left(E_{\text{out}} - \sum_{h \in \mathcal{C}_{\text{out}}} \omega_h\right), \tag{5.1}$$

where $d\sigma_n$ — differential cross section for the production of $n$ hadrons;
$\sigma_T$ — total annihilation cross section $e^+e^-$ into hadrons;
$\omega_h$ — energy of hadron $h$.

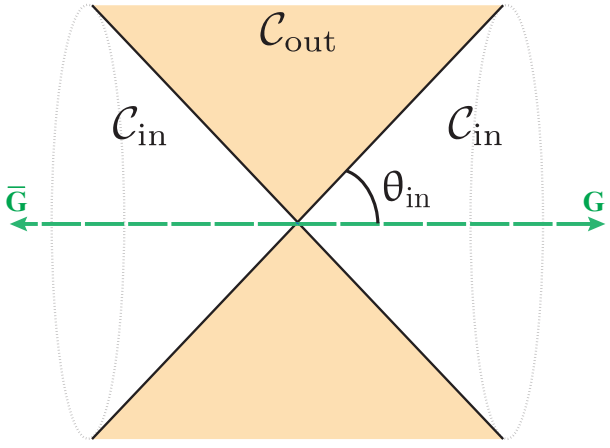


Figure 5.1 — Definition of $\mathcal{C}_{\text{in}}$ and $\mathcal{C}_{\text{out}}$ regions in $e^+e^-$ annihilation.

At the parton level, the probability (5.1) can be calculated within QCD by summing contributions from processes with $n$ gluons in the final state

$$e^+e^- \to k_\alpha k_1 .... k_n k_\beta, \tag{5.2}$$

where $k_\alpha$ and $k_\beta$ — momenta of primary quark and antiquark;
$k_i$ — gluon momenta.

The process (5.1) is dominated by the contribution with two jets flying in opposite directions. If $\theta_{\text{in}}$ is large enough, then the main radiation energy is released in the $\mathcal{C}_{\text{in}}$ region. The energy in the region $\mathcal{C}_{\text{out}}$ is gained due to soft gluons, so the main contribution to the probability (5.1) comes from processes with $E_{\text{out}} \ll Q$. Thus, the probability can be normalized to unity in the kinematic limit $E_{\text{out}} \simeq Q$. Three-jet events, when $E_{\text{out}} \simeq Q$, are suppressed by $\alpha_s(Q)$ and the angular distribution of the third jet. The main contribution from soft gluon radiation is provided by a parton cascade that is highly ordered in energy (transverse momentum).

The contributions from the $p_\perp$-ordered cascade can be summed up using the BMS evolution equation [49]. In a more general case, when the directions of the momenta of the primary quark-antiquark pair (color dipole) $\Omega_\alpha$ and $\Omega_\beta$ are arbitrary, and the $\mathcal{C}_{\text{in}}$ region is defined so that it contains $\Omega_\alpha$ and $\Omega_\beta$, the BMS equation can be written as:

$$\partial_\tau P_\tau(\Omega_\alpha, \Omega_\beta) = -\int_{\mathcal{C}_{\text{out}}} \frac{d^2\Omega_\gamma}{4\pi} \frac{1-\cos\theta_{\alpha\beta}}{(1-\cos\theta_{\alpha\gamma})(1-\cos\theta_{\gamma\beta})} P_\tau(\Omega_\alpha, \Omega_\beta) + \int_{\mathcal{C}_{\text{in}}} \frac{d^2\Omega_\gamma}{4\pi} \frac{1-\cos\theta_{\alpha\beta}}{(1-\cos\theta_{\alpha\gamma})(1-\cos\theta_{\gamma\beta})} (P_\tau(\Omega_\alpha, \Omega_\gamma) P_\tau(\Omega_\gamma, \Omega_\beta) - P_\tau(\Omega_\alpha, \Omega_\beta)), \tag{5.3}$$

where $\tau$ — evolutionary variable defined below;
$\theta_{ij}$ — angle between directions $\Omega_i$ and $\Omega_j$.

The evolutionary variable $\tau$ is determined by the formula:

$$\tau = \int_{p_{\perp\text{veto}}}^{p_\perp} \frac{dk_\perp}{k_\perp} \frac{\alpha_s(k_\perp) C_A}{\pi}, \tag{5.4}$$

where $p_{\perp\text{veto}}$ — threshold for transverse momentum, above which the veto is imposed on hadronic jets in the region $\mathcal{C}_{\text{out}}$;
$p_\perp$ — transverse momentum of the initial dipole. Within the framework of the approach under consideration, the dipole hardness $Q \approx p_\perp$.

The right side of the BMS equation (formula (5.3)) consists of two integrals. The first is the integral over the $\mathcal{C}_{\text{out}}$ region, which sums up the contributions from

the initially emitted gluons, i.e., the so-called Sudakov logarithms (the probability of not emitting the gluons with $p_\perp$ higher than $p_{\perp\text{veto}}$ into the $\mathcal{C}_{\text{out}}$ region). The second is the integral over the region $\mathcal{C}_{\text{in}}$, which sums up the contributions from secondary gluons in the cascade, the so-called non-global logarithms. In the second part of the BMS equation, the emission of primary gluons into the $\mathcal{C}_{\text{in}}$ region is allowed, which leads to the splitting of the initial dipole into two daughter dipoles, the emission from which can subsequently lead to violation of the veto condition.

The initial and boundary conditions for the equation (5.3) are as follows:

– $P_{\tau=0}(\Omega_\alpha, \Omega_\beta) = 1$, for all directions $\Omega_\alpha$ and $\Omega_\beta$ within $\mathcal{C}_{\text{in}}$ region. This condition is required due to the strict $p_\perp$-ordering of the cascade.

– $P_\tau(\Omega_\alpha, \Omega_\alpha) = 1$ for all $\tau$ and $\Omega_\alpha$. The fulfillment of this condition is ensured by the screening the color charge.

To assess the mutual contribution of Sudakov and non-global logarithms, it is possible to obtain a solution in the case when only Sudakov logarithms are taken into account. In this case, the equation (5.3) takes the form:

$$\partial_\tau P_\tau(\Omega_\alpha, \Omega_\beta) = -\int_{\mathcal{C}_{\text{out}}} \frac{d^2\Omega_\gamma}{4\pi} \frac{1-\cos\theta_{\alpha\beta}}{(1-\cos\theta_{\alpha\gamma})(1-\cos\theta_{\gamma\beta})} P_\tau(\Omega_\alpha, \Omega_\beta), \tag{5.5}$$

The solution of Eq. (5.5):

$$P_\tau(\Omega_\alpha, \Omega_\beta) = \exp\left\{ -\tau \int_{\mathcal{C}_{\text{out}}} \frac{d^2\Omega_\gamma}{4\pi} \frac{1-\cos\theta_{\alpha\beta}}{(1-\cos\theta_{\alpha\gamma})(1-\cos\theta_{\gamma\beta})} \right\}. \tag{5.6}$$

## 5.3 Application of the BMS equation for calculation of the inclusive cross section for dijet production with veto in hadron collisions

.

The inclusive cross section for dijet production in hadron collisions in the hard regime (and semi-hard regime at large $\Delta y$) can be calculated according to the factorization formula (4.1).

The calculation of the influence of the veto condition in the parton subprocess depends on the color configuration, which determines the direction of movement of the color dipoles. Let us first consider the simplest process ($12 \to 34$) of scattering of a quark on a quark of another flavor ($qq'$) (an antiquark on an antiquark of another flavor ($\bar{q}\bar{q}'$)), as shown in Figure 5.2.

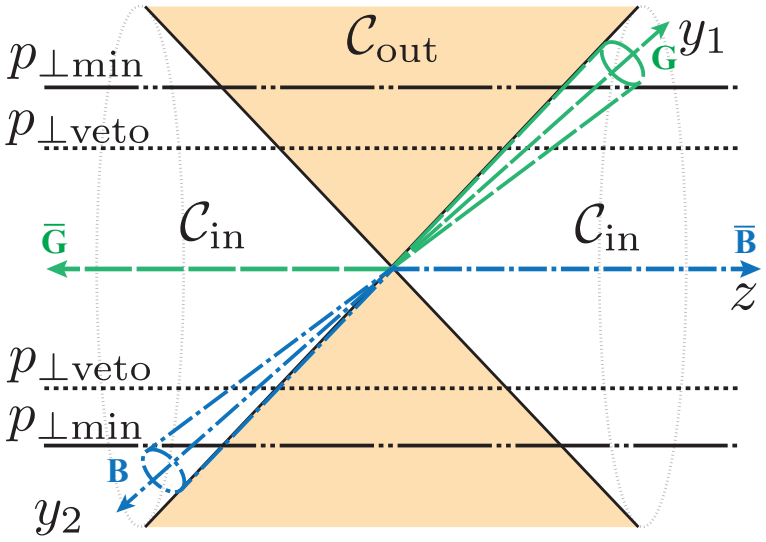


Figure 5.2 — Definition of thresholds $p_{\perp\min}$ and $p_{\perp\text{veto}}$, areas $\mathcal{C}_{\text{in}}$ and $\mathcal{C}_{\text{out}}$, color dipoles $\text{B}\overline{\text{B}}$ and $\text{G}\overline{\text{G}}$.

$\hat{\sigma}_{qq'}$ in the LO of perturbation theory.

$$\frac{d\hat{\sigma}_{qq'}}{d\hat{t}} = \frac{1}{16\pi\hat{s}^2}\frac{g^4 C_F}{N_c}\left(\frac{\hat{s}^2+\hat{u}^2}{\hat{t}^2}\right), \tag{5.7}$$

where $\hat{s}$, $\hat{t}$ and $\hat{u}$ — Mandelstam variables for the parton subprocess $2 \to 2$;
$g$ — $\sqrt{4\pi\alpha_s}$;
$N_c$ — number of colors.

To determine the color flow it is necessary to use the approximation of large number of colors. Then the one-gluon exchange leads to that the proton residue «1» (the remnant of the proton «1» after the parton «3» has been knocked out of it) and the parton «4» (the parton knocked out from the proton «2») become color connected, as well as proton residue «2» (the remnant of the proton «2» after the parton «4» is knocked out of it) and the parton «3» become color connected. Thus, two color dipoles are formed: «14», designated in Figure 5.2 by $\text{G}\overline{\text{G}}$, and «23», designated in the same figure by $\text{B}\overline{\text{B}}$. The end of the dipole «1» (proton remnant «1») propagates to the direction $\theta = 0$ or $\eta_1 = +\infty$. The end of the dipole «2» (proton remnant «2») propagates to the direction $\theta = \pi$ or $\eta_2 = -\infty$. The end of the dipole «3» propagates to the direction $\eta_3 = y_1$, and the end of the dipole «4» propagates to the direction $\eta_4 = y_2$. In the present approach, the quark masses are neglected, so the pseudorapidity, $\eta$, is equal to the rapidity $y$.

Let us define for further convenience:

$$h^A(s,t,u) = \frac{g^4 C_F}{N_c}\left(\frac{s^2+u^2}{t^2}\right),$$
$$h^B(s,t,u) = \frac{g^4 C_F}{N_c}\left(\frac{s^2+u^2}{t^2} + \frac{2}{N_c}\frac{s}{t}\right),$$
$$h^C(s,t,u) = g^4 C_F \frac{u}{t}\left(\frac{t^2+u^2}{s^2} - \frac{1}{N_c^2}\right),$$
$$h^D(s,t,u) = 2g^4 \frac{N_c^2}{N_c^2-1}\left(1 - \frac{tu}{s^2} - \frac{su}{t^2} + \frac{u^2}{st}\right), \tag{5.8}$$

Then the veto cross section can be calculated using the solution to equation (5.3) as:

$$\frac{d\hat{\sigma}^{\text{veto}}_{qq'}}{d\hat{t}} = \frac{1}{16\pi\hat{s}^2}(h^A(\hat{s},\hat{t},\hat{u})P_{14}P_{23} + h^A(\hat{s},\hat{u},\hat{t})P_{13}P_{24}), \tag{5.9}$$

where $P_{ij}$ — the probability of not violating the veto by QCD radiation from the dipole $ij$, calculated using formula (5.3).

In formula (5.9) the $u$-channel is added, despite the fact that $q$ and $q'$ are distinguishable, in order to take into account the contributions of $y_1 - y_2 > 0$ and $y_1 - y_2 < 0$.

For cross sections of other parton subprocesses, the following formulas can be written:

– $q\bar{q}' \to q\bar{q}'$ scattering of a quark by an antiquark of a different flavor

$$\frac{d\hat{\sigma}^{\text{veto}}_{q\bar{q}'}}{d\hat{t}} = \frac{1}{16\pi\hat{s}^2}(h^A(\hat{u},\hat{t},\hat{s})P_{12}P_{34} + h^A(\hat{t},\hat{u},\hat{s})P_{12}P_{34}), \tag{5.10}$$

– $q\bar{q} \to q'\bar{q}'$ conversion to a pair of another flavor

$$\frac{d\hat{\sigma}^{\text{veto}}_{q\bar{q}\to q'\bar{q}'}}{d\hat{t}} = \frac{1}{16\pi\hat{s}^2}(h^A(\hat{t},\hat{s},\hat{u})P_{14}P_{23} + h^A(\hat{u},\hat{s},\hat{t})P_{13}P_{24}), \tag{5.11}$$

– $qq \to qq$ scattering of a quark on a quark of the same flavor (also for $\bar{q}\bar{q} \to \bar{q}\bar{q}$)

$$\frac{d\hat{\sigma}^{\text{veto}}_{qq}}{d\hat{t}} = \frac{1}{16\pi\hat{s}^2}(h^B(\hat{s},\hat{t},\hat{u})P_{14}P_{23} + h^B(\hat{s},\hat{u},\hat{t})P_{13}P_{24}), \tag{5.12}$$

– $q\bar{q} \to q\bar{q}$ scattering of a quark by an antiquark of the same flavor

$$\frac{d\hat{\sigma}^{\text{veto}}_{q\bar{q}\to q\bar{q}}}{d\hat{t}} = \frac{1}{16\pi\hat{s}^2}(h^B(\hat{u},\hat{t},\hat{s})P_{12}P_{34} + h^B(\hat{u},\hat{s},\hat{t})P_{13}P_{24} + h^B(\hat{t},\hat{u},\hat{s})P_{12}P_{34} + h^B(\hat{t},\hat{s},\hat{u})P_{14}P_{23}), \tag{5.13}$$

– $q\bar{q} \to gg$ conversion to gluon-gluon pair

$$\frac{d\hat{\sigma}^{\text{veto}}_{q\bar{q}\to gg}}{d\hat{t}} = \frac{1}{16\pi\hat{s}^2}(h^C(\hat{s},\hat{t},\hat{u})P_{34}P_{13}P_{24} + h^C(\hat{s},\hat{u},\hat{t})P_{34}P_{14}P_{23}), \tag{5.14}$$

– $gg \to q\bar{q}$ conversion of gluons into a quark-antiquark pair

$$\frac{d\hat{\sigma}^{\text{veto}}_{gg\to q\bar{q}}}{d\hat{t}} = \frac{1}{16\pi\hat{s}^2}\left(\frac{3}{8}\right)^2(h^C(\hat{s},\hat{t},\hat{u})P_{34}P_{13}P_{24} + h^C(\hat{s},\hat{u},\hat{t})P_{34}P_{14}P_{23}) \times 2, \tag{5.15}$$

– $qg \to qg$ scattering of a quark on a gluon (also for $\bar{q}g \to \bar{q}g$)

$$\begin{aligned}\frac{d\hat{\sigma}^{\text{veto}}_{qg}}{d\hat{t}} = \frac{-1}{16\pi\hat{s}^2}\left(\frac{3}{8}\right)&(h^C(\hat{t},\hat{s},\hat{u})P_{24}P_{12}P_{34} + h^C(\hat{t},\hat{u},\hat{s})P_{24}P_{14}P_{23} \\ &+ h^C(\hat{u},\hat{s},\hat{t})P_{23}P_{12}P_{34} + h^C(\hat{u},\hat{t},\hat{s})P_{23}P_{13}P_{24}),\end{aligned} \tag{5.16}$$

– $gg \to gg$ gluon-gluon scattering

$$\begin{aligned}\frac{d\hat{\sigma}^{\text{veto}}_{gg\to gg}}{d\hat{t}} = \frac{1}{16\pi\hat{s}^2}&(h^D(\hat{s},\hat{t},\hat{u})P_{12}P_{13}P_{24}P_{34} + h^D(\hat{s},\hat{u},\hat{t})P_{12}P_{14}P_{23}P_{34} \\ &+ h^D(\hat{u},\hat{t},\hat{s})P_{14}P_{24}P_{13}P_{23}),\end{aligned} \tag{5.17}$$

Using parton subprocesses with veto (5.9-5.17) in formula (4.1), we obtain the inclusive cross section for dijet production with veto for additional hadronic jets with $p_\perp > p_{\perp\text{veto}}$ imposed in the region $\mathcal{C}_{\text{out}}$ away from the dijet. As can be seen, this approach, in principle, makes it possible to take into account the veto condition in the $\mathcal{C}_{\text{out}}$ region of arbitrary complex configuration, the main thing is that the hard jets should fall into the complementary $\mathcal{C}_{\text{in}}$ region. However, the analytical solution is known only for a certain configuration of $\Omega_\alpha$, $\Omega_\beta$ and $\mathcal{C}_{\text{in}}$ [128]. In the case of experimental observables that are interesting, such as inter-jet veto (veto in the interval $\Delta y$ between jets in a pair) or jet veto, when the veto condition is imposed in the entire experimentally accessible rapidity range, it is necessary to use numerical methods to solve the equation (5.3). The next paragraph discusses the numerical solution of the equation (5.3) for the case of inter-jet veto.

## 5.4 Numerical solution of the BMS equation for the case of inter-jet veto

A numerical solution is obtained in the system of the center of mass of colliding partons. In this system, the rapidities of the jets in the pair are $y_1^{\text{cm}} = -y_2^{\text{cm}} = \Delta y/2$. Stepping back from the jets by the jet size $R$, as shown in Figure 5.2, the inter-jet veto area can be defined by the angle:

$$\theta_{\text{in}} = 2\text{arctg}\left[\exp\left\{-\left(\frac{\Delta y}{2} - R\right)\right\}\right], \tag{5.18}$$

Thus, the region $\mathcal{C}_{\text{out}}$ is a function of the parameter $\Delta y$ only. For each $\Delta y$ it is necessary to solve the equation (5.3). For the numerical solution, it is convenient to make a transformation to the new function $g_\tau(\Omega_\alpha, \Omega_\beta)$:

$$P_\tau(\Omega_\alpha, \Omega_\beta) = e^{-\tau f_{\alpha\beta}(\mathcal{C}_{\text{out}})} g_\tau(\Omega_\alpha, \Omega_\beta), \tag{5.19}$$

where $f_{\alpha\beta}(\mathcal{C}_{\text{out}})$:

$$f_{\alpha\beta}(\mathcal{C}_{\text{out}}) = \int_{\mathcal{C}_{\text{out}}} \frac{d\Omega_\gamma}{4\pi} w_{\alpha\beta}(\Omega_\gamma), \tag{5.20}$$

and $w_{\alpha\beta}(\Omega_\gamma)$:

$$w_{\alpha\beta}(\Omega_\gamma) = \frac{1 - \cos\theta_{\alpha\beta}}{(1 - \cos\theta_{\alpha\gamma})(1 - \cos\theta_{\gamma\beta})}, \tag{5.21}$$

After the transformation, the equation for $g_\tau(\Omega_\alpha, \Omega_\beta)$ is:

$$\partial_\tau g_\tau(\Omega_\alpha, \Omega_\beta) = \int_{\mathcal{C}_{\text{in}}} \frac{d\Omega_\gamma}{4\pi} w_{\alpha\beta}(\Omega_\gamma) U_{\alpha\beta\gamma} \big[g_\tau(\Omega_\alpha, \Omega_\gamma) g_\tau(\Omega_\gamma, \Omega_\beta) - g_\tau(\Omega_\alpha, \Omega_\beta)\big], \tag{5.22}$$

where $U_{\alpha\beta\gamma}$:

$$U_{\alpha\beta\gamma} = e^{-\tau(f_{\alpha\gamma}(\mathcal{C}_{\text{out}}) + f_{\gamma\beta}(\mathcal{C}_{\text{out}}) - f_{\alpha\beta}(\mathcal{C}_{\text{out}}))}. \tag{5.23}$$

To solve the equation (5.22) numerically, we define a lattice in the space of angles ($\theta$, $\varphi$). Let us divide the interval for the polar angle $[0., \theta_{\text{in}}] \cup [\pi - \theta_{\text{in}}, \pi]$ into 80 parts. For the azimuthal angle $\varphi$, we divide the interval $[0., \pi]$ into 20 parts. In this case, we take advantage of the symmetry of the problem. First, we count the azimuthal angle from the azimuthal angle of the parton «3». The proton

residues propagate along the $z$ axis, so the azimuthal angle remains only for the parton «4». Secondly, symmetry with respect to the replacement of $\varphi$ by $-\varphi$, for the parton «4». Thus, it is necessary to construct the evolution of $g_\tau(\Omega_\alpha, \Omega_\beta)$ at $81 \times 81 \times 21 = 137781$ nodes. Without using these symmetries, the number of nodes would increase by 80 times with the same accuracy. We will regularize the integrand by neglecting contributions when $\Omega_\gamma = \Omega_\alpha$ or $\Omega_\gamma = \Omega_\beta$. This rough approach, however, reproduces well the results of other authors [127; 128].

Considering the lattice described in the previous paragraph, the equation (5.22) breaks down into a system of $\sim 140000$ simple ordinary differential equations:

$$\partial_\tau g_{ij}(\tau) = \sum_{k\neq i, k\neq j, k\in \mathcal{C}_{\text{in}}} \frac{\Delta\Omega_k}{4\pi} w_{ij}(k) U_{ijk} \big[ g_{ik}(\tau) g_{kj}(\tau) - g_{ij}(\tau) \big], \tag{5.24}$$

For LHC energies, it is enough to construct the evolution in $\tau$ from 0. to 0.8. The evolution was constructed by the 4th order Runge-Kutta method, with a step of 0.01. Solutions were obtained for 100 equidistant $\theta_{\text{in}}$ values for the interval $[0, \pi/2]$ with the «Konstantinov» supercomputer facility of PIK Data Center at NRC «Kurchatov Institute»-PNPI. The function values between lattice nodes were restored by the piecewise linear interpolation. The solutions obtained can be used in calculating the cross sections for dijet production with inter-jet veto. It should be noted that from the point of view of calculating cross sections with veto, the solutions to the BMS equation described in this paragraph must be obtained before the calculation, since searching for one solution for a particular $\theta_{\text{in}}$ takes more than 10 hours on one CPU (Central Processing Unit).

## 5.5 BMS evolution for jet veto

The procedure described in paragraph 5.3 is suitable for $\mathcal{C}_{\text{out}}$ regions of any complexity. Recall that for the inter-jet veto, $\mathcal{C}_{\text{out}}$ was a function of only $\Delta y$. In the case of jet veto, when the veto condition is imposed over the entire available rapidity interval, the region $\mathcal{C}_{\text{out}}$ can be defined as the union of disjoint rapidity regions. Table 7 presents the definition of the $\mathcal{C}_{\text{out}}$ regions depending on the type of color dipole. In Table 7 $y_{\min}$, $y_{\max}$ are the minimum and maximum rapidity available

in the experiment. So for jet veto $\mathcal{C}_{\text{out}}$ the area depends on: $\Delta y$; $y^{\text{cm}} = (y_1 + y_2)/2$ - the rapidity of the center of mass of the colliding partons; $y_{\min}$; $y_{\max}$; type of color dipole. This results in a large number of possible configurations that must be computed in advance, requiring a large amount of CPU time to compute and memory to store the solutions. It follows that the approach chosen for the inter-jet veto turns out to be impractical for the jet veto.

Table 7 — Definition of the $\mathcal{C}_{\text{out}}$ area depending on the type of color dipole

| Color dipole | Range $\mathcal{C}_{\text{out}}$ |
|---|---|
| «12» | $[y_{\min}, y_{\max}]$ |
| «13» | $[y_{\min}, y_1 - R] \cup [y_1 + R, y_{\max}]$ |
| «14» | $[y_{\min}, y_2 - R] \cup [y_2 + R, y_{\max}]$ |
| «23» | $[y_{\min}, y_1 - R] \cup [y_1 + R, y_{\max}]$ |
| «24» | $[y_{\min}, y_2 - R] \cup [y_2 + R, y_{\max}]$ |
| «34» | $[y_{\min}, y_2 - R] \cup [y_2 + R, y_1 - R] \cup [y_1 + R, y_{\max}]$ |

To calculate the jet veto, two approaches are considered in this work: a simplified one, based on the assumption of independence of veto violation for each of the disjoint ranges (in Table 7), and an approach based on MC modeling of the BMS evolution, considered in the next paragraph.

First, let's look at the simplified approach in a more general form. It is assumed that in the available rapidity interval there are $k$ hard ordered in rapidity hadronic jets $y_{\min} < y_k < y_{k-1} < ... < y_1 < y_{\max}$, then we define the region $\mathcal{C}_{\text{out}}$ as union $[y_{\min}, y_k - R] \cup [y_k + R, y_{k-1} - R] \cup ... \cup [y_1 + R, y_{\max}] = {\mathcal{C}_{\text{out}}}^{(k)} \cup {\mathcal{C}_{\text{out}}}^{(k-1)} \cup ... \cup {\mathcal{C}_{\text{out}}}^{(0)}$. Assuming independence of events not to violate the veto in each of the regions ${\mathcal{C}_{\text{out}}}^{(i)}$, the probability of not violating the veto is factorized:

$$P_\tau(\Omega_\alpha, \Omega_\beta) = \prod_{i=0}^{k} P_\tau^{(i)}(\Omega_\alpha, \Omega_\beta), \tag{5.25}$$

where $P_\tau^{(i)}(\Omega_\alpha, \Omega_\beta)$ — the probability of not violating the veto in the region ${\mathcal{C}_{\text{out}}}^{(i)}$, calculated independently of other regions (solving equation (5.3) with $\mathcal{C}_{\text{out}} = {\mathcal{C}_{\text{out}}}^{(i)}$).

In order to use the solution of the BMS equation for the interjet veto, obtained in paragraph 5.4, to calculate $P_\tau^{(i)}(\Omega_\alpha, \Omega_\beta)$ in (5.25), it is necessary to perform a Lorentz transformation to place the region ${\mathcal{C}_{\text{out}}}^{(i)}$ at the center of rapidity.

## 5.6 MC algorithm for BMS evolution

In the work [129] an algorithm was proposed that reproduces the evolution of the BMS. The algorithm allows the generation of multiple gluon production events, which can then be used to estimate the probabilities of not violating the veto in the $\mathcal{C}_{\text{out}}$ region.

Resummation of virtual contributions is carried out using the Sudakov form factor. In order to separate virtual and real terms, it is necessary to introduce a threshold of the transverse momentum, $Q_0$. Then the Sudakov form factor is defined by the expression:

$$\ln S_{\alpha\beta}(Q, Q_0) = -\int_{Q_0}^{Q} \frac{d\omega_\gamma}{\omega_\gamma} \frac{d\Omega_\gamma}{4\pi} \overline{\alpha}_s(q_{\alpha\beta\perp}) w_{\alpha\beta}(\Omega_\gamma) \Theta(q_{\alpha\beta\perp} - Q_0), \tag{5.26}$$

where $q_{\alpha\beta\perp} = \frac{2\omega_\gamma^2}{w_{\alpha\beta}(\Omega_\gamma)}$ — radiation scale transverse to the dipole «$\alpha\beta$».

The Sudakov form factor can be interpreted as the probability of not emitting a gluon with transverse momentum greater than $Q_0$ by a dipole on the $Q$ scale with ends moving to the $\Omega_\alpha$ and $\Omega_\beta$ directions.

Using the Sudakov form factor, it is possible to generate the scale of splitting $\omega_g$ of the dipole (due to gluon emission) using a random variable $r$ uniformly distributed on the interval [0,1], solving the equation:

$$S_{\alpha\beta}(\omega_g, Q_0) \cdot r = S_{\alpha\beta}(Q, Q_0), \tag{5.27}$$

If $r < S_{\alpha\beta}(Q, Q_0)$, then we assume that the dipole has not split to the scale $Q_0$. Otherwise, by solving (5.27), we determine the splitting scale $\omega_g$. The direction of emission is determined by the angular distribution:

$$\frac{dR_{\alpha\beta}(\Omega_g)}{d\Omega_g} = \frac{\overline{\alpha}_s(q_{\alpha\beta\perp}(\omega_\gamma = \omega_g) w_{\alpha\beta}(\Omega_g))}{N_{\alpha\beta}(\omega_g)} \Theta(q_{\alpha\beta\perp} - Q_0), \tag{5.28}$$

After the splitting scale $\omega_g$ and direction $\Omega_g$ are determined, we assume that the initial dipole «$\alpha\beta$» has split into two daughter dipoles «$\alpha g$» and «$g\beta$». Next, the procedure is repeated for the new scale $Q = \omega_g$, for two daughter dipoles, and further until the threshold $Q_0$ is reached. As a result, we will have a generated final state with $\alpha$ and $\beta$ partons and $k$ gluons. For each gluon, the direction $\Omega_g^{(i)}$ and transverse momentum are known. This information is enough to determine whether

a given event violates the veto or not. By generating the events of gluon emission from the «$\alpha\beta$» dipole several times, it is possible to estimate the probability of not violating the veto. The speed of calculation does not depend on the complexity of the region $\mathcal{C}_{\text{out}}$.

Note, however, that the algorithm just described introduces a scale $q_{\alpha\beta\perp}$, which was not present in the original BMS equation (5.3). This bindes the scale of splitting $\omega_\gamma$ and the direction $\Omega_\gamma$. The Sudakov form factor (5.26) includes integration over angles $\Omega_\gamma$, which is, among other things, limited by the function $\Theta(q_{\alpha\beta\perp} - Q_0)$. This causes the harder gluons to gain more weight. In other words, a correlation appears between the radiation angle $\Omega_g$ and the scale $\omega_g$, which was not in the original BMS equation. Because of this, the distribution over $p_\perp$ of emitted gluons changes, and a strong dependence on $Q_0$ appears. Moreover, calculations have shown that if $Q_0$ is chosen too low, the soft gluon approximation actually stops working. The emitted gluons become comparable in scale to the scale of the original dipole $Q$. This, in turn, requires taking into account the law of momentum-energy conservation, which is not taken into account in the BMS of evolution. In the BMS evolution, the law of momentum-energy conservation is neglected due to the strong ordering in energy, which is violated in the considered algorithm, when $Q_0$ is set low. This circumstance will not, however, play a big role if the veto region is sufficiently far (in angle) from the ends of the dipole «$\alpha\beta$». At high rapidities, however, the angles become small, so at high rapidities, difficulties may arise when using the algorithm just described.

The introduction of $q_{\alpha\beta\perp}$ also makes it difficult to compare the results of the MC algorithm with calculations performed numerically for the BMS equation (5.3). To be able to compare the performance of the algorithm and numerical calculations for the BMS equation (5.3), consider the Sudakov form factor without $q_{\alpha\beta\perp}$:

$$\ln S_{\alpha\beta}(Q, Q_0) = -\int_{Q_0}^{Q} \frac{d\omega_\gamma}{\omega_\gamma} \frac{d\Omega_\gamma}{4\pi} \overline{\alpha}_s(\omega_\gamma) w_{\alpha\beta}(\Omega_\gamma) \Theta(c_{\max} - \cos\theta_{\alpha\gamma}) \Theta(c_{\max} - \cos\theta_{\gamma\beta}), \tag{5.29}$$

where $c_{\max}$ — parameter limiting the minimum angle $\theta_{ij}$ between the directions $\Omega_i$ and $\Omega_j$.

As can be seen, integration over $\omega_\gamma$ in (5.29) does not depend on integration over angles $\Omega_\gamma$, as it was in the case in the original BMS equation (5.3).

As discussed above, the MC algorithm can lead to gluon emission on a scale comparable to that of the emitting dipole. In this case, the effects of recoil and the

energy-momentum conservation law become significant. In this paper, we consider a simplified recoil model that takes into account only the conservation of energy and the $z$ component of momentum, in the approximation of massless partons, and the assumption that the pseudorapidity of the partons does not change during recoil. The model recalculates the energy of the partons of the radiating dipole after gluon emission by solving a system of two linear equations. Moreover, if the emitted gluon is sufficiently hard, then this greatly reduces the energy of the initial dipole, leading to less radiation in the future.

## 5.7 Comparison of $R^{\text{incl}}$ calculations with the CMS measurements in $pp$ collisions at $\sqrt{s} = 7$ TeV and discussion

This section presents the results of calculations $R^{\text{incl}}$ of the ratio of the cross section for the inclusive dijet production to the cross section for the production of «exclusive» dijets, measured in $pp$ collisions at $\sqrt{s} = 7$ TeV by the CMS experiment [37]. The measurement considers hadronic jets with $p_\perp > p_{\perp\min} = 35$ GeV and rapidity $|y| < 4.7$. «Exclusive» hadron jet pair production is essentially dijet production with the veto imposed for additional hadron jets with $p_{\perp\text{veto}} = p_{\perp\min} = 35$ GeV. The size of hadronic jets is defined by the parameter $R = 0.5$.

The comparison of the calculations [A4; 130] with the experimental results [37] are presented in Fig. 5.3. Calculations are presented that take into account veto only in the interval $\Delta y$ between hadronic jets in the dijet «interjet veto», as well as taking into account veto in the entire available rapidity range $-4.7 < y < 4.7$ «jet veto».

Fig. 5.3a shows the calculation results based on the simplified approach (5.25) for the full BMS evolution (5.24) «BMS (jet veto)», and only for Sudakov logarithms (5.6) «Sudakov (jet veto)». For comparison, calculations are also presented for the inter-jet veto «BMS (interjet veto)» and «Sudakov (interjet veto)». Figure 5.3a demonstrates the significant contribution from non-global logarithms. It is also clear that the «jet veto» calculation significantly overestimates the measured $R^{\text{incl}}$ ratio for $\Delta y < 5$. A large contribution for small $\Delta y$ is given by the veto regions outside $\Delta y$, that is, $[-4.7, y_2 - R]$ and $[y_1 + R, 4.7]$. This may be due to the fact that at high rapidities, the angles effectively become small, which leads to an easier violation of the veto by the BMS evolution, since it operates with angles, not rapidities.

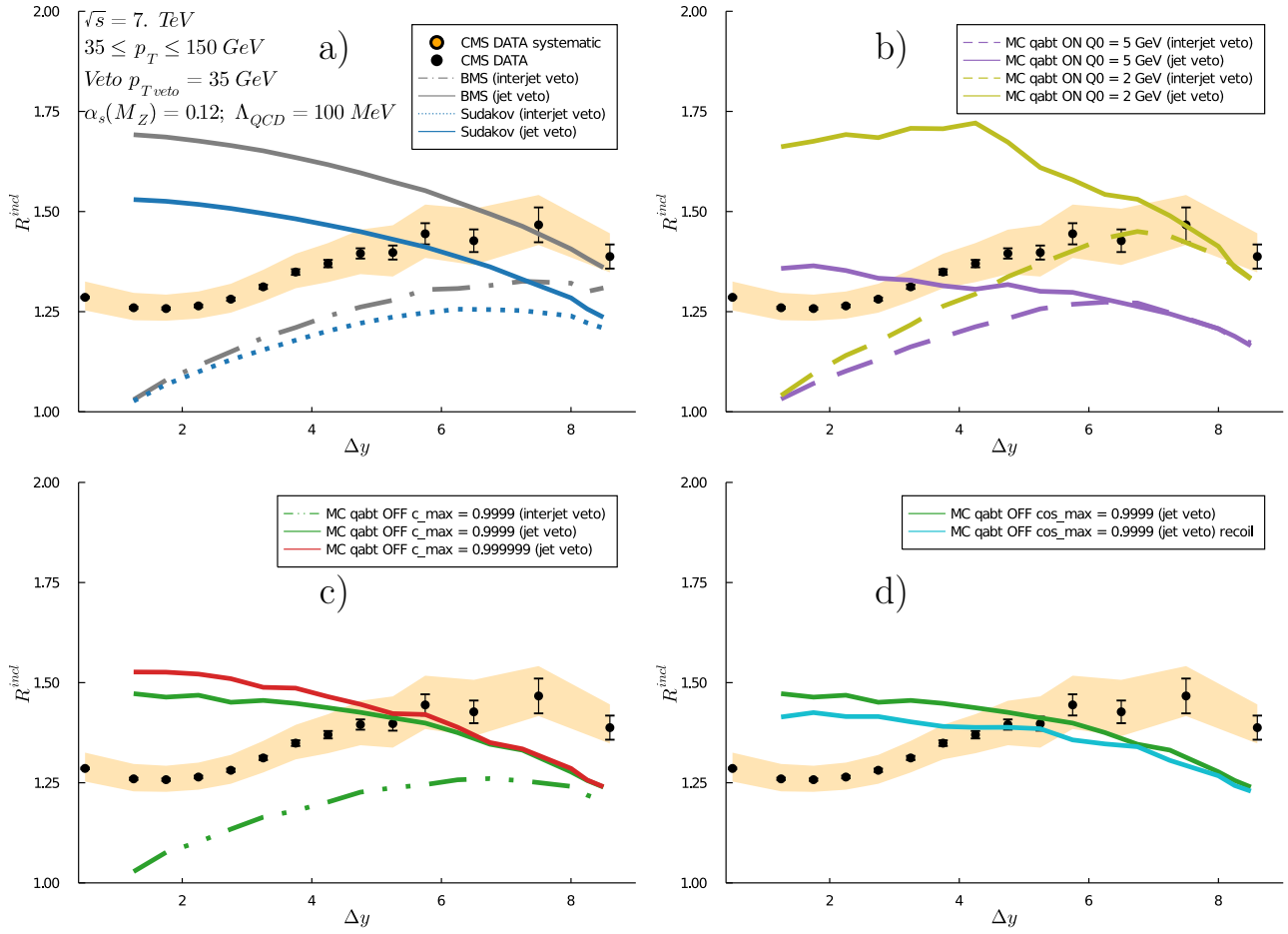


Figure 5.3 — Comparison of the results of $R^{\text{incl}}$ calculations based on the evolution of the BMS [A4; 130] with the results of the CMS measurements at $\sqrt{s} = 7$ TeV [37]. The experimental results are represented by black dots. The vertical lines are statistical measurement uncertainties, and the yellow band is the systematic uncertainty. Colored lines are the calculation results.

Fig. 5.3b shows the results of calculations for the MC algorithm taking into account the scale transverse to the radiating dipole, $q_{\alpha\beta\perp}$, that is, for the Sudakov form factor calculated by the formula (5.26). Calculations are presented for different choices of $Q_0$. «MC qabt ON Q0 = 5 GeV» the calculation was performed for $Q_0 = 5$ GeV in two versions: «interjet veto» and «jet veto». Similarly for $Q_0 = 2$ GeV «MC qabt ON Q0 = 2 GeV». Fig. 5.3b demonstrates a strong dependence on the choice of scale $Q_0$, which is explained by the appearance of an additional correlation between the angular distribution and radiation hardness. At lower $Q_0$, harder gluons are emitted, violating the veto. Qualitatively, the predictions coincide with the predictions for the simplified model of the jet veto and the numerical solution of the BMS equation in Fig. 5.3a.

Fig. 5.3c shows the calculation results for the MC algorithm without introducing the $q_{\alpha\beta\perp}$ scale, that is, for the Sudakov form factor (5.29). The calculation was performed for two parameter values $c_{\max} = 0.9999$ «MC qabt OFF c_max = 0.9999» and 0.999999 «MC qabt OFF c_max = 0.999999» for jet veto «jet veto». The calculation for the inter-jet veto «interjet veto» was performed only for $c_{\max} = 0.9999$. As can be seen from Fig. 5.3c there is no strong dependence on the choice of the value of the parameter $c_{\max}$. Qualitatively, the predictions coincide with those presented in figures 5.3a and 5.3b. Quantitatively, the results of the «MC qabt OFF» calculation are closer to the calculation taking into account only the Sudakov form factor in the BMS evolution in Fig. 5.3a.

Fig. 5.3d shows a comparison of the calculation «MC qabt OFF c_max = 0.9999 (jet veto)» with the same calculation, but taking into account the law of energy-momentum conservation «MC qabt OFF c_max = 0.9999 (jet veto) recoil», implemented using the simple model described in the previous paragraph. As you can see, taking into account the conservation law leads to a decrease in the jet veto impact in the region of small $\Delta y$, showing the correct trend. A more complete account of the law of energy-momentum conservation may lead to better agreement with the experimental results.

The considered methods for taking into account the jet veto based on the BMS evolution are in poor agreement with measurements of the $R^{\text{incl}}$ region of small $\Delta y$. However, the obtained solutions of the BMS equation can be used to calculate the $R^{\text{MN}}$ and $R^{\text{MN}}_{\text{veto}}$ ratios of the cross sections for the production of the pairs of the hadronic MN jets with veto. The MN dijet is the pair most separated by $\Delta y$ in an event among jets with $p_\perp > p_{\perp\min}$, therefore the inter-jet veto will make the main contribution to the ratio of cross sections with veto.

Note also that in the presented calculations the Born QCD approximation was used to calculate the parton subprocess in the inclusive cross section. As we saw in the previous chapter, the Born subprocess does not take into account contributions that are important at large $\Delta y$, and poorly describes the absolute values of the cross sections (see Fig. 4.1). In the cross section ratios, many important contributions cancel out. This explains the relative agreement of calculations based on the Born subprocess with experimentally measured cross section ratios. Thanks to the measurement of the absolute values of the cross sections for dijet production with a large rapidity separation, carried out in the works [A1; A3; 108; 110] and presented in Chapter 3, it became possible to better test phenomenological models.

In subsequent sections, numerical solutions of the BMS equation will be applied to take into account the inter-jet veto in $R^{\rm MN}$ and $R^{\rm MN}_{\rm veto}$. The calculation of the parton-parton cross sections for the MN dijet production will be performed in the NLL BFKL approximation.

## 5.8 Calculation of the impact of the veto on the jets additional to a MN dijet within the NLL BFKL+BMS approximation

As we saw from the comparison results presented at the end of Chapter 4, the $\Delta y$-differential cross section for the MN dijet production, $d\sigma^{\rm MN}/d\Delta y$, calculated taking into account the NLL BFKL using the procedure of BFKLP for selecting the optimal ultraviolet renormalization scale is consistent with the experimental results performed in the CMS experiment in $pp$ collisions at $\sqrt{s} = 2.76$ TeV. At the same time, the results of calculations based on the Born subprocess greatly overestimate the experimental results. Thus, the Born subprocess does not take into account all QCD contributions that are important for large $\Delta y$.

In this section we will briefly describe how the BMS approach presented above can be applied in the case of the parton-parton cross section calculated in the BFKL approximation. We will also consider a modification of the method that eliminates double counting of gluon radiation when exchanging a color octet.

To begin with, we note that in calculations based on the BFKL evolution, the approximation of large $\Delta y$ ($|\hat{t}| \ll \hat{s}$ and $|\hat{u}| \sim \hat{s}$) is used. In this approximation, all parton-parton cross sections become proportional to each other up to color factors. This circumstance, on the one hand, makes it possible to perform calculations based on the gluon-gluon scattering cross section and the effective PDF (1.8). On the other hand, this allows us to separate the BMS probabilities $P_{ij}$ from the parton-parton cross sections (5.9-5.17), and average them over the effective PDFs, obtaining the

effective BMS probability:

$$
\begin{aligned}
P^{\text{eff}} = & \frac{1}{f^{\text{eff}}(x_1) f^{\text{eff}}(x_2)} \\
& \times \Bigg[ \left( \frac{C_A}{C_F} \right)^2 f_g(x_1) f_g(x_2) P_{gg} \\
& + \frac{C_A}{C_F} \left( f_g(x_1) \sum_{i=q,\bar{q}} f_i(x_2) + f_g(x_2) \sum_{i=q,\bar{q}} f_i(x_1) \right) P_{gq} \\
& + \left( \sum_{\substack{i=q \\ j=q}} f_i(x_1) f_j(x_2) + \sum_{\substack{i=\bar{q} \\ j=\bar{q}}} f_i(x_1) f_j(x_2) \right) P_{qq} \\
& + \left( \sum_{\substack{i=q \\ j=\bar{q}}} f_i(x_1) f_j(x_2) + \sum_{\substack{i=\bar{q} \\ j=q}} f_i(x_1) f_j(x_2) \right) P_{q\bar{q}} \Bigg],
\end{aligned}
\tag{5.30}
$$

where $P_{gg}$, $P_{gq}$, $P_{qq}$ и $P_{q\bar{q}}$ are defined as:

$$
\begin{aligned}
P_{gg} &= \frac{1}{2} \big( P_{12} P_{13} P_{24} P_{34} + P_{14} P_{24} P_{13} P_{23} \big), \\
P_{gq} &= \frac{1}{2} \big( P_{24} P_{12} P_{34} + P_{24} P_{14} P_{23} \big), \\
P_{qq} &= P_{14} P_{23}, \\
P_{q\bar{q}} &= P_{12} P_{34},
\end{aligned}
\tag{5.31}
$$

where the BMS probabilities $P_{ij}$ are defined in section 5.3.

The effective BMS probability, $P^{\text{eff}}$, calculated this way can be used as an additional factor in (4.48) and (4.50) to obtain a veto cross sections. Further, $R^{\text{MN}}$ and $R^{\text{MN}}_{\text{veto}}$ can be calculated as the ratio of the cross section calculated using the formulas (4.48) and (4.50) to the veto cross section calculated using the same formulas, but with an additional factor, which takes into account the BMS probability $P^{\text{eff}}$.

It is worth noting that the dominant process during the MN dijet production with large $\Delta y$ is the exchange of the color octet in the $t$ channel. The color octet in the approximation of large number of colors, $N_c \to \infty$, is represented by two color flows (dipoles), described in paragraph 5.3. In the large $\Delta y$ approximation, two dipoles are stretched across the rapidity interval between the MN jets. In this case, violation of the veto condition occurs mainly due to radiation from these dipoles. It is also worth noting that each end of the dipole is in the color triplet or antitriplet state. That is, if there is a triplet at one end of the dipole, then at the other there

is a corresponding antitriplet (the ends of the dipole are in a singlet state in color). Color counting shows that each dipole should emit gluons proportionally to $\alpha_s C_F$. Then the two dipoles together will emit as the color octet, that is, in proportion to $\alpha_s C_A \simeq 2\alpha_s C_F$ (to within the suppressed $1/N_c$ terms). The emission of a gluon leads to the splitting of the dipole into two daughter dipoles. The ends of each daughter dipole are again in a singlet (triplet-antitriplet) color state. Therefore, each daughter dipole again emits gluons proportionally to $\alpha_s C_F$. Thus, gluon emission is proportional to $\alpha_s C_F$ throughout the entire BMS evolution. If we allow each dipole to emit in proportion to $\alpha_s C_A$, then the gluon emission will be counted twice

At the same time, in the original BMS equation it is assumed that the radiation is proportional to $\alpha_s C_A$ as follows from the equation (5.4). That is, the radiating dipole is assumed to be an octet-antioctet state. If we want to use the procedure for accounting for the veto condition based on the BMS equation described in paragraph 5.3 and the beginning of this section, then it is necessary to replace $C_A$ with $C_F$ in the definition of the evolution variable, $\tau$, in equation (5.4) to avoid double counting. Let us denote the evolution variable, $\tau$, calculated with the equation (5.4) as $\tau_A$, and with $C_A$ replaced by $C_F$, as $\tau_F$. Results for both calculation options will be provided at the end of this chapter.

## 5.9 Numerical calculations and theoretical uncertainty of the MN cross sections with inter-jet veto, and the ratios of cross sections $R^{\rm MN}$ and $R^{\rm MN}_{\rm veto}$ in the NLL BFKL+BMS approximation

The calculation of the MN cross section $d\sigma^{\rm MN}/d\Delta y$ is described in chapter 4. The MN cross section with inter-jet veto, $d\sigma^{\rm MN}_{\rm inter-jet\ veto}/d\Delta y$, is calculated using the same formulas, but with an additional factor taking into account the effective BMS probability, formula (5.30). Taking into account that at large $\Delta y$ the main contribution to the veto is provided by the inter-jet veto, we will assume that $d\sigma^{\rm excl}/d\Delta y \approx d\sigma^{\rm MN}_{\rm inter-jet\ veto}/d\Delta y$ at $p_{\perp \rm veto} = 35$ GeV and $d\sigma^{\rm excl}_{\rm veto}/d\Delta y \approx d\sigma^{\rm MN}_{\rm inter-jet\ veto}/d\Delta y$ at $p_{\perp \rm veto} = 20$ GeV

The ratios of cross sections with veto $R^{\rm MN}$ and $R^{\rm MN}_{\rm veto}$ were calculated as the ratios of $d\sigma^{\rm MN}/d\Delta y$ to $d\sigma^{\rm MN}_{\rm inter-jet\ veto}/d\Delta y$ for $p_{\perp \rm veto} = 35$ and 20 GeV accordingly. The ratio $R^{\rm MN}$ was calculated for $pp$ collisions at $\sqrt{s} = 2.76$, 7 and 13 TeV, and

$R^{\mathrm{MN}}_{\mathrm{veto}}$ at 2.76 and 13 TeV. The calculation of the ratios was performed for the BMS evolution with both $\tau_A$ and $\tau_F$. Theoretical uncertainty is estimated only for calculations with $\tau_F$.

Selected values $p_{\perp\min} = 35$ GeV, $|y| < 4.7$ and $p_{\perp\mathrm{veto}} = 35$ and 20 GeV, correspond to the experimental selections in the CMS measurements at $\sqrt{s} = 2.76$ and 7 TeV [37; A1; A3; 108; 110]. In the calculations, the size of hadronic jets is chosen to be 0.5 for $\sqrt{s} = 2.76$ and 7 TeV and 0.4 for 13 TeV. Number of open flavors $n_f = 5$. The strong coupling constant $\alpha_s$ and the PDFs are provided with the NLO in the LHAPDF [106] library in the MSTW2008nlo68cl [124] set.

The calculation of the theoretical uncertainty for $d\sigma^{\mathrm{MN}}/d\Delta y$ is described in paragraph 4.2. When calculating cross sections with veto, the uncertainty in the choice of the scale of the radiating dipole in the BMS equation is additionally taken into account. The latter uncertainty is estimated by varying the upper limit in equation (5.4). To calculate the central value, this scale is chosen as the geometric mean of the absolute values of the transverse momenta of the MN jets, $\sqrt{|\vec{k}_1||\vec{k}_2|}$. This scale was varied from $\min(|\vec{k}_1|, |\vec{k}_2|)$ to $\max(|\vec{k}_1|, |\vec{k}_2|)$ to estimate the theoretical uncertainty of the BMS scale. This uncertainty makes the maximum contribution to the $R^{\mathrm{MN}}$ and $R^{\mathrm{MN}}_{\mathrm{veto}}$ ratios, since there is no cancellation between the numerator and the denominator.

The total theoretical uncertainty is calculated as the root of the sum of squared uncertainties from the sources.

## 5.10 Calculation of ratios of cross sections with veto in the LL GLAPD approximation

For clearer conclusions about the manifestation of the effects of the BFKL evolution, it is useful to have predictions based on the «pure» GLAPD evolution, without taking into account color coherence. Such predictions can be obtained analytically in the LL approximation. As before, the convolution of the Born subprocess with the PDFs according to the formula (4.1) will be used to calculate the inclusive cross section for dijet production. To take into account the veto, the

Sudakov factors can be used:

$$T_a(p_\perp, p_{\perp\text{veto}}) = \exp\left\{ -\int_{p_{\perp\text{veto}}}^{p_\perp} \frac{dk^2}{k^2} \sum_{a'} \int_0^{1-\Delta} dz z P_{a'a}(z) \right\}, \tag{5.32}$$

where $a$, $a'$ — quark $q$ or gluon $g$;
$\Delta = \frac{k}{p_\perp}$ — this definition corresponds to strict $p_\perp$-ordering;
$P_{a'a}(z)$ — the GLAPD splitting functions.

It is convenient in calculations instead of $\Delta = \frac{k}{p_\perp}$ to use $\tilde{\Delta} = \frac{p_{\perp\text{veto}}}{p_\perp}$, then Sudakov factors (5.32) can be calculated analytically [131]:

$$T_q(\tilde{\Delta}) = \exp\left\{ -\frac{4C_F}{\beta_0}\left( \ln\left(\frac{1}{\tilde{\Delta}}\right) - \frac{3}{4}(1-\tilde{\Delta})^2 \right) \ln\left( \frac{\alpha_s({p_{\perp\text{veto}}}^2)}{\alpha_s({p_\perp}^2)} \right) \right\}, \tag{5.33}$$

$$T_g(\tilde{\Delta}) = \exp\left\{ -\frac{4C_A}{\beta_0}\left( \ln\left(\frac{1}{\tilde{\Delta}}\right) - \left(1 - \frac{n_f}{4C_A}\right)(1-\tilde{\Delta})^2 + \frac{1-n_f/C_A}{12}(1-\tilde{\Delta})^3(1+3\tilde{\Delta}) \right) \ln\left( \frac{\alpha_s({p_{\perp\text{veto}}}^2)}{\alpha_s({p_\perp}^2)} \right) \right\}, \tag{5.34}$$

Using $\tilde{\Delta}$ instead of $\Delta$ in the equation (5.32) slightly expands the integration interval over $z$. Consequently, this leads to a decrease of the Sudakov factor, that is, to an increase of the impact of the veto condition, and to an increase of the ratio of cross sections with the veto in the denominator. However, as we will see from comparison of the calculation results with the experimental results and with the results of other calculations, even with this gain, the calculation results obtained using $\tilde{\Delta}$ predicts the smallest values of the ratios with veto $R^{\text{MN}}$ and $R^{\text{MN}}_{\text{veto}}$ at large $\Delta y$. Thus, calculations based on the Sudakov factors (5.33) and (5.34) will be sufficient to draw conclusions about the behavior of the LL GLAPD predictions without taking into account color coherence at large $\Delta y$.

In the case of initial state radiation (ISR), the Sudakov factors are corrected by the PDF ratio:

$$T_a^{\text{ISR}}(p_\perp, p_{\perp\text{veto}}) = T_a(p_\perp, p_{\perp\text{veto}}) \frac{f_a(x, p_{\perp\text{veto}})}{f_a(x, p_\perp)}, \tag{5.35}$$

The case when $T_a^{\text{ISR}} > 1$ is interpreted as the absence of radiation violating the veto condition, $T_a^{\text{ISR}} = 1$.

Calculation based on the LL GLAPD approximation without color coherence will be presented taking into account two sources of theoretical uncertainty:

1. Uncertainty in the choice of renormalization and factorization scales. The central value for the scales is chosen to be $p_\perp$ in the hard subprocess. The scales are varied independently by multiplying by the factors 2 and 0.5. The resulting theoretical uncertainty is the envelope of the resulting variations.
2. Uncertainty of the PDFs. The calculation is performed using the PDF set NNPDF31_lo_as_0130 [132]. The uncertainty of the PDFs of this set was used to determine the theoretical uncertainty of the calculation.

The total theoretical uncertainty of the calculation is the square root of the sum of the squares of the uncertainties from individual sources.

## 5.11 Results of calculation of the MN cross sections with inter-jet veto, and cross section ratios $R^{\mathrm{MN}}$ and $R^{\mathrm{MN}}_{\mathrm{veto}}$ in the NLL BFKL+BMS approximation, comparison with the experimental results of the CMS experiment and discussion

The experimental results for the cross sections $d\sigma^{\mathrm{excl}}/d\Delta y$ and $d\sigma^{\mathrm{excl}}_{\mathrm{veto}}/d\Delta y$ are not presented in the work [A1; 108]. However, their values can be estimated for $pp$ collisions at $\sqrt{s} = 2.76$ TeV based on the results presented by the CMS collaboration in [A1; 108]:

$$\frac{d\sigma^{\mathrm{excl}}}{d\Delta y} = \frac{1}{R^{\mathrm{MN}}}\frac{d\sigma^{\mathrm{MN}}}{d\Delta y} \tag{5.36}$$

$$\frac{d\sigma^{\mathrm{excl}}_{\mathrm{veto}}}{d\Delta y} = \frac{1}{R^{\mathrm{MN}}_{\mathrm{veto}}}\frac{d\sigma^{\mathrm{MN}}}{d\Delta y} \tag{5.37}$$

The experimental uncertainty of the veto cross sections obtained this way can be considered approximately equal to the measured uncertainty of the MN cross section $d\sigma^{\mathrm{MN}}/d\Delta y$. This level of accuracy is sufficient for comparison. The comparison of the calculation results with the results of the CMS measurements in $pp$ collisions at $\sqrt{s} = 2.76$ TeV is presented in Figure 5.4 for $d\sigma^{\mathrm{excl}}/d\Delta y$ and in Figure 5.5 for $d\sigma^{\mathrm{excl}}_{\mathrm{veto}}/d\Delta y$. Predictions of MC calculations in the LO+LL GLAPD, obtained using the generator PYTHIA8 [41], are also presented in Figs. 5.4 and 5.5 for two tunes: 4C [72] and CP5 [73]. The figure shows the results of analytical calculations based on the LO+LL GLAPD without color coherence («GLAPD»), described in the previous paragraph. Also in Figs. 5.4 and 5.5 calculations based

on the Born subprocess, the approximation of large $\Delta y$ and BMS evolution «large $\Delta y$ Born + BMS» and on the NLL BFKL + BMS approach «NLL BFKL + BMS» are presented. Calculations using the BMS equation to account for the veto are presented in two versions: for the evolutionary variable $\tau_A$ and $\tau_F$.

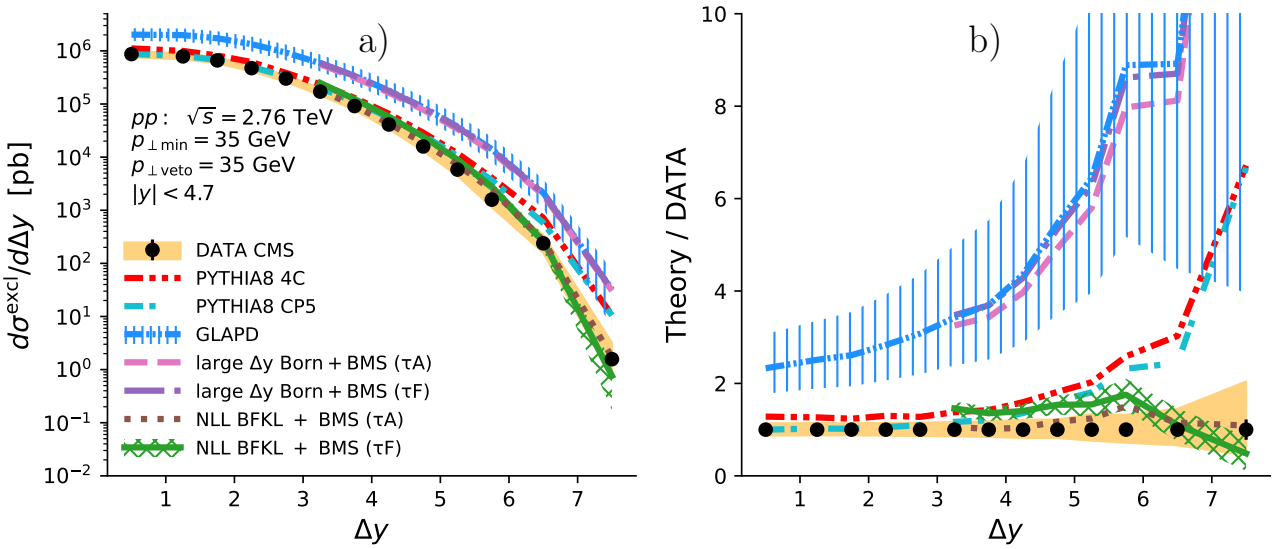


Figure 5.4 — Comparison of the results of calculation of the «exclusive» cross section, $d\sigma^{\mathrm{excl}}/d\Delta y$, based on the NLL BFKL+BMS approximation, with the results of the CMS measurements in $pp$ collisions at $\sqrt{s} = 2.76$ TeV [A1; A3; 108; 110]. a) «exclusive» cross section $d\sigma^{\mathrm{excl}}/d\Delta y$; b) the ratio of the calculation results to the experimental results. The experimental results are represented by black dots. Vertical lines are the statistical uncertainties of the experimental results. Yellow band is the systematic uncertainty of the experimental results. Colored lines are the calculation results. The band shaded with vertical blue lines is the theoretical uncertainty of the LO+LL GLAPD calculation without color coherence. The band shaded with a green grid is the theoretical uncertainty of the NLL BFKL+BMS calculation with $\tau_F$.

As can be seen from the comparison presented in Figs. 5.4 and 5.5, taking into account the NLL BFKL corrections in the parton subprocess significantly improves the agreement between the results of the cross section calculations and the results of the CMS measurements at large $\Delta y$. Both versions of the NLL BFKL+BMS calculation with $\tau_A$ and $\tau_F$ are consistent with measurements within the limits of theoretical and experimental uncertainty. It can be seen that the absolute values of the cross sections are more sensitive to the correct calculation of the parton subprocess, rather than to the calculation of the impact of the veto condition

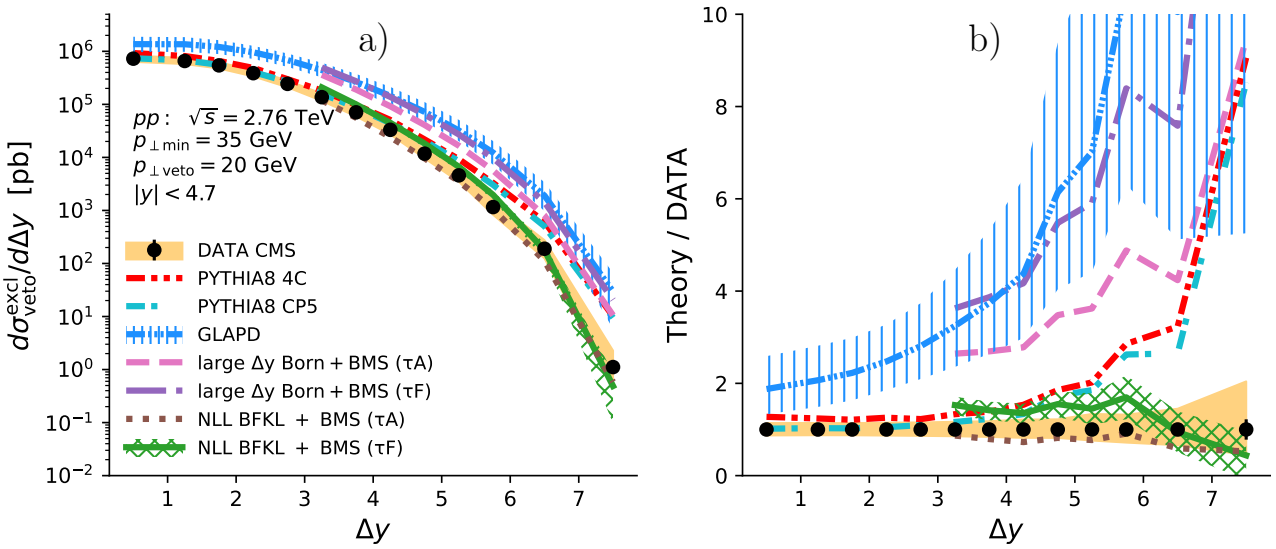


Figure 5.5 — Comparison of the results of calculation of the «exclusive» with veto cross section, $d\sigma^{\mathrm{excl}}_{\mathrm{veto}}/d\Delta y$, based on the NLL BFKL+BMS approximation, with the results of the CMS measurements in $pp$ collisions at $\sqrt{s} = 2.76$ TeV [A1; A3; 108; 110]. a) «exclusive» with veto cross section $d\sigma^{\mathrm{excl}}_{\mathrm{veto}}/d\Delta y$; b) the ratio of the calculation results to the experimental results. The experimental results are represented by black dots. Vertical lines are the statistical uncertainties of the experimental results. Yellow band is the systematic uncertainty of the experimental results. Colored lines are the calculation results. The band shaded with vertical blue lines is the theoretical uncertainty of the LO+LL GLAPD calculation without color coherence. The band shaded with a green grid is the theoretical uncertainty of the NLL BFKL+BMS calculation with $\tau_F$.

The results of comparison of the calculations of $R^{\mathrm{MN}}$ and $R^{\mathrm{MN}}_{\mathrm{veto}}$ with the results of the CMS measurements in $pp$ collisions at $\sqrt{s} = 2.76$ TeV [A1; A3; 108; 110] are presented in Fig. 5.6. It can be seen that the calculation based on the LO+LL GLAPD without taking into account color coherence («GLAPD») predicts a decrease of the ratios with increasing $\Delta y$. At large $\Delta y$ the GLAPD calculation without taking into account color coherence predicts the smallest values of the ratios $R^{\mathrm{MN}}$ and $R^{\mathrm{MN}}_{\mathrm{veto}}$. The inclusion of the corrections for color coherence in models based on the GLAPD $p_\perp$-ordered parton cascade (PYTHIA8 and BMS) leads to an increase of $R^{\mathrm{MN}}$ and $R^{\mathrm{MN}}_{\mathrm{veto}}$ ratios with increasing $\Delta y$. As can be seen from Fig. 5.6b, the calculation version using the variable $\tau_A$ in the BMS of evolution significantly overestimates the impact of the veto, confirming our assumption of double counting of radiation and the need to replace $C_A$ with $C_F$ . The difference

between the calculation based on the BMS for the Born subprocess and for the subprocess in NLL BFKL accuracy is noticeable, although not as strong as for the absolute values of the cross sections. This suggests that these observables are more sensitive to corrections accounting for the impact of the veto condition rather than to the parton subprocess. As can be seen from Fig. 5.6a, the BMS evolution predicts insufficient radiation when $p_{\perp\text{min}} = p_{\perp\text{veto}}$, that is, when there is no phase space for the development of a parton cascade ordered in $p_\perp$. The inclusion of the NLL BFKL corrections increases the values of the ratios, improving the agreement with the experimental results compared to calculations with the Born subprocess. All the above indicates the need to develop method for accounting for jet veto based on the NLL BFKL approximation due to its $p_\perp$-diffusion.

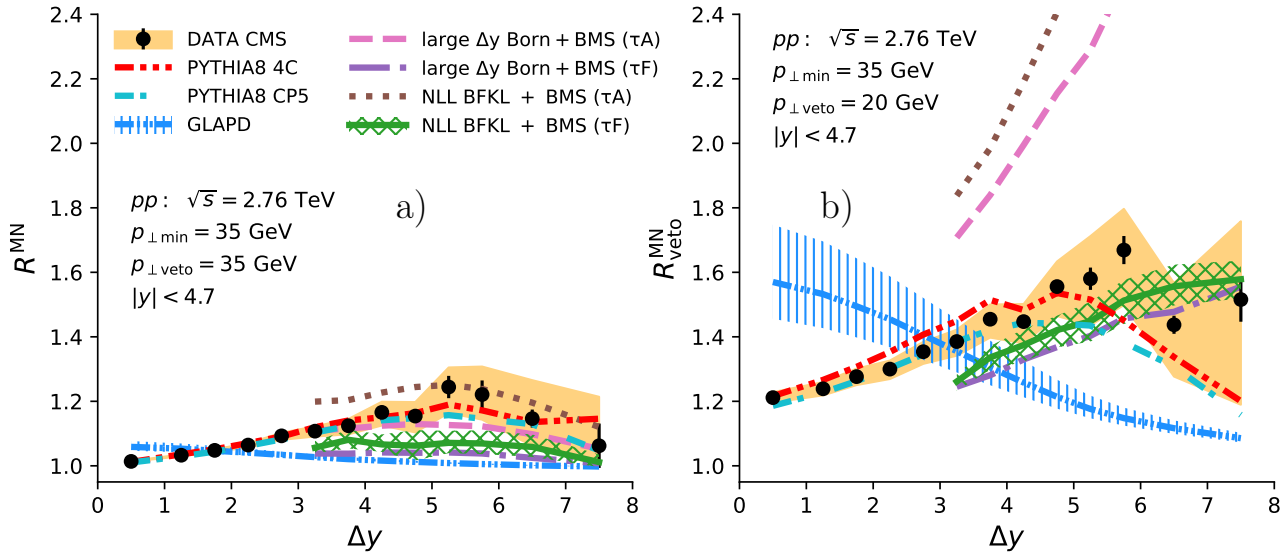


Figure 5.6 — Comparison of the results of the calculations of $R^{\text{MN}}$ and $R^{\text{MN}}_{\text{veto}}$ based on the NLL BFKL+BMS approximation with the results of the CMS measurements in $pp$ collisions at $\sqrt{s} = 2.76$ TeV [A1; A3; 108; 110]. a) $R^{\text{MN}}$; b) $R^{\text{MN}}_{\text{veto}}$. The experimental results are represented by black dots. Vertical lines are the statistical uncertainties of the experimental results. Yellow band is the systematic uncertainty of the experimental results. Colored lines are the calculation results. The band shaded with vertical blue lines is the theoretical uncertainty of the LO+LL GLAPD calculation without color coherence. The band shaded with a green grid is the theoretical uncertainty of the NLL BFKL+BMS calculation with $\tau_F$.

MC calculations with the LO+LL GLAPD generator PYTHIA8 are consistent with $R^{\text{MN}}$ measurements at $\sqrt{s} = 2.76$ TeV Fig. 5.6a, despite the fact that its parton shower is also ordered in $p_\perp$. This may be due to the fact that color coherence is

implemented in PYTHIA8 in a manner different from the evolution of the BMS. As we saw in Chapter 3, the PYTHIA8 and HERWIG++ models using color coherence also give very different predictions at large $\Delta y$. These observations demonstrate a strong dependence on the implementation of color coherence models and suggest that color coherence models do not take into account all important contributions at large $\Delta y$. This also indicates the need to develop method for calculating the impact of the veto condition, based on the BFKL evolution, as a formalism that consistently takes into account the main contributions at large $\Delta y$.

A comparison of the results of calculation of $R^{\mathrm{MN}}$ with the CMS experimental results in $pp$ collisions at $\sqrt{s} = 7$ TeV [37] is presented in Figure 5.7. The calculation based on the LO+LL GLAPD without taking into account color coherence predicts the smallest value of $R^{\mathrm{MN}}$ for large $\Delta y$. All calculations using the BMS evolution underestimate the growth of the ratio at large $\Delta y$. Comparing the ratio $R^{\mathrm{MN}}$ at energies $\sqrt{s} = 2.76$ and 7 TeV, presented in Figs. 5.6a and 5.7, it is clear that the BMS evolution has weaker $\sqrt{s}$ dependence than observed in the data. This is not surprising, since $\sqrt{s}$ is not explicitly included in the BMS equation (5.3). The implicit dependence on $\sqrt{s}$ appears in calculations based on the BMS evolution only due to changes in the slopes of the $p_\perp$ spectra with increasing of $\sqrt{s}$. The BFKL-based veto accounting method, when developed, will also take into account the dependence on $\sqrt{s}$. The MC calculation in the LO+LL GLAPD PYTHIA8 better reproduces the $\sqrt{s}$ dependence of the $R^{\mathrm{MN}}$ ratio, although it underestimates it at the maximum $\Delta y$ at $\sqrt{s} = 7$ TeV.

Predictions for $R^{\mathrm{MN}}$ and $R^{\mathrm{MN}}_{\mathrm{veto}}$ in $pp$ collisions at $\sqrt{s} = 13$ TeV are presented in Figure 5.8. The calculation based on the LO+LL GLAPD without taking into account color coherence predicts the smallest values of the $R^{\mathrm{MN}}$ and $R^{\mathrm{MN}}_{\mathrm{veto}}$ ratios for large $\Delta y$. As can be seen from Figure 5.8b, the NLL BFKL+BMS ($\tau_A$) calculation predicts the greatest increase in $R^{\mathrm{MN}}_{\mathrm{veto}}$ with $\Delta y$. At the same time, the calculation based on the BMS evolution with $\tau_F$ demonstrates the weakest dependence on $\Delta y$ and $\sqrt{s}$ among models using color coherence. Figure 5.8a shows that calculations based on the BMS evolution predict smaller values of $R^{\mathrm{MN}}$ than PYTHIA8. These trends have already been observed at lower energies $\sqrt{s} = 2.76$ TeV (see Fig. 5.6) and $\sqrt{s} = 7$ TeV (see Fig. 5.7). Measurements at the LHC will help establish the correct $\sqrt{s}$ and $\Delta y$ behavior.

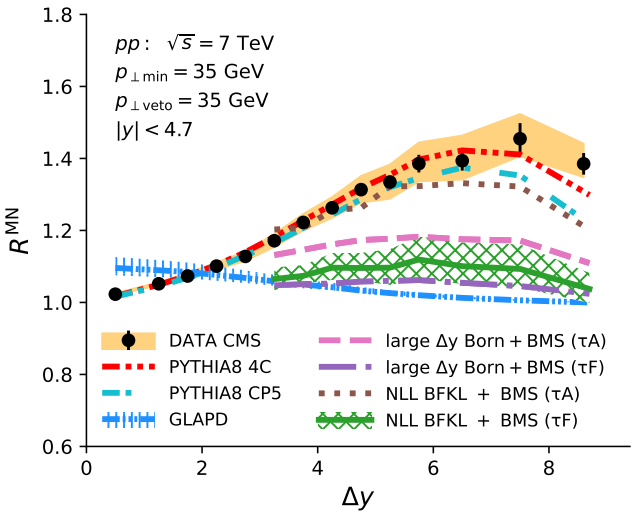


Figure 5.7 — Comparison of the results of calculations of $R^{\mathrm{MN}}$ based on the NLL BFKL+BMS approximation with the results of the CMS measurements in $pp$ collisions at $\sqrt{s} = 7$ TeV [37]. The experimental results are represented by black dots. Vertical lines are the statistical uncertainties of the experimental results. Yellow band is the systematic uncertainty of the experimental results. Colored lines are the calculation results. The band shaded with vertical blue lines is the theoretical uncertainty of the LO+LL GLAPD calculation without color coherence. The band shaded with a green grid is the theoretical uncertainty of the NLL BFKL+BMS calculation with $\tau_F$.

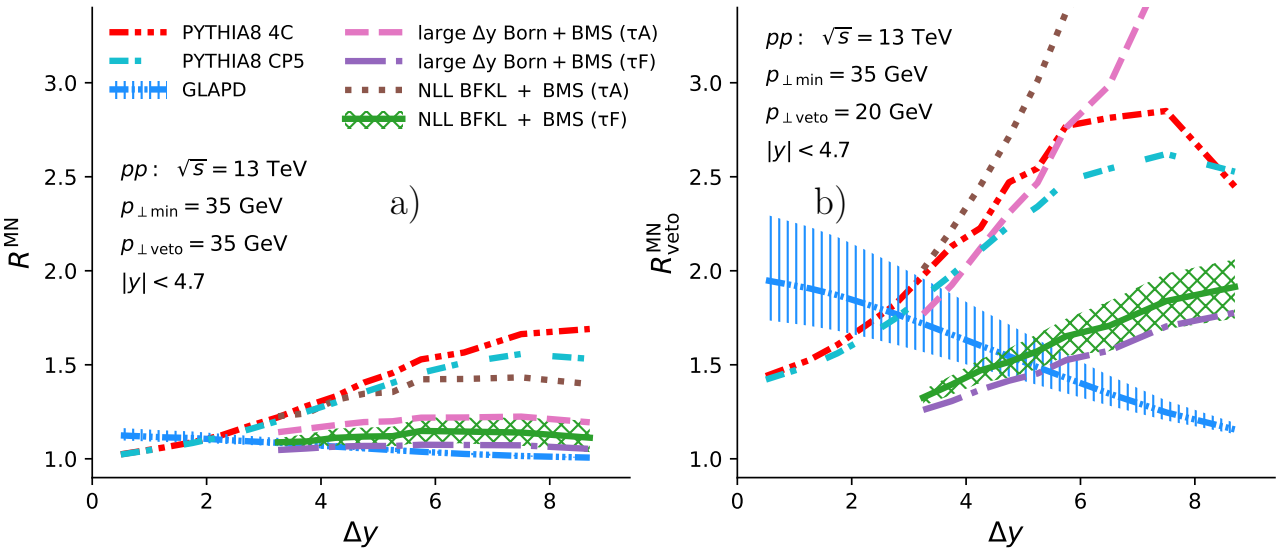


Figure 5.8 — Predictions $R^{\mathrm{MN}}$ and $R^{\mathrm{MN}}_{\mathrm{veto}}$ based on the NLL BFKL+BMS in $pp$ collisions at $\sqrt{s} = 13$ TeV. a) $R^{\mathrm{MN}}$; b) $R^{\mathrm{MN}}_{\mathrm{veto}}$. Colored lines are the calculation results. The band shaded with vertical blue lines is the theoretical uncertainty of the LO+LL GLAPD calculation without color coherence. The band shaded with a green grid is the theoretical uncertainty of the NLL BFKL+BMS calculation with $\tau_F$.

## Conclusions

The main **results** of the work are as follows:

1. A technique has been developed for measuring $\Delta y$-differential cross sections for the production of the Mueller-Navelet (MN) dijets, $d\sigma^{\mathrm{MN}}/d\Delta y$, and the inclusive dijets, $d\sigma^{\mathrm{incl}}/d\Delta y$, as well as the ratios of cross sections with veto $R^{\mathrm{MN}}_{\mathrm{veto}}$ and $R^{\mathrm{incl}}_{\mathrm{veto}}$ as functions of $\Delta y$. The technique for measuring the ratios of cross sections $R^{\mathrm{MN}}$ and $R^{\mathrm{incl}}$ as functions of $\Delta y$ has been modified. The developed and modified techniques comply with the new measurement standards of Run II cycle of the LHC operation, and include the study of an extended set of systematic effects, as well as the use of the new methods in the analysis of detector distortions.
2. $R^{\mathrm{MN}}$, $R^{\mathrm{incl}}$ were measured for the first time in $pp$ collisions at $\sqrt{s} = 2.76$ TeV, and a comparison was made with the measurements performed earlier, at $\sqrt{s} = 7$ TeV, as well as with predictions of MC models based on the LO+LL GLAPD: PYTHIA8, HERWIG++; NLO+LL GLAPD: POWHEG+PYTHIA8, POWHEG+HERWIG++, POWHEG+HERWIG7; and LL BFKL: HEJ+ARIADNE.
3. $d\sigma^{\mathrm{MN}}/d\Delta y$, $d\sigma^{\mathrm{incl}}/d\Delta y$, $R^{\mathrm{MN}}_{\mathrm{veto}}$ and $R^{\mathrm{incl}}_{\mathrm{veto}}$ were measured for the first time in $pp$ collisions at $\sqrt{s} = 2.76$ TeV and compared with predictions of MC models based on the LO+LL GLAPD: PYTHIA8, HERWIG++; NLO+LL GLAPD: POWHEG+PYTHIA8, POWHEG+HERWIG++, POWHEG+HERWIG7; and LL BFKL: HEJ+ARIADNE.
4. For the first time, a comparison has been made of the NLL BFKL calculation for the differential cross section $d\sigma^{\mathrm{MN}}/d\Delta y$ of the MN dijet production with the experimental CMS data. New indications of the manifestation of the effects of the BFKL evolution in $pp$ collisions at $\sqrt{s} = 2.76$ TeV have been obtained. Predictions for $pp$ collisions at $\sqrt{s} = 8$ and 13 TeV are presented.
5. The sensitivity to the BFKL evolution signals is shown for the ratios of differential cross sections for the MN dijet production at different $\sqrt{s}$: $R^{\mathrm{MN}}_{13/2.76}$, $R^{\mathrm{MN}}_{8/2.76}$, $R^{\mathrm{MN}}_{13/8}$. These ratios can be measured experimentally and calculated taking into account the NLL BFKL corrections.

6. For the first time, a method is presented for calculating the inclusive cross sections for dijet production with veto to additional jets with $p_\perp > p_{\perp\text{veto}}$ in the entire rapidity interval based on the solution of the BMS equation and a comparison is made with the experimental CMS data for $pp$ collisions at $\sqrt{s} = 7$ TeV.
7. For the first time, a method is presented for calculating the MN cross sections for the production of pairs of hadronic jets with the veto on additional jets with $p_\perp > p_{\perp\text{veto}}$ between the MN jets based on the NLL BFKL evolution and the BMS equation. A comparison is made with the experimental CMS data for $pp$ collisions at $\sqrt{s} = 2.76$ and 7 TeV and predictions are presented for $pp$ collisions at $\sqrt{s} = 13$ TeV.

Based on the results of the work, the following **conclusions** were drawn:

1. The measured $\Delta y$-differential cross sections $d\sigma^{\text{incl}}/d\Delta y$ and $d\sigma^{\text{MN}}/d\Delta y$ decrease rapidly with increasing of the rapidity interval $\Delta y$. The drop is stronger than predicted by the considered MC generators based on the GLAPD and BFKL approximations. The introduction of perturbation theory NLO corrections into the calculation based on the LL GLAPD evolution improves agreement with measurements only in the region of small $\Delta y < 4$. The analytical NLL BFKL calculation agrees at large $\Delta y$ within theoretical and experimental uncertainties with the measurements of $d\sigma^{\text{MN}}/d\Delta y$ in $pp$ collisions at $\sqrt{s} = 2.76$ TeV, $p_{\perp\text{min}} = 35$ GeV and $|y| < 4.7$. These observations indicate the manifestation of the BFKL effects in $pp$ collisions at the studied energy, $\sqrt{s} = 2.76$ TeV.
2. The ratios of cross sections with veto $R^{\text{incl}}$, $R^{\text{MN}}$, $R^{\text{incl}}_{\text{veto}}$, $R^{\text{MN}}_{\text{veto}}$ increase with increasing $\Delta y$, which is associated with an increase in the phase space for rapidity-ordered radiation, as expected in the BFKL evolution. At the highest $\Delta y$, the increase gives way to a decrease, which is associated with the kinematic restrictions on the emission of hadronic jets additional to the «exclusive» dijet. The ratios $R^{\text{incl}}$ and $R^{\text{MN}}$ increase faster at the energy $\sqrt{s} = 7$ TeV than at 2.76 TeV, and the transition from increase to decrease is observed at larger values of $\Delta y$.
3. A comparison of the ratios of cross sections with veto $R^{\text{incl}}$, $R^{\text{MN}}$, $R^{\text{incl}}_{\text{veto}}$, $R^{\text{MN}}_{\text{veto}}$ with the predictions of MC generators and analytical calculations based on the GLAPD evolution show that the GLAPD calculations without taking into account the color coherence predict a decrease in the ratios with

increasing $\Delta y$, which contradicts the experimental results. The introduction of color coherence leads to a change in the behavior of predictions based on the GLAPD evolution, namely this leads to an increase in the ratios with increasing $\Delta y$. Only the predictions of the PYTHIA8 generator, based on the LO+LL GLAPD and the dipole model of color coherence, are in satisfactory agreement with the experimental results. Although there is some (at the level of two standard deviations) local deviation of the PYTHIA8 predictions from the experimental results for $R^{\mathrm{MN}}_{\mathrm{veto}}$. The difference between the predictions of the generators PYTHIA8, HERWIG++ and the calculation based on the BMS evolution, increasing with increase of $\Delta y$, indicates a strong dependence on the implementation of color coherence models, which, in turn, indicates the need to use the BFKL approximation as a formalism that consistently and correctly takes into account the main contributions at large $\Delta y$. The inclusion of NLO perturbation theory corrections into the calculation based on the LL GLAPD using the MC generator POWHEG does not improve the agreement of the predictions with the ratio measurements.

4. The predictions of the LL BFKL-based generator HEJ+ARIADNE greatly overestimate the growth of cross section ratios with veto $R^{\mathrm{incl}}$, $R^{\mathrm{MN}}$, $R^{\mathrm{incl}}_{\mathrm{veto}}$, and $R^{\mathrm{MN}}_{\mathrm{veto}}$, indicating the need to obtain the NLL BFKL-based predictions for these observables.
5. Predictions for the ratios of the MN dijet cross sections at various $\sqrt{s}$ energies $R^{\mathrm{MN}}_{13/2.76}$, $R^{\mathrm{MN}}_{8/2.76}$ and $R^{\mathrm{MN}}_{13/8}$, made in the NLL BFKL and LO+LL GLAPD approximations, show the sensitivity of these ratios to the BFKL effects. These ratios can be measured in the experiments at the LHC.
6. A comparison of the calculation results, based on the evolution of the BMS, of the ratio of the inclusive cross section to the veto cross section $R^{\mathrm{incl}}$, when the veto is applied over the entire rapidity range, shows that the violation of the veto is overestimated in the region where $\Delta y$ is small between the jets forming the inclusive pair. This is explained by the overestimation of violation of the veto outside the $\Delta y$ region. Regions outside $\Delta y$ extend to high rapidity $|y| < y_{\max} = 4.7$. At high rapidity, the values of polar angles between successive radiations become small, and the BMS radiation becomes harder, violating the main approximation used in

the BMS evolution, i.e. violating the approximation of soft gluon radiation at large angles. Thus, BMS evolution is not applicable at large rapidities.

7. The comparison of the calculation results based on the evolution of the BMS for the ratios of cross sections with veto $R^{\mathrm{MN}}$ and $R^{\mathrm{MN}}_{\mathrm{veto}}$ shows that the energy flow does not provide enough radiation to achieve agreement with the experimental results when $p_{\perp\mathrm{min}} = p_{\perp\mathrm{veto}}$, that is, when there is no phase space for the development of a $p_\perp$-ordered GLAPD parton cascade. Moreover, BMS evolution predicts a weaker dependence on $\sqrt{s}$ than observed in the experimental CMS data. This also indicates the need to develop methods for calculating the impact of the veto condition in $p_\perp$ on additional jets, based on the BFKL evolution, since this evolution is characterized by the diffusion in $p_\perp$ and explicit dependence on $\sqrt{s}$.

Finally, the author expresses gratitude and great appreciation to the scientific supervisor Kim Victor Timofeevich for support, assistance, discussion of the results and scientific guidance, as well as to the chair of Experimental Nuclear Physics Department of SPBPU Berdnikov Yaroslav Alexandrovich for support, assistance, discussion of the results. The author also thanks Ryskin Mikhail Grigorievich for discussing the results and valuable comments, Murzin Victor Aleksandrovich, Oreshkin Vadim Anatolevich and Safronov Grigory Borisovich for assistance in mastering the software, assistance in MC modeling and for discussing the results. The author thanks Daria Kunitsyna for help with the preparation of the manuscript. The author thanks the staff of the High Energy Physics Division of NRC «Kurchatov Institute»-PNPI, and the Department of Experimental Nuclear Physics of SPBPU. The author thanks his colleagues Yuri Mitrankov, Maria Mitrankova, Daria Larionova, Sergei Zharko, Daniil Suetin, Dmitry Kotov, Malik Sultanov, Dmitry Sosnov and Andrei Zelenov for friendly and stimulating creative research environment. The author expresses special gratitude to his mother Egorova Nadezhda Ivanovna, his loved ones, relatives and friends for their support and belief in success for many years.

## List of abbreviations and symbols

| | |
|---|---|
| $\alpha_s$ | strong coupling constant, p. 18 |
| $\eta$ | pseudorapidity, p. 31 |
| $\hat{}$ | hat indicates that the variable belongs to the parton-parton system, p. 20 |
| $Q$ | hard scale, p. 5 |
| $s_0$ | Gribov's parameter, which determines the transition to the asymptotic high-energy semi-hard regime., p. 21 |
| ARIADNE | MC generator for the dipole paroton shower and hadronisation modelling, p. 10 |
| CASCADE | MC generator, based on the evolution equation of Catani – Ciafaloni – Fiorani – Marchesini, p. 12 |
| $\Delta y$ | rapidity separation between the jets forming a dijet, p. 6 |
| HEJ | MC generator, based on the LL BFKL approximation, p. 10 |
| HERWIG | MC generator based on LO+LL GLAPD using color coherence implemented in the form of angular ordering, p. 6 |
| $\Lambda_{\mathrm{QCD}}$ | QCD scale, p. 5 |
| POWHEG | MC generator for modelling the hard subprocess in the NLO of perturbation theory, p. 10 |
| $pp$ | proton-proton, p. 7 |
| $p_\perp$ | component of momentum which is transverse to the beam axis, p. 7 |
| PYTHIA8 | MC generator based on LO+LL GLAPD using color coherence, implemented in the form of a dipole cascade, p. 6 |
| $R^{\mathrm{incl}}$ | ratio of the inclusive to the «exclusive» dijet production cross sections, see Eq. (2) |
| $R^{\mathrm{incl}}_{\mathrm{veto}}$ | ratio of the inclusive to the «exclusive» with veto dijet production cross sections, see Eq. (2) |
| $R^{\mathrm{MN}}$ | ratio of the MN to the «exclusive» dijet production cross sections, see Eq. (2) |
| $R^{\mathrm{MN}}_{8/2.76}$ | ratio of the MN cross section at $\sqrt{s} = 8$ TeV to the MN cross section at $\sqrt{s} = 2.76$ TeV, p. 11 |

| | |
|---|---|
| $R^{\mathrm{MN}}_{13/8}$ | ratio of the MN cross section at $\sqrt{s} = 13$ TeV to the MN cross section at $\sqrt{s} = 8$ TeV, p. 11 |
| $R^{\mathrm{MN}}_{13/2.76}$ | ratio of the MN cross section at $\sqrt{s} = 13$ TeV to the MN cross section at $\sqrt{s} = 2.76$ TeV, p. 11 |
| $R^{\mathrm{MN}}_{\mathrm{veto}}$ | ratio of the MN to the «exclusive» with veto dijet production cross sections, see Eq. (2) |
| $\sigma^{\mathrm{excl}}$ | «exclusive» dijet production cross section, p. 8 |
| $\sigma^{\mathrm{incl}}$ | inclusive dijet production cross section, p. 8 |
| $\sigma^{\mathrm{MN}}$ | MN dijet production cross section , p. 8 |
| $\sigma^{\mathrm{excl}}_{\mathrm{veto}}$ | «exclusive» with veto dijet production cross section, p. 8 |
| SHERPA | MC generator simulating the tree parton subprocess $2 \to n$ and the LL GLAPD parton shower, p. 28 |
| $\sqrt{s}$ | ceter of mass energy, p. 5 |
| $y$ | rapidity, p. 6 |
| ak5PF | hadronic jets reconstructed by the anti-$k_\perp$ algorithm, with a jet size parameter of 0.5, based on particles reconstructed by the Particle-Flow algorithm, p. 46 |
| ATLAS | A Toroidal LHC ApparatuS, experiment at the LHC, p. 7 |
| BFKL | Balitsky–Fadin–Kuraev–Lipatov, p. 5 |
| BFKLP | Brodsky–Fadin–Kim–Lipatov–Pivovarov, p. 22 |
| BLM | Brodsky–Lepage–Mackenzie, p. 22 |
| BMS | Banfi–Marchesini–Smye, p. 10 |
| CDF | Collider Detector at Fermilab, experiment at the Tevatron, p. 7 |
| CMS | Compact Muon Solenoid, experiment at the LHC, p. 7 |
| CSC | Cathode Strip Chambers of the CMS detector, p. 43 |
| D0 | experiment at the Tevatron, p. 7 |
| DIS | deeply inelastic scattering, p. 17 |
| DoubleJet20 | trigger HLT_PADoubleJet20_ForwardBackward_v1, p. 48 |
| DT | Drift Tubes of the CMS detector, p. 43 |
| EB | ECAL Barrel of the CMS detector, p. 38 |
| ECAL | Electromagnetic Calorimeter of the CMS detector, p. 38 |
| EE | ECAL Endcap of the CMS detector, p. 38 |
| FASTJET | software package implementing algorithms for reconstructing hadronic jets, p. 46 |

| | |
|---|---|
| FCC | Future Circular Collider, p. 30 |
| ForJet20Eta3 | trigger HLT_PAForJet20Eta3_v1, p. 48 |
| GEANT4 | software package for detector simulation, p. 56 |
| GLAPD | Gribov–Lipatov–Altarelli–Parisi–Dokshitzer, p. 5 |
| H1 | experiment at the HERA collider, p. 7 |
| HB | HCAL Barrel of the CMS detector, p. 40 |
| HCAL | Hadronic Calorimeter of the CMS detector, p. 38 |
| HE | HCAL Endcap of the CMS detector, p. 40 |
| HE-LHC | High Energy LHC, p. 30 |
| HERA | Hadron–Electron Ring Accelerator, electron-proton collider, DESY, Hamburg, Germany, p. 5 |
| HF | HCAL Forward, forward hadronic calorimeter of the CMS detector, p. 38 |
| HLT | High Level Trigger, p. 45 |
| HO | HCAL Outer of the CMS detector, p. 40 |
| ISR | initial state radiation, p. 126 |
| JER | Jet Energy Resolution, p. 68 |
| JES | Jet Energy Scale, p. 68 |
| Jet20 | trigger HLT_PAJet20_NoJetID_v1, p. 47 |
| L1 | Level 1 trigger, p. 45 |
| LHC | Large Hadron Collider, CERN, Geneva, Switzerland, p. 5 |
| LL | leading logarithmic, p. 5 |
| LO | leading order, p. 10 |
| Lumi | Luminosity, p. 68 |
| MC | Monte Carlo, p. 6 |
| MCS | Monte Carlo Statictics, p. 68 |
| MD | Model Dependence, p. 68 |
| MinBias | trigger HLT_PAMinBiasHF_OR_v1, p. 47 |
| MN | Mueller-Navelet, p. 7 |
| NLL | next-to-leading logarithmic, p. 5 |
| NLO | next-to-leading order, p. 10 |
| PDF | parton distribution function, p. 18 |
| PF | Particle-Flow is the event reconstruction algorithm with particle identification, p. 44 |

| | |
|---|---|
| PIXEL | pixel tracker, part of the CMS detector tracker, p. 36 |
| Preshower | preshower detector of ECAL of the CMS detector, p. 38 |
| PU | pileup, overlap of $pp$ collisions in the same or adjacent intersections of beam bunches, p. 34 |
| QCD | quantum chromodynamics, p. 5 |
| ROOT | software package that provides a framework for data processing and analysis, p. 65 |
| RooUnfold | software package that implements various unfolding methods, p. 65 |
| RPC | Resistive Plate Chambers of the CMS detector, p. 43 |
| SVD | A software package that implements the unfolding method based on likelihood maximization with Tikhonov regularization based on singular value decomposition of the migration matrix, p. 65 |
| TEC | Tracker Endcaps, part of the CMS detector tracker, p. 36 |
| TEC | Trigger Efficiency Corrections, p. 68 |
| Tevatron | proton-antiproton collider, Fermilab, Batavia, USA, p. 5 |
| TIB | Tracker Inner Barrel, part of the CMS detector tracker, p. 36 |
| TID | Tracker Inner Disk, part of the CMS detector tracker, p. 36 |
| TOB | Tracker Outer Barrel, part of the CMS detector tracker, p. 36 |
| TOTEM | TOTal Elastic and diffractive cross section Measurement, experiment at the LHC, p. 7 |
| TUnfold | software package that implements the unfolding method based on likelihood maximization with Tikhonov regularization, p. 65 |
| UPDFs | unintegrated parton distribution functions, p. 29 |
| WLS | Wave Length Shifting, p. 41 |
| ZeroBias | trigger HLT_PAZeroBiasPixel_SingleTrack_v1, p. 47 |
| ZEUS | experiment at the HERA collider, p. 7 |

## Bibliography


1. *Kuraev E. A.*, *Lipatov L. N.*, *Fadin V. S.* Multi-Reggeon processes in the Yang-Mills theory // Sov. Phys. JETP. — 1976. — Vol. 44. — P. 443.
2. *Kuraev E. A.*, *Lipatov L. N.*, *Fadin V. S.* The Pomeranchuk singularity in nonabelian gauge theories // Sov. Phys. JETP. — 1977. — Vol. 45. — P. 199.
3. *Balitsky I. I.*, *Lipatov L. N.* The Pomeranchuk singularity in quantum chromodynamics // Sov. J. Nucl. Phys. — 1978. — Vol. 28. — P. 822.
4. *Gribov V. N.*, *Lipatov L. N.* Deep inelastic e p scattering in perturbation theory // Sov. J. Nucl. Phys. — 1972. — Vol. 15. — P. 438.
5. *Gribov V. N.*, *Lipatov L. N.* e+e- pair annihilation and deep inelastic ep scattering in perturbation theory // Sov. J. Nucl. Phys. — 1972. — Vol. 15. — P. 675.
6. *Lipatov L. N.* The parton model and perturbation theory // Sov. J. Nucl. Phys. — 1975. — Vol. 20. — P. 94.
7. *Altarelli G.*, *Parisi G.* Asymptotic freedom in parton language // Nucl. Phys. B. — 1977. — Vol. 126. — P. 298. — DOI: 10.1016/0550-3213(77)90384-4.
8. *Dokshitzer Y. L.* Calculation of the structure functions for deep inelastic scattering and e+e- annihilation by perturbation theory in quantum chromodynamics. // Sov. Phys. JETP. — 1977. — Vol. 46. — P. 641.
9. HERA - A Proposal for a Large Electron Proton Colliding Beam Facility at DESY : tech. rep. / J. L. Augneres [et al.]. — Hamburg, 1981. — P. 292. — DESY-HERA-81—10. — DOI: 10.3204/PUBDB-2017-01301. — URL: https://bib-pubdb1.desy.de/record/318643.
10. Design Report Tevatron 1 project : tech. rep. — Batavia, 1984. — P. 518. — FERMILAB-DESIGN-1984—01. — URL: https://cds.cern.ch/record/1478620.
11. LHC Design Report / O. S. Brüning [et al.]. — Geneva : CERN, 2004. — (CERN Yellow Reports: Monographs). — DOI: 10.5170/CERN-2004-003-V-1. — URL: https://cds.cern.ch/record/782076.

12. *Fadin V. S.*, *Lipatov L. N.* BFKL pomeron in the next-to-leading approximation // Phys. Lett. B. — 1998. — Vol. 429. — P. 127—134. — DOI: 10.1016/S0370-2693(98)00473-0. — arXiv: hep-ph/9802290.

13. *Ciafaloni M.*, *Camici G.* Energy scale(s) and next-to-leading BFKL equation // Phys. Lett. B. — 1998. — Vol. 430. — P. 349—354. — DOI: 10.1016/S0370-2693(98)00551-6. — arXiv: hep-ph/9803389.

14. The QCD pomeron with optimal renormalization / S. J. Brodsky [et al.] // JETP Lett. — 1999. — Vol. 70. — P. 155—160. — DOI: 10.1134/1.568145. — arXiv: hep-ph/9901229.

15. A comprehensive guide to the physics and usage of PYTHIA 8.3 / C. Bierlich [et al.]. — 2022. — Mar. — DOI: 10.21468/SciPostPhysCodeb.8. — arXiv: 2203.11601 [hep-ph].

16. Herwig 7.0/Herwig++ 3.0 release note / J. Bellm [et al.] // Eur. Phys. J. C. — 2016. — Vol. 76, № 4. — P. 196. — DOI: 10.1140/epjc/s10052-016-4018-8. — arXiv: 1512.01178 [hep-ph].

17. *Mueller A. H.*, *Navelet H.* An inclusive minijet cross section and the bare pomeron in QCD // Nucl. Phys. B. — 1987. — Vol. 282. — P. 727. — DOI: 10.1016/0550-3213(87)90705-X.

18. *Kim V. T.*, *Pivovarov G. B.* BFKL QCD pomeron in high energy hadron collisions: inclusive dijet production // Phys. Rev. D. — 1996. — Vol. 53. — P. 6. — DOI: 10.1103/PhysRevD.53.R6. — arXiv: hep-ph/9506381 [hep-ph].

19. Forward dijets with wide rapidity separation in pp-collisions at LHC and Tevatron: dijet ratios and azimuthal decorrelations / V. B. Gavrilov [et al.] // Nucl. Phys. B Proc. Suppl. / ed. by S. Dubnička, A. Z. Dubničková, E. Bartoš. — 2013. — Vol. 245. — P. 153. — DOI: 10.1016/j.nuclphysbps.2013.10.029.

20. *Del Duca V.*, *Schmidt C. R.* Mini - jet corrections to Higgs production // Phys. Rev. D. — 1994. — Vol. 49. — P. 177—182. — DOI: 10.1103/PhysRevD.49.177. — arXiv: hep-ph/9305346.

21. *Stirling W. J.* Production of jet pairs at large relative rapidity in hadron hadron collisions as a probe of the perturbative pomeron // Nucl. Phys. B. — 1994. — Vol. 423. — P. 56—79. — DOI: 10.1016/0550-3213(94)90565-7. — arXiv: hep-ph/9401266.

22. *Sabio Vera A.*, *Schwennsen F.* The Azimuthal decorrelation of jets widely separated in rapidity as a test of the BFKL kernel // Nucl. Phys. B. — 2007. — Vol. 776. — P. 170—186. — DOI: 10.1016/j.nuclphysb.2007.03.050. — arXiv: hep-ph/0702158.

23. *Mueller A. H.*, *Tang W.-K.* High-energy parton-parton elastic scattering in QCD // Phys. Lett. B. — 1992. — Vol. 284. — P. 123—126. — DOI: 10.1016/0370-2693(92)91936-4.

24. *Enberg R.*, *Ingelman G.*, *Motyka L.* Hard color singlet exchange and gaps between jets at the Tevatron // Phys. Lett. B. — 2002. — Vol. 524. — P. 273—282. — DOI: 10.1016/S0370-2693(01)01379-X. — arXiv: hep-ph/0111090.

25. *Kepka O.*, *Marquet C.*, *Royon C.* Gaps between jets in hadronic collisions // Phys. Rev. D. — 2011. — Vol. 83. — P. 034036. — DOI: 10.1103/PhysRevD.83.034036. — arXiv: 1012.3849 [hep-ph].

26. Transverse energy and forward jet production in the low x regime at HERA / S. Aid [et al.] // Phys. Lett. B. — 1995. — Vol. 356. — P. 118—128. — DOI: 10.1016/0370-2693(95)00804-T. — arXiv: hep-ex/9506012.

27. Measurement of the Azimuthal Correlation between the most Forward Jet and the Scattered Positron in Deep-Inelastic Scattering at HERA / F. D. Aaron [et al.] // Eur. Phys. J. C. — 2012. — Vol. 72. — P. 1910. — DOI: 10.1140/epjc/s10052-012-1910-8. — arXiv: 1111.4227 [hep-ex].

28. Forward jet production in deep inelastic scattering at HERA / J. Breitweg [et al.] // Eur. Phys. J. C. — 1999. — Vol. 6. — P. 239—252. — DOI: 10.1007/s100529801018. — arXiv: hep-ex/9805016.

29. Forward-jet production in deep inelastic ep scattering at HERA / S. Chekanov [et al.] // Eur. Phys. J. C. — 2007. — Vol. 52. — P. 515—530. — DOI: 10.1140/epjc/s10052-007-0418-0. — arXiv: 0707.3093 [hep-ex].

30. The Azimuthal decorrelation of jets widely separated in rapidity / S. Abachi [et al.] // Phys. Rev. Lett. — 1996. — Vol. 77. — P. 595—600. — DOI: 10.1103/PhysRevLett.77.595. — arXiv: hep-ex/9603010.

31. Probing Hard Color-Singlet Exchange in $p\bar{p}$ Collisions at $\sqrt{s} = 630$ GeV and 1800 GeV / B. Abbott [et al.] // Phys. Lett. B. — 1998. — Vol. 440. — P. 189—202. — DOI: 10.1016/S0370-2693(98)01238-6. — arXiv: hep-ex/9809016.

32. Probing BFKL dynamics in the dijet cross section at large rapidity intervals in $p\bar{p}$ collisions at $\sqrt{s} = 1800$ GeV and 630-GeV / B. Abbott [et al.] // Phys. Rev. Lett. — 2000. — Vol. 84. — P. 5722—5727. — DOI: 10.1103/PhysRevLett.84.5722. — arXiv: hep-ex/9912032.

33. Dijet production by color - singlet exchange at the Fermilab Tevatron / F. Abe [et al.] // Phys. Rev. Lett. — 1998. — Vol. 80. — P. 1156—1161. — DOI: 10.1103/PhysRevLett.80.1156.

34. Measurement of dijet production with a veto on additional central jet activity in $pp$ collisions at $\sqrt{s} = 7$ TeV using the ATLAS detector / G. Aad [et al.] // JHEP. — 2011. — Vol. 09. — P. 053. — DOI: 10.1007/JHEP09(2011)053. — arXiv: 1107.1641 [hep-ex].

35. Measurements of jet vetoes and azimuthal decorrelations in dijet events produced in $pp$ collisions at $\sqrt{s} = 7$ TeV using the ATLAS detector / G. Aad [et al.] // Eur. Phys. J. C. — 2014. — Vol. 74, № 11. — P. 3117. — DOI: 10.1140/epjc/s10052-014-3117-7. — arXiv: 1407.5756 [hep-ex].

36. Measurement of the inclusive production cross sections for forward jets and for dijet events with one forward and one central jet in $pp$ collisions at $\sqrt{s} = 7$ TeV / S. Chatrchyan [et al.] // JHEP. — 2012. — Vol. 06. — P. 036. — DOI: 10.1007/JHEP06(2012)036. — arXiv: 1202.0704 [hep-ex].

37. Ratios of dijet production cross sections as a function of the absolute difference in rapidity between jets in proton-proton collisions at $\sqrt{s} = 7$ TeV / S. Chatrchyan [et al.] // Eur. Phys. J. C. — 2012. — Vol. 72. — P. 2216. — DOI: 10.1140/epjc/s10052-012-2216-6. — arXiv: 1204.0696 [hep-ex].

38. Azimuthal decorrelation of jets widely separated in rapidity in pp collisions at $\sqrt{s} = 7$ TeV / V. Khachatryan [et al.] // JHEP. — 2016. — Vol. 08. — P. 139. — DOI: 10.1007/JHEP08(2016)139. — arXiv: 1601.06713 [hep-ex].

39. Study of dijet events with a large rapidity gap between the two leading jets in pp collisions at $\sqrt{s} = 7$ TeV / A. M. Sirunyan [et al.] // Eur. Phys. J. C. — 2018. — Vol. 78, № 3. — P. 242. — DOI: 10.1140/epjc/s10052-018-5691-6. — arXiv: 1710.02586 [hep-ex]. — [Erratum: Eur.Phys.J.C 80, 441 (2020)].

40. Hard color-singlet exchange in dijet events in proton-proton collisions at $\sqrt{s} =$ 13 TeV / A. M. Sirunyan [et al.] // Phys. Rev. D. — 2021. — Vol. 104. — P. 032009. — DOI: 10.1103/PhysRevD.104.032009. — arXiv: 2102.06945 [hep-ex].

41. *Sjostrand T.*, *Mrenna S.*, *Skands P. Z.* A Brief Introduction to PYTHIA 8.1 // Comput. Phys. Commun. — 2008. — Vol. 178. — P. 852—867. — DOI: 10.1016/j.cpc.2008.01.036. — arXiv: 0710.3820 [hep-ph].

42. Herwig++ Physics and Manual / M. Bahr [et al.] // Eur. Phys. J. — 2008. — Vol. C58. — P. 639—707. — DOI: 10.1140/epjc/s10052-008-0798-9. — arXiv: 0803.0883 [hep-ph].

43. Jet pair production in POWHEG / S. Alioli [и др.] // JHEP. — 2011. — Т. 04. — С. 081. — DOI: 10.1007/JHEP04(2011)081. — arXiv: 1012.3380 [hep-ph].

44. HEJ 2.1: High-energy resummation with vector bosons and next-to-leading logarithms / J. R. Andersen [et al.] // Comput. Phys. Commun. — 2022. — Vol. 278. — P. 108404. — DOI: 10.1016/j.cpc.2022.108404. — arXiv: 2110.15692 [hep-ph].

45. *Lonnblad L.* ARIADNE version 4: a program for simulation of QCD cascades implementing the colour dipole model // Comput. Phys. Commun. — 1992. — Vol. 71. — P. 15. — DOI: 10.1016/0010-4655(92)90068-A.

46. Mueller-Navelet small-cone jets at LHC in next-to-leading BFKL / F. Caporale [и др.] // Nucl. Phys. B. — 2013. — Т. 877. — С. 73—94. — DOI: 10.1016/j.nuclphysb.2013.09.013. — arXiv: 1211.7225 [hep-ph].

47. *Ducloue B.*, *Szymanowski L.*, *Wallon S.* Confronting Mueller-Navelet jets in NLL BFKL with LHC experiments at 7 TeV // JHEP. — 2013. — Т. 05. — С. 096. — DOI: 10.1007/JHEP05(2013)096. — arXiv: 1302.7012 [hep-ph].

48. Brodsky-Lepage-Mackenzie optimal renormalization scale setting for semihard processes / F. Caporale [и др.] // Phys. Rev. D. — 2015. — Т. 91, № 11. — С. 114009. — DOI: 10.1103/PhysRevD.91.114009. — arXiv: 1504.06471 [hep-ph].

49. *Banfi A.*, *Marchesini G.*, *Smye G.* Away from jet energy flow // JHEP. — 2002. — Vol. 08. — P. 006. — DOI: 10.1088/1126-6708/2002/08/006. — arXiv: hep-ph/0206076.

50. The CMS experiment at the CERN LHC / S. Chatrchyan [et al.] // JINST. — 2008. — Vol. 3. — S08004. — DOI: 10.1088/1748-0221/3/08/S08004.

51. The ATLAS Experiment at the CERN Large Hadron Collider / G. Aad [et al.] // JINST. — 2008. — Vol. 3. — S08003. — DOI: 10.1088/1748-0221/3/08/S08003.

52. CASCADE3 A Monte Carlo event generator based on TMDs / S. Baranov [et al.] // Eur. Phys. J. C. — 2021. — Vol. 81, № 5. — P. 425. — DOI: 10.1140/epjc/s10052-021-09203-8. — arXiv: 2101.10221 [hep-ph].

53. *Feynman R. P.* Very high-energy collisions of hadrons // Phys. Rev. Lett. / ed. by L. M. Brown. — 1969. — Vol. 23. — P. 1415—1417. — DOI: 10.1103/PhysRevLett.23.1415.

54. *Bjorken J. D.*, *Paschos E. A.* Inelastic Electron Proton and gamma Proton Scattering, and the Structure of the Nucleon // Phys. Rev. — 1969. — Vol. 185. — P. 1975—1982. — DOI: 10.1103/PhysRev.185.1975.

55. *Bjorken J. D.* AN INEQUALITY FOR ELECTRON AND MUON SCATTERING FROM NUCLEONS // Phys. Rev. Lett. — 1966. — Vol. 16. — P. 408. — DOI: 10.1103/PhysRevLett.16.408.

56. *Bjorken J. D.* Asymptotic Sum Rules at Infinite Momentum // Phys. Rev. — 1969. — Vol. 179. — P. 1547—1553. — DOI: 10.1103/PhysRev.179.1547.

57. *Marage P.* Hadronic structure, low x physics and diffraction // 1999 International Europhysics Conference on High-Energy Physics. — 07/1999. — P. 71—90. — arXiv: hep-ph/9911426.

58. *Martin A. D.* Proton structure, Partons, QCD, DGLAP and beyond // Acta Phys. Polon. B / ed. by R. Fiore, A. Papa, C. Royon. — 2008. — Vol. 39. — P. 2025—2062. — arXiv: 0802.0161 [hep-ph].

59. A Measurement of sigma(tot) (gamma p) at s**(1/2) = 210-GeV / M. Derrick [et al.] // Phys. Lett. B. — 1992. — Vol. 293. — P. 465—477. — DOI: 10.1016/0370-2693(92)90914-P.

60. Total photoproduction cross-section measurement at HERA energies / T. Ahmed [et al.] // Phys. Lett. B. — 1993. — Vol. 299. — P. 374—384. — DOI: 10.1016/0370-2693(93)90277-O.

61. Measurement of the Proton - anti-Proton Total and Elastic Cross-Sections at the CERN SPS Collider / M. Bozzo [et al.] // Phys. Lett. B. — 1984. — Vol. 147. — P. 392—398. — DOI: 10.1016/0370-2693(84)90139-4.

62. Antiproton-proton cross sections at 200 and 900 GeV c.m. energy / G. J. Alner [et al.] // Z. Phys. C. — 1986. — Vol. 32. — P. 153—161. — DOI: 10.1007/BF01552491.

63. Measurement of ρ, the Ratio of the Real to Imaginary Part of the $\bar{p}p$ Forward Elastic Scattering Amplitude, at $\sqrt{s}$ = 1.8-TeV / N. A. Amos [et al.] // Phys. Rev. Lett. — 1992. — Vol. 68. — P. 2433—2436. — DOI: 10.1103/PhysRevLett.68.2433.

64. Measurement of the $\bar{p}p$ Total Cross-Section at $\sqrt{s} = 546$ GeV and 1800 GeV / F. Abe [et al.] // Phys. Rev. D. — 1994. — Vol. 50. — P. 5550—5561. — DOI: 10.1103/PhysRevD.50.5550.

65. Total hadronic cross-section of photon-photon interactions at LEP / G. Abbiendi [и др.] // Eur. Phys. J. C. — 2000. — Т. 14. — С. 199—212. — DOI: 10.1007/s100520000352. — arXiv: hep-ex/9906039.

66. Cross-section of hadron production in gamma gamma collisions at LEP / M. Acciarri [et al.] // Phys. Lett. B. — 1997. — Vol. 408. — P. 450—464. — DOI: 10.1016/S0370-2693(97)00933-7.

67. Luminosity-Independent Measurement of the Proton-Proton Total Cross Section at $\sqrt{s} = 8$ TeV / G. Antchev [et al.] // Phys. Rev. Lett. — 2013. — Vol. 111, № 1. — P. 012001. — DOI: 10.1103/PhysRevLett.111.012001.

68. Luminosity-independent measurements of total, elastic and inelastic cross-sections at $\sqrt{s} = 7$ TeV / G. Antchev [et al.] // EPL. — 2013. — Vol. 101, № 2. — P. 21004. — DOI: 10.1209/0295-5075/101/21004.

69. Measurement of the total cross section from elastic scattering in pp collisions at $\sqrt{s} = 7$ TeV with the ATLAS detector / G. Aad [et al.] // Nucl. Phys. B. — 2014. — Vol. 889. — P. 486—548. — DOI: 10.1016/j.nuclphysb.2014.10.019. — arXiv: 1408.5778 [hep-ex].

70. *Brodsky S. J.*, *Lepage G. P.*, *Mackenzie P. B.* On the Elimination of Scale Ambiguities in Perturbative Quantum Chromodynamics // Phys. Rev. D. — 1983. — T. 28. — C. 228. — DOI: 10.1103/PhysRevD.28.228.

71. *Del Duca V.*, *Schmidt C. R.* Dijet production at large rapidity intervals // Phys. Rev. D. — 1994. — Vol. 49. — P. 4510—4516. — DOI: 10.1103/PhysRevD.49.4510. — arXiv: hep-ph/9311290.

72. *Corke R.*, *Sjostrand T.* Interleaved Parton Showers and Tuning Prospects // JHEP. — 2011. — Vol. 03. — P. 032. — DOI: 10.1007/JHEP03(2011)032. — arXiv: 1011.1759 [hep-ph].

73. Extraction and validation of a new set of CMS PYTHIA8 tunes from underlying-event measurements / A. M. Sirunyan [et al.] // Eur. Phys. J. C. — 2020. — Vol. 80, № 1. — P. 4. — DOI: 10.1140/epjc/s10052-019-7499-4. — arXiv: 1903.12179 [hep-ex].

74. Herwig++ 2.5 Release Note / S. Gieseke [et al.]. — 2011.

75. Event generation with SHERPA 1.1 / T. Gleisberg [et al.] // JHEP. — 2009. — Vol. 02. — P. 007. — DOI: 10.1088/1126-6708/2009/02/007. — arXiv: 0811.4622 [hep-ph].

76. *Ciafaloni M.* Coherence Effects in Initial Jets at Small q**2 / s // Nucl. Phys. B. — 1988. — Vol. 296. — P. 49—74. — DOI: 10.1016/0550-3213(88)90380-X.

77. *Catani S.*, *Fiorani F.*, *Marchesini G.* Small x Behavior of Initial State Radiation in Perturbative QCD // Nucl. Phys. B. — 1990. — Vol. 336. — P. 18—85. — DOI: 10.1016/0550-3213(90)90342-B.

78. *Marchesini G.* QCD coherence in the structure function and associated distributions at small x // Nucl. Phys. B. — 1995. — Vol. 445. — P. 49—80. — DOI: 10.1016/0550-3213(95)00149-M. — arXiv: hep-ph/9412327.

79. HE-LHC: The High-Energy Large Hadron Collider: Future Circular Collider Conceptual Design Report Volume 4 / A. Abada [et al.] // Eur. Phys. J. ST. — 2019. — Vol. 228, № 5. — P. 1109—1382. — DOI: 10.1140/epjst/e2019-900088-6.

80. FCC-hh: The Hadron Collider: Future Circular Collider Conceptual Design Report Volume 3 / A. Abada [et al.] // Eur. Phys. J. ST. — 2019. — Vol. 228, № 4. — P. 755—1107. — DOI: 10.1140/epjst/e2019-900087-0.

81. *Egorov A. I.*, *Berdnikov Y. A.* Asymptotic effects in dijet production in proton-proton collisions at extremely high energies // St. Petersburg Polytech. Univ. J. Phys. Math. — 2019. — Vol. 12, № 2. — P. 118—125. — DOI: 10.18721/JPM.12210. — (VAK, WoS).

82. First computation of Mueller Tang processes using a full NLL BFKL approach / D. Colferai [и др.] // JHEP. — 2023. — Т. 06. — С. 091. — DOI: 10.1007/JHEP06(2023)091. — arXiv: 2304.09073 [hep-ph].

83. Description and performance of track and primary-vertex reconstruction with the CMS tracker / S. Chatrchyan [et al.] // JINST. — 2014. — Vol. 9. — P10009. — DOI: 10.1088/1748-0221/9/10/P10009. — arXiv: 1405.6569 [physics.ins-det].

84. *Fruhwirth R.* Application of Kalman filtering to track and vertex fitting // Nucl. Instrum. Meth. — 1987. — Vol. A262. — P. 444—450. — DOI: 10.1016/0168-9002(87)90887-4.

85. Vertex Fitting in the CMS Tracker : tech. rep. / T. Speer [et al.] ; CERN. — Geneva, 2006. — URL: https://cds.cern.ch/record/927395.

86. Particle-flow reconstruction and global event description with the CMS detector / A. M. Sirunyan [et al.] // JINST. — 2017. — Vol. 12. — P10003. — DOI: 10.1088/1748-0221/12/10/P10003. — arXiv: 1706.04965 [physics.ins-det].

87. *Cacciari M.*, *Salam G. P.*, *Soyez G.* The Anti-k(t) jet clustering algorithm // JHEP. — 2008. — Vol. 04. — P. 063. — DOI: 10.1088/1126-6708/2008/04/063. — arXiv: 0802.1189 [hep-ph].

88. *Cacciari M.*, *Salam G. P.*, *Soyez G.* FastJet User Manual // Eur. Phys. J. — 2012. — Vol. C72. — P. 1896. — DOI: 10.1140/epjc/s10052-012-1896-2. — arXiv: 1111.6097 [hep-ph].

89. Jet energy scale and resolution in the CMS experiment in pp collisions at 8 TeV / V. Khachatryan [et al.] // JINST. — 2017. — Vol. 12, № 02. — P02014. — DOI: 10.1088/1748-0221/12/02/P02014. — arXiv: 1607.03663 [hep-ex].

90. The CMS trigger system / V. Khachatryan [et al.] // JINST. — 2017. — Vol. 12. — P01020. — DOI: 10.1088/1748-0221/12/01/P01020. — arXiv: 1609.02366 [physics.ins-det].

91. Calorimeter Jet Quality Criteria for the First CMS Collision Data. — 2010.

92. Description and performance of track and primary-vertex reconstruction with the CMS tracker / S. Chatrchyan [et al.] // JINST. — 2014. — Vol. 9, № 10. — P10009. — DOI: 10.1088/1748-0221/9/10/P10009. — arXiv: 1405.6569 [physics.ins-det].

93. An analysis of unfolding methods for measurement of hadron dijet production cross sections / A. Y. Egorov [et al.] // St. Petersburg Polytech. Univ. J. Phys. Math. — 2019. — Vol. 12, № 3. — P. 123—130. — DOI: 10.18721/JPM.12310. — (VAK, WoS).

94. GEANT4: A Simulation toolkit / S. Agostinelli [et al.] // Nucl. Instrum. Meth. — 2003. — Vol. A506. — P. 250—303. — DOI: 10.1016/S0168-9002(03)01368-8.

95. Determination of Jet Energy Calibration and Transverse Momentum Resolution in CMS / S. Chatrchyan [et al.] // JINST. — 2011. — Vol. 6. — P11002. — DOI: 10.1088/1748-0221/6/11/P11002. — arXiv: 1107.4277 [physics.ins-det].

96. *Schmitt S.* TUnfold: an algorithm for correcting migration effects in high energy physics // JINST. — 2012. — Vol. 7. — T10003. — DOI: 10.1088/1748-0221/7/10/T10003. — arXiv: 1205.6201 [physics.data-an].

97. *Hocker A., Kartvelishvili V.* SVD approach to data unfolding // Nucl. Instrum. Meth. — 1996. — Vol. A372. — P. 469—481. — DOI: 10.1016/0168-9002(95)01478-0. — arXiv: hep-ph/9509307 [hep-ph].

98. *D'Agostini G.* A Multidimensional unfolding method based on Bayes' theorem // Nucl. Instrum. Meth. — 1995. — Vol. A362. — P. 487—498. — DOI: 10.1016/0168-9002(95)00274-X.

99. *Brun R., Rademakers F.* ROOT: An object oriented data analysis framework // Nucl. Instrum. Meth. — 1997. — Vol. A389. — P. 81—86. — DOI: 10.1016/S0168-9002(97)00048-X.

100. *Adye T.* Unfolding algorithms and tests using RooUnfold // Proceedings, PHYSTAT 2011 Workshop on Statistical Issues Related to Discovery Claims in Search Experiments and Unfolding, CERN,Geneva, Switzerland 17-20 January 2011. — CERN. Geneva : CERN, 2011. — P. 313—318. — DOI: 10.5170/CERN-2011-006.313. — arXiv: 1105.1160 [physics.data-an]. — URL: https://inspirehep.net/record/898599/files/arXiv:1105.1160.pdf.

101. New generation of parton distributions with uncertainties from global QCD analysis / J. Pumplin [et al.] // JHEP. — 2002. — Vol. 07. — P. 012. — DOI: 10.1088/1126-6708/2002/07/012. — arXiv: hep-ph/0201195 [hep-ph].

102. PDF4LHC recommendations for LHC Run II / J. Butterworth [et al.] // J. Phys. — 2016. — Vol. G43. — P. 023001. — DOI: 10.1088/0954-3899/43/2/023001. — arXiv: 1510.03865 [hep-ph].

103. Parton distributions for the LHC Run II / R. D. Ball [et al.] // JHEP. — 2015. — Vol. 04. — P. 040. — DOI: 10.1007/JHEP04(2015)040. — arXiv: 1410.8849 [hep-ph].

104. New parton distribution functions from a global analysis of quantum chromodynamics / S. Dulat [et al.] // Phys. Rev. — 2016. — Vol. D93, № 3. — P. 033006. — DOI: 10.1103/PhysRevD.93.033006. — arXiv: 1506.07443 [hep-ph].

105. Parton distributions in the LHC era: MMHT 2014 PDFs / L. A. Harland-Lang [et al.] // Eur. Phys. J. — 2015. — Vol. C75, № 5. — P. 204. — DOI: 10.1140/epjc/s10052-015-3397-6. — arXiv: 1412.3989 [hep-ph].

106. LHAPDF6: parton density access in the LHC precision era / A. Buckley [et al.] // Eur. Phys. J. — 2015. — Vol. C75. — P. 132. — DOI: 10.1140/epjc/s10052-015-3318-8. — arXiv: 1412.7420 [hep-ph].

107. Luminosity Calibration for the 2013 Proton-Lead and Proton-Proton Data Taking : tech. rep. / CERN. — Geneva, 2014. — URL: https://cds.cern.ch/record/1643269.

108. Study of dijet events with large rapidity separation in proton-proton collisions at $\sqrt{s} = 2.76$ TeV / A. I. Egorov, A. Tumasyan, [et al.] // JHEP. — 2022. — Vol. 03. — P. 189. — DOI: 10.1007/JHEP03(2022)189. — arXiv: 2111.04605 [hep-ex]. — (Scopus).

109. *Andersen J. R.*, *Smillie J. M.* Multiple Jets at the LHC with High Energy Jets // JHEP. — 2011. — Vol. 06. — P. 010. — DOI: 10.1007/JHEP06(2011)010. — arXiv: 1101.5394 [hep-ph].

110. *Egorov A. I.* Dijet Events with Large Rapidity Separation in Proton–Proton Collisions at $\sqrt{s}$= 2.76 TeV with CMS Detector // Phys. Atom. Nucl. — 2022. — Vol. 85, № 6. — P. 951. — DOI: 10.1134/S1063778823010192. — (Scopus).

111. *Ivanov D. Y.*, *Papa A.* The next-to-leading order forward jet vertex in the small-cone approximation // JHEP. — 2012. — T. 05. — C. 086. — DOI: 10.1007/JHEP05(2012)086. — arXiv: 1202.1082 [hep-ph].

112. *Kotikov A. V.*, *Lipatov L. N.* NLO corrections to the BFKL equation in QCD and in supersymmetric gauge theories // Nucl. Phys. B. — 2000. — Vol. 582. — P. 19—43. — DOI: 10.1016/S0550-3213(00)00329-1. — arXiv: hep-ph/0004008.

113. *Kotikov A. V.*, *Lipatov L. N.* DGLAP and BFKL equations in the $N = 4$ supersymmetric gauge theory // Nucl. Phys. B. — 2003. — Vol. 661. — P. 19—61. — DOI: 10.1016/S0550-3213(03)00264-5. — arXiv: hep-ph/0208220. — [Erratum: Nucl.Phys.B 685, 405–407 (2004)].

114. *Furman M.* Study of a Nonleading QCD Correction to Hadron Calorimeter Reactions // Nucl. Phys. B. — 1982. — T. 197. — C. 413—445. — DOI: 10.1016/0550-3213(82)90452-7.

115. *Colferai D.*, *Niccoli A.* The NLO jet vertex in the small-cone approximation for kt and cone algorithms // JHEP. — 2015. — T. 04. — C. 071. — DOI: 10.1007/JHEP04(2015)071. — arXiv: 1501.07442 [hep-ph].

116. Longitudinally invariant $K_t$ clustering algorithms for hadron hadron collisions / S. Catani [и др.] // Nucl. Phys. B. — 1993. — T. 406. — C. 187—224. — DOI: 10.1016/0550-3213(93)90166-M.

117. *Ким В. Т.* Померон в вквантовой хромодинамике и асимптотические эффекты при высоких энергиях : дис. ... д-ра физ.-мат. наук : 01.04.02, 01.04.16. — Гатчина, 2003. — 124 с.

118. *'t Hooft G.* Dimensional regularization and the renormalization group // Nucl. Phys. B. — 1973. — Vol. 61. — P. 455—468. — DOI: 10.1016/0550-3213(73)90376-3.

119. Deep Inelastic Scattering Beyond the Leading Order in Asymptotically Free Gauge Theories / W. A. Bardeen [et al.] // Phys. Rev. D. — 1978. — Vol. 18. — P. 3998. — DOI: 10.1103/PhysRevD.18.3998.

120. *Celmaster W.*, *Gonsalves R. J.* QCD Perturbation Expansions in a Coupling Constant Renormalized by Momentum Space Subtraction // Phys. Rev. Lett. — 1979. — Vol. 42. — P. 1435. — DOI: 10.1103/PhysRevLett.42.1435.

121. *Mackenzie P. B.*, *Lepage G. P.* QCD Corrections to the Gluonic Width of the Upsilon Meson // Phys. Rev. Lett. — 1981. — Vol. 47. — P. 1244. — DOI: 10.1103/PhysRevLett.47.1244.

122. *Celmaster W.*, *Gonsalves R. J.* The Renormalization Prescription Dependence of the QCD Coupling Constant // Phys. Rev. D. — 1979. — Vol. 20. — P. 1420. — DOI: 10.1103/PhysRevD.20.1420.

123. Mueller–Navelet jets at 13 TeV LHC: dependence on dynamic constraints in the central rapidity region / F. G. Celiberto [и др.] // Eur. Phys. J. C. — 2016. — Т. 76, № 4. — С. 224. — DOI: 10.1140/epjc/s10052-016-4053-5. — arXiv: 1601.07847 [hep-ph].

124. Parton distributions for the LHC / A. D. Martin [et al.] // Eur. Phys. J. C. — 2009. — Vol. 63. — P. 189—285. — DOI: 10.1140/epjc/s10052-009-1072-5. — arXiv: 0901.0002 [hep-ph].

125. PDF4LHC recommendations for LHC Run II / J. Butterworth [et al.] // Journal of Physics G: Nuclear and Particle Physics. — 2016. — Jan. — Vol. 43, № 2. — P. 023001. — DOI: 10.1088/0954-3899/43/2/023001. — URL: https://dx.doi.org/10.1088/0954-3899/43/2/023001.

126. *Egorov A. I.*, *Kim V. T.* Next-to-leading BFKL evolution for dijets with large rapidity separation at different LHC energies // Phys. Rev. D. — 2023. — Vol. 108, № 1. — P. 014010. — DOI: 10.1103/PhysRevD.108.014010. — arXiv: 2305.19854 [hep-ph]. — (Scopus).

127. A QCD description of the ATLAS jet veto measurement / Y. Hatta [et al.] // Phys. Rev. D. — 2013. — Vol. 87, № 5. — P. 054016. — DOI: 10.1103/PhysRevD.87.054016. — arXiv: 1301.1910 [hep-ph].

128. *Hatta Y.*, *Ueda T.* Jet energy flow at the LHC // Phys. Rev. D. — 2009. — Vol. 80. — P. 074018. — DOI: 10.1103/PhysRevD.80.074018. — arXiv: 0909.0056 [hep-ph].

129. *Marchesini G.* Soft gluon emission at large angles // Gribov-75: Memorial Workshop on Quarks, Hadrons, and Strong Interactions. — 12/2005. — P. 91—104. — DOI: 10.1142/9789812773784_0011. — arXiv: hep-ph/0601068.

130. *Egorov A. Y.*, *Kim V. T.* Production of dijets with large rapidity separation at colliders // J. Phys. Conf. Ser. / ed. by P. Teterin. — 2020. — Vol. 1690, № 1. — P. 012158. — DOI: 10.1088/1742-6596/1690/1/012158. — (Scopus).

131. Transverse momentum dependent parton densities in a proton from the generalized DAS approach / A. V. Kotikov [et al.] // JHEP. — 2020. — Vol. 02. — P. 028. — DOI: 10.1007/JHEP02(2020)028. — arXiv: 1911.01445 [hep-ph].

132. Parton distributions from high-precision collider data / R. D. Ball [et al.] // Eur. Phys. J. C. — 2017. — Vol. 77, № 10. — P. 663. — DOI: 10.1140/epjc/s10052-017-5199-5. — arXiv: 1706.00428 [hep-ph].

## List of the figures

## List of the tables